ELECTRICAL AND MECHANICAL MECHANISMS FOR COLOR VARIATION IN THE SPRAYING OF METALLIC PAINTS

by

STUART INKPEN

B. Eng., Memorial University of Newfoundland
(1982)

S.M., Massachusetts Institute of Technology
(1984)

Submitted in Partial Fulfillment

of the Requirements for the

Degree of

DOCTOR OF PHILOSOPHY

at the

MASSACHUSETTS INSTITUTE OF TECHNOLOGY

April, 1986

Signature of Author.....
Department of Electrical Engineering and Computer Science,
April 29, 1986

Certified by.....
James R. Melcher
Thesis Supervisor

Accepted by.....
Arthur C. Smith
Chairman, Department Committee

Table of Contents

Abstract 11

Acknowledgements 12

Chapter 1 Introduction 13

1.1 Motivation for Electrostatic Painting 14

1.2 General Objective 15

1.3 General Painting Process 16

1.3.1 Paint Atomization 17

1.3.2 Transport of Paint to the Surface 20

1.3.3 Dynamics of the Deposited Paint Layer 22

1.3.4 Curing of Paint 23

1.4 Color Variation using Flaked Paints 23

Chapter 2 Spray Painting Equipment and Paint 28

2.1 Electrostatic Paint Sprayer 28

2.2 Description of Mechanical Spray Gun 32

2.3 Macroscopic Properties of Paint 35

Chapter 3 Orientation of Flake 42

3.1 Orientation Times in Painting Stages 43

3.1.1 Experimental Investigation of Formation and Impact Stages 50

3.1.2 Experimental Investigation of In-flight Stage 58

3.1.3 Experimental Investigation of Post-impact Stage 62

3.1.4 Cross-sections of Mechanical and Electrostatic Paint Samples 62

3.2 Forced Flake Alignment 65

3.2.1 Capacitive Coupling 66

3.2.2 Corona Current 69

Chapter 4 Selective Mass Transfer 76

4.1 Bell-Hochberg Postulate 76

4.2 Characterization of Paint Spraying Devices 78

4.2.1 Analysis of Drop and Flake Distributions at the Paint Surface for an Electrostatic Sprayer 79

4.2.1.1 Sampling Drops at the Paint Surface 80

4.2.1.2 Data Processing Technique 90

4.2.1.3 Results of Electrical Shutter Experiment 94

4.2.2 Analysis of Drop and Flake Distributions both Deposited and in the Overspray of a Mechanical Sprayer 104

4.2.2.1 Drop Sampling: Precipitators for Collection of the Overspray 108

4.2.2.2 Results 110

4.3 Average Flake Deposited and Mass Balance 118

4.3.1 Atomic Absorption Measurements 118

4.3.2 Mass Balance 121

4.4 Contrasts: Electrostatic and Mechanical Spraying 122

Chapter 5 Corona Induced Color Control 127

5.1 Spatial Resolution of Corona Current 128

5.2 Observed Flake Orientation 133

5.3 Scaling with Field Duration and Intensity for a Newtonian Fluid 136

5.4 A Technique for Determining the Viscoelastic Nature of Sprayed Paint 141

5.5 Flake Orientation in a Viscoelastic Fluid 148

5.6 Effects of the Corona Current other than Flake Orientation 153

Chapter 6 Conclusions 159

6.1 Dominant Mechanism for Color Variation 159

6.2 Second Order Effects 166

6.3 Characterization of a Paint Spraying Process 167

6.4 Corona Induced Color Control 169

6.5 Airless Paint Sprayer 171

6.6 Computer Simulation 172

Appendix A Electrostatic Airless Paint Sprayer 175

A.1 Configuration 176

A.2 Experimental Results 181

A.3 Implications of the Experimental Results 200

A.4 Industrial Feasibility 203

Appendix B Computer Simulation of Drop Flight 207

B.1 State Space Model 207

B.2 Continuum Model 220

Appendix C Solvent Diffusion in a Paint Drop 224

Appendix D Drop Height versus Drop Diameter 230

Appendix E Electrical Shutter Data 234

Appendix F Mechanical Sprayer Results 256

List of Figures and Tables

1.1 Stages of Paint Spraying 18

1.2 Color Space 25

2.1 Configuration of Electrostatic Painting Facility 29

2.2 Detail: Electrostatic Paint Sprayer 30

2.3 Detail: Spray Head for Binks Gun 34

2.4 Electrical Properties of Paint Mixed for Spraying 36

2.5 Electrical Properties of Unmixed Paint 37

2.6 Viscosity vs. Strain Rate 38

2.7 Electrical Properties of Sprayed Paint 40

3.1 Proposed Drop Shapes 44

3.2 Single Drop Sprayer 51

3.3 Single Drop Sprayer: Breakup of Jet 56

3.4 Single Drop Sprayer: Kink Instability 57

3.5 Optical Measurement of In-flight Orientation 59

3.6 Apparatus to Control Drop Charge and Imposed Field 60

3.7 Cross-section: Mechanically Sprayed Paint Layer 63

3.8 Cross-section: Electrostatically Sprayed Paint Layer 64

3.9 Capacitive Coupling to the Paint Layer 67

3.10 Capacitive Coupling Electrode Structure 68

3.11 Single Corona Pin Configuration 71

3.12 Cross-section: Paint Layer Exposed to Corona Current 72

3.13 Sample Pattern in Metallic Paint 74

4.1 Electrical Shutter: Electric Field Plot 83

4.2 Electrical Shutter: X-directed Electric Field 84

4.3 Single Plate Electrical Shutter 88

4.4 Back Illuminated Drops 91

4.5 Configuration of Electrical Shutter Target 95

4.6 Mass vs. Radius 97

4.7 Mass Percent Aluminum vs. Radius 98

4.8 Average Drop Diameter vs. Radius: Flake Paint 99

4.9 Average Drop Diameter vs. Radius: No-flake Paint 100

4.10 Average Flake Area vs. Radius 101

4.11 Electrostatic Sprayer: Flake Paint - Total 102

4.12 Electrostatic Sprayer: No-flake Paint - Total 103

4.13 Drop Distribution: Flake Paint - Total 105

4.14 Drop Distribution: No-flake Paint - Total 106

4.15 Electrostatic Sprayer: Flake Area Distribution 107

4.16 Details of Electrostatic Precipitator 109

4.17 Positions for Electrostatic Precipitators 111

4.18 Mechanical Sprayer: Flake Paint #4 113

4.19 Mechanical Sprayer: No-flake Paint #4 114

4.20 Drop Distribution: Flake Paint #4 115

4.21 Drop Distribution: No-flake Paint #4 116

4.22 Mechanical Sprayer: Flake Area Distribution #4 117

4.23 Mass Percent Aluminum vs. Radius 120

4.24 Color vs. Mass Percent Aluminum: Mechanical Sprayer 125

5.1 Beam Focusing: Simple Electrode Structure 129

5.2 Beam Focusing: Multiple Electrode Structure 130

5.3 Corona Color Variation Experiment 135

5.4 Results of Corona Color Variation 137

5.5 Normalized Results of Corona Color Variation 140

5.6 Jeffrey's Circuit Model for a Viscoelastic Fluid 142

5.7 Apparatus to Measure Viscoelastic Properties 143

5.8 Response of Sprayed Paint: Amplitude vs. Frequency 146

5.9 Simulated Flake Transient - Long Time 150

5.10 Simulated Flake Transient - Short Time 151

5.11 Simulated Results of Flake Orientation 152

6.1 Analysis of the Electrostatic Sprayer 161

6.2 Analysis of the Mechanical Sprayer 162

A.1 Airless Electrostatic Paint Sprayer I 178

A.2 Configuration of New Spray System 179

A.3 Airless Electrostatic Paint Sprayer II 180

A.4 Airless Sprayer: Flake Paint at 50kV 183

A.5 Airless Sprayer: Flake Paint at 70kV 184

A.6 Airless Sprayer: No-flake Paint at 50kV 186

A.7 Airless Sprayer: No-flake Paint at 70kV 187

A.8 Sketch of Jet Formation 190

B.1 Flow Chart of the Main Program 214

B.2 Flow Chart of the Subroutine Force 215

B.3 List of Subroutines 216

B.4 Simulation Run 218

B.5 Drop Trajectory 219

D.1 Measurement of Splattered Drop Height 232

D.2 Drop Profile 233

E.1 Electrostatic Sprayer: Flake Paint #1 235

E.2 Drop Distribution: Flake Paint #1 236

E.3 Electrostatic Sprayer: Flake Paint #2 237

E.4 Drop Distribution: Flake Paint #2 239

E.5 Electrostatic Sprayer: Flake Paint #3 240

E.6 Drop Distribution: Flake Paint #3 241

E.7 Electrostatic Sprayer: Flake Paint #4 242

E.8 Drop Distribution: Flake Paint #4 243

E.9 Electrostatic Sprayer: Flake Paint #5 244

E.10 Drop Distribution: Flake Paint #5 245

E.11 Electrostatic Sprayer: No-flake Paint #1 246

E.12 Drop Distribution: No-flake Paint #1 247

E.13 Electrostatic Sprayer: No-flake Paint #2 248

E.14 Drop Distribution: No-flake Paint #2 249

E.15 Electrostatic Sprayer: No-flake Paint #3 250

E.16 Drop Distribution: No-flake Paint #3 251

E.17 Electrostatic Sprayer: No-flake Paint #4 252

E.18 Drop Distribution: No-flake Paint #4 253

E.19 Electrostatic Sprayer: No-flake Paint #5 254

E.20 Drop Distribution: No-flake Paint #5 255

F.1 Mechanical Sprayer: Flake Paint #1 257

F.2 Drop Distribution: Flake Paint #1 258

F.3 Mechanical Sprayer: Flake Paint #2 259

F.4 Drop Distribution: Flake Paint #2 260

F.5 Mechanical Sprayer: Flake Paint #3 261

F.6 Drop Distribution: Flake Paint #3 262

F.7 Mechanical Sprayer: Flake Paint #4 263

F.8 Drop Distribution: Flake Paint #4 264

F.9 Mechanical Sprayer: No-flake Paint #1 265

F.10 Drop Distribution: No-flake Paint #1 266

F.11 Mechanical Sprayer: No-flake Paint #2 267

F.12 Drop Distribution: No-flake Paint #2 268

F.13 Mechanical Sprayer: No-flake Paint #3 269

F.14 Drop Distribution: No-flake Paint #3 271

F.15 Mechanical Sprayer: No-flake Paint #4 272

F.16 Drop Distribution: No-flake Paint #4 273

Abstract

Color differences in metallic paints sprayed by traditional mechanical sprayers and newer electrostatic sprayers have motivated the detailed investigation of these devices. The dominant mechanism for this color difference has been identified. The amount and size distribution of the metallic flake deposited by the electrostatic sprayer is significantly different than that deposited by the mechanical process. For the specific devices investigated, the mass percent of flake deposited by the mechanical sprayer is approximately twice that of the electrostatic sprayer. The average flake size obtained from the mechanical sprayer is more than twice that obtained from the electrostatic sprayer. These results are directly related to the low efficiency of the mechanical sprayer. The mechanical sprayer acts like a flake filter, separating the smaller drops containing lower flake content and smaller flakes from the larger drops. These smaller drops constitute most of the waste paint and are responsible for substantial cost in both paint and environmental protection. The high efficiency of the electrostatic spraying process reduces the amount of waste and, therefore, increases the amount of paint solids deposited.

These results imply a different approach to paint spraying for highly efficient processes. The sprayer can no longer be used to "tune" the color by varying the flake content and size distribution. However, the high efficiency of the electrostatic process does make it easy to predict how the paint can be tuned to obtain a desired flake content and size distribution.

This research has resulted in two innovative designs. Using a corona current, patterns can be written in a metallic paint layer while it is still wet and then locked into the finish when the paint is cured. An investigation of the physical processes involved in this technique shows that the viscoelastic nature of the sprayed paint must be considered for accurate scaling of the process. Secondly, an airless electrostatic sprayer has been designed. This device eliminates moving parts and has the ability to spray highly viscous paints. Preliminary investigation indicates the possibility that this device is a feasible paint sprayer.

Acknowledgements

Numerous people have been involved in this project and directly or indirectly aided in the completion of this thesis. I will attempt to mention the major contributors both technical and personal.

Professor Melcher has been the backstay of both moral and technical support. My own growth since my rather hesitant steps into the MIT community is a direct result of our interaction. This type of personal contact is truly the best form of education.

The other members of my thesis committee, Dr. Chathan Cooke, Professor Ain Sonin and Professor Marcus Zahn, have been quite helpful. They have actively pointed out areas of concern and provided suggestions for improvement.

This research was funded by General Motors Research. They provided an understanding of the problem from both an industrial and research viewpoint. Our primary contacts in the Electrical Engineering Department, Dr. T.C. Wang and Dr. Carlton Speck, were particularly helpful.

The electrostatic spray equipment was supplied by the Ransburg Corporation. Discussions of the problem with Bill Smart and Emery Miller proved quite helpful.

All paints were supplied by E.I du Pont de Nemoirs & Company. Conversations with Dr. J. Hochberg were invaluable to the development of the project.

Measurement of the paint's electrical properties was performed by Mr. W. Westphal. The assistance always available from him was a valuable resource for this project and is an asset to the laboratory.

Paul Warren provided general support in the laboratory and assisted with those practical problems that often result in failure. Students having substantial input into the project and also providing a different type of personal learning experience are David Lyon, Becky Gray, and particularly Pradeep Jeganathan who gathered most of the data used in Chapter 5.

My wife, Michelle, has been both supportive and actively involved with the project. She has aided both in experimental work and in the preparation of this thesis.

Chapter 1

Introduction

The use of electrostatic paint spraying equipment is increasing in industry. This equipment has many advantages but has introduced several problems. These problems indicate the lack of scientific background for the paint process in general. This project started as an investigation of electrostatic spray equipment, specifically the color shift obtained using metallic paints. However, it was soon realized that the traditional spray methods, mostly air spray guns, were more complex than electrostatic ones and perhaps more at the root of the color variation problem. Unfortunately, these spray devices are used to establish the standard for judging other devices. It appears from outside the industry that the standard is skewed, placing an unusual restriction on new devices. This view is not in general shared by the industry for both historical and some valid practical reasons. Because both spray gun and paint technologies developed in parallel the interaction has evolved to obtain a required finish. This coupling adds to the inertia opposing a general shift to more efficient equipment. Providing a scientific explanation of the dominant differences between the traditional and electrostatic spray processes may overcome some of the hesitancy in changing equipment and eventually the industry

standard.

1.1 Motivation for Electrostatic Painting

The painting industry is responding to environmental concerns by developing ways of restricting the amount of waste being released into the atmosphere. A natural response is to use processes that more efficiently deposit the paint coating. Electrostatic spraying can increase the deposition efficiency dramatically. In the automotive industry the efficiency is between 10 and 40 percent for a mechanically applied paint coat but between 60 and 90 percent when applied electrostatically. The matching of paint finishes can be difficult, even using the same equipment, when application techniques differ, the problem is exacerbated. A solution could be to paint totally electrostatically, however, this has two major problems. First, repair work in the field is dominated by mechanical sprayers. A match between the final factory finish and the repair finish is essential. Electrostatic equipment is blamed for the discoloration and often avoided. Indeed because industry color standards are based on mechanically applied coatings conversion to high efficiency electrostatic processes is impeded. Mechanical sprayers are often used in applying the dress or final coat to circumvent these problems.

Using these two different processes, most paints can be matched by varying standard painting parameters. However, problems encountered with the use of metallic paints are often insurmountable. Metallic paints are most often used in the automotive industry where they have a high market value. These paints give a dimensional look to the automobile due to the presence of shiny metallic flakes that give rise to a finish quality called color flop. Color flop is the propensity to exhibit a color that depends on the angle of observation. The shiny finish itself is also felt to be a desirable market item.

1.2 General Objective

The painting industry developed mainly from empirical data. Expert painters have acquired what is best described as an artistic talent for using different devices and paints to obtain a desired finish. Unfortunately, the fact that painting is more an art than a science is responsible for many misconceptions that create difficulties when results are transferred to other paint processes. The aim of this research is to provide a scientific background for at least some of the processes involved while providing the framework into which other detailed research focusing on related issues can be incorporated.

The specific problem of color variation, when applying metallic paints with a mechanical versus an electrostatic sprayer, is an excellent example of the industry's restrictions in applying its developed expertise. The paint finishes cannot be matched by varying standard painting parameters. An understanding of the mechanisms underlying the process is required to effectively deal with the problem.

1.3 General Painting Process

The many types of paint sprayers can be categorized into five broad divisions by their atomization and delivery mechanisms. These are:

(1) Mechanical atomization and delivery;
(2) Mechanical atomization and mechanical and electrostatic delivery;
(3) Mechanical and electrostatic atomization and delivery;
(4) Mechanical and electrostatic atomization and electrostatic delivery; and
(5) Electrostatic atomization and delivery.

At the present time, there are few practical devices in category 5. Although not a central part of the work described here, a category 5 device was designed, built, and

subjected to preliminary testing. This development is described in Appendix A.

Although these types of devices can be extremely different, they must perform the same tasks of delivery of the paint to the atomization area, atomization, and transport of the drops to the paint surface. The process also involves driving off the remaining solvents and, in some paints, includes a high temperature curing stage. The basic configuration of a high speed turbobell electrostatic painter (actually a type 3 device) is shown in Fig. 1.1, where the four primary stages of concern in any device are indicated. These stages are:

(1) Drop formation;

(2) Flight to the target;

(3) Impact with the target; and

(4) Post-impact.

1.3.1 Paint Atomization

In a standard device that uses mechanical atomization the paint is forced under pressure through a small orifice into a region where it has a free surface and is impacted by high velocity air. The combination of forces from surface tension and high velocity air impact cause the paint to atomize. Because the interaction between liquid and air is

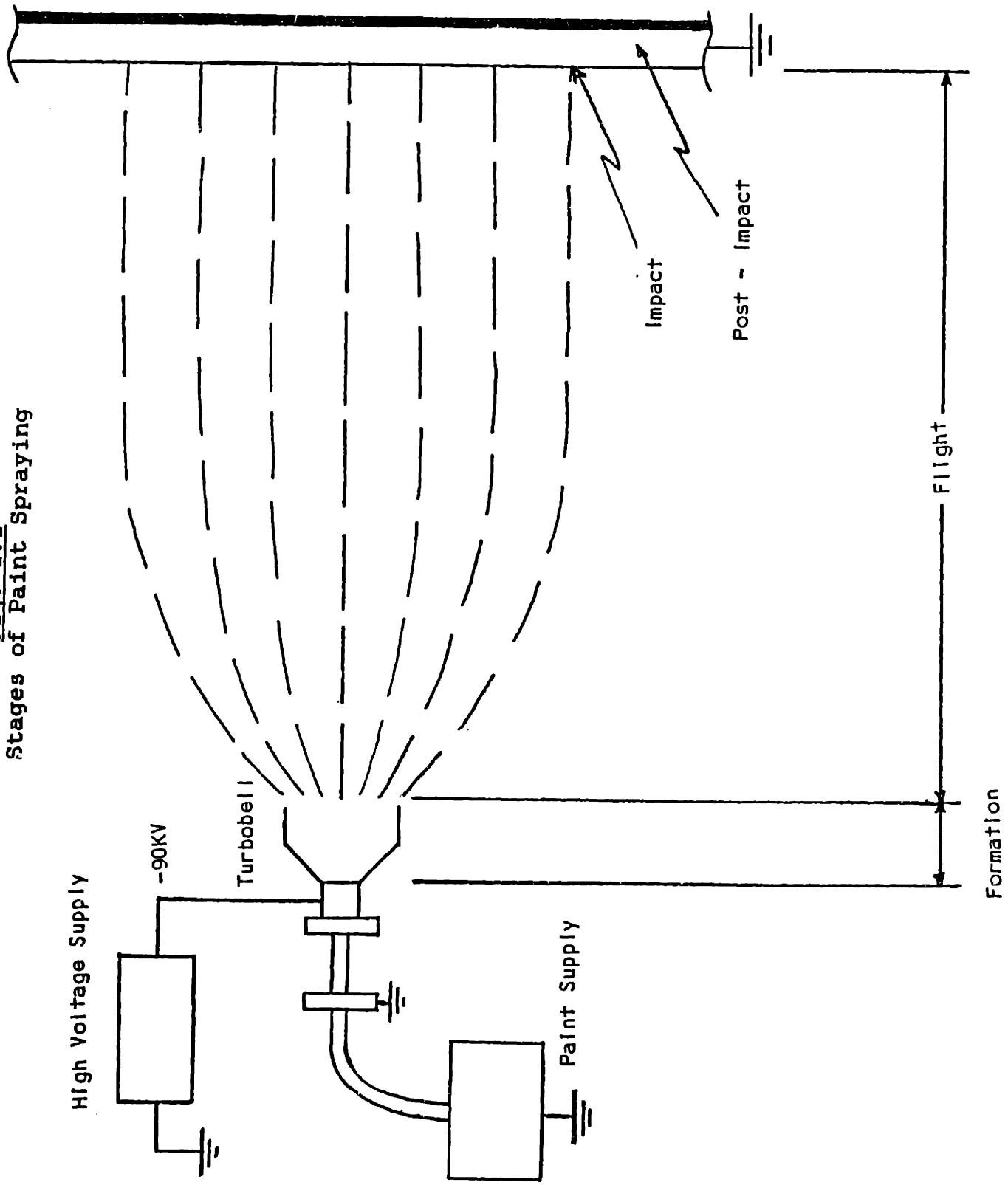

Fig. 1.1
Stages of Paint Spraying

unstable, and the incident air often turbulent, this technique results in a wide spectrum of drop sizes.

Early electrostatic paint sprayers were devices that used electrostatic atomization. These sprayers typically consisted of a conducting surface that ended in a sharp edge, for example a razor blade. In such devices paint flows down the surface to the edge, usually under the influence of gravity. The resulting field concentration at this edge causes an electrohydrodynamic instability that gives rise to a current driven jet. These jets have been analyzed by Melcher [1] and Hines [2]. The jet disintegrates into drops under the influence of the fluid forces in competition with the stabilizing electrical force. These devices are not used extensively owing to the difficulty in delivering the paint to the edge and to unreliable atomization. However, these devices did have advantages. They were capable of spraying very high solids paint and did not require an imposed air flow for delivery. This greatly reduces the environmental impact of the device. Also, there are no moving parts. Therefore, the structure of the device is uncomplicated and reduces the cost of construction and increases the reliability.

High speed discs and bells have been developed in response to the problems associated with edge devices. These

newer devices rely on both mechanical and electrostatic atomization, though the dominant mechanism is mechanical. The paint is delivered onto a disc or bell that spins at high speed and forces the paint into a thin film over the surface as it flows to the outer edge. Drops form as the film leaves the tip through fluid mechanical (and to some extent electrohydrodynamic) processes that begin with film instability [3] , then jet formation [1], and finally drop formation [2] [4] . This occurs under the influence of centrifugal and electrical forces as well as drag forces from the air in the vicinity of the bell or disk [5].

Metallic paints introduce a new aspect to atomization: the effects of irregular shaped objects in the paint, viz. the metallic flakes. The bulk fluid properties do not accurately represent the paint when the size scale of interest is on the order of the flake size. The electrical properties are similarly affected. Because the flake diameter distribution overlaps that of the drops, this makes it difficult to apply surface instability theories such as are presented by Melcher [6].

1.3.2 Transport of Paint to the Surface

Since the paint drops must travel through air there is always some interaction with the air flow. In mechanical

transport, the air flow is imposed, and drop entrainment is responsible for their transport during the bulk of the flight. It is, however, a drop's inertia that causes it to leave the flow and be deposited on the surface. The velocity of the air can be high. The air flow can be approximately represented as a submerged turbulent jet. These jets are discussed by Abramovich [7]. This implies that there is turbulent mixing and a turbulent boundary layer near the paint surface. The source of the air is often a series of small directed nozzles that cause the flow to be further complicated. The addition of an electric force causes a large increase in the painting efficiency partially owing to the modified trajectories of the drops in the early stages of transport, but primarily because the inertia of the particles, is no longer the only factor that deposits the drops on the surface.

Once the paint is sprayed into the air, evaporation of the solvents becomes important. The mass transfer depends on the chemical composition of the paint and the paint/air interface, the temperature, the degree of turbulence, and the surface-to-volume ratio [8] . This ratio is often required to be high (small drops) to release a large percentage, in many systems 40-50%, of the solvents during transport. The flow of the surrounding gas is modified by the presence of both solvents and drops. The transport time

and relative velocity between the drop and the gas are other factors that influence the evaporation. Also, the evaporation modifies the temperature of the drop that arrives at the paint surface.

1.3.3 Dynamics of the Deposited Paint Layer

The dynamics of a drop impacting on the surface depends on the properties of the fluid (modified due to evaporation during flight), the charge on the drop, and the surface properties (the surface is either a hard metallic surface or a previously deposited paint layer). Again, the effects of the metallic flake are important because the drop size is of the order of the flake size. Once deposited on the surface, the paint drops flow together to form the paint layer. This mechanism is important in obtaining the final finish texture.

The evaporation of solvents causes a net fluid velocity and a temperature gradient in the layer. This evaporation is influenced by the fluid mechanics and the gas composition over the layer. During electrostatic painting, the layer may also be influenced by the imposed field and by the current carried by the charged drops. The chemical reaction involved with curing the paint may also be initiated if enough solvent has evaporated either during flight or while the

layer is being deposited.

1.3.4 Curing of Paint

The chemical aspects of curing the paint can be initiated by the evaporation of the solvents or may require an elevated temperature. In non-aqueous enamels, an elevated temperature is required to cure the paint; a similar reaction as experienced in thermoset plastics. These reactions can be exothermic, adding to the elevated temperature in the paint layer, causing the remaining solvent to be driven off quickly. The paint layer will shrink due to the loss of solvents and the curing process. This shrinkage and the final state of the air/paint interface, as the paint forms the hardened layer, are the final factors influencing the quality of the finish.

1.4 Color Variation using Flaked Paints

The amount of color variation between the two processes, mechanical and electrostatic, is very dependent on the specific type of device and the particular paint. There are, however, general trends that are obvious. Electrostatic paint finishes tend to be darker and exhibit more of the color of the base paint, i.e. the paint material with the flake removed. One of the paint colors that

exhibits the largest variation is light blue. The color difference is dramatic, though it should be noted that little attempt was made to match the finishes. There are several differences in the two colors that are best indicated from the color vector. Color space is illustrated in Fig. 1.2. This system is a means of representing color in a quantified way yet produce numbers closely representing the normal perception of color. The coordinates in color space correspond to the normal perception of white/black, L^*, red/green, a^*, and blue/yellow, b^*. The results are:

Electrostatic sample

$L^* = 41.6$

$a^* = -3.8$

$b^* = -28.8$

Mechanical sample

$L^* = 52.3$

$a^* = -3.4$

$b^* = -19.4$

The L^* for the electrostatic sample is lower than the mechanical sample; the sample is darker. The coordinate b^* has greater magnitude indicating a bluer color. The total difference, ΔE, is the distance in color space between the two samples. In the example above, $\Delta E=15.8$ (the average

Fig. 1.2
Color Space

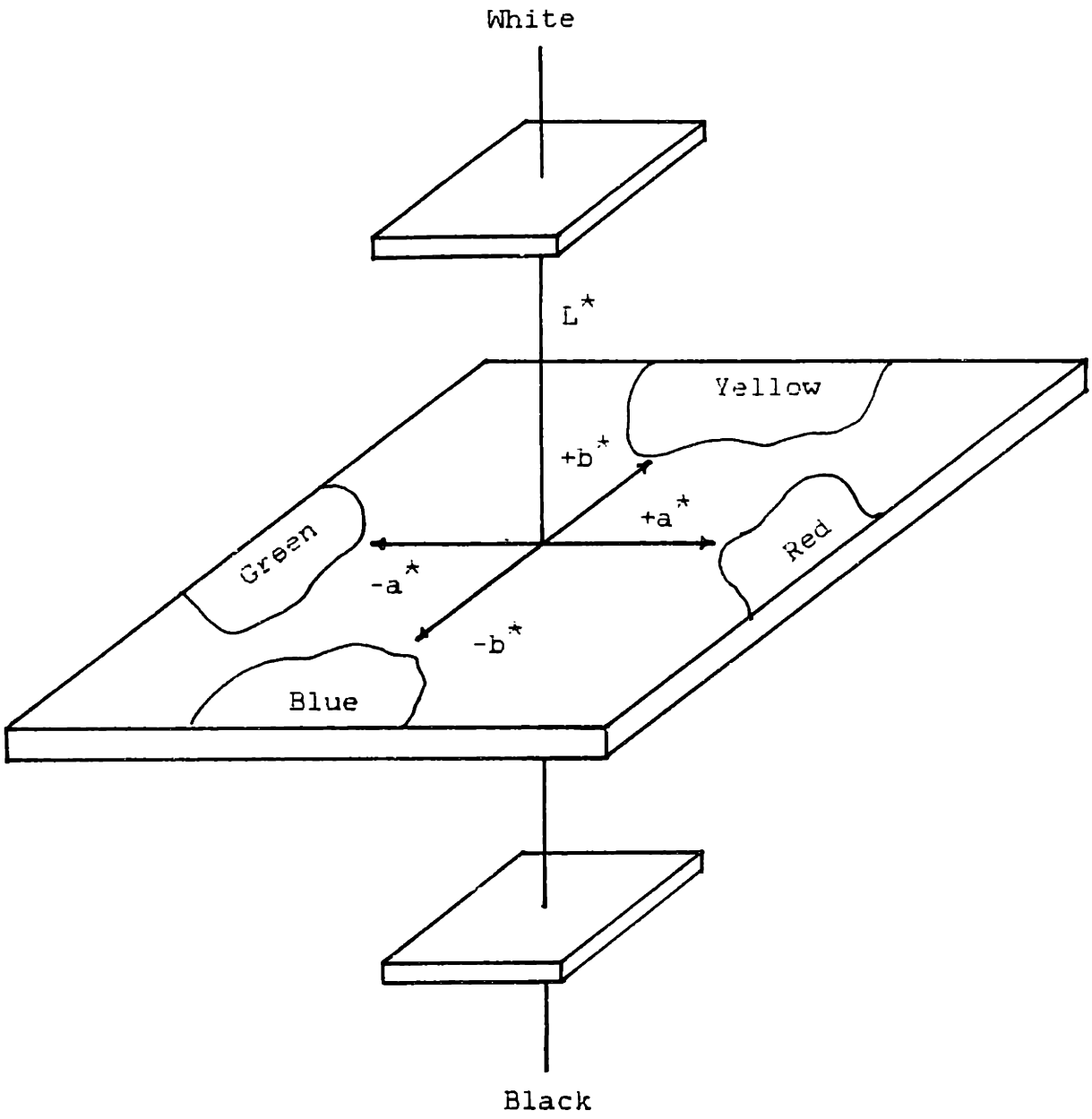

person can detect a $\Delta E \simeq 0.9$).

The color difference can be described in more subjective terms. The color of the electrostatic sample seems to be less solid or pure. The end result is a sample that appears less finished and definitely less aesthetically desirable.

There are four mechanisms proposed that may contribute to the color variation. These mechanisms are:

(1) Flake orientation;

(2) Electrophoresis of the flake or other pigments;

(3) Evaporation of solvents (painting stages have different solvent content); and

(4) Variation in the amount and size of deposited flake.

Each mechanism is dealt with, however, most effort has been spent on the dominant mechanism, the variation in the amount and size of deposited flake.

References

[1] Melcher, J.R. and Warren, E.P., "Electrohydrodynamics of a current-carrying semi-insulating jet", J. Fluid Mech., 47, 1971

[2] Hines, R.L., "Electrostatic atomization and paint spraying", J. Appl. Phys., 37(7), 1966

[3] Taylor, G.I., "The dynamics of thin sheets of fluid II. Disintegration of fluid sheets", Proc. Royal Soc., A, 253, 1959

[4] Baretto, E., "Electrically produced submicroscopic aerosols", Aerosol Science, 2, 1971

[5] Kayano, A., and Kamiya, T., "Calculation of the mean size of the droplets purged from the rotating disk", ICLASS 78, 1978

[6] Melcher, J.R., Field-coupled Surface Waves , MIT Press, 1963

[7] Abramovich, G.N., The Theory of Turbulent Jets , MIT Press, 1963

[8] Bird, R.B., Stewart, W.E., and Lightfoot, E.N., Transport Phenomena , John Wiley and Sons, New York, 1960

Chapter 2

Spray Painting Equipment and Paint

The specific equipment and paint used in the experiments were chosen on two basic requirements. First, the equipment and paint must be used industrially and second, it should represent some of the most dramatic problems of color variation. Since our facilities for proper ventilation are limited, it should be noted that only small batch paint jobs could be done safely. This limited the paint finish quality, however, it was reasonable and reproducible. Although the present investigation centres on specific equipment, the mechanisms identified should be applicable to other processes.

2.1 Electrostatic Paint Sprayer

The sprayer is a Ransburg Turbobell II using a 70351-01 Bell. The configuration of the electrostatic spray facility is shown in Fig. 2.1 and Fig. 2.2 shows the details of the sprayer.

The bell is driven by an air turbine at speeds up to 35,000rpm, though usual operation is at 28,000rpm, resulting in an edge speed of 108m/s. Voltages in the range of -45000V to -100000V can be applied with -90000V typical. Paint is forced at a controlled rate onto the inner surface of the

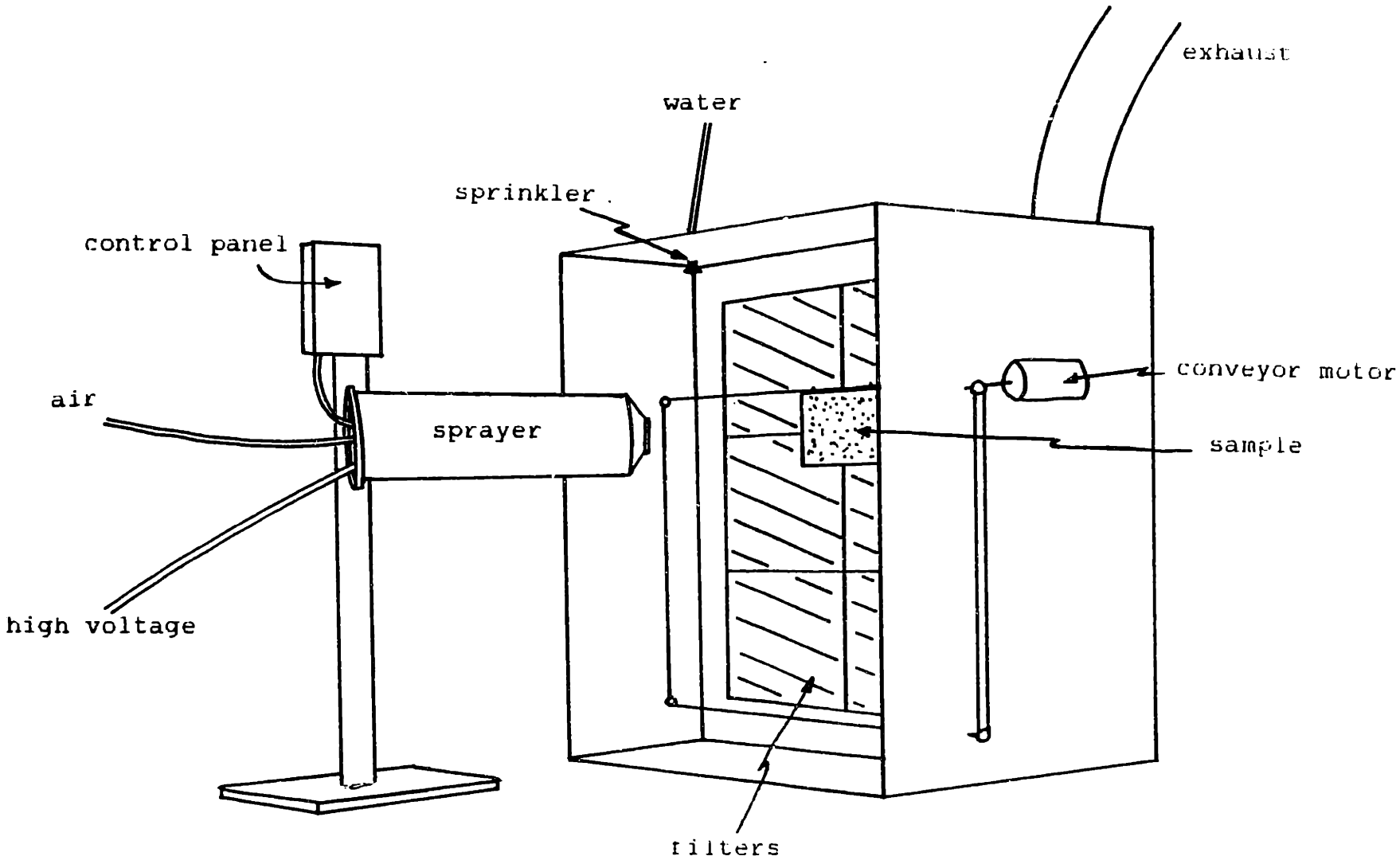

Fig. 2.1
Configuration of Electrostatic Painting Facility

Scale 1:2

Bell - -90kV
- 28000 rpm

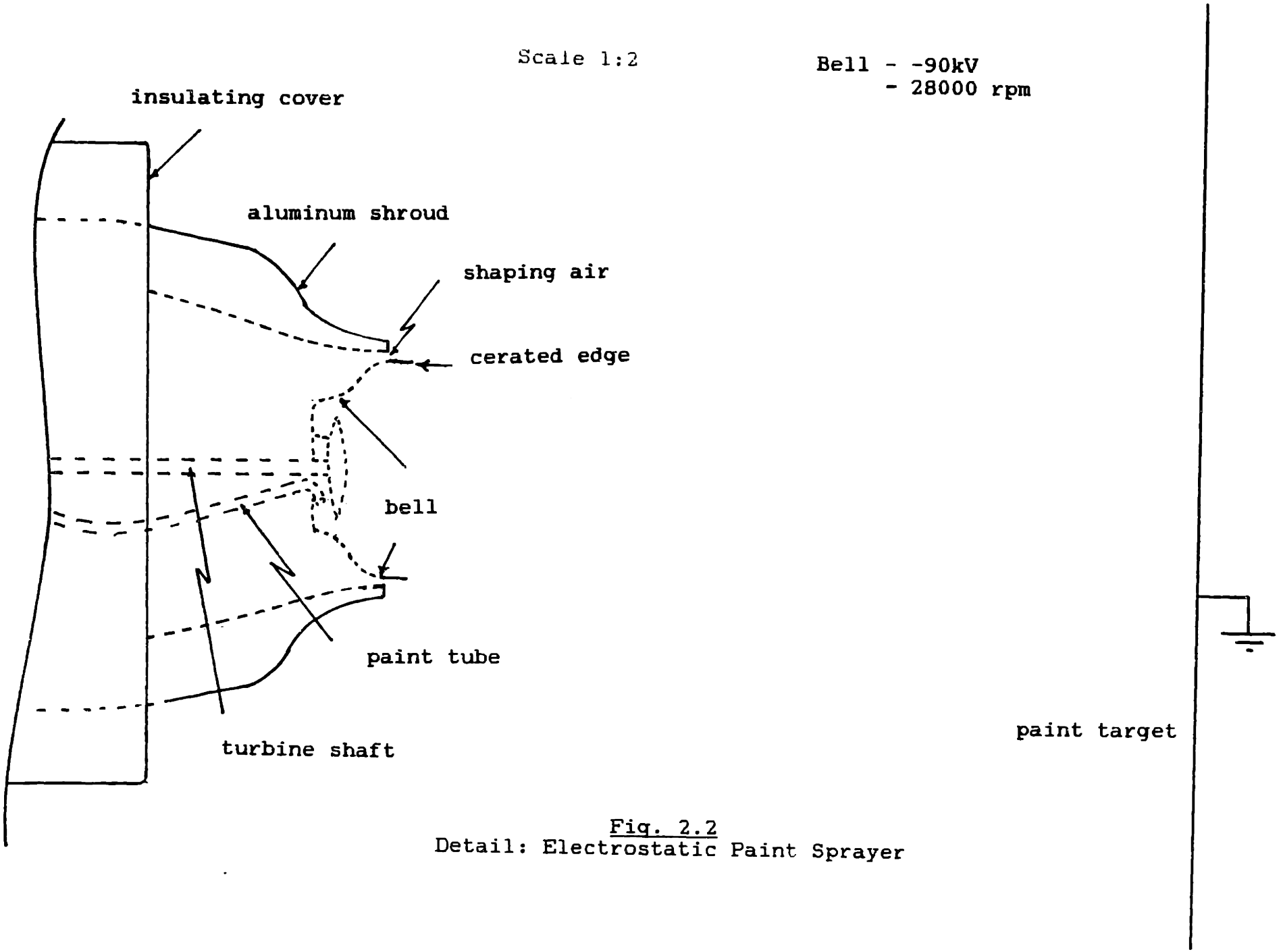

Fig. 2.2
Detail: Electrostatic Paint Sprayer

bell where the centrifugal force causes the formation of a thin sheet of paint that flows to the serrated edge of the bell. At the bell edge a combination of electrical and fluid forces cause the sheet to break into drops. These drops are then carried to the surface by the air flowing around the outer edge of the bell (shaping air) and by the electrical forces. The high angular velocity at the bell results in large radial momentum that causes the drops' initial trajectory to have a large radial component. The paint is highly conducting (the charge relaxation time is short compared to times of interest) and in electrical contact with the bell. Because of the high field strength at the bell there is a surface charge induced on the paint. As the fluid breaks into drops the charge remains on the drops. This process is called induction charging and is an efficient method for obtaining charged drops. Induction charging has been shown to be the dominant charging method, not impact charging from corona emission [1] . Corona emission is likely eliminated by the electric field reduction caused by the charge on the paint drops in the spray and by the jets of paint at the lip of the bell.

The paint target is grounded and fixed approximately 0.3m from the bell tip. The paint flow rate can be varied between 50 and 400ml/min, although it is usually kept at 100ml/min, and the shaping air pressure can be as high as

40psi but is usually maintained at 20psi. This pressure results in a maximum air velocity at the bell tip of approximately 20m/s. The deposited spray pattern is approximately 35cm in radius and this area is "covered" in roughly 45secs.

The practical controls in this device do not independently control parameters of the spray cloud. For example, bell speed, paint flow rate, and the applied potential all effect the atomization of the paint. Also, one control may effect many parameters. Bell speed not only effects drop size but also the initial drop trajectory and the rotation of the shaping air. To provide a means of predicting the effect these controls have on the shape and content of the spray cloud a model consisting of both theoretical models and empirical results was developed. This model is implemented numerically and is described in Appendix B.

2.2 Description of Mechanical Spray Gun

The mechanical spray gun is a Binks Model 98-1081. The gun atomizes the paint by forcing it through a cylindrical nozzle into a region where the paint is impacted by high velocity air. Approximately 1cm downstream from the atomizing region the spray is shaped by several jets of air.

With the target approximately 10 inches from the nozzle, the resulting spray pattern on impact is approximately elliptical with a major axis of 14cm and a minor axis of 4cm. A detail of the spray gun nozzle is shown in Fig. 2.3. Although this pattern represents the dense part of the spray, paint is not confined solely to this region. The waste paint outside the main spray constitutes the overspray and accounts for the low efficiency of the process, industrially between 10 and 40 percent. Delivery of the paint to the target is due to drop entrainment in the air flow. This air flow is highly turbulent and has a high average velocity, 30m/s, 7.5cm from the nozzle.

The basic operating parameters are paint pressure, air pressure, nozzle opening, air valve opening, and the distance to the paint target. The paint pressure and air pressure are easily controlled by conventional methods (they are usually set to 10psi and 30psi, respectively). During spraying, the spacing between the target and the gun is kept in the range of 8 to 10 inches. The other operating parameters are set by adjusting uncalibrated control knobs. This demands extensive experience to obtain consistent high quality finishes. The frustration of obtaining different finishes using the same paint and spray device is a prime indicator of the skill required in spray painting. Throughout the project the painting quality did improve and

Side View

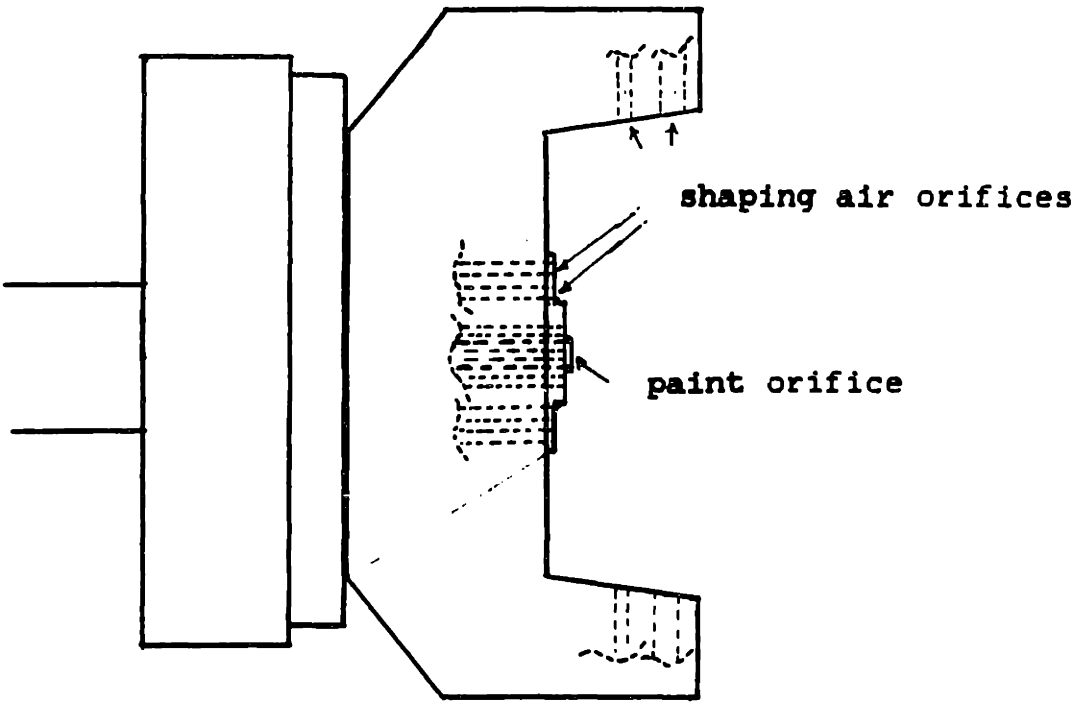

Scale 1:½

Front View

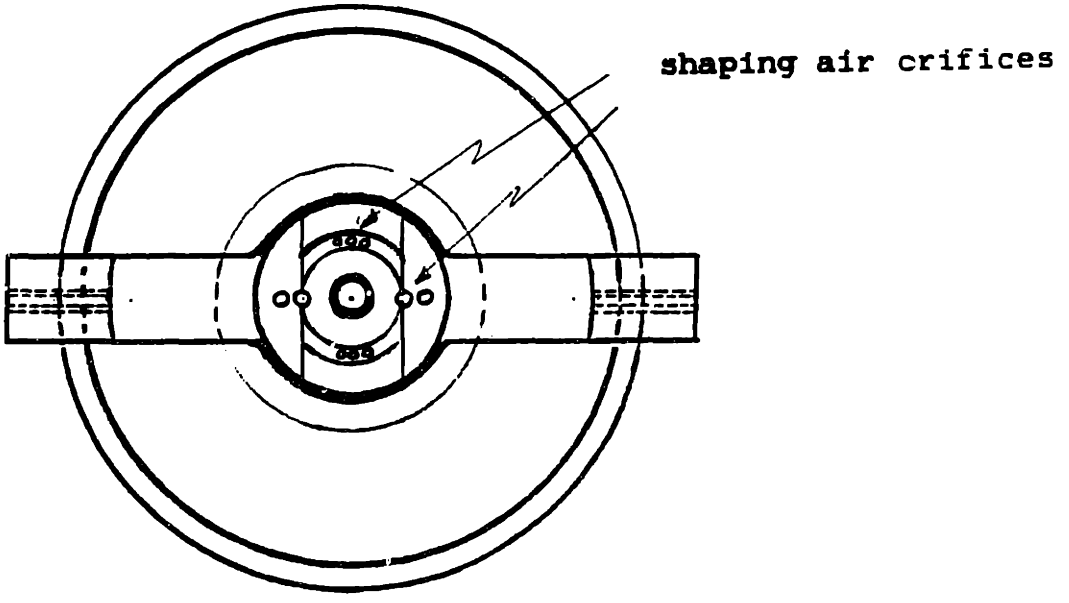

Fig. 2.3
Detail: Spray Head for Binks Gun

Side View

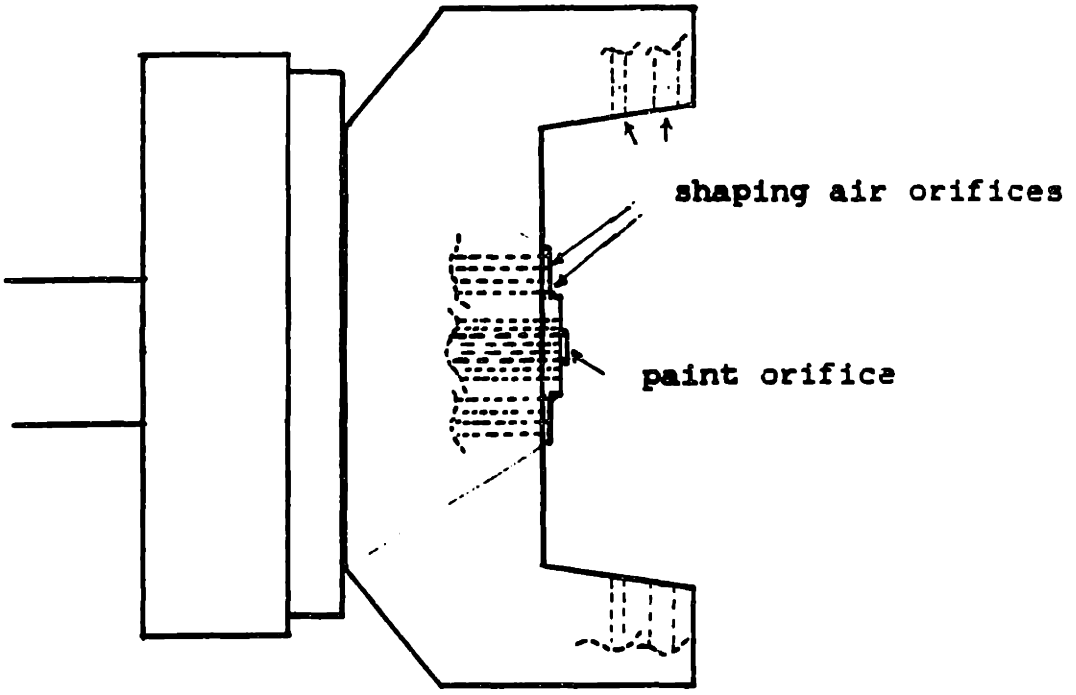

Scale 1:½

Front View

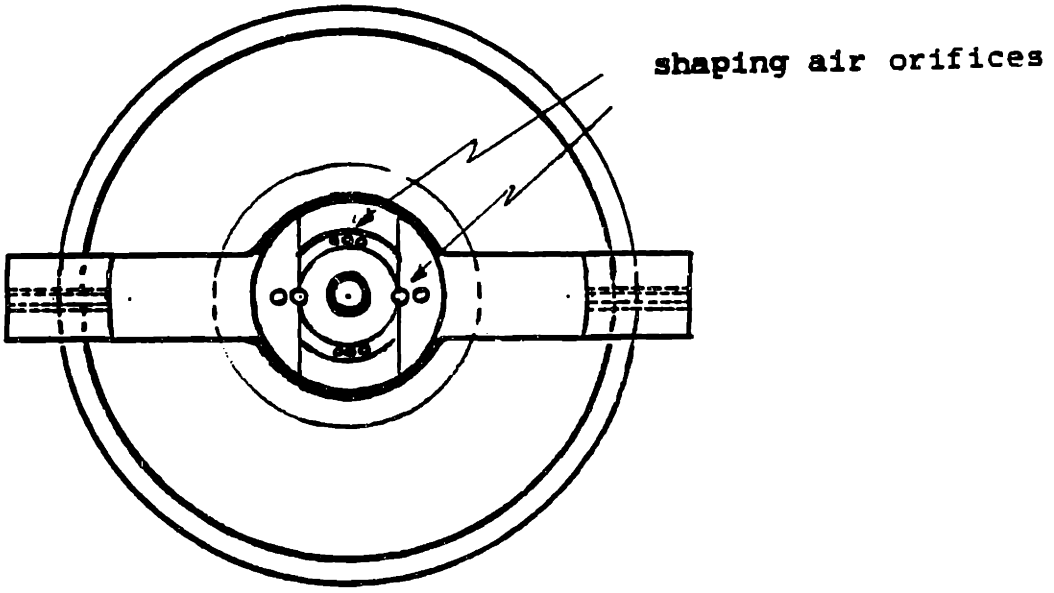

Fig. 2.3
Detail: Spray Head for Binks Gun

approached professional quality.

2.3 Macroscopic Properties of Paint

The paint chosen for testing was a non-aqueous automotive enamel, Dupont number K-383Y-BR055, a light blue metallic paint. This paint exhibits a large color variation when applied electrostatically versus mechanically. For comparison purposes the same paint with the flake removed was acquired.

The electrical properties of these two paints were measured for both paint mixed with xylene for spraying in the equipment described in Sections 2.1 and 2.2 and for the paint as supplied. The results are presented in Table 2.4 and Table 2.5 . For spraying, either electrostatic or mechanical, the paint is mixed with xylene until the viscosity is sufficient to require 30secs to empty a Zahn #2 cup, approximately 0.7poise(0.07kg/sec-m). The viscosity of the unmixed paint as a function of strain rate was measured using a Couette viscometer. The results are shown in Fig. 2.6. The mass density before spraying for flake paint is 928kg/m^3 while for no-flake paint it is 916kg/m^3. After curing the mass density of both paints is 1080kg/m^3. As seen from these macroscopic properties, the paints are not radically different.

	Flake Paint		No-flake Paint	
freq	ε_r	σ	ε_r	σ
100	6.20	3.84×10^{-7}	6.34	5.12×10^{-7}
1×10^{3}	5.74	3.98×10^{-7}	5.73	5.28×10^{-7}
1×10^{4}	5.31	4.17×10^{-7}	5.63	5.51×10^{-7}

Key

freq - frequency in hertz[hz]

ε_r - relative permittivity[f/m]

σ - conductivity[Ω^{-1}/m]

Table 2.4
Electrical Properties of Paint Mixed for Spraying

	Flake Paint		No-flake Paint	
freq	ε_r	σ	ε_r	σ
100	7.28	1.02×10^{-6}	8.88	1.17×10^{-6}
1×10^{3}	6.52	1.03×10^{-6}	7.96	1.18×10^{-6}
1×10^{4}	6.38	1.05×10^{-6}	7.44	1.20×10^{-6}

Key

freq - frequency in hertz[hz]

ε_r - relative permittivity[f/m]

σ - conductivity[Ω^{-1}/m]

Table 2.5
Electrical Properties of Unmixed Paint

Fig. 2.6
Viscosity vs. Strain Rate

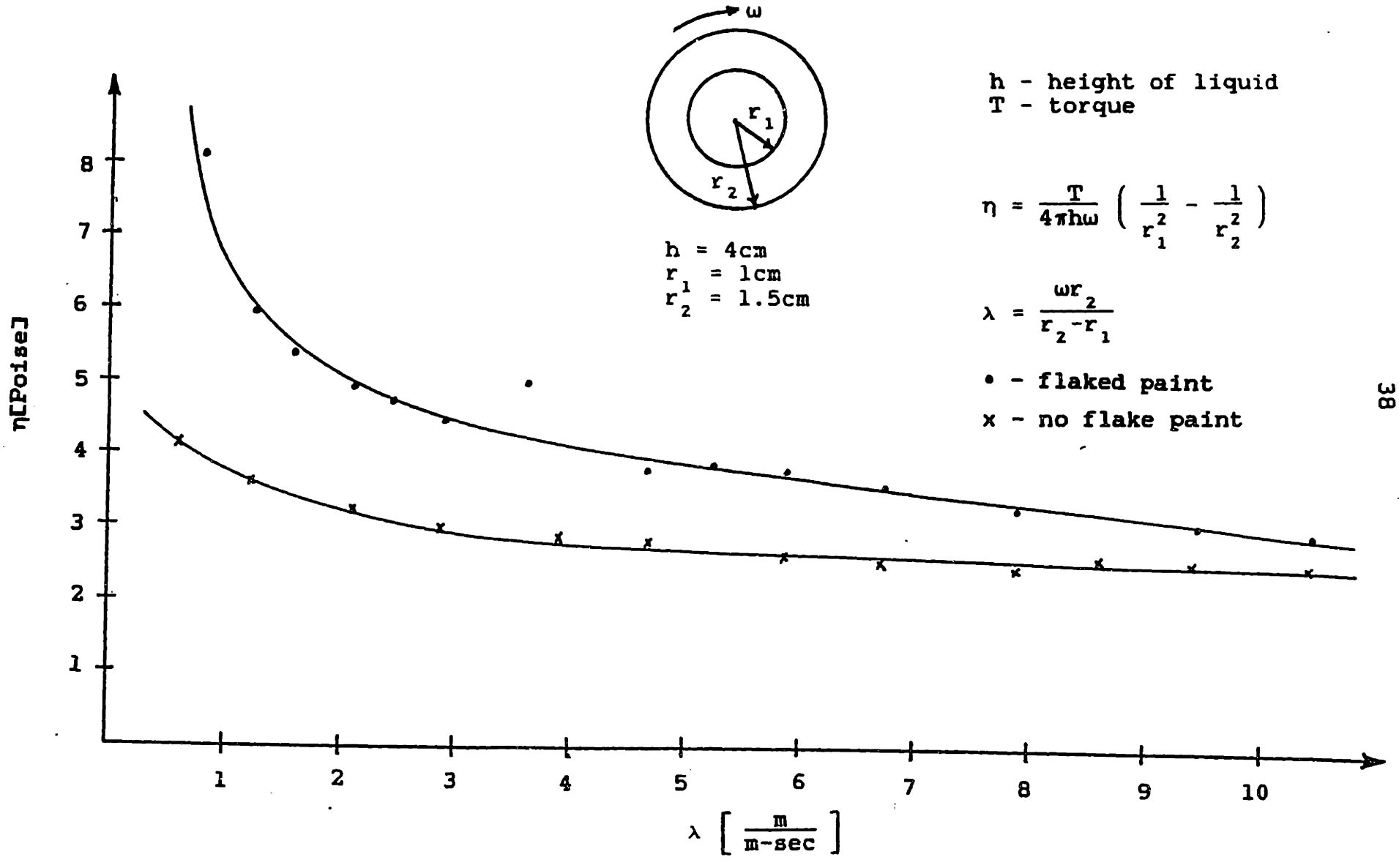

The properties of the flaked paint immediately after spraying with the Binks sprayer are also of interest. The electrical properties are given in Table 2.7. The viscosity is approximately 2.4poise(0.24kg/sec-m).

	Flake Paint	
freq	ε_r	σ
DC	-	6.00×10^{-8}
100	6.56	8.33×10^{-8}
1×10^{3}	5.91	6.66×10^{-8}
1×10^{4}	5.86	1.23×10^{-7}

Key

freq - frequency in hertz[hz]

ε_r - relative permittivity

σ - conductivity in mhos per meter[Ω^{-1}/m]

Table 2.7
Electrical Properties of Sprayed Paint

References

[1] Bell, G.C. and Hochberg, J., "Mechanics of electrostatic atomization, transport, and deposition of coatings", Seventh International Conference in Organic Science and Technology, Proc. of, Athens, Greece, 1981

Chapter 3

Orientation of Flake

Flake orientation could occur in each of the painting stages either under the influence of electric forces or fluid forces. The more likely stages are identified and the orientation times are estimated. Experiments on most stages have not been totally conclusive. The earlier an alignment mechanism comes into play, the more likely its influence is erased by subsequent phenomena, such as the surface impact dynamics. Some of this work was done by other students early in the project. This work is briefly mentioned for completeness and references to the applicable reports are provided.

A method for forcing the flake alignment under controlled conditions has been developed. This provides an indication of the possible effects flake alignment would have on the color. This technique may also be useful industrially. However, with proper use of electrostatic equipment, at least of the type studied here, flake orientation is not the dominant cause of the color difference between the electrostatic and mechanical spraying processes.

3.1 Orientation Times in Painting Stages

Metallic flake alignment could occur at any stage of the painting process. However, because orientation requires a finite time, the stages that are the longest in duration, transport and post deposition, are likely to dominate the process. The characteristic time for electrical orientation in a Newtonian fluid, ignoring inertial effects, is the electroviscous time [1] (discussed in detail in Chapter 5).

$$\tau_{ev} = g\frac{\eta}{\varepsilon E^2} \tag{3.1}$$

where η is the absolute viscosity, ε is the electrical permittivity, E is the electric field strength, and g is a function of the geometry. Because this time is used to obtain order of magnitude estimates the function g is approximated as unity. This time has been used successfully to describe electrohydrodynamic mixing in which there is a competition between electric and viscous forces [2].

Orientation during flight has been divided into two separate categories. These categories are defined by two possible shapes of drops. In one case the drop is large enough to completely contain the flake and is, therefore, assumed spherical. In the other case, called a "wetted flake", the flake is large enough to distort the drop to an oblong shape. These two proposed drop shapes are illustrated in Fig. 3.1. If the drop is spherical, orientation of the flake occurs due to an electric polarization force [3]

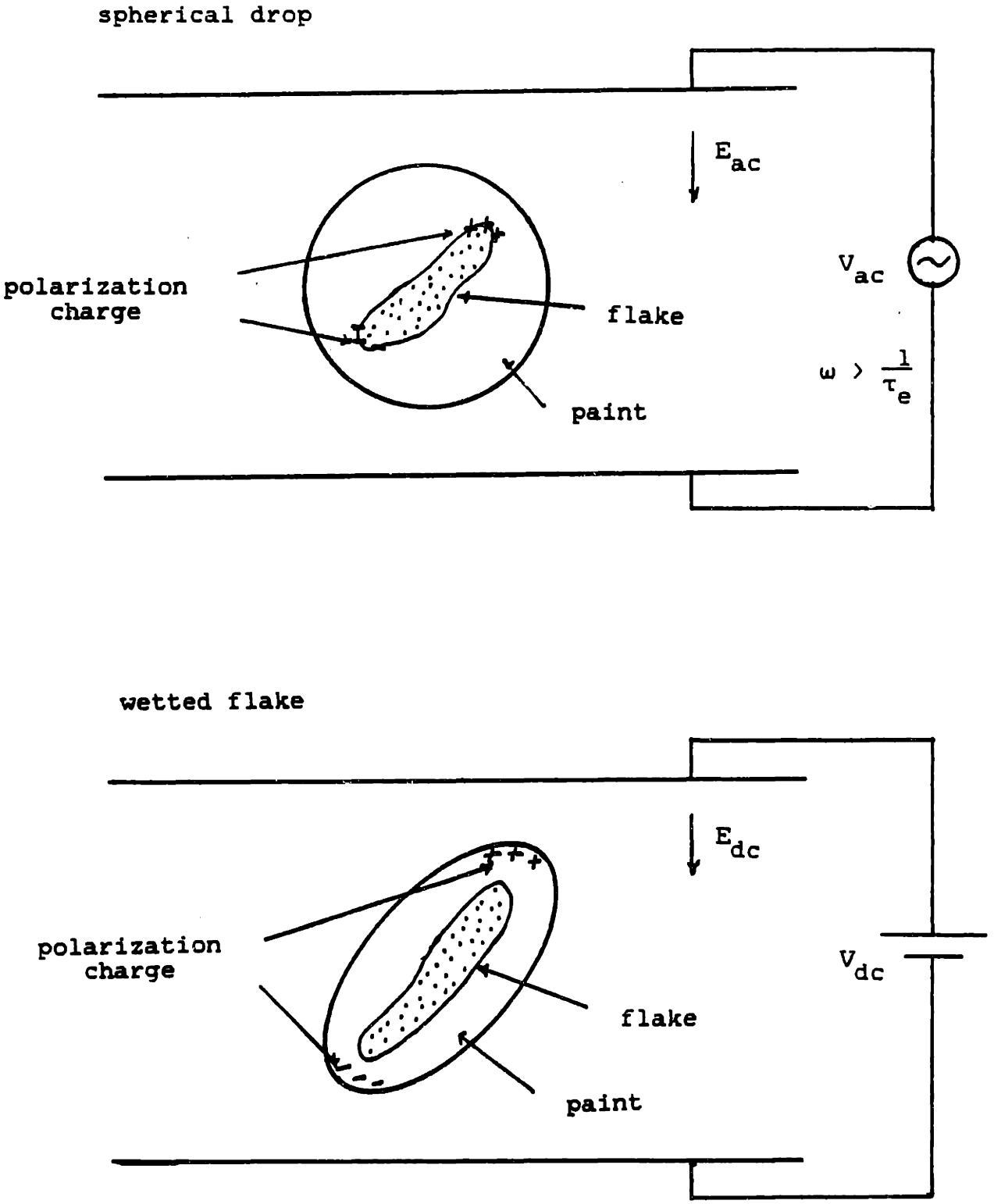

Fig. 3.1
Proposed Drop Shapes

applied to the flake. A wetted flake is subjected to both an electric polarization force and a fluid torque caused by the relative motion between the drop and the air due to the net electrical force on the drop.

Although the drop is subjected to a large DC field, the paint is highly conducting, having an electrical relaxation time on the order of 10^{-4} secs. Therefore, there is practically no penetration of the DC field inside the drop. A spherical drop enveloping one or more flakes could experience a torque in an alternating electric field. The AC electric field strength in the paint increases with frequency, $f=\omega/2\pi$, reaching a maximum when the frequency is greater than the inverse charge relaxation time for the paint, τ_p.

$$\omega > \frac{1}{\tau_p}$$

This field will exert a torque on the flake. Because the viscosity of the paint is substantially higher than that of air the flake will not move relative to the paint. Rather, the paint and flake will approximately respond as a rigid body, slipping relative to the air. The power supply ripple was measured and an electroviscous time for this field is calculated using the viscosity of air.

AC Ripple at 120 Hz. = 10% at 90kV

The spacing between the bell and the grounded target is 0.3m. Therefore, the peak AC field is

$$E_{ac} \simeq \frac{0.1(9\times10^{4})}{0.3}$$
$$\simeq 3 \times 10^{4} V/m$$

Solving for the field inside the drop, assuming $\varepsilon_p/\sigma \ll 1/\omega$, gives

$$E_p \simeq \frac{2\omega\varepsilon_o}{\sigma} E_{ac}$$

The electroviscous time based on the rms electric field and the viscosity of air but the permittivity of the paint is

$$\tau_{ev} = \frac{\eta_{air}}{\varepsilon_p E_{prms}^{2}} = 0.15secs$$

This is on the order of the flight time, approximately 0.1secs, therefore, alignment by the AC ripple is just possible.

If the drop is spherical, it follows that no torque is experienced due to the DC field. However, if the drop is oblong and polarized by the DC field a substantial torque is applied. The electroviscous time, again based on the viscosity of air but on the DC rather than the AC ripple field, is

$$\tau_{ev} = \frac{\eta_{air}}{\varepsilon_o E^{2}} \simeq 2.3 \times 10^{-5} secs$$

This time is short compared to the flight time. Because this

time is quite short this type of orientation could be inertially dominated. Assuming the orientation is limited by inertia the time for orientation is the electro-inertia time [1], τ_i.

$$\tau_i = \ell \left(\frac{\rho_{Al}}{\varepsilon_o E^2} \right)^{\frac{1}{2}}$$

where the length ℓ is taken as the flake radius. Again this time is modified by the geometry but this factor is assumed of order unity. A typical flake radius is 20μm and, therefore, the electro-inertial time is

$$\tau_i = 5 \times 10^{-4} \text{secs}$$

This time is also substantially less than the transit time. Therefore, it should be expected that wetted flakes, if they exist, align during flight.

Fluid forces due to the relative motion between the drop and the air would also only tend to align the flake if the drop is oblong, i.e. a wetted flake. The electric field and the charge on the drop result in a net force on the drop. This causes relative motion between the drop and the air that causes a fluid torque on an oblong drop.

The results of Chapter 4 show the number of wetted flakes is insignificant, therefore, in-flight orientation is just possible due to the AC ripple on the power supply.

However, the time for this alignment, 0.15secs, is approximately the same as the flight time and yet this time is only accurate to within an order of magnitude. Therefore, it is concluded that this type of alignment may just be possible.

The deposited paint layer is also conducting though the conductivity is modified during flight. The DC field does not penetrate the layer so once again sources of an AC field must be considered for electrical orientation. Using the power supply ripple, the same calculation as done previously for a spherical drop, provides an estimate of the field in the layer. However, the flake can no longer transmit its torque to the paint/air interface but must rotate relative to the paint. The viscosity of paint is four orders of magnitude higher than that of air and the resulting electroviscous time is larger than any reasonable resident time of the sample in the field. AC post deposition flake alignment has been demonstrated, but only by raising the frequency and field strength and reducing the viscosity of the paint (see Section 3.2.1).

There is a DC field in the layer resulting from the current due the charge carried by the paint drops. This current causes an electric field in the layer that depends only on the current density and the conductivity of the

layer. The total current to the layer, I, is 25μA. The electric field, E, is the total current divided by the total spray area, A, and the conductivity, σ.

$$E = \frac{I}{\sigma A}$$

The spray area is approximately 35cm in radius resulting in an electric field of 150V/m. Using this field the electroviscous time is on the order of tens of hours, again much longer than reasonable residence times.

Electrophoresis of the flake, as well as other pigments, has also been investigated. However, to substantially alter (in reasonable residence times) the flake or the pigment it has been found experimentally that fields on the order of 10^4 V/m are required. Fields in the layer are approximately two orders of magnitude less.

The higher efficiency of the electrostatic paint process does give a wetter paint layer (i.e., more solvent). The possibility exists that evaporation of the solvent after deposition tends to align the flake. From experimental measurements the paint has a total change in mass during the application and curing process of approximately 60 percent. During mechanical application of the paint the change is approximately 35 percent; electrostatic application results in a change of approximately 25 percent. It is possible,

though unlikely, that this difference accounts for flake alignment.

3.1.1 Experimental Investigation of Formation and Impact Stages

A device that produces a single stream of drops in a regular, well defined, and predictable position would allow an analysis of drop formation and the impact dynamics using high speed photographic techniques. A single drop sprayer was designed using a needle at high potential as the atomizing orifice. The paint is forced through the needle and forms a current driven jet. This jet becomes unstable a certain distance from the needle and breaks into drops. These drops can be similar in size to those observed in the electrostatic sprayer. The configuration is shown in Fig. 3.2.

It is necessary to have a large orifice (approximately 500 microns) so that the metal flakes do not block the hole. However, to obtain drops of the appropriate size, the jet must be reduced in size by a factor of 50. This is accomplished using an electrical field to both accelerate and stabilize the jet (current driven jet) [4] allowing it to narrow before the pinch instability causes a breakup into drops. The tangential electric field, specified by the

Fig. 3.2
Single Drop Sprayer

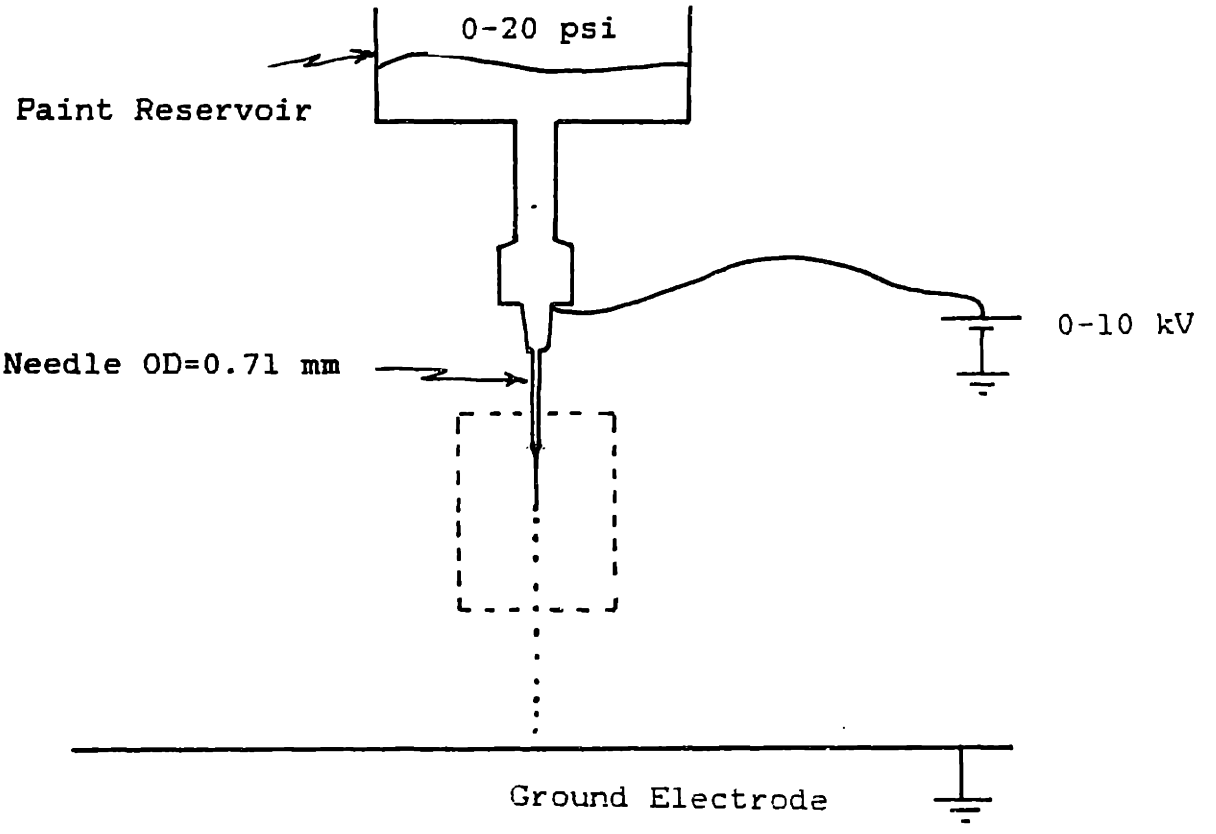

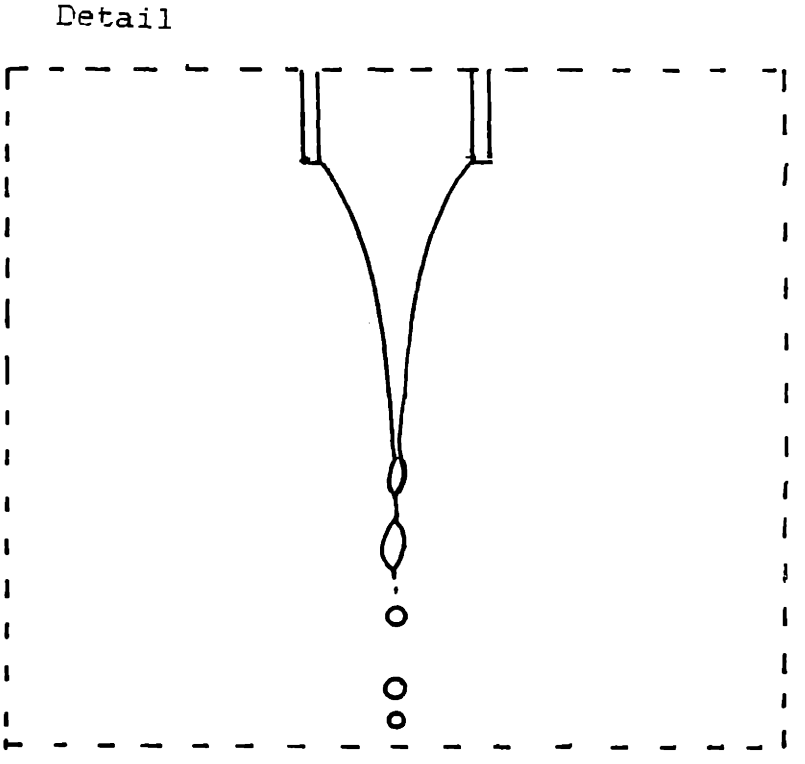

current, is the stabilizing force. As the jet accelerates, charge convection becomes important at the expense of the tangential electric field. Therefore, the stabilizing force is reduced. An estimate of the drop size can be made by equating the conduction and convection currents. It is assumed that this represents the point where the tangential field is reduced sufficiently such that the jet is marginally stable. The surface charge, σ_s, is

$$\sigma_s \simeq \varepsilon_o E \tag{3.2}$$

where E electric field normal to the jet and ε_o is the permittivity of air. The convection current is

$$I_c = \sigma_s U 2\pi r \tag{3.3}$$

where r is the radius of the jet and U is the velocity of the jet. The velocity of the jet is given by

$$U = \frac{Q_v}{\pi r^2} \tag{3.4}$$

where Q_v is the volume flow rate. The conduction current is

$$I_d = \pi r^2 \sigma E \tag{3.5}$$

where σ is the conductivity of paint. Note the tangential electric field is assumed to be of the same order as the normal field. Using Eqns. 3.3 and 3.4 for the convection current and equating it to Eqn. 3.5, the conduction current

gives

$$r^3 \simeq \frac{2\varepsilon_o Q_v}{\pi\sigma} \tag{3.6}$$

Approximate values for these parameters are

$$Q_v = 10^{-10}\ m^3/s$$

$$\sigma = 10^{-7}\ mho/m$$

This indicates that the jet radius is approximately 17μm when it becomes marginally stable. The wavelength, λ, for a disturbance on a charged jet has been shown by Mutoh, Kaieda, and Kamimura [5] to be related to the jet radius by

$$\lambda = \frac{2\pi r}{0.418} \tag{3.7}$$

Note, this expression is for liquids having a viscosity an order of magnitude less than the paint and from the experimental results under estimates the wavelength, λ. The volume in a wavelength of the jet is expected to equal the volume in a drop

$$\pi r^2 \lambda = 4/3\pi R^3$$

or using Eqn. 3.7 for λ

$$R = 2.2 \times r$$

$$= 37\mu m$$

Hines [6] predicts the breakup of these jets using an energy argument avoiding consideration of the stabilizing mechanisms. Hine's equation for the drop radius is

$$R^3 = \frac{9\gamma\varepsilon_o}{4\pi\varepsilon E^2 C}$$

where γ is the surface tension.

$$C = \left(\frac{\varepsilon\sigma^2}{4\pi^2 Q_v^2} \right)^{1/3}$$

Approximately

$$E = 3 \times 10^5 V/m$$

$$\gamma = 0.03nt/m$$

$$\varepsilon = 6 \times \varepsilon_o f/m$$

This gives a drop radius of 150μm. These two approaches predict drop sizes within a factor of four and Hine's estimation predicts, almost exactly, the drop sizes commonly observed. However, the poor estimate of the wavelength, λ, given by Eqn. 3.7 may account for this discrepancy. The apparent absence of the electric field in the first estimate is misleading as the flow, Q_v, is effected by the field. The largest difference appears in the surface tension, implicitly used in Hine's estimate and absent in the other.

In order to properly freeze the motion, a high speed strobe is required. To achieve the necessary magnification, a special lens is required. These are opposing requirements

since a high speed strobe has low energy input and a magnifying lens dramatically reduces the light received by the film. Some of these problems have been overcome using a strobe of 6.5J with a pulse duration of 0.5μsecs and a Questar QM1 telescope. However, the magnification is not as high as desired. The current driven jet poses another problem. At the field strengths required to get the necessary narrowing, the jet has a low margin of stability for the kink mode. The kink instability, usually associated with a corona discharge, is close to incipience and causes wild oscillations to occur periodically.

The objective is not only to get a picture of the jet as it breaks into drops but to be able to see the flake inside the drop. This would allow the effects of the flakes on the jet to be evaluated while following the flake orientation during breakup and on impact. The light and stability problems made this impractical. Fig. 3.3 shows an example picture of the jet breakup. Note that the paint is opaque and prevents any information on the flake from being obtained. This is not unexpected as the amount of light penetrating the drop decreases as the radius of curvature decreases. Using this method, drops as small as 100μm were obtained. However, this occurred at high applied potentials where problems with the kink instability made repeatability difficult. Fig. 3.4 shows this instability in a very

moderate state. The whipping motion of the jet makes focusing difficult, and these particular pictures are in partial focus only due to the number of repetitions and luck. The lack of stability makes it very difficult, if not impossible, to get pictures of drops impacting on the surface: because the point of impact is statistical, focusing at the right place is almost impossible.

3.1.2 Experimental Investigation of In-flight Stage

In-flight orientation has been investigated by a light scattering experiment, shown in Fig. 3.5 . A laser beam illuminates the spray cloud and the reflected light is measured. If alignment is occurring in-flight, differences in reflected light might be expected as the potential applied to the sprayer is varied. The reflected light is a function of the applied potential, but a similar dependence occurs using paint containing no flakes. It is felt that this variation is due to the slight change in atomization as the electric field changes. For details on this experiment the reader is referred to David Lyon's Bachelors Thesis [7].

An experiment was constructed to separately control the charge on a drop and the imposed electric field. The apparatus is shown in Fig. 3.6 . The paint is sprayed from a mechanical sprayer through a small hole in the grounded

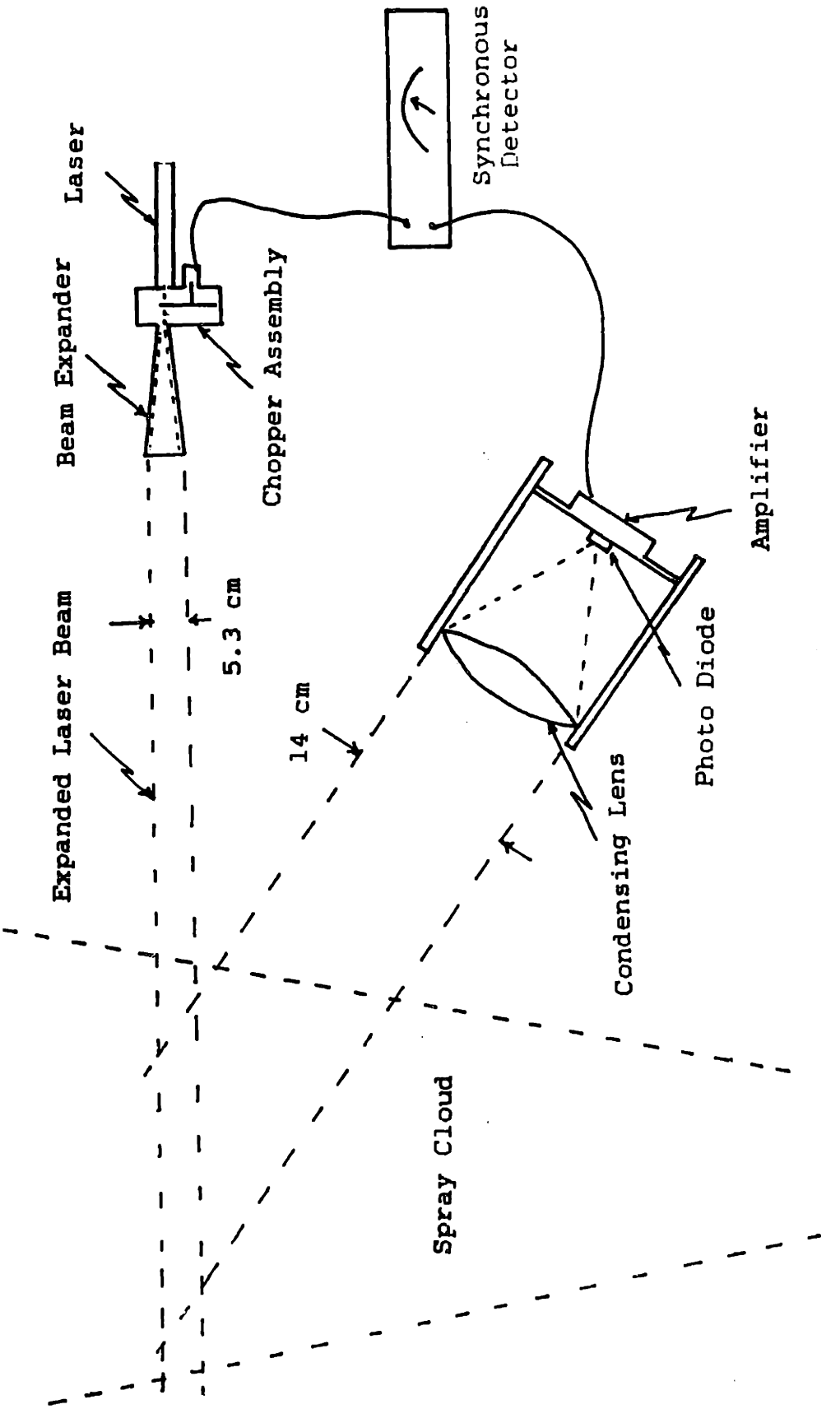

Fig. 3.5
Optical Measurement of In-flight Orientation

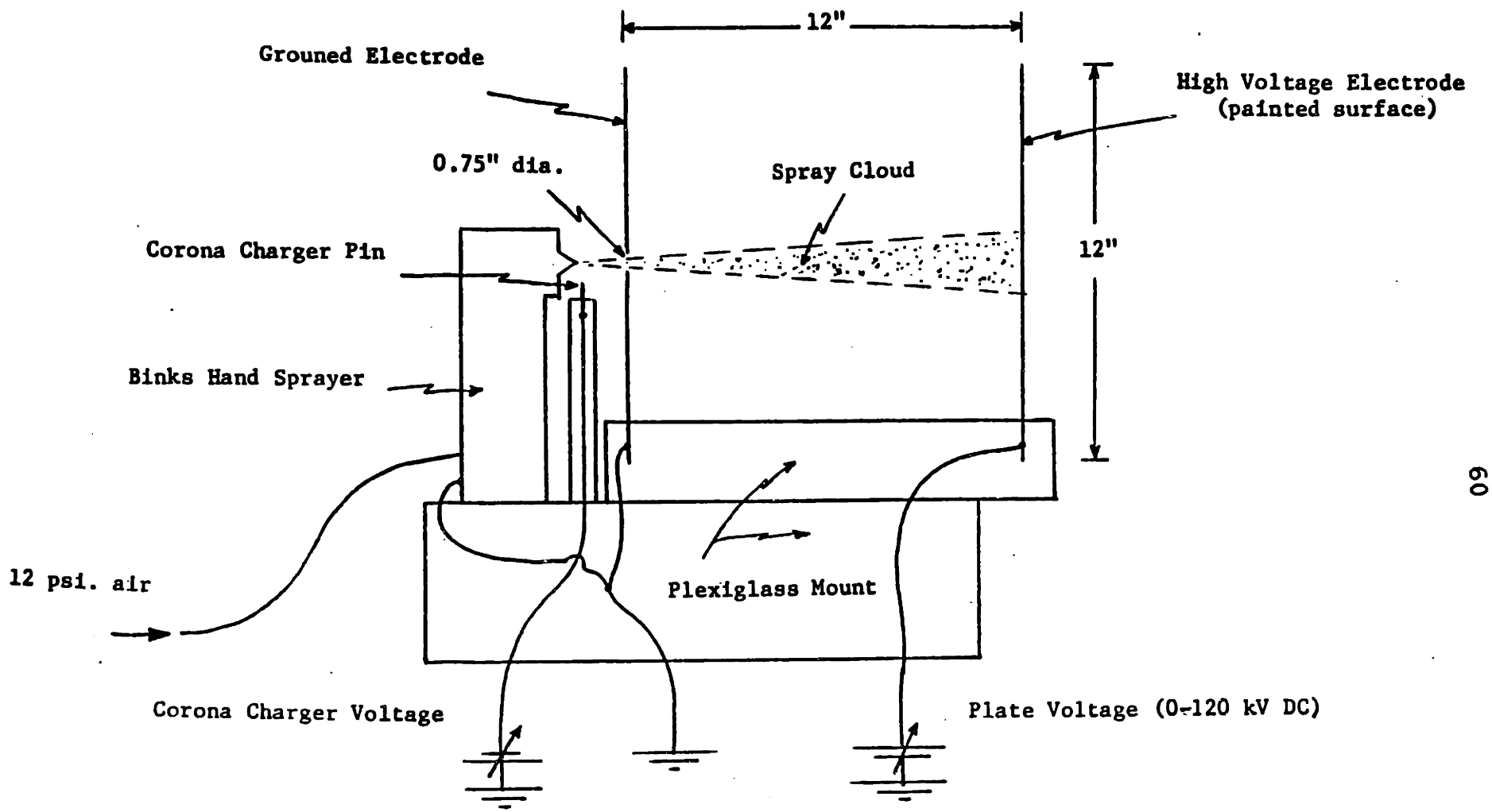

Fig. 3.6
Apparatus to Control Drop Charge and Imposed Field

plate. The plate electrically shields the spray nozzle from the electric field. Therefore, the drops are not charged by the electric field imposed between the two plates. A corona pin is placed near the spray nozzle and can be used to independently charge the drops by ion impact.

Distinguishing between flake orientation caused by electric polarization forces and fluid forces requires independent control of the charge on the drops and the electric field. Uncharged drops in an electric field would be entrained in the air flow and the drops would, therefore, not have a velocity relative to the air. Any flake alignment observed with the drops not charged is due to electric polarization forces on the drop. A fluid torque would result if there are wetted flakes (oblong drops) and there is relative motion between the drop and the air. This relative velocity is controlled by the electric field and the charge on the drops.

The results from the optical measurement of flake orientation and the paint layer cross-sections, discussed in the next section, provided little incentive for proceeding with this experiment. Although preliminary tests showed independent control of the field and the charge, there was no further experimentation using this device.

3.1.3 Experimental Investigation of Post-impact Stage

Work on this stage has focussed mainly on the forced alignment of flakes, discussed in detail in Section 3.2. Earlier work attempted to show that alignment could produce similar color shifts in a mechanically sprayed paint layer as is seen in an electrostatically sprayed paint layer. This work was moderately successful in showing that alignment can be forced using high frequency fields resulting in a color that is similar to that obtained electrostatically. However, the work did not indicate a mechanism that occurs during electrostatic spraying that could simulate these conditions. For more details of these experiments the reader is referred to Jeffrey Goodman's Bachelors Thesis [8].

3.1.4 Cross-sections of Mechanical and Electrostatic Paint Samples

Cured samples of both mechanically and electrostatically applied paint layers were sliced to expose the cross-section. After this surface was polished to 0.1μm the flakes could be observed in the paint layer. Two sample cross-sections are shown in Fig. 3.7 and Fig. 3.8. The angles between the flakes and the substrate, for flakes larger than 2μm in length, were measured. The mean angle for the mechanically sprayed sample is 17.8μm with a standard

Fig. 3.7
Cross-section: Mechanically Sprayed Paint Layer

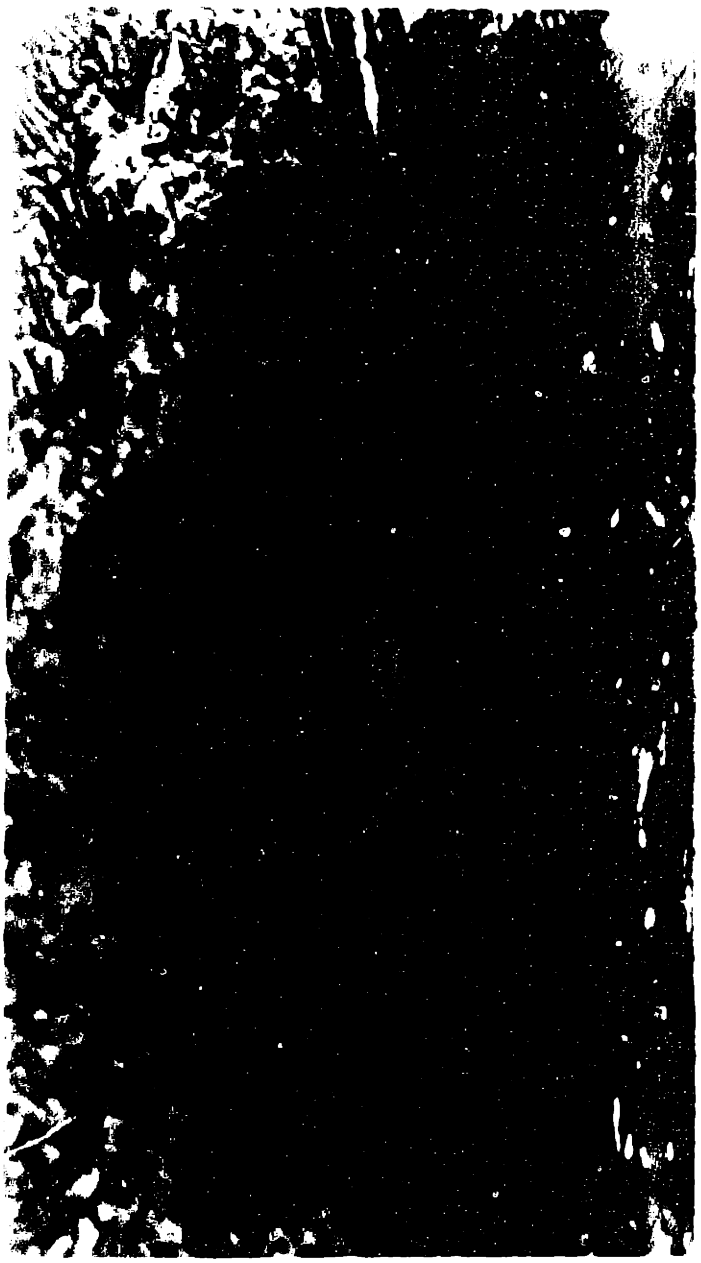

Fig. 3.8
Cross-section: Electrostatically Sprayer Paint Layer

error of 2.4μm while the mean angle for the electrostatically sprayed sample is 15.8μm with a standard error of 1.8μm. There is no evidence of vertical flake alignment in the electrostatic sample. Note, however, that the average flake angle is small; the flakes are almost parallel to the painted surface. This indicates that the impact dynamics may well dominate both painting processes in terms of flake orientation.

From Figs. 3.7 and 3.8 it should also be noted that the electrostatic sample appears to have less flake present. This could result in two ways. First, the flakes could be aligned. Thus, in a single slice less flake would be present (however, the occasional flake standing on end would be expected and is generally not observed). The other possibility is that there is simply less flake in the layer. This is pursued in Chapter 4.

3.2 Forced Flake Alignment

Electrical orientation requires a substantial field inside the paint layer. The paint is conducting, with a charge relaxation time, τ_e, of approximately 10^{-4}secs. Given that contact with the layer is not possible if the paint finish is to be preserved, a DC field will be completely shielded from the layer. The next two sections describe two

methods for obtaining an electric field in the paint layer.

3.2.1 Capacitive Coupling

An alternating electric field can penetrate the paint layer if the frequency of excitation is greater than the inverse charge relaxation time.

$$\omega > 1/\tau_e = 10^4 \text{ rad/sec or } 1.6 \text{ kHz}$$

If $\omega >> 1/\tau_e$ then the layer can be treated as an insulator. The maximum field within the layer can be calculated using a maximum field in the air gap equal to the breakdown field, approximately 10^6V/m. Since the permittivity of a typical automotive enamel is approximately $6\varepsilon_o$ the maximum value of the field in the layer is

$$E_{max} = \frac{10^6}{6} = 1.7 \times 10^5 \text{ V/m peak}$$

Fig. 3.9 shows the basic configuration of capacitive coupling indicating typical dimensions of the paint layer and a reasonable spacing for the electrode. The supply must be able to provide 10,000V peak at a frequency of at least 16 kHz to obtain this maximum value.

Using available equipment a value of 1000V peak at 13kHz is obtainable. The electrode structure used is shown in Fig. 3.10. The spacing is approximately 2.5mm to account

Fig. 3.9
Capacitive Coupling to the Paint Layer

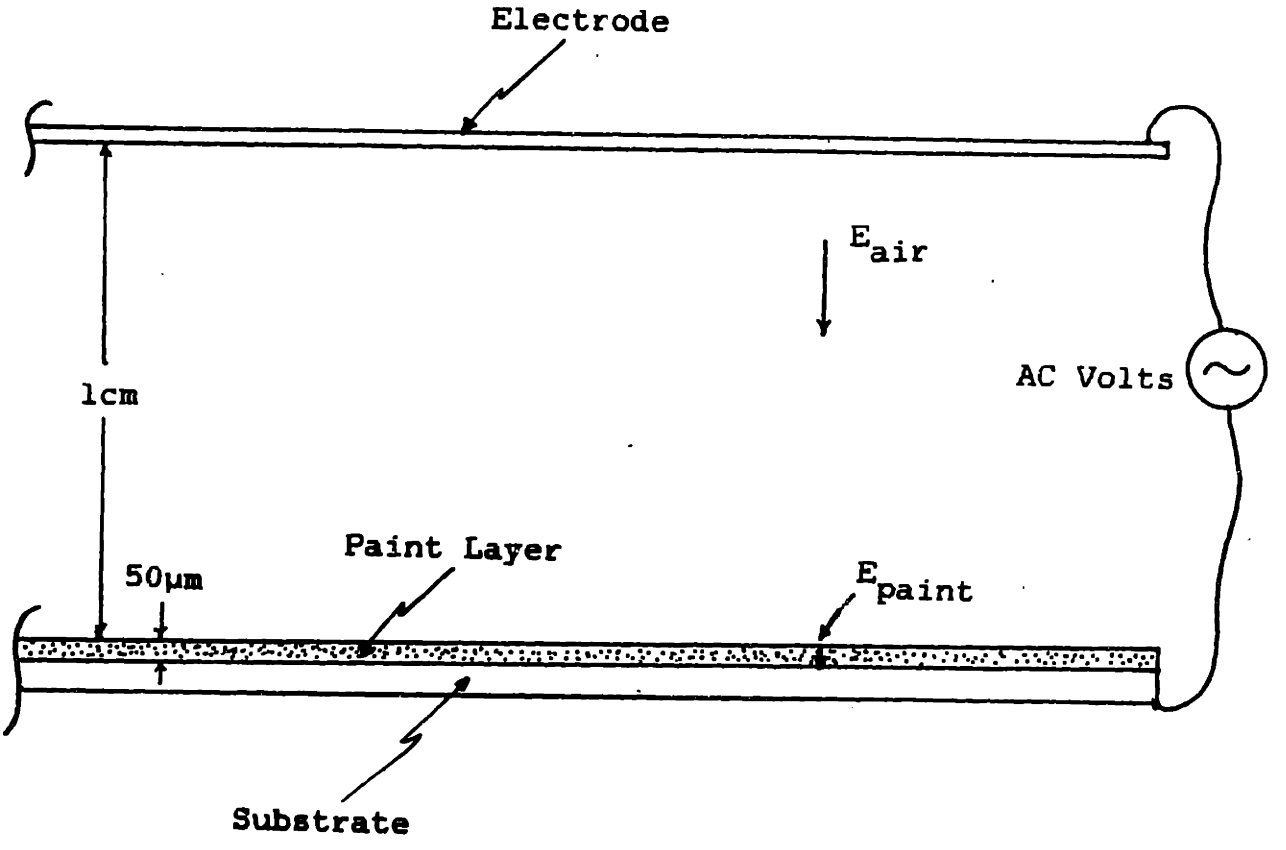

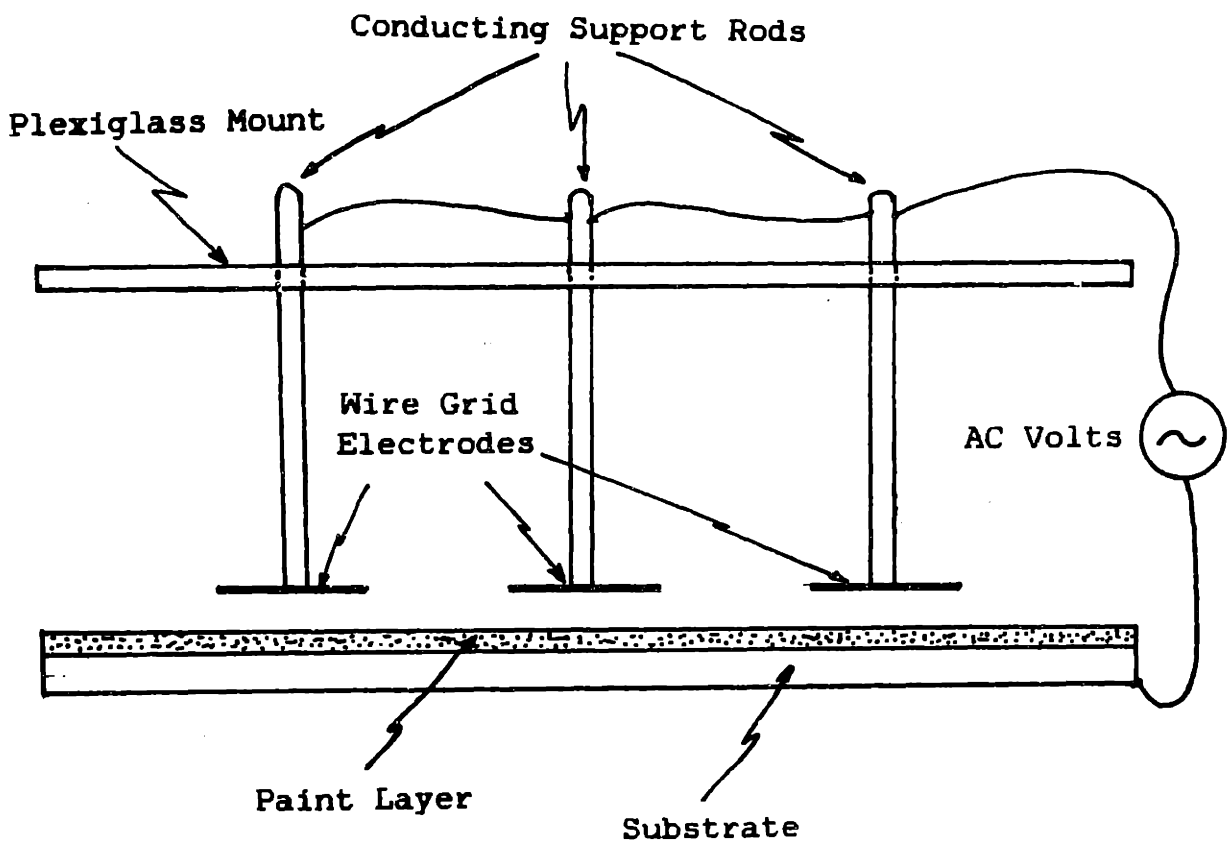

Fig. 3.10
Capacitive Coupling Electrode Structure

for the lower applied potential. The flake is assumed to respond to the rms value of the field, approximately 4.6 x 10^4V/m rms. The electrodes are constructed out of metal grids to allow air circulation over the paint layer so evaporation occurs unhampered by the electrodes. The field is applied for 60secs while the paint is still wet. Evaporation of the solvents occurs throughout the experiment changing the paint properties. Therefore, the experiments are completed within five minutes after the paint is sprayed.

A normal paint finish does not appear to exhibit a noticeable color shift in these experiments. However, if the paint is applied very wet, i.e. with large solvent concentration in the deposited layer, noticeable color variation occurs under the electrodes. The amount of color variation depends greatly on the thickness and the wetness of the paint layer. If field controlled darkening were desired, the long times required and the necessity to paint an unusually wet paint layer make this technique impractical.

3.2.2 Corona Current

A current driven through the paint layer can give rise to an electric field in the layer. This field, E, depends

only on the current density, J, and the paint conductivity,σ.

$$E = J/\sigma$$

Because contact to the layer is to be avoided, a corona source is used to generate a current. A single corona pin arrangement is shown in Fig. 3.11. For a pin spacing of approximately 1cm an easily obtainable corona current is 3μA, affecting an area of 0.6cm in radius. The electric field from this source is

$$E = \frac{I}{\pi R^2 \sigma} = 5.3 \times 10^5 \text{ V/m} \qquad (3.8)$$

This DC field is approximately an order of magnitude larger than the rms value of the field obtained using an AC source and capacitive coupling. Experiments using a corona current show substantial color variation in standard paint finishes in times of less than a second.

The affected areas on these samples were cut to expose the cross-section. This section was polished using a 0.1μm paste to allow high magnification pictures of the flakes in the layer. Fig. 3.12 shows the cross-section for a paint layer exposed to a corona current. Comparison with Fig. 3.7, a standard paint layer, indicates substantial flake alignment. In Chapter 5 the details of this technique are developed for use in pattern construction in wet paint

Fig. 3.11
Single Corona Pin Configuration

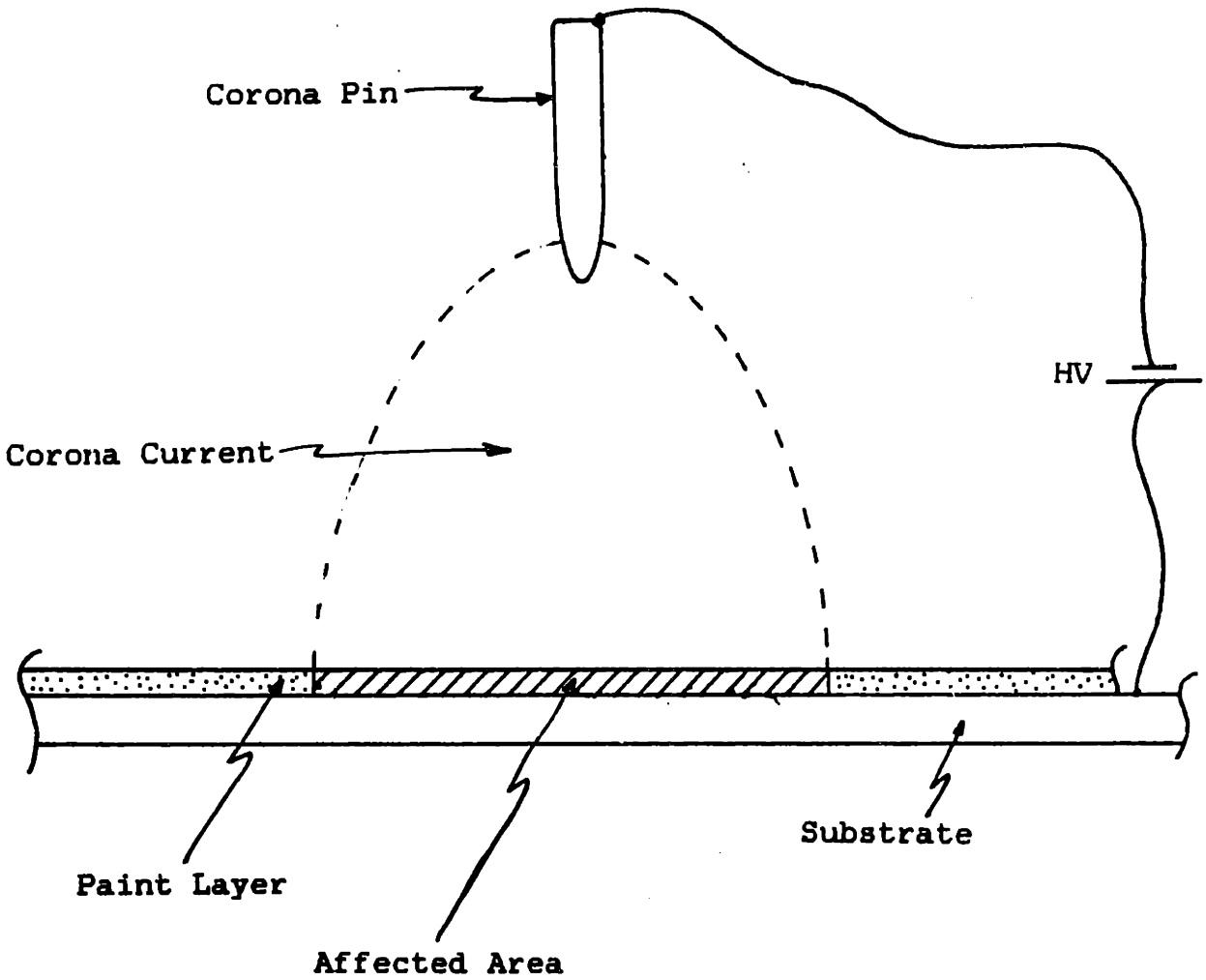

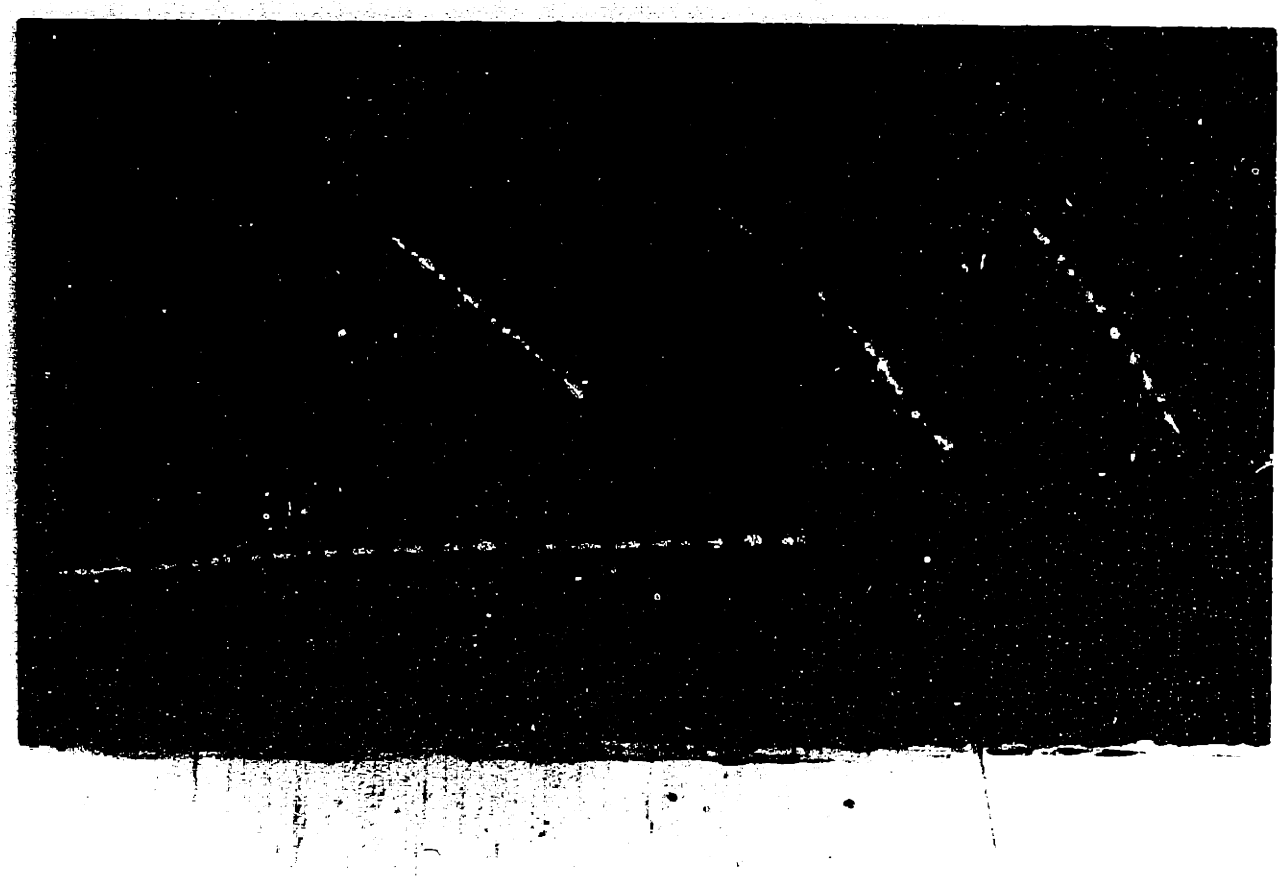

Fig. 3.12
Cross-section: Paint Layer Exposed to Corona

layers. The pattern is locked into the paint finish when the paint is cured. Fig. 3.13 is a sample of the patterns easily obtained using this technique.

Fig. 3.13
Sample Pattern in Metallic Paint

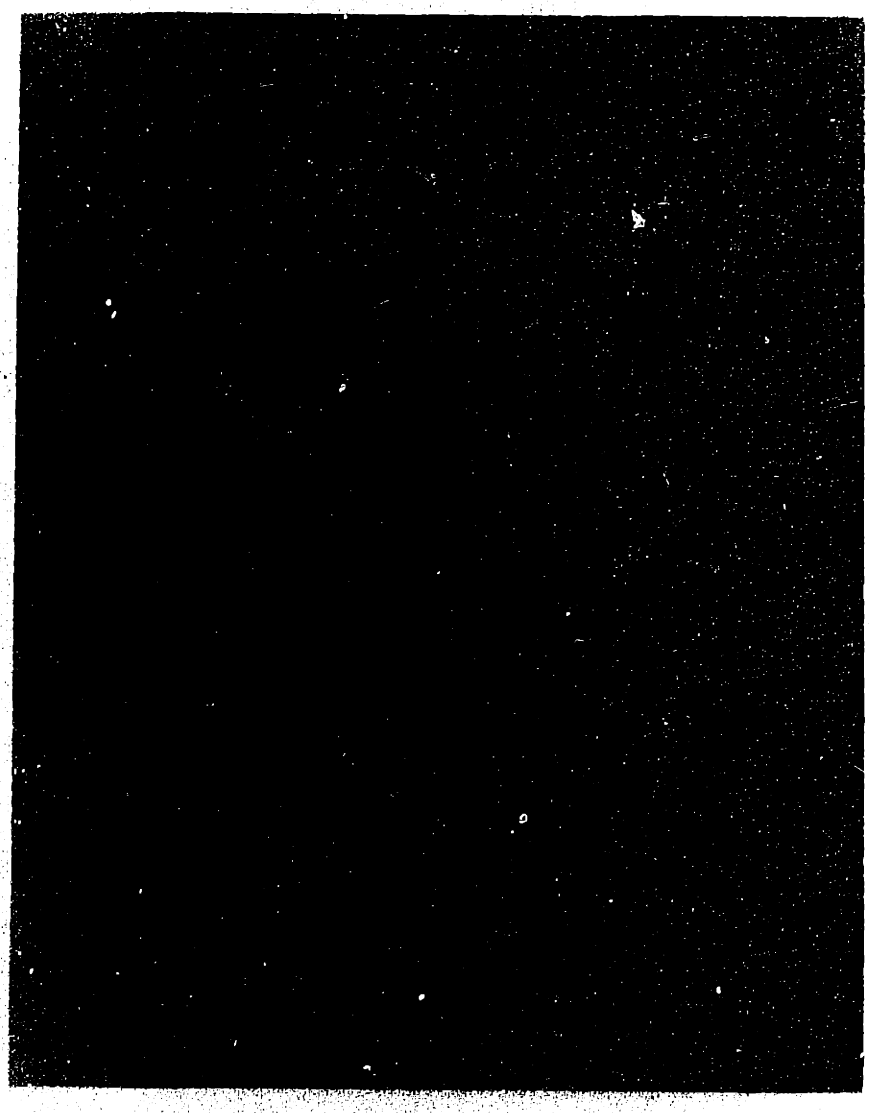

Fig. 3.13
Sample Pattern in Metallic Paint

References

[1] Melcher, J.R., Continuum Electromechanics , MIT Press, Cambridge, 1981

[2] Hoburg, J.F. and Melcher, J.R., "Electrohydrodynamic mixing and instability induced by co-linear fields and conductivity gradients", Phys. Fluids 20, 6 (1977).

[3] Shine, A.D., MIT Doctoral Thesis, 1982

[4] Melcher, J.R. and Warren, E.P., "Electrohydrodynamics of a current-carrying semi-insulating jet", J. Fluid Mech., 47, 1971

[5] Mutoh, M., Kaieda, S., and Kamimura, K., J. Appl. Phys., 50(5),1979

[6] Hines, R.L., "Electrostatic atomization and paint spraying", J. Appl. Phys., 37, 7(1966)

[7] Lyon, D., MIT Bachelors Thesis, 1985

[8] Goodman, J., MIT Bachelors Thesis, 1984

Chapter 4

Selective Mass Transfer

Data obtained during investigation of flake orientation indicated the possibility of selective mass transfer. The flake deposited using the electrostatic painting process appeared different than that deposited using the mechanical process. This difference was first noticed by Bell and Hochberg [1] . The first section deals with their proposed postulate. This postulate is used as the base to formulate the required data needed to characterize the mass transfer. Experiments for both the electrostatic sprayer and the mechanical sprayer are used to acquire this data. This information is then used to identify the dominant mechanisms that account for the color variation between the two processes.

4.1 Bell-Hochberg Postulate

One of the bench marks established in electrostatic painting is a report by Bell and Hochberg [2]. Through private communication they have proposed a mechanism that may account for the increased deposition of non-metallic solids. This has the effect of creating a lower metallic flake content in electrostatically applied paint. Their postulate is as follows:

(1) Large drops carry more metallic flake per unit mass than small drops;

(2) Small drops are entrained in the air flow and generally constitute the majority of the overspray (waste); and

(3) The electrostatic process deposits more small drops than a standard mechanical sprayer.

While this postulate is a starting point for further work it does not provide any quantitative insight into the mechanisms that are controlled by the spray device inputs. A typical sprayer may have numerous operating parameters to adjust. Each parameter may have an effect on each stage of the spraying process and variations in these inputs are likely interrelated. The fluid mechanics and paint atomization are strong influences in the steps of this postulate. The efficiency of the process is as much a function of the drop distribution and fluid flow as the application of electric forces. For example, the efficiency of a typical mechanical sprayer can be easily changed by varying the pressure of the shaping air and that applied to the atomizing nozzle. As the shaping air velocity and the atomization pressure is increased the efficiency typically decreases because the number of small drops increases and the higher air velocity causes more turbulent mixing. The effects of varying these two parameters are interrelated as

both cause finer atomization and change the velocity profile in the spray as well as the degree of turbulence. Most parameters are similarly related and affect the atomization, evaporation, and transport. The operator of a spray device can also adjust the contents of the paint, usually by the addition of solvents, again affecting most processes in the system. A means of providing evidence for the Bell-Hochberg postulate led to the experiments described in the following sections. The results actually provide much more information about the processes than required to validate the postulated mechanism.

4.2 Characterization of Paint Spraying Devices

Modeling of spray devices has been largely empirical. The inputs are often the sprayer parameters (air presure, voltage, spacing, etc.) and the outputs are variables associated with the quality of the surface finish (color, color flop, roughness, etc.). Although this process of curve fitting can be useful, it has its limitations because it provides little understanding of the mechanisms involved. The objective of this work is to gain a physical understanding of the spray process that would help to provide some alternative to simple curve fitting Characterizing a device involves following the specific mass transfer for each drop size. This requires information on

the contents and size of individual drops as a function of their position in the spray cloud. Ideally this would be done wnile the drops are in flight, requiring complex sampling techniques. The compromise is to sample only at the surface where the drops impact. The reward is a detailed understanding of the mechanisms involved in the device.

Drop sampling techniques depend on the particular paint sprayer. Therefore, a different technique is used for the electrostatic sprayer than the mechanical sprayer. The raw data is then processed and digitized to allow basic statistical calculations. All data is taken after the drops have been cured, so the data is in terms of dried paint solids. This avoids problems of evaporation during processing, at the expense of ignoring the evaporation data for each drop size.

4.2.1 Analysis of Drop and Flake Distributions at the Paint Surface for an Electrostatic Sprayer

The details of the electrostatic sprayer are shown in Fig. 2.2. Operating conditions for the sprayer are maintained constant during the experiment. These conditions are:

(1) Turbine speed = 28,000 rpm (edge speed = 108 m/s);

(2) Voltage = -90kV;

(3) Distance from bell tip to grounded target = 0.3 m;

(4) Paint flow rate = 100 ml/min; and

(5) Shaping air pressure = 20 psi.

This shaping air pressure results in a maximum air velocity at the bell tip of approximately 20m/s. The paint drops are highly charged; the charge to mass ratio for an average size drop, 10μm in diameter, is approximately 6μC/g. The deposited spray pattern is approximately 35cm in radius and this area is "covered" in roughly 45secs. Recall that the process is highly efficient - approximately 100 percent efficient using a target twice the size of the spray pattern. At the bell tip the angular momentum is large. Therefore, as a drop leaves the bell edge, it has a large radial velocity in comparison to its longitudinal velocity. However, it is the longitudinal velocity that accounts for the delivery of the paint to the surface.

4.2.1.1 Sampling Drops at the Paint Surface

Mechanical shutters have been used to sample the drops at the paint surface [2]. A grounded shield is placed over the sampling area, then quickly removed and replaced to momentarily expose the test area to the spray cloud. Generally, a sample time less than 0.25secs is required to

prevent the drops from flowing together and erasing the required discrete drop information. There are two major problems with this technique: (1) the movement of the shield will disturb the fluid boundary layer over the test area; and (2) building and operating the device is relatively time consuming and complicated.

As an alternative, an electrical shielding device was developed. Although restricted to the study of charged drops, the electric shutter has the advantage of being switched off essentially instantaneously, of not interfering with the gas flow during the critical time just after it is switched off, and of leaving the test surface essentially as it is on the actual work piece while the sample is being taken.

To prevent drop deposition, the sampling plate is insulated from the rest of the grounded target and taken to high potential. The same polarity is used as for the bell. This creates a field near the surface that prevents the charged drops from impacting the sampling plate. This plate is then momentarily grounded, collapsing the electrical shield, to sample the spray cloud. Thus, during the sampling period, field and flow are not modified by the device.

The field shape around the high-potential electrode, assuming it is two dimensional, i.e. very long compared to

its width, is calculated numerically using the method of charge simulation and is shown in Fig. 4.1. This figure illustrates the strong field at the edges of the plate in comparison to the weaker field at the centre. Moving outward along this centre line perpendicular to the electrode the field decreases, eventually reaching zero, at a critical point where the field due to the electrode balances that due to the spray equipment. This electric critical point, x_o, is illustrated in Fig. 4.1. The details of the drop trajectories depend on the specific gas velocity and the drop conditions in the vicinity of the electrode. However, for design purposes the field on this centre line represents the worst case for electrical shielding because it represents the lowest electric field strength.

Ignoring inertia, and in the absence of particle drag, the drops will follow the field lines exactly. Therefore, ensuring the critical point exists provides a rough estimate of the shutter potential, V, required to effectively shield the drops. Fig. 4.2 shows a plot of the normalized x-directed electric field strength due to the sampling electrode as a function of the distance from the centre of the electrode. For a critical point to exist the applied field from the painter, E_p, must be less than the maximum field in Fig. 4.2, in normalized units approximately 0.6. Therefore

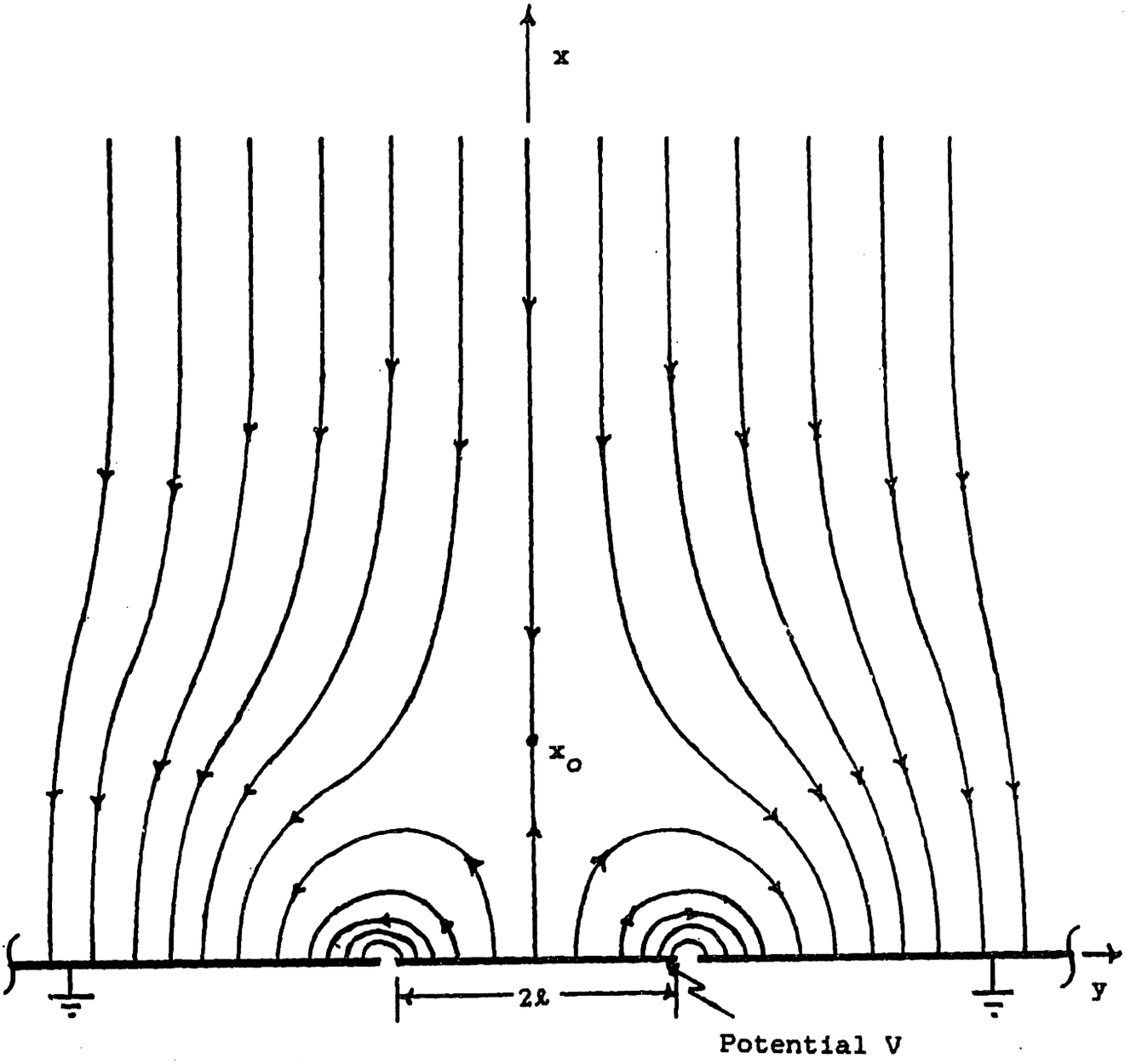

Fig. 4.1
Electrical Shutter: Electric Field Plot

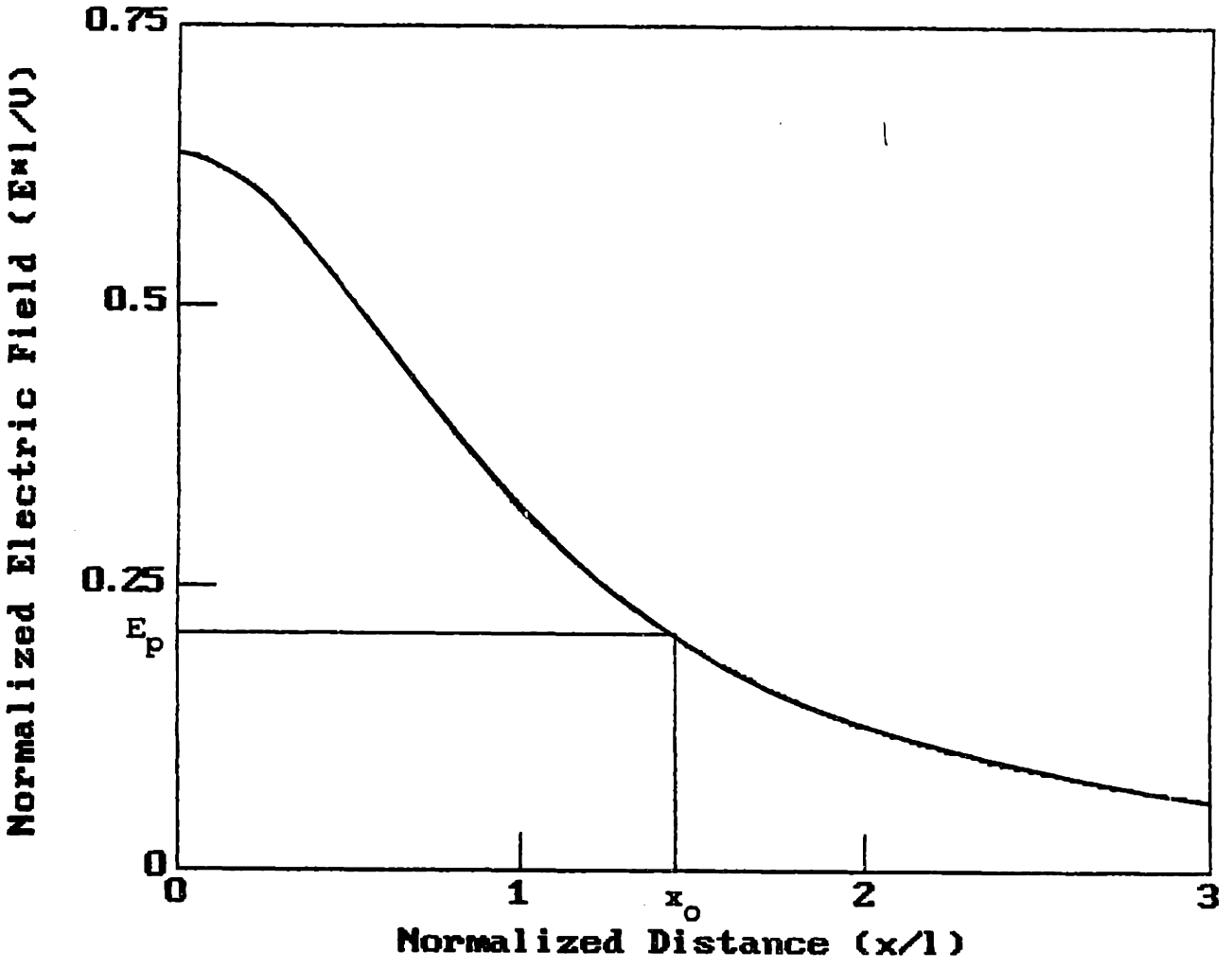

Fig. 4.2
Electrical Shutter: X-directed Electric Field

$$E_p < 0.6\frac{V}{\ell} \text{ or } \frac{V}{\ell} > 1.67E_p \qquad (4.1)$$

where V is the potential applied to the electrode and ℓ is half the width of the electrode. Because the fluid flow at the surface is zero, the effects of the flow will not change the validity of this result. Inertia however, will have an effect, especially for the large drops.

Inertial effects can be estimated for a drop trajectory along the centre line, perpendicular to the electrode, by using an energy argument. In the short distance between the critical point and the electrode the drop motion is assumed to be dominated by inertia and the electric force. Therefore, viscous drag is insignificant and the energy of the drop is conserved. The total drop energy is the kinetic energy plus the electrical potential energy

$$\tfrac{1}{2}mv^2 + q\Phi = \text{constant} \qquad (4.2)$$

where Φ is the electrical potential and q is the charge on the drop. The energy of the drop at the critical point should be less than the energy of the drop as it arrives at the surface with zero velocity. If the drop is not to impact

$$\tfrac{1}{2}mv_o^2 + q\Phi_o < q\Phi_p \qquad (4.3)$$

Therefore

$$\frac{mv_o^2}{2q} < \Phi_p - \Phi_o \qquad (4.4)$$

Even though the inertia is important as the drop approaches the surface, its velocity farther away from the surface is determined by migration and viscous drag. Therefore, the velocity at the critical point is approximated as the mobility, b, of the drop times the field applied by the paint sprayer. Assuming low Reynold's Number flow such that the drag is essentially Stoke's drag, the mobility is

$$b = \frac{q}{6\pi\eta R}$$

Therefore

$$v_o = \frac{q}{6\pi\eta R} E_p \tag{4.5}$$

where R is the radius of the drop and η is the viscosity of air. This over estimates the velocity as the field drops to zero at the critical point. However, space charge effects are not included and these have been shown [3] near the paint target. Using Eqn. 4.4 in Eqn. 4.5

$$\frac{mq}{(6\pi\eta R)^2} E_p^2 < \Phi_p - \Phi_o \tag{4.6}$$

As shown in Eqn. 4.6 the potential difference between the shutter electrode and the critical point is required to evaluate the ability to electrically shield the drops from the electrode.

A linear estimate of the shutter field for the region between the electrode and the critical point can be used to

calculate the potential due to the shutter. At the critical point

$$\Phi_{shutter} = V - \frac{C_o V x_o^2}{2\ell^2} \tag{4.7}$$

where C_o is the slope of the electric field, Fig. 4.2. Assuming a linear field at the critical point due to the spray equipment gives the potential

$$\Phi_{sprayer} = E_p x_o \tag{4.8}$$

Eqns. 4.7 and 4.8 are combined to find the total potential at x_o

$$\begin{aligned} \Phi_o &= \Phi_{shutter} + \Phi_{sprayer} \\ &= V - \frac{C_o V x_o^2}{2\ell^2} + E_p x_o \end{aligned} \tag{4.9}$$

Substituting Eqn. 4.9 into Eqn. 4.6 gives

$$\frac{mq}{(6\pi\eta R)^2} E_p^2 < \frac{C_o V x_o^2}{2\ell^2} - E_p x_o \tag{4.10}$$

Solving for x_o and eliminating the negative root

$$\frac{x_o}{\ell} > \frac{E_p \ell}{C_o V}\left[1 + \left(1 + \frac{mqC_oV}{(6\pi\eta R\ell)^2}\right)^{\frac{1}{2}}\right] \tag{4.11}$$

Practically, the shutter potential is limited by the size of the insulator between the test area and the rest of the paint target. Corona emission and the possibility of arcing must be avoided. Several geometries and potentials were tried before 6.5 kV and the geometry shown in Fig. 4.3

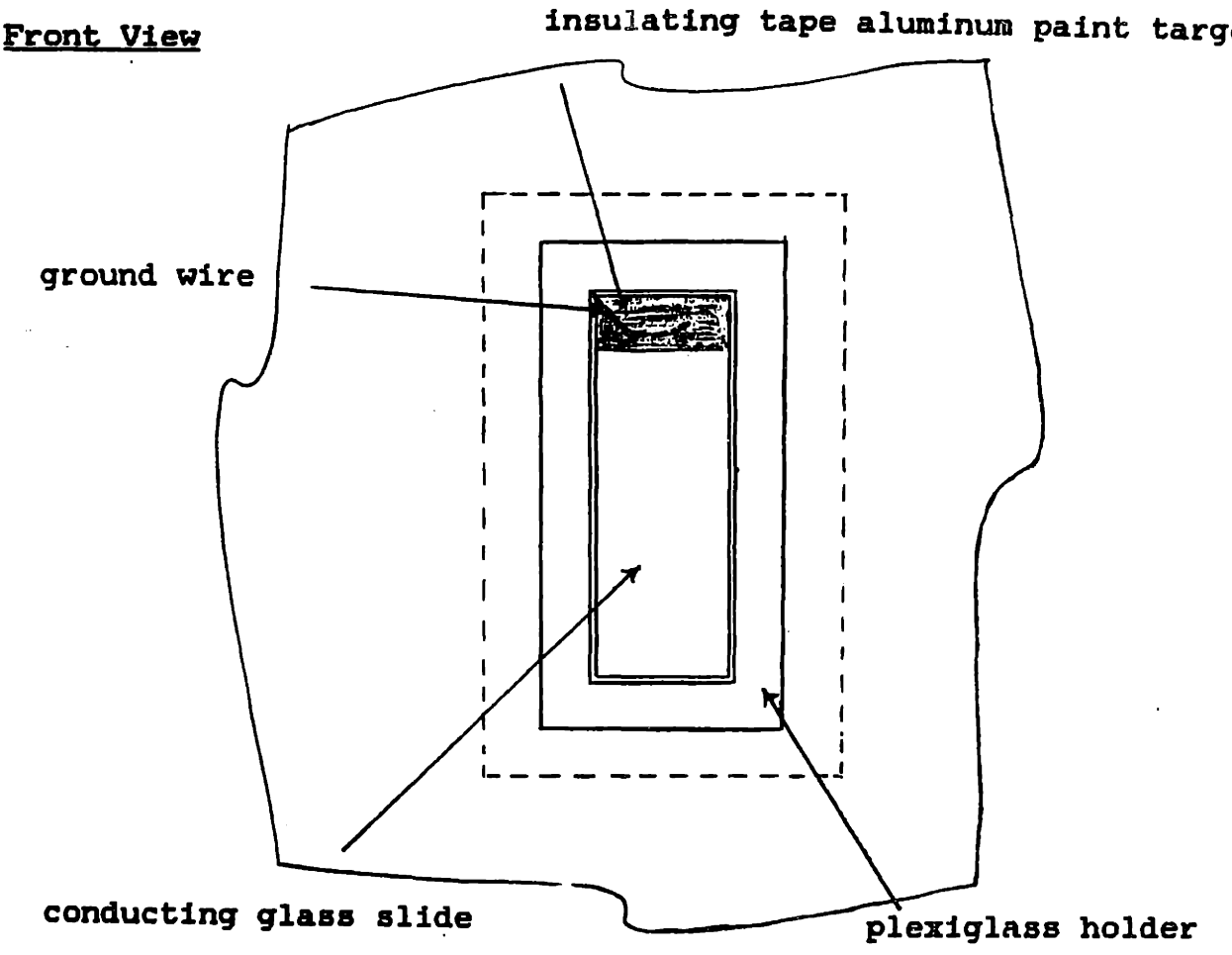

Fig.4.3
Single Plate Electrical Shutter

was chosen. Typical numbers from the Ransburg Turbobell are $m=3.2\times10^{-11}$Kg, $R=20\mu m$, $q=1.7\times10^{-14}$C, and $\eta=1.83\times10^{-5}$kg/sec-m. The slope, C_o, is approximated from Fig. 4.2 to be 0.286. Ignoring space charge, a typical field strength due to the sprayer is $E_p=3\times10^{5}$V/m. Plotting this field on Fig. 4.2 gives

$$\frac{x_o}{\ell} = 1.4$$

Using Eqn. 4.11

$$\frac{x_o}{\ell} > 1.7 \qquad (4.12)$$

This indicates that the geometry and shutter potential are close to the criteria given by Eqn 4.11. Experimentally the effectiveness of the shutter is tested by exposing two test plates to the spray cloud for approximately 20secs and grounding one plate for 0.25secs. The density of splattered paint on the samples is compared. The ratio of the area density for the non-grounded sample to the grounded sample is 0.18. In the experiment the samples are subjected to the spray cloud for 10secs indicating there should be less than 10% error. Actually, the error is substantially less because the data is taken from the edge of the sample where the shield is much more efficient. The criteria in Eqn. 4.11 does represent a worse case situation, with the exception of space charge effects, and from the experimental

observations, provides an engineering estimate of the shutter's effectiveness.

The switching of the test plate between 6.5kV and ground is accomplished using a high voltage vacuum relay that can be controlled electronically. Therefore, the length of time the test plate is grounded can be measured electronically. The capacitance of the test plate is small, approximately C=0.6pf, and the time constant, RC, using the power supply resistance of R=10kΩ, is 6×10^{-9}secs, much smaller than the time the test plate is grounded. Therefore, many test plates are easily switched simultaneously.

4.2.1.2 Data Processing Technique

The test plates used in the electrical shutter are glass slides coated with tin oxide to make one surface conducting. This allows the drops to be examined under a microscope using both front and back illumination. A photograph of a back illuminated sample at a magnification of 200 is shown in Fig. 4.4. The flake appears opaque in these pictures making it easily identified yet at the same time the drop outline is clear. Information can be obtained on both the flake size and the drop size as well as the amount of flake in a given drop. To assemble this data in a statistical manner the drops and associated flakes are

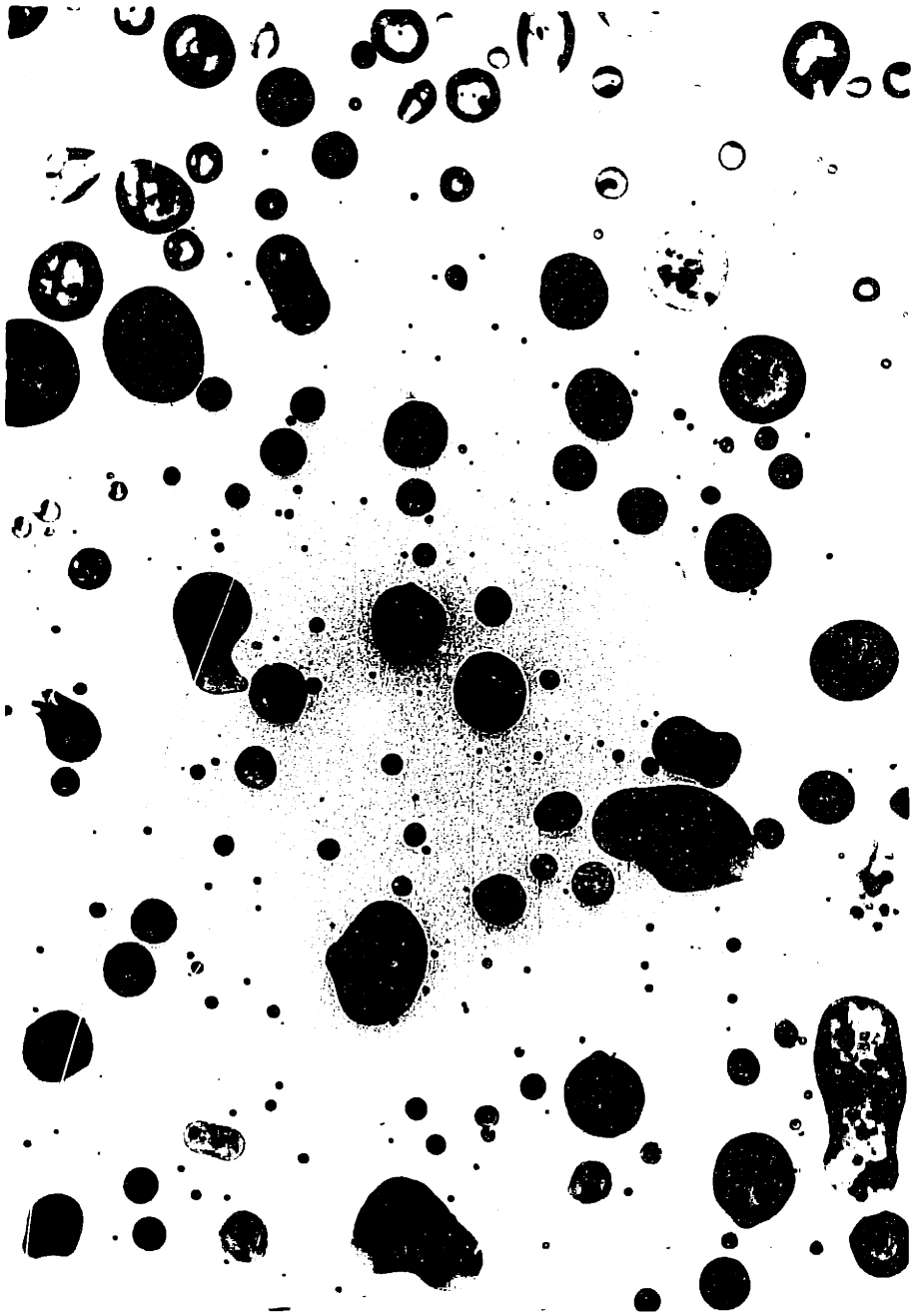

approx. mag. x200

Fig. 4.4
Back Illuminated Drops

digitized using an electromagnetic tablet. The drop and flake area are measured by estimating a diameter that is judged to best represent the area. This greatly aids in the speed of processing the data and suggests how best to automate the method using computerized pattern recognition equipment.

The raw data is in terms of the splattered drop area and the flake area. However, the mass of the drop and the flake are of most interest. Given the dried density of the paint, this requires the volume of each drop and flake. The flake, as seen in the cross-section of Fig. 3.1 , is approximately uniform in thickness with an average thickness of 0.75μm. Therefore, flake volume is approximately equal to flake area multiplied by 0.75μm. Drop volume is more difficult to calculate as the drop profile depends on the splattered drop radius. Drop profiles were measured for a range of drop sizes using a Dektak surface analyzer. The measurement tip of this device has a radius close to the drop sizes measured requiring that the profiles be corrected to account for the finite size of the tip. The average height was fitted to a fourth order curve in drop radius. The details of this procedure are presented in Appendix D. The data is processed by computer to obtain the drop size distribution, the flake size distribution, the mass percent of flake in a drop interval and for the entire data set, the

percent of total flake, the average flake area, and the total mass. Also, basic statistics on the entire sample such as averages, standard deviations, and an estimate of their error is calculated. The data represents discrete points from two number distributions and statistics on subsets of these distributions. The drop number distribution function, D, is a function of the drop size, diameter w, and the total flake area in a drop, f_d.

$$D = D(w,f_d)$$

Therefore, the number of drops, $\#_d$, with diameters between w and w+Δ is

$$\#_d = \int_w^{w+\Delta} \int_0^{\infty} D(w,f_d)\, df_d\, dw$$

Similarly, the flake number distribution, F, is also a function of the drop size and the flake area, f.

$$F = F(w,f)$$

Therefore, the number of flakes, $\#_f$, within drops having diameters between w and w+Δ is

$$\#_f = \int_w^{w+\Delta} \int_0^{\infty} F(w,f)\, df\, dw$$

All data can be written in terms of these two distribution functions, and appropriate scaling functions. For example, mass in the drop diameter interval w to w+Δ as a percent of

the total mass in a sample is

$$\frac{\int_{w}^{w+\Delta}\left(\rho_p \frac{\pi w^2}{4} C(w) \int_0^{\infty} D(w,f_d)\, df_d\right)dw + \int_{w}^{w+\Delta}\left(\rho_{Al} t_o f \int_0^{\infty} F(w,f)\, df\right)dw}{\int_0^{\infty}\left(\rho_p \frac{\pi w^2}{4} C(w) \int_0^{\infty} D(w,f_d)\, df_d\right)dw + \int_0^{\infty}\left(\rho_{Al} t_o f \int_0^{\infty} F(w,f)\, df\right)dw}$$

where C(w) is the drop height as a function of diameter, t_o is the thickness of the flake, ρ_p is the density of dried paint, and ρ_{Al} is the density of Aluminum.

4.2.1.3 Results of Electrical Shutter Experiment

Samples are taken at the paint surface, 0.3m from the bell, at 7 radial positions. Starting at the centre of the target and moving horizontally to the right a sample is taken every 10cm. The samples are numbered consecutively starting at the outer edge of the pattern and moving into the centre. Therefore, the sample at the centre is number 5. The other two samples are taken at 40cm to the left of centre and 20cm up from the centre providing a check on the symmetry of the spray pattern. The configuration of the target is shown in Fig. 4.5. The experiment is carried out using paint with flake and the same paint with the flake removed. The detailed data as well as plots of the drop distributions are given in Appendix E.

Mass as a percentage of the total on all samples is

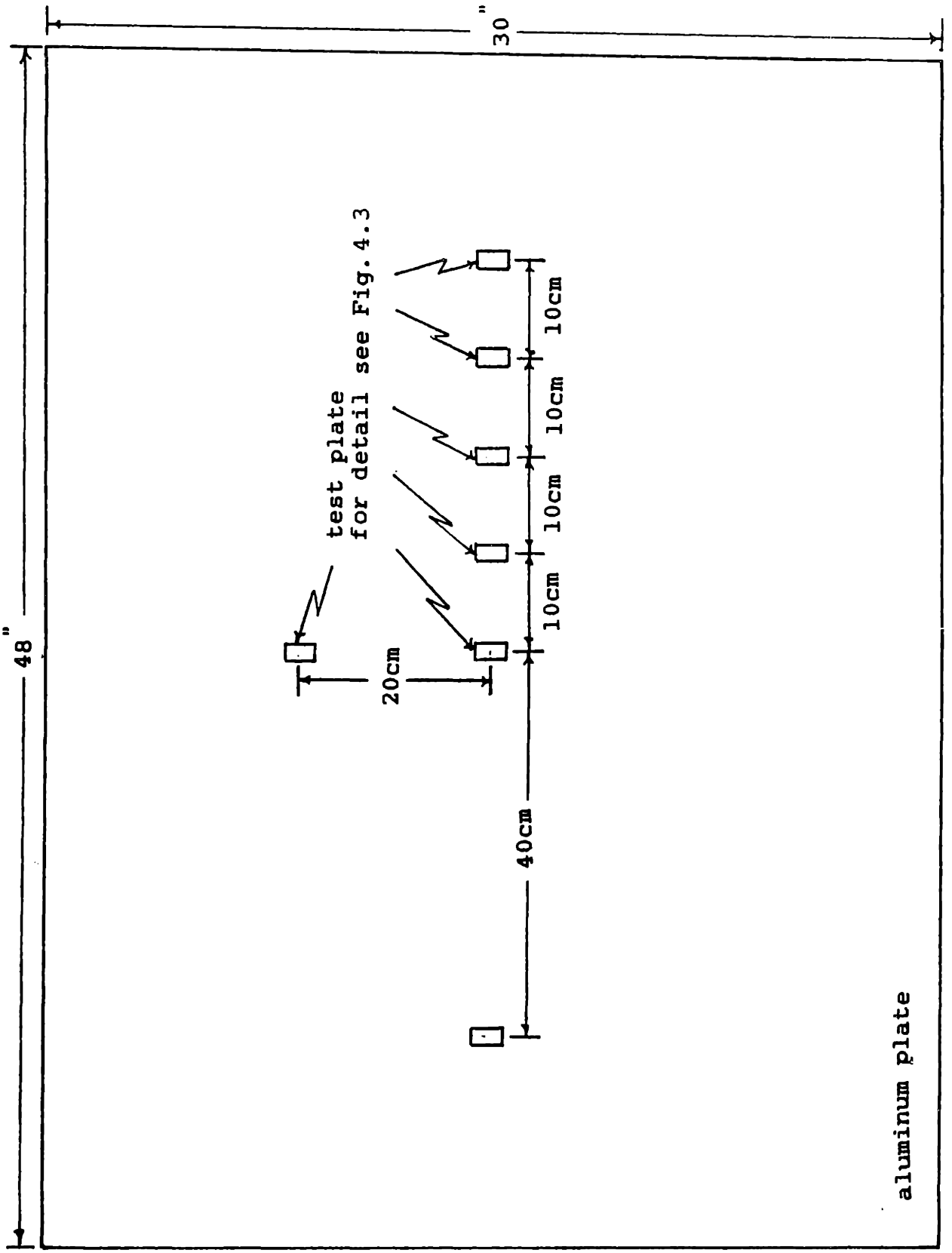

Fig. 4.5
Configuration of Electrical Shutter Target

plotted in Fig. 4.6 for flake paint and for no-flake paint. The mass percentage of aluminum flake is plotted in Fig. 4.7 as a function of radius. An object is painted by passing it through the spray cloud. Therefore, it experiences a mass average of the spray cloud over radius. This average, from the sampled data, gives a mass percent of aluminum flake equal to 1.82%. Fig. 4.8 is a plot of average drop size versus radius for flake paint and Fig. 4.9 is the same plot for no-flake paint. These curves have the same trend as Fig. 4.6, mass versus radius, increasing towards the center then decreasing slightly at the center. Note, the very different average drop sizes between flake and no-flake paint. Fig. 4.10 is a plot of the average flake area versus radius. The average flake area has approximately the opposite trend as the mass and drop size, increasing towards the edge of the spray pattern and then decreasing at the extreme edge. It should be noted that, the standard deviation of the average flake area has this same trend. The plot of mass percent of aluminum, Fig. 4.7 exhibits a similar trend as Fig. 4.10, for flake area, of increasing towards the outer edge of the spray cloud. The error bars on the graphs represent the error in the mean with a probability of 95%.

The statistics for the sum of the five test positions, representing the mass average, are shown in Table 4.11 for flake paint and in Table 4.12 for no-flake paint. Care

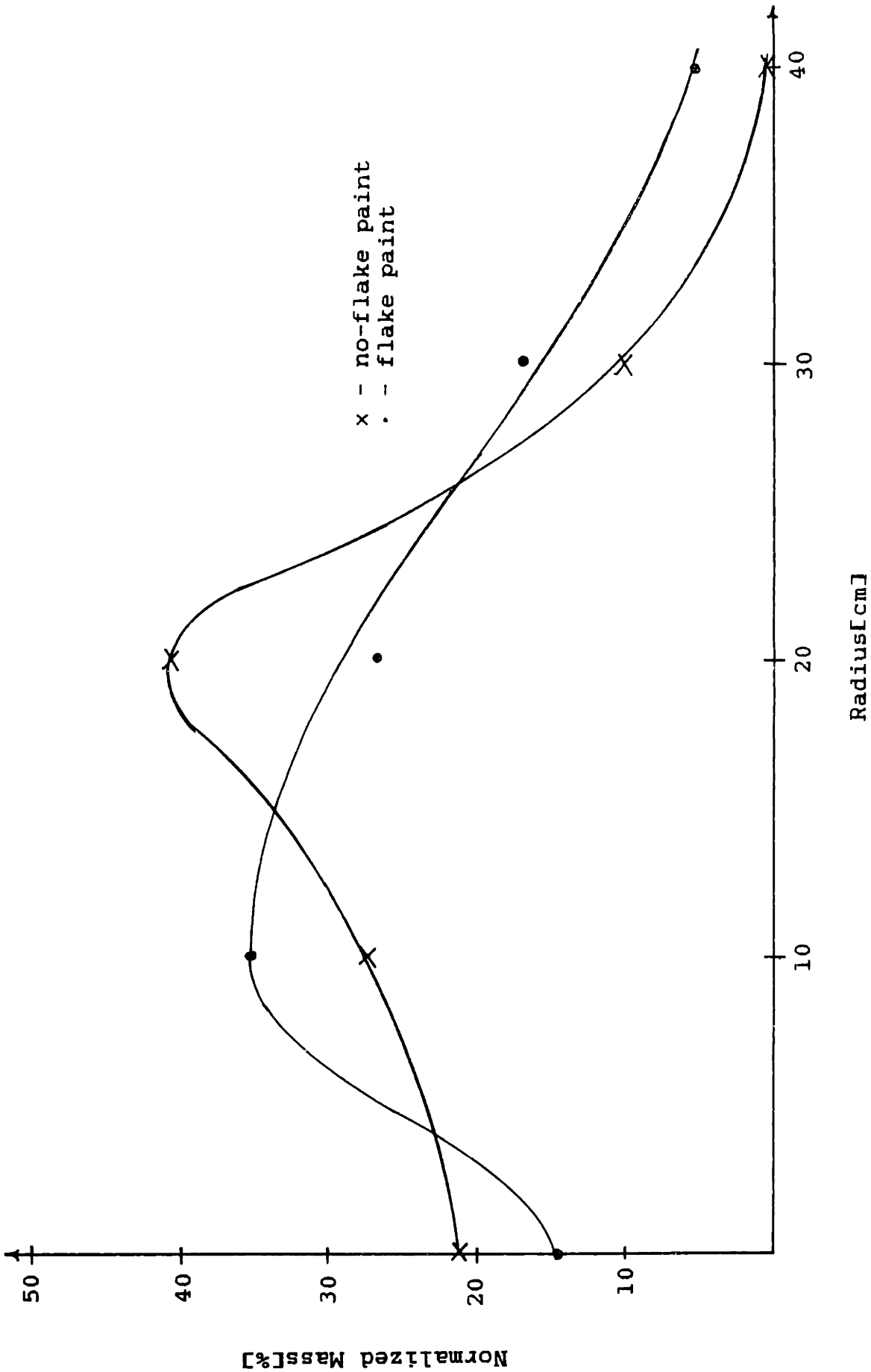

Fig. 4.6
Mass vs. Radius

Fig. 4.7
Mass Percent Aluminum vs. Radius

Fig. 4.8
Average Drop Diameter vs. Radius: Flake Paint

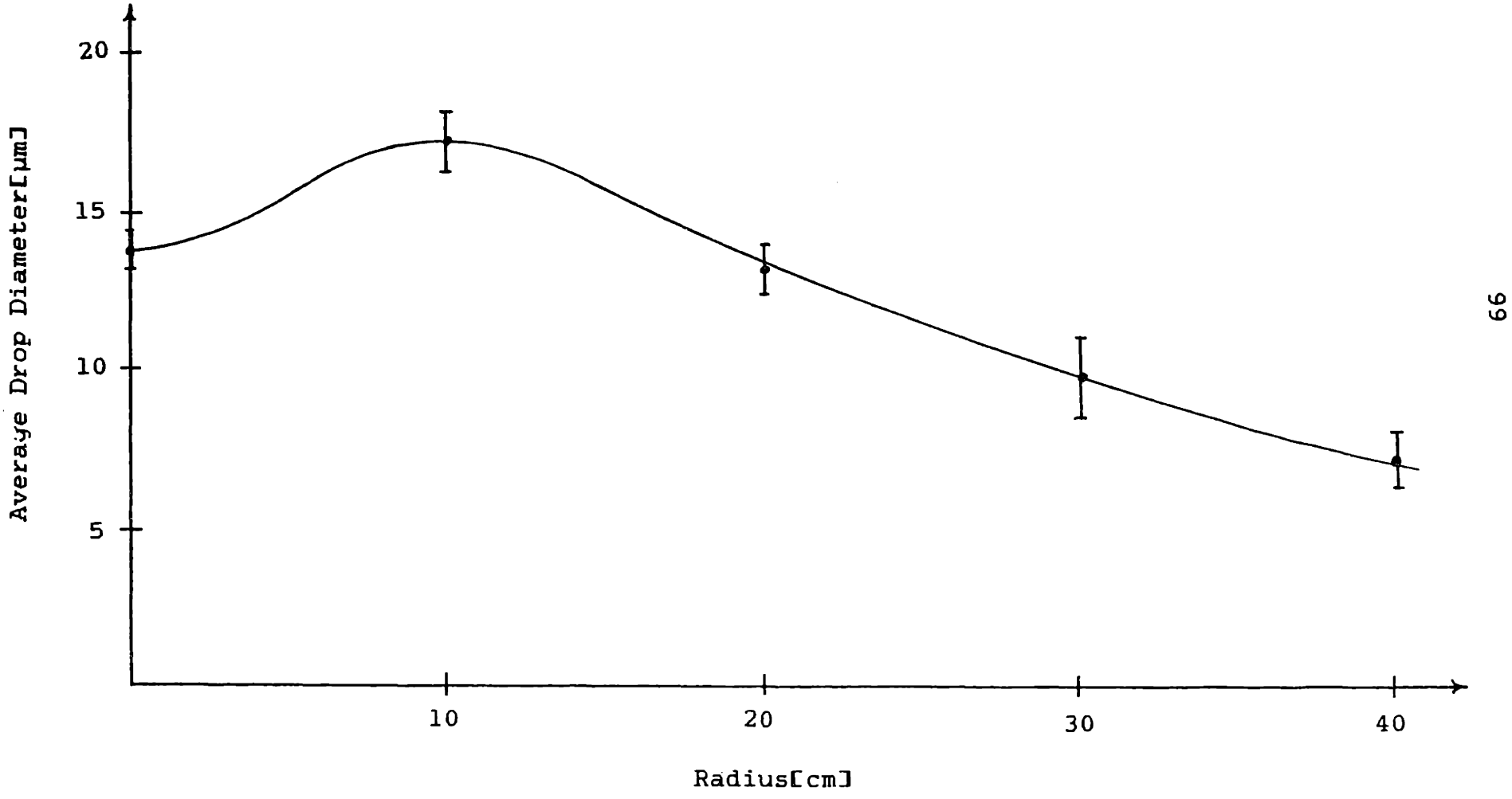

Fig. 4.9
Average Drop Diameter vs. Radius: No-flake Paint

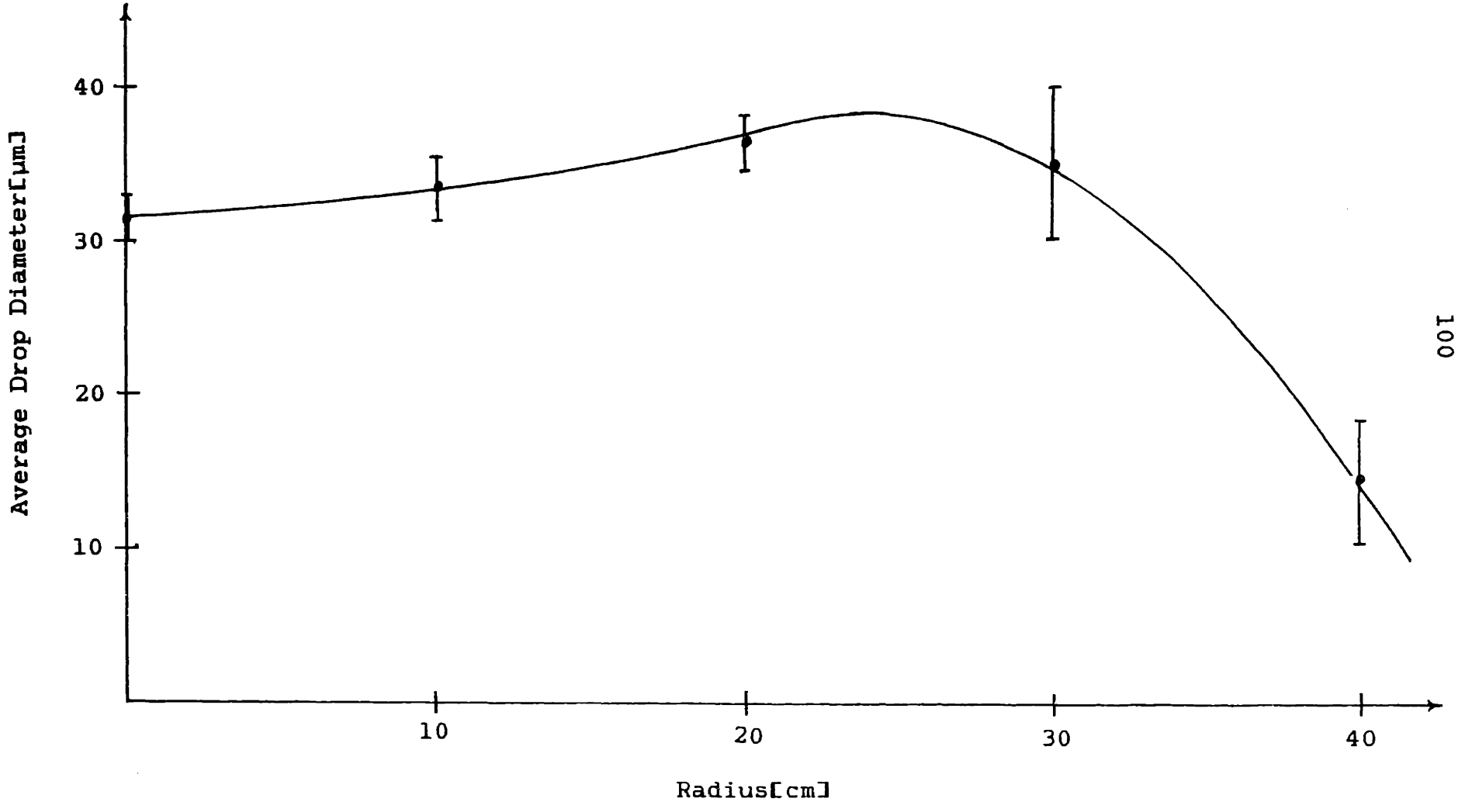

Fig. 4.10
Average Flake Area vs. Radius

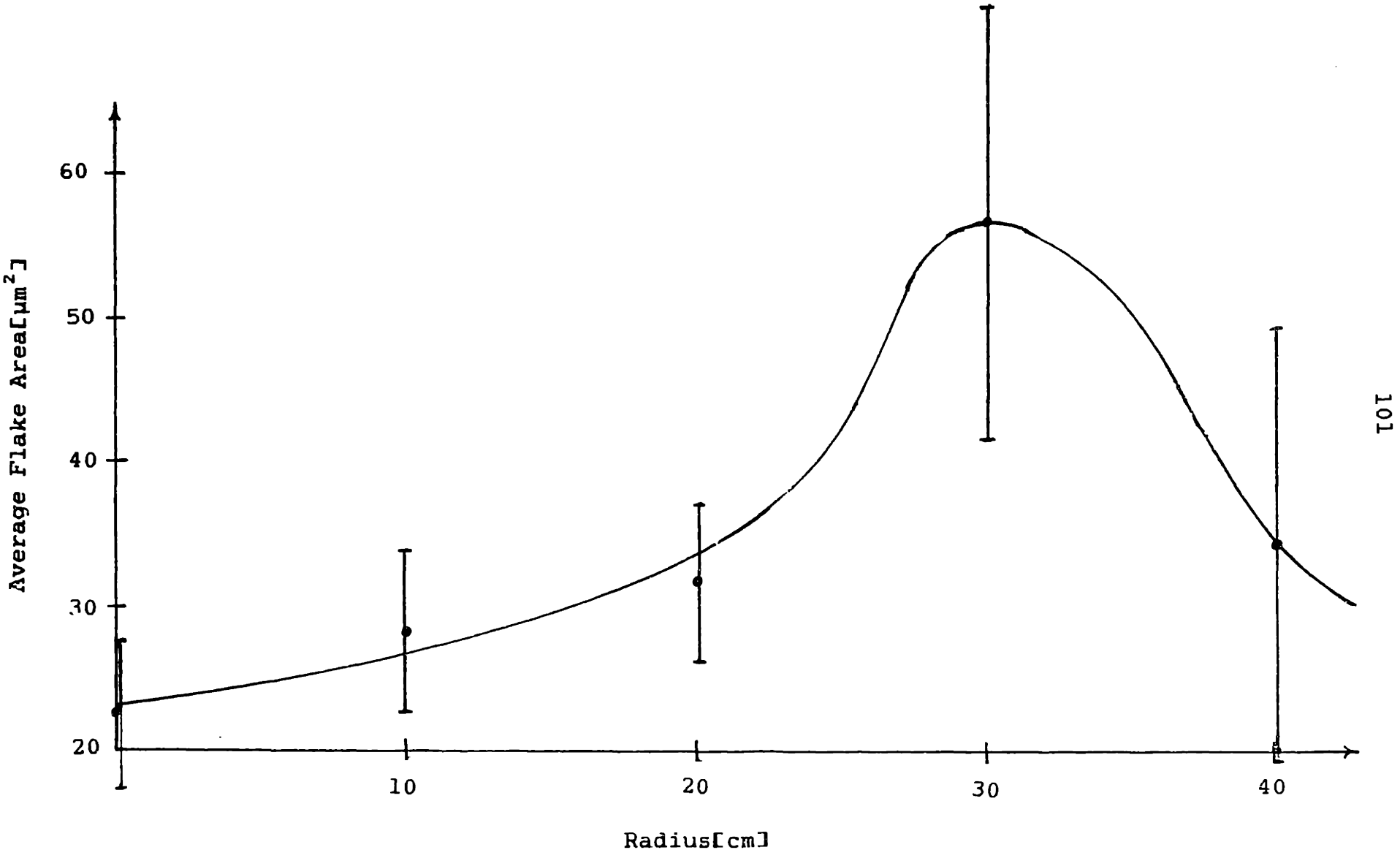

Drops

Average drop diameter(μm) = 12.9 Std. dev.(μm) = 13.4

With a probability of 95%
Error in the mean = 0.42
Standard deviation is between 13.21 and 13.64

Total number of drops = 3860

Flakes

Average flake area(μm^2) = 33.1 Std. dev.(μm^2) = 71.7

With a probability of 95%
Error in the mean = 4.00
Standard deviation is between 69.78 and 73.78

Total number of flakes = 1234

Mass Data

Total mass(μg): drops = 4.55 flake = 8.28×10^{-2}

Percentage of flake by mass = 1.82

Data for Drop Intervals

1	2	3	4	5	6	7
37.07	0.00*	0.17	0.00	0.00	-	5.0
23.89	0.08*	0.75	0.01	0.03	4.5	10.0
9.53	0.97	1.61	0.20	0.22	6.7	15.0
8.06	2.76	3.63	0.75	0.37	9.0	20.0
5.78	4.54	5.27	1.60	0.55	11.7	25.0
4.43	9.64	7.07	4.37	1.12	15.0	30.0
3.68	11.18	9.63	6.07	1.15	18.0	35.0
2.23	11.83	8.79	7.03	1.52	20.6	40.0
1.66	12.07	9.28	11.23	2.20	30.8	45.0
1.22	9.08	9.26	8.19	1.61	29.9	50.0
2.46	37.84	44.54	60.25	2.46	52.8	∞

Key
1 - Number of drops as a percent of the total
2 - Number of flakes as a percent of the total
3 - Mass as a percent of the total
4 - Flake mass as a percent of the total flake mass
5 - Mass percent of flake
6 - Average flake area
7 - Maximum drop diameter for this interval

Table 4.11
Electrostatic Sprayer: Flake Paint - Total

Drops

Average drop diameter(μm) = 33.4 Std. dev.(μm) = 18.6

With a probability of 95%
Error in the mean = 1.02
Standard deviation is between 18.14 and 19.16

Total number of drops = 1282

Total number of flakes = 0

Mass Data

Total mass(μg): drops = 7.81

Data for Drop Intervals

Number of Drops % of Total	Mass % of Total	Maximum Drop Diameter
2.57	0.00	5.0
6.71	0.05	10.0
7.41	0.25	15.0
9.98	0.90	20.0
10.76	1.96	25.0
9.91	3.15	30.0
10.53	5.42	35.0
9.91	7.64	40.0
7.57	8.13	45.0
5.23	7.69	50.0
19.42	64.81	∞

Table 4.12
Electrostatic Sprayer: No-flake Paint - Total

should be taken in interpreting the data as some of the intervals have an insignificant number of data points. The intervals where the number of flakes or the number of drops is less than 10 are marked with an asterisk. Table 4.11 for flake paint shows that in drops smaller than 15μm the flake content is extremely small, almost non-existent. This data is used to plot the drop distributions for flake paint, Fig. 4.13, and for no-flake, Fig. 4.14. Not only are the average drop sizes much different but the drop distribution for no-flake paint is almost flat in comparison to the distribution for flake paint. The flake area distribution is shown in Fig. 4.15 , note the high percentage(72%) of flakes with an area less than $50\mu m^2$. Further details of this data are contained in Appendix E.

4.2.2 Analysis of Drop and Flake Distributions Both Deposited and in the Overspray of a Mechanical Sprayer

Sampling, in the case of the mechanical sprayer, is actually more difficult than using the electrostatic sprayer because the drops are not already charged. The trajectory of charged drops is easily modified with the application of an electric field. The actual geometry of the spray gun and the mechanisms used in atomization and delivery of the paint greatly affect the sampling technique. As described in Section 2.2, the mechanical sprayer involves high velocity

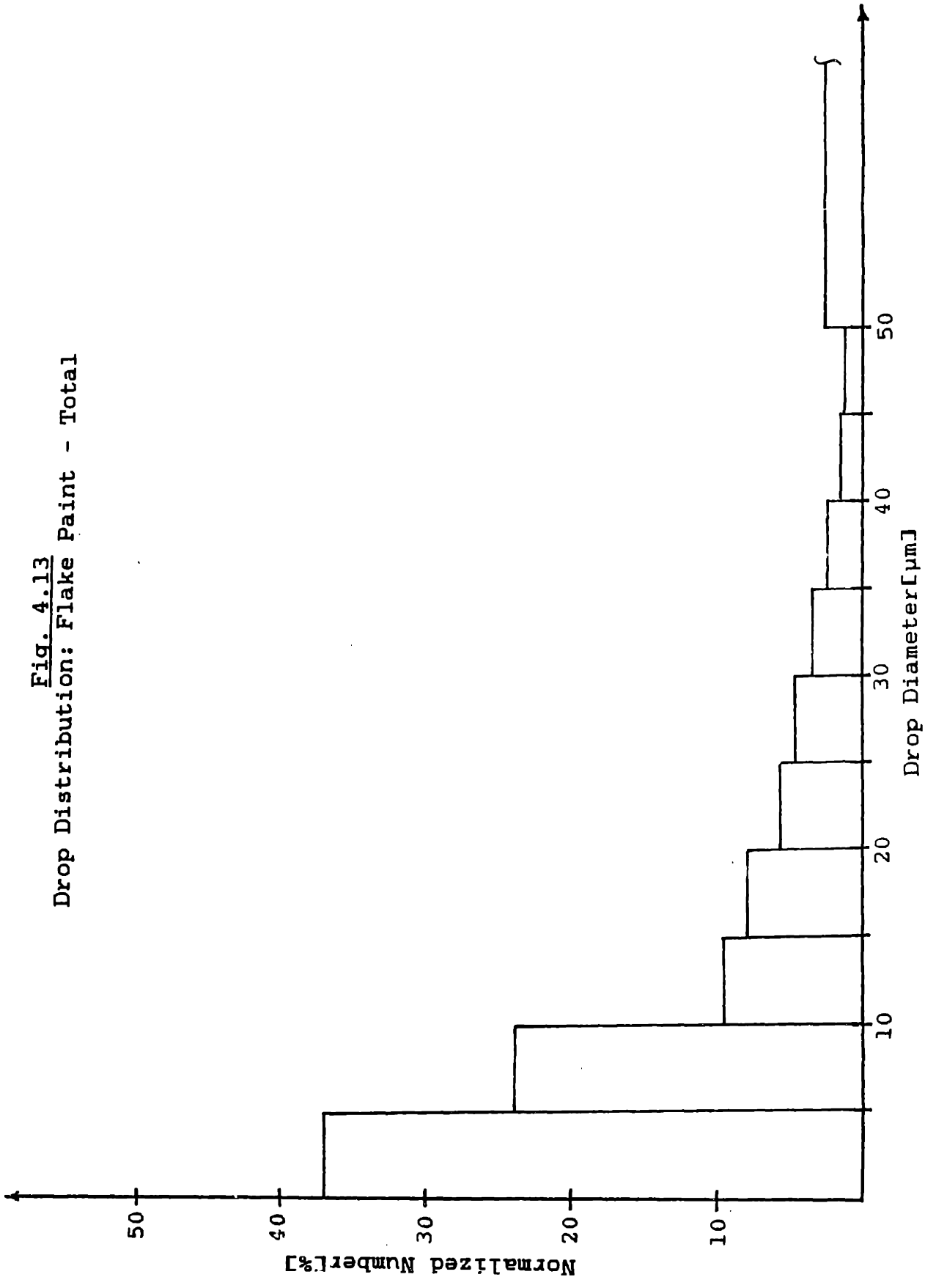

Fig. 4.13
Drop Distribution: Flake Paint - Total

Fig. 4.14
Drop Distribution: No-flake Paint - Total

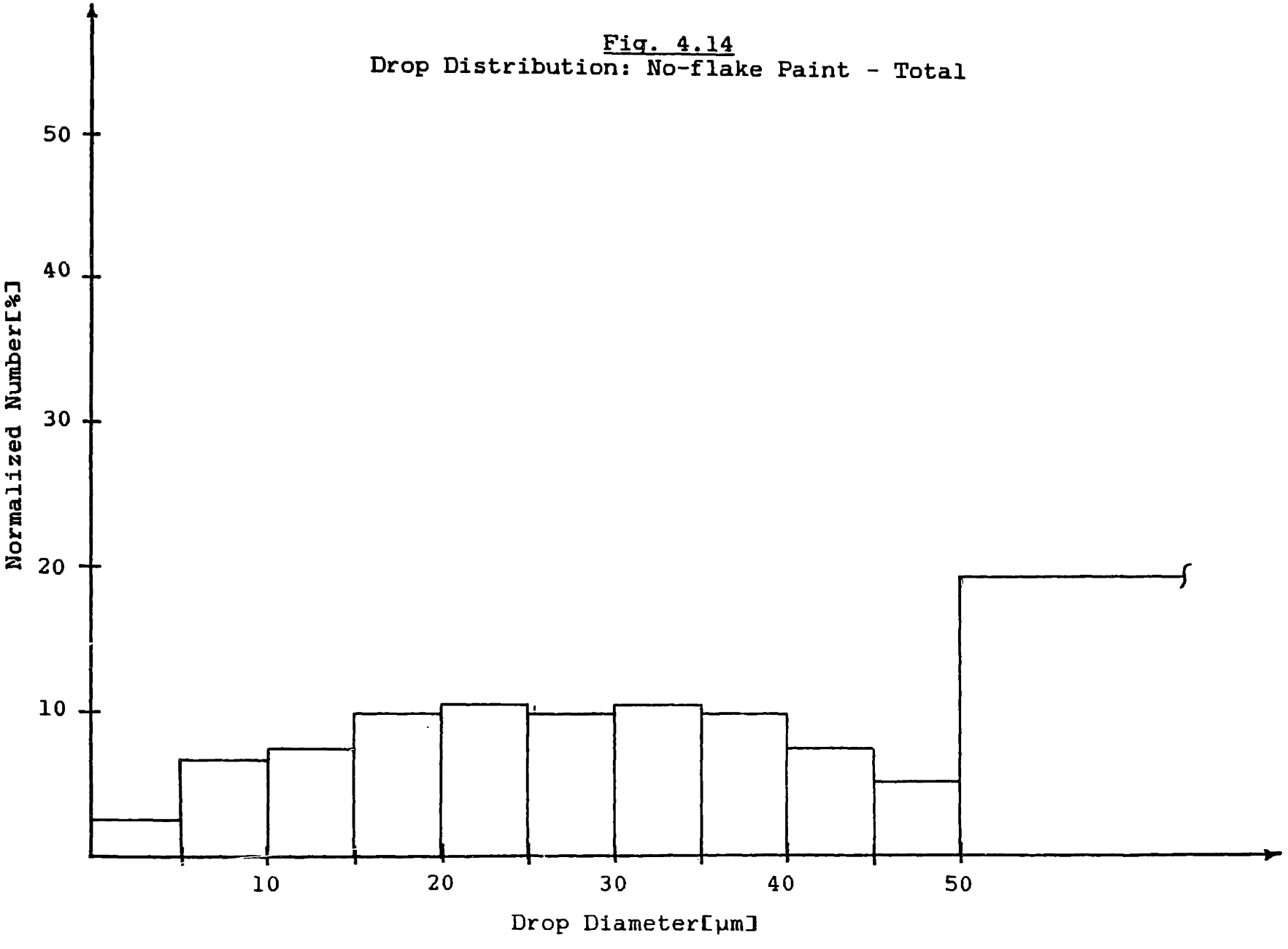

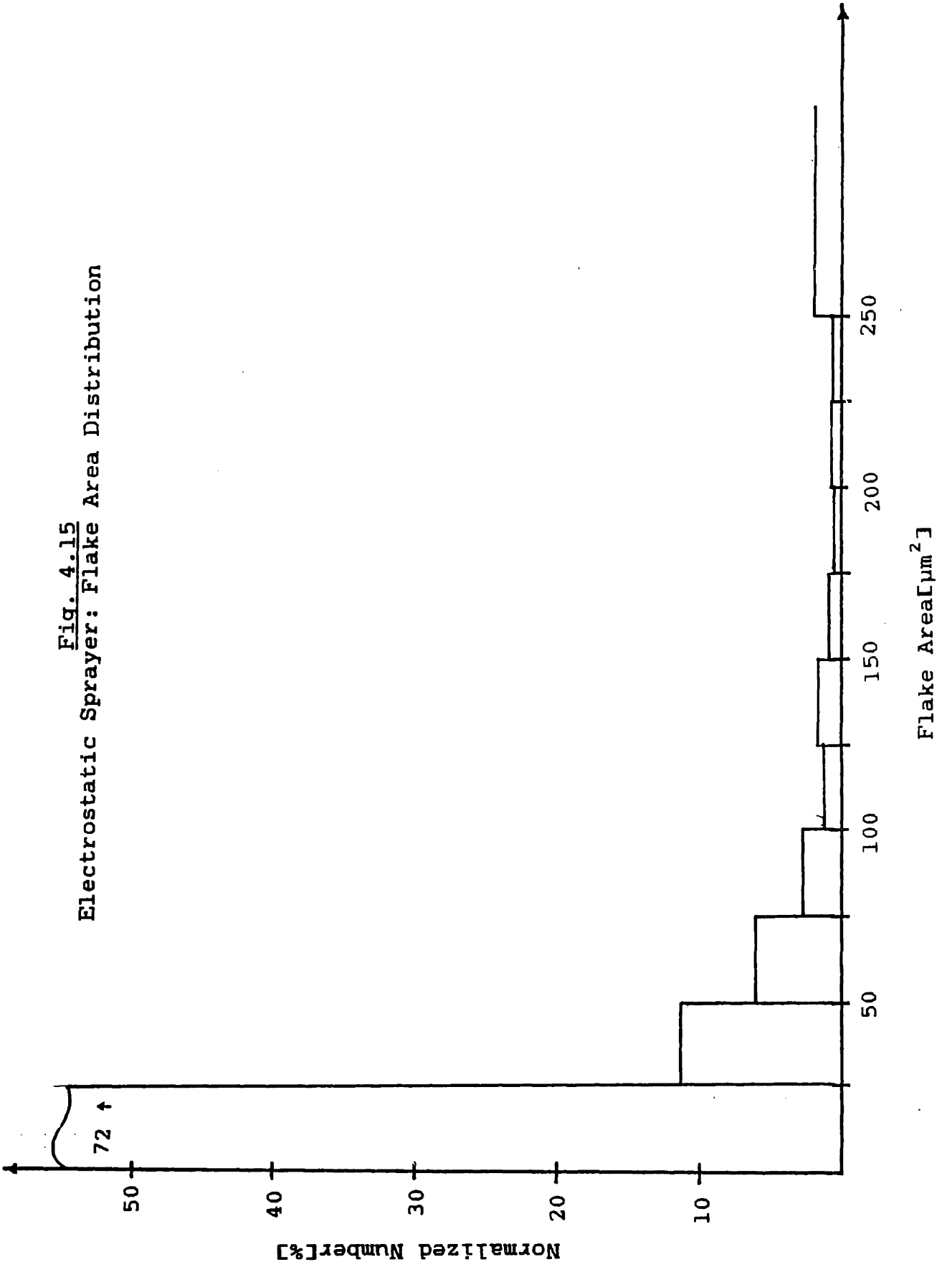

Fig. 4.15
Electrostatic Sprayer: Flake Area Distribution

turbulent air flow and very low deposition efficiencies. The spray pattern from the mechanical sprayer, though harder to define than that obtained using the electrostatic sprayer, is much smaller. The process is controlled using subjective device settings causing repeatability to be user sensitive.

4.2.2.1 Drop Sampling: Precipitators for Collection of the Overspray

Unlike the electrostatic sprayer, where (if the target is large enough) the electrical attraction deposits practically all of the paint, the mechanical sprayer has a significant amount of overspray. To obtain a picture of the spray cloud, it was sampled at four positions, three at various positions between the spray gun and the paint target, and one in the main spray cloud at the paint target. The sample at the paint target was an average of the main spray pattern. It was obtained by passing the gun over the target fast enough so that a coating of discrete drops is obtained. The samples from the positions between the spray gun and the target were more difficult to obtain.

Small electrostatic precipitators have been constructed to sample the cloud. The details of these devices are shown in Fig. 4.16. The exit of the precipitator is connected to a variable pump so that the entrance velocity can be

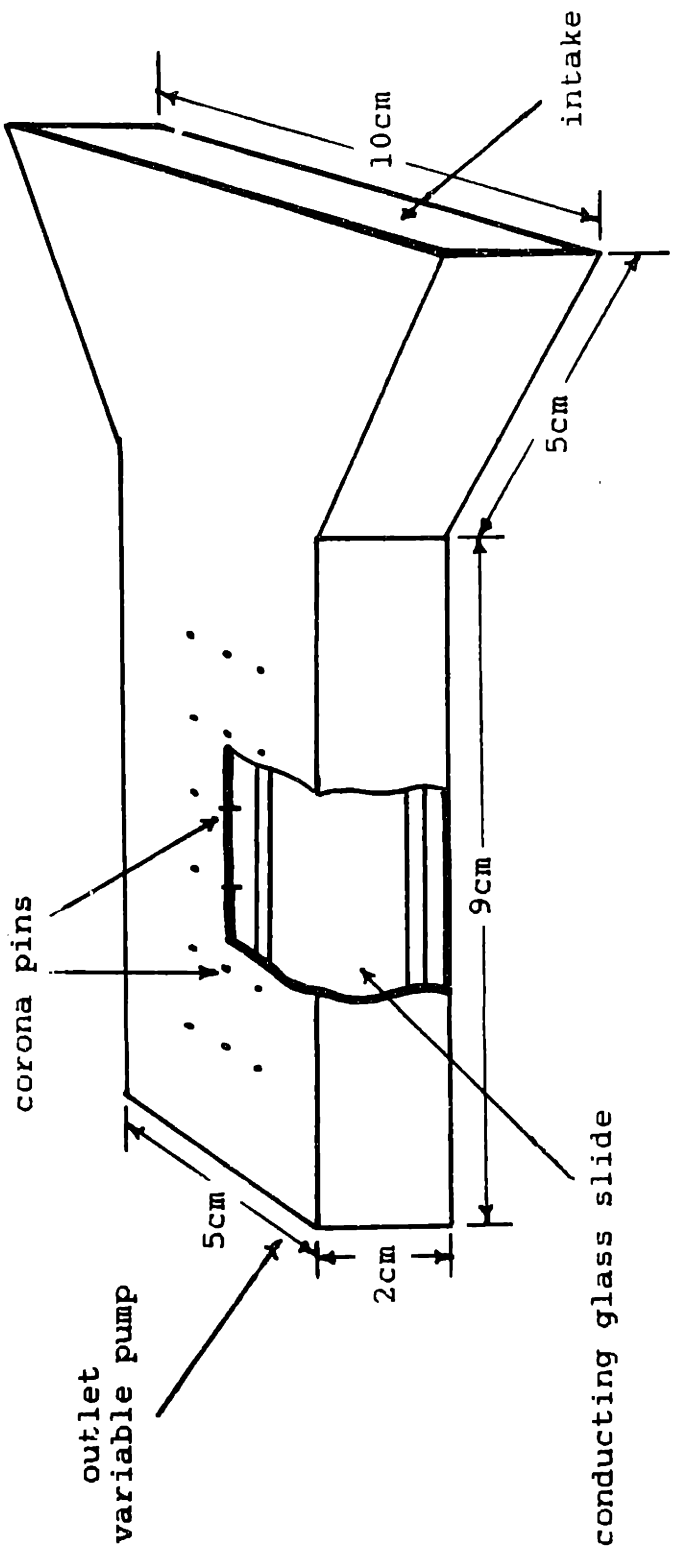

Fig. 4.16
Details of Electrostatic Precipitator

approximately matched to the velocity in the absence of the precipitator, providing a means of iso-kinetically sampling. The three positions between the spray gun and the paint target are shown in Fig. 4.17. As shown in this figure the samples are numbered in order of increasing distance from the spray gun, number 4 being on the paint target. Note, the precipitators are outside of the main spray stream in order to obtain paint that would normally constitute the overspray. The flow is predominantly radial at these three positions, directly into the precipitators.

4.2.2.2 Results

As in the electrostatic sprayer, samples are taken using both flake and no-flake paint. The spray gun parameters are adjusted by painting several test plates before the experiment. Because the overspray is precipitated while the gun is in a fixed position, no feedback on the quality of the painting is possible. Also, for the sample at the paint surface, a single pass of the spray gun makes it impossible for the operator to ensure appropriate gun settings. The quality of the spray is totally dependent on the previous spraying of the test samples.

The same processing technique as described in Section 4.2.1.2 for the electrostatic sprayer is used. Each position

Top View

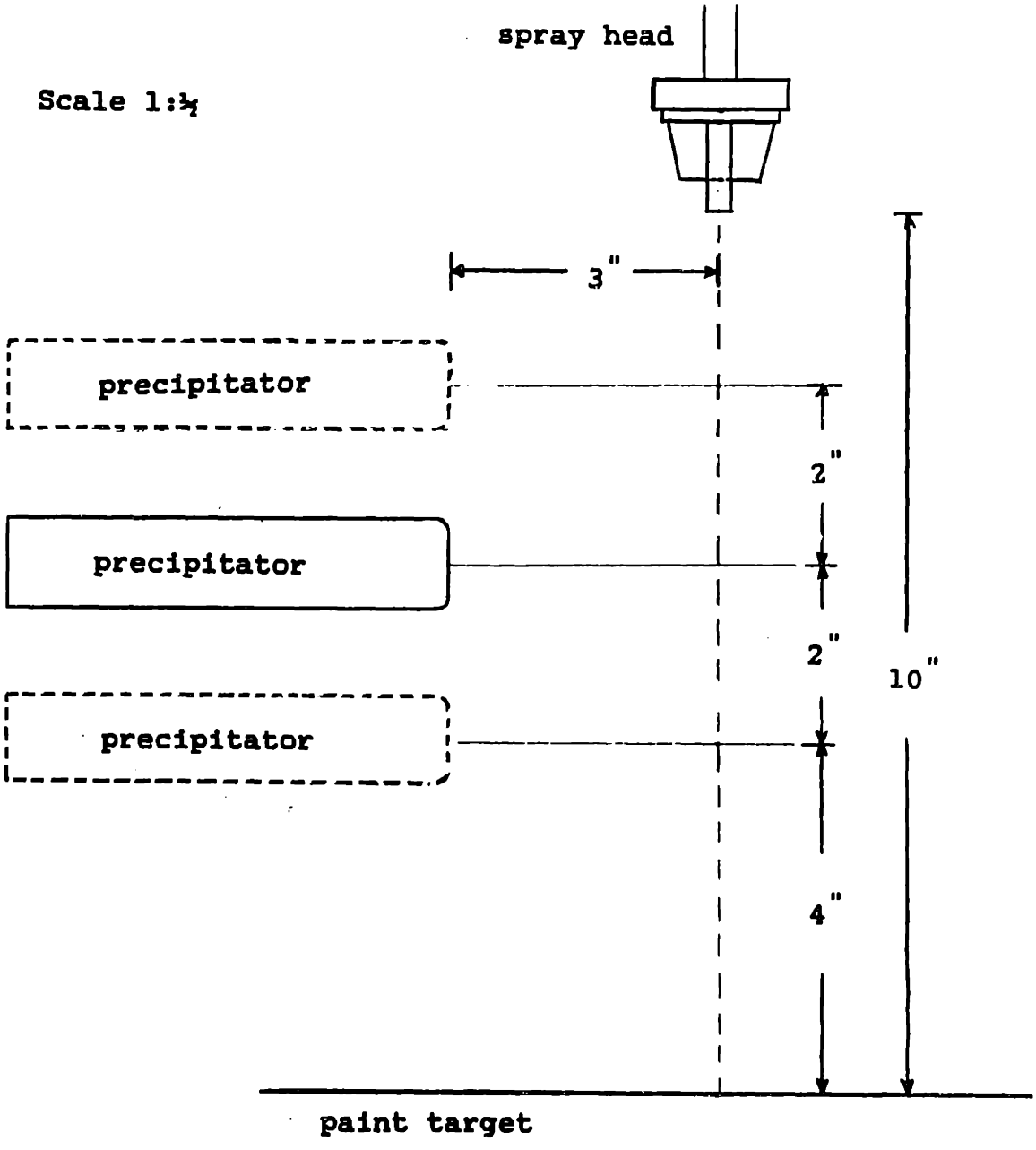

Fig. 4.17
Positions for Electrostatic Precipitators

in the overspray can be treated as discrete information. However, the sample at the paint surface is an average of the spray making it to the target and should represent the statistics of a normal paint finish. The detailed data as well as plots of the drop distributions are given in Appendix F.

The average drop diameters for samples 1, 2, and 3 are similar regardless of the presence of flake with an overall average of 6.4μm. Sample 4, at the surface of the paint target, has an average drop diameter of 36μm with flake and 38μm without flake. The standard error for both of these latter samples is approximately 4μm indicating the average drop diameters are not significantly different. The aluminum mass percent is 0.99 for sample 1, 0.32 for sample 2, 0.80 for sample 3, and 1.94 for sample 4. The drops in the overspray (collected as samples 1,2 and 3 and found to be small) contain very little flake while the drops deposited on the paint target(collected as sample 4 and found to be large) carry a high flake content. Data from sample 4 is shown in Table 4.18 for flake paint and in Table 4.19 for no-flake paint. The drop distribution for sample 4 is shown in Fig. 4.20 for flake paint and in Fig. 4.21 for no-flake paint. The flake area distribution for sample 4 is shown in Fig. 4.22 . By contrast with the electrostatic sprayer, where all samples are taken at the paint target, sample 4

Drops

Average drop diameter(μm) = 36.0 Std. dev.(μm) = 29.0

With a probability of 95%
Error in the mean = 3.76
Standard deviation is between 27.28 and 31.06

Total number of drops = 229

Flakes

Average flake area(μm^2) = 74.2 Std. dev.(μm^2) = 149.6

With a probability of 95%
Error in the mean = 15.77
Standard deviation is between 142.16 and 157.97

Total number of flakes = 346

Mass Data

Total mass(μg): drops = 2.68 flake = 5.20×10^{-2}

Percentage of flake by mass = 1.94

Data for Drop Intervals

1	2	3	4	5	6	7
1.75*	0.00*	0.00	0.00	0.00	-	5.0
8.30	0.00*	0.04	0.00	0.00	-	10.0
13.10	0.00*	0.21	0.00	0.00	-	15.0
13.97	1.73*	0.66	0.86	2.55	37.0	20.0
12.66	2.60*	1.24	0.52	0.82	14.9	25.0
8.73	2.89	1.50	1.28	1.66	33.0	30.0
7.86*	2.89*	2.03	2.00	1.91	51.4	35.0
2.18*	1.16*	0.93	0.64	1.34	41.3	40.0
3.49	3.18	2.03	0.90	0.85	20.9	45.0
4.80	7.23	3.60	1.35	0.73	13.8	50.0
23.14	78.32	87.77	92.44	2.04	87.5	∞

Key
1 - Number of drops as a percent of the total
2 - Number of flakes as a percent of the total
3 - Mass as a percent of the total
4 - Flake mass as a percent of the total flake mass
5 - Mass percent of flake
6 - Average flake area
7 - Maximum drop diameter for this interval

Table 4.18
Mechanical Sprayer: Flake Paint #4

Drops

Average drop diameter(μm) = 38.0 Std. dev.(μm) = 37.1

With a probability of 95%
Error in the mean = 5.32
Standard deviation is between 34.60 and 39.95

Total number of drops = 187

Total number of flakes = 0

Mass Data

Total mass(μg): drops = 3.25

Data for Drop Intervals

Number of Drops % of Total	Mass % of Total	Maximum Drop Diameter
1.60*	0.00	5.0
11.76	0.04	10.0
13.90	0.19	15.0
15.51	0.42	20.0
11.23*	0.69	25.0
4.81*	0.53	30.0
4.81*	0.90	35.0
3.21*	0.85	40.0
3.74*	1.45	45.0
3.74*	1.90	50.0
25.67	93.40	∞

Table 4.19
Mechanical Sprayer: No-flake Paint #4

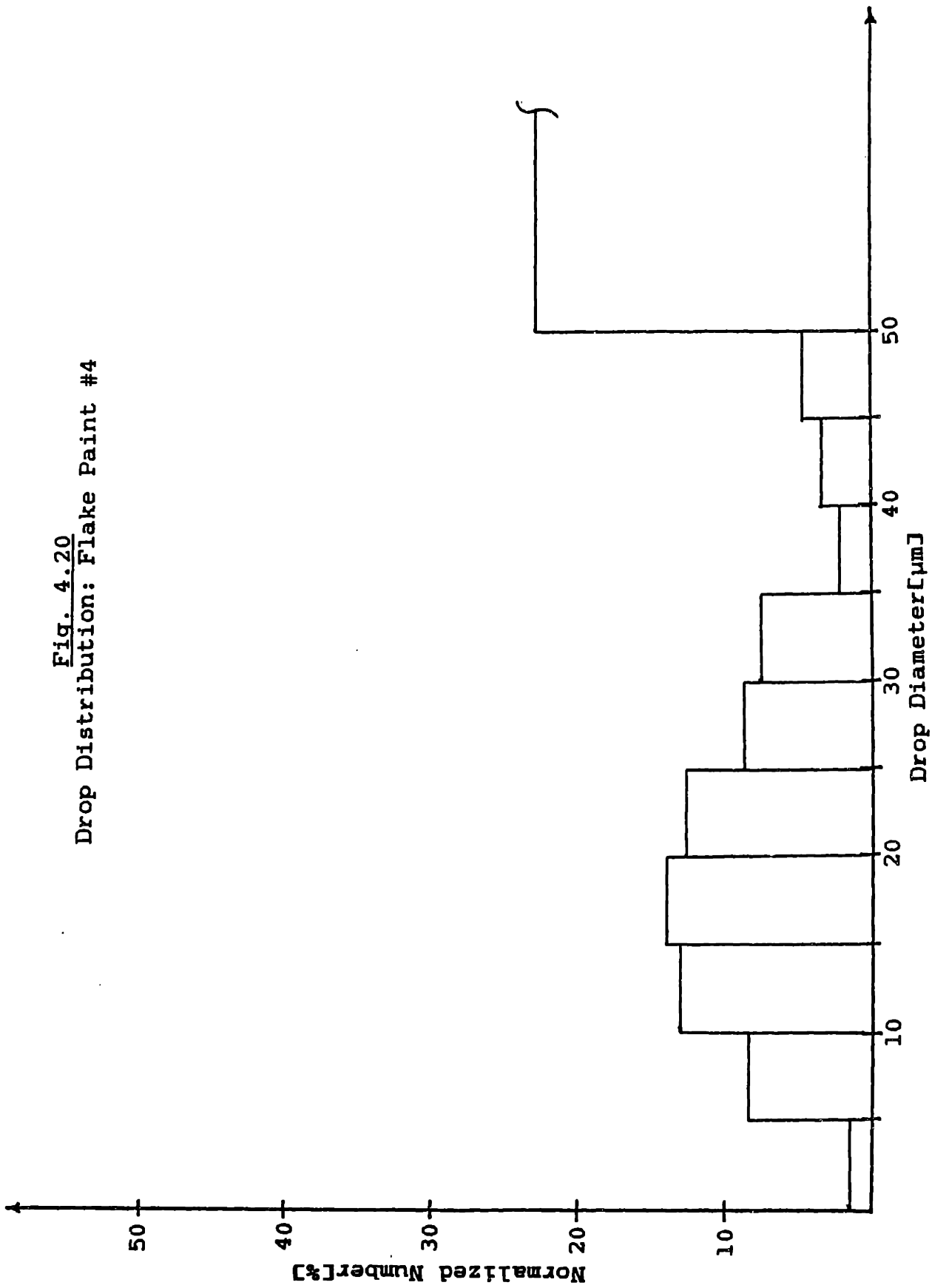

Fig. 4.20
Drop Distribution: Flake Paint #4

Fig. 4.21
Drop Distribution: No-flake Paint #4

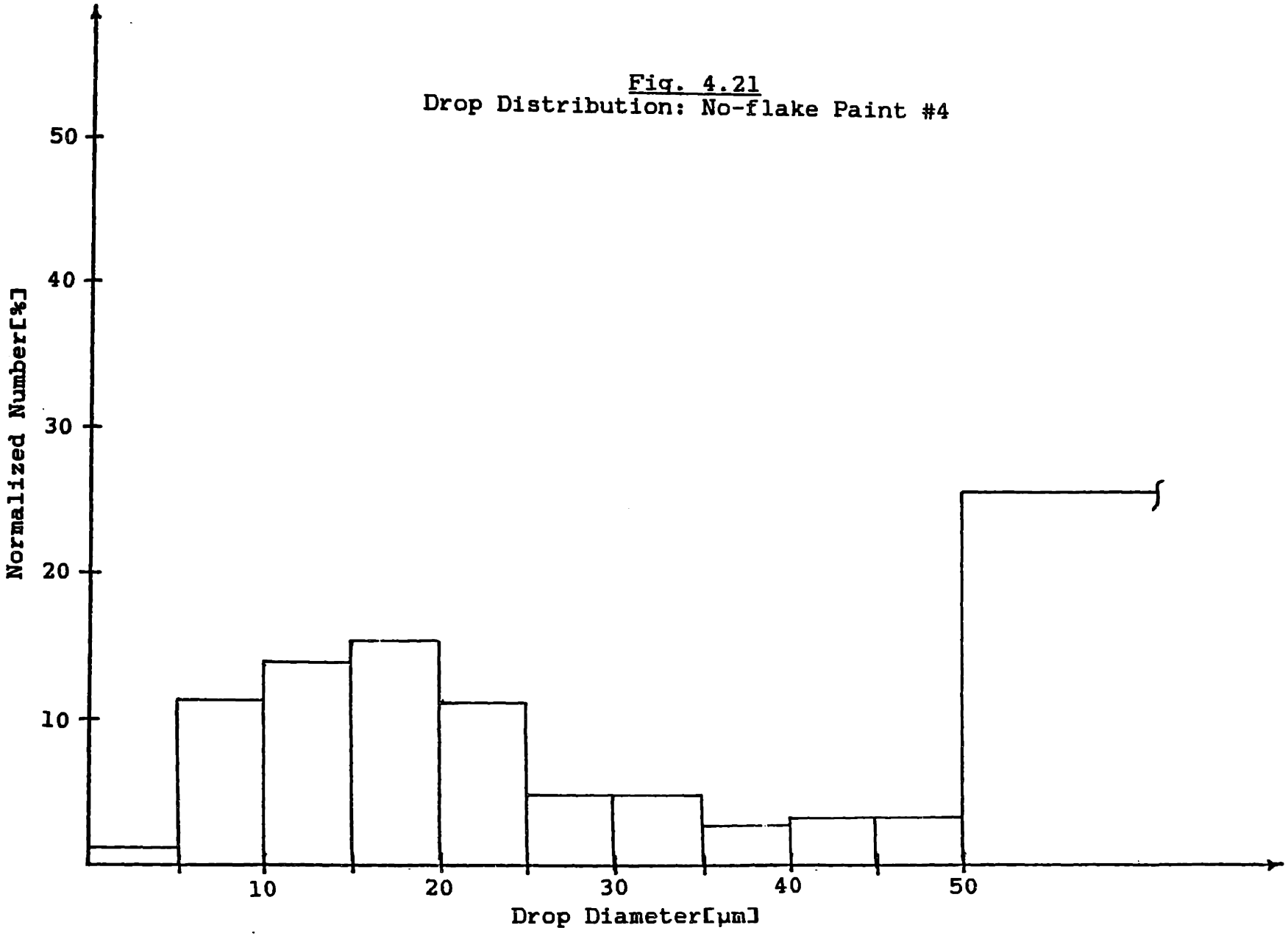

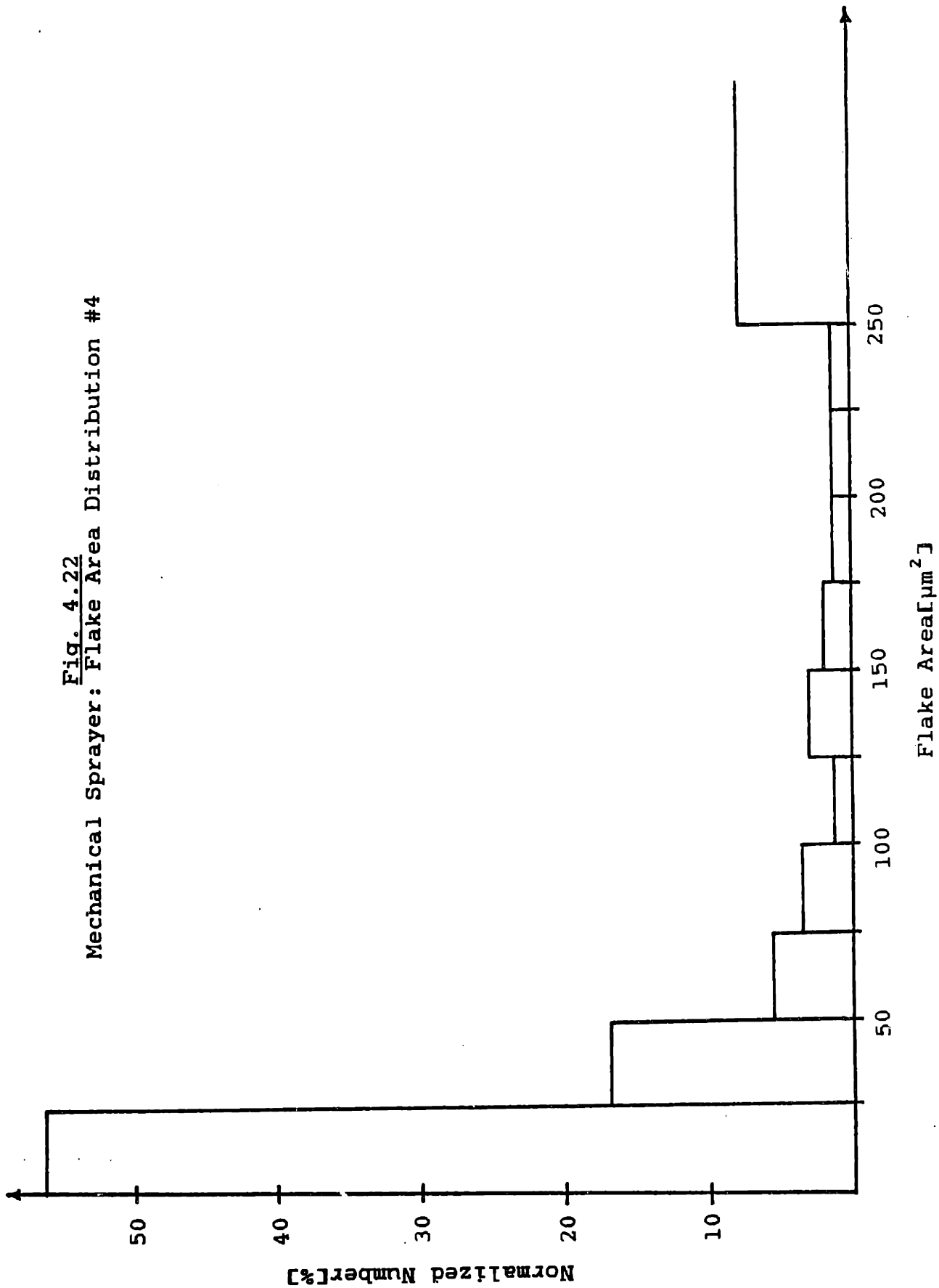

Fig. 4.22
Mechanical Sprayer: Flake Area Distribution #4

represents an average over that part of the spray that strikes the paint target. The other samples represent the overspray.

4.3 Average Flake Deposited and Mass Balance

The estimates involved in digitizing the data introduces some error, as may the sampling techniques. An alternate means of obtaining similar information to provide a check on the average mass percent is to use atomic absorption measurements. These measurements can then be compared to the discrete drop results providing an estimate of the average error because only the average flake content, not the discrete drop information, is obtained using these measurements. This data along with the discrete data provides a check on the mass balance during the painting process by using information on the total mass loss during the painting and curing process.

4.3.1 Atomic Absorption Measurements

The Central Analytical Facility at MIT performed the atomic absorption measurements on the paint samples. Samples are painted and then the paint is scraped off the substrate. The paint scrapings are dissolving, ensuring all the paint, including the aluminum flakes, is in solution. All samples

are cured so that results could be expressed as a mass percentage of dried solids. The resulting solution was measured for aluminum content. Samples that were tested in this manner were painted on stainless steel slides to avoid any increase in aluminum due to the base material.

Samples were painted using both the electrostatic and mechanical sprayer. The samples painted electrostatically produced consistent values of 1.86 % ±0.02 %. The mechanical sprayer, however, provided samples with a wide range of aluminum content between 2.02% and 3.31%. This reflected the difficulty experienced in obtaining consistent quality finishes. As a general rule, the higher the aluminum content the better the quality of the sample. A target similar to the electrical shutter, see Fig. 4.5, is used so that a comparison of the aluminum content for each of the samples taken, using the electrical shutter, was made. A measurement of the aluminum content of the paint before spraying yielded 0.73% aluminum. The amount of mass lost in the painting and curing process is 60%. This yields a final value for the flake content deposited, assuming the process is 100% efficient, of 1.83% aluminum.

A plot of the mass percentage of aluminum versus radius using the atomic absorption data and the electrical shutter data is shown in Fig. 4.23. These results are quite close.

Fig. 4.23
Mass Percent Aluminum vs. Radius

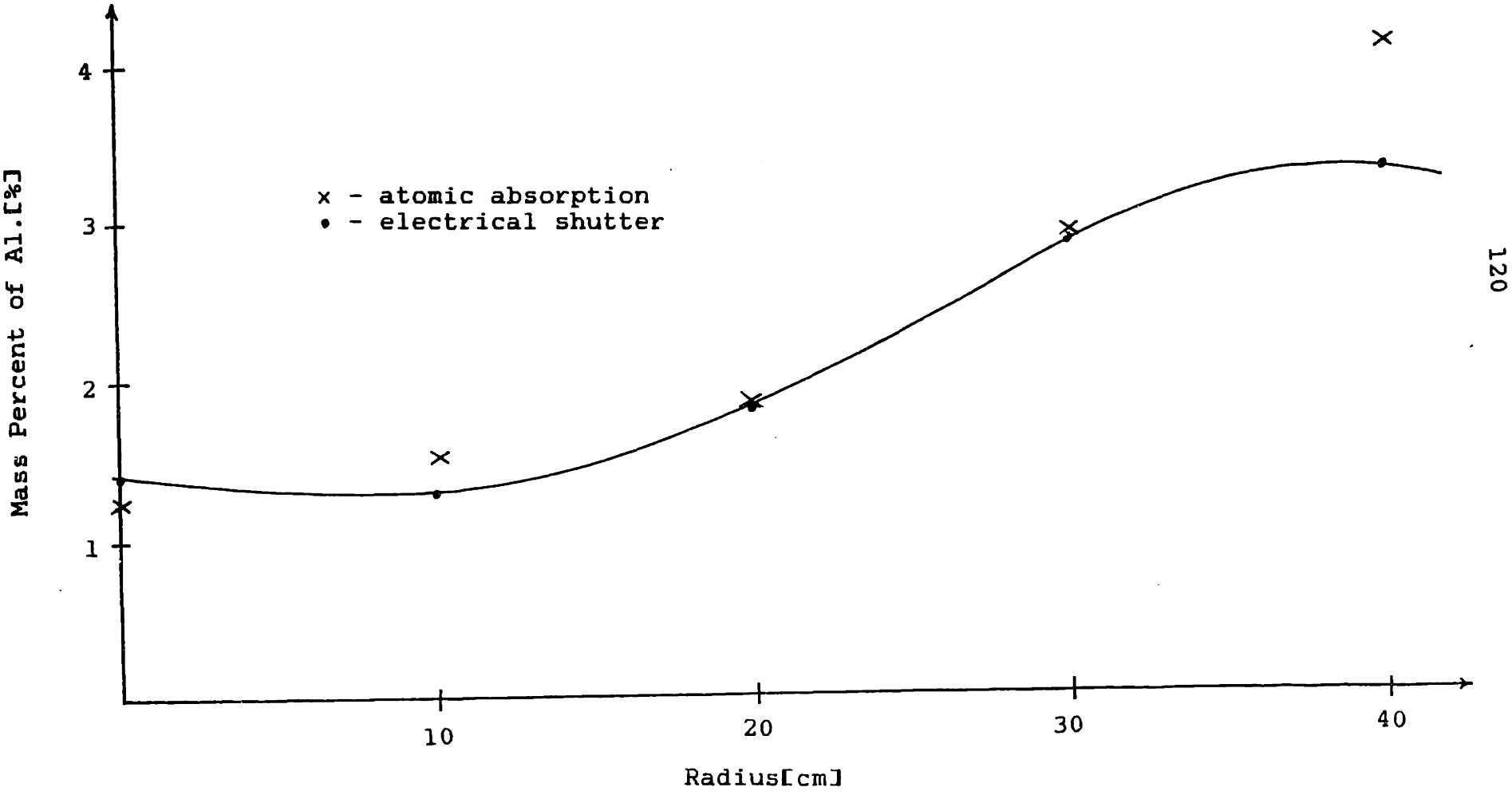

An exception is the point farthest from the centre where the number of drops is quite small increasing the error in the electrical shutter results. Similarly, because the mass is small, there is a high error in the atomic absorption measurements. The mass average of the electrical shutter results across the spray pattern radius should reflect the mass percent of aluminum in a electrostatic paint sample. Again this result, 1.82%, compares quite closely to the atomic absorption result of 1.86%.

The mechanical sprayer results do not, however, coincide. The discrete results at the paint surface, sample 4, give a mass percent of aluminum of 1.94%. This is just slightly outside the range of 2.02% to 3.31% measured using the atomic absorption technique. Recall, from Section 4.1.3, that the volume of the paint solids is calculated using an empirical relationship between drop height and drop radius. The difference between the atomic absorption data and the discrete results may be accounted for by noting that the curve for drop height is based on drops mainly of a smaller size than some of the larger drops in this sample.

4.3.2 Mass Balance

The aluminum content is totally accounted for in the electrostatic sprayer. The mass percent for a 100% efficient

process(1.83%) is almost identical to the electrostatic sprayer result(1.82% or 1.86%). This is consistent with the assumption that the electrostatic sprayer is 100% efficient; all the aluminum flake and paint solids are deposited on the target.

However, the results for the mechanical sprayer, 1.94% to 3.31%, reflect the low efficiency of the mechanical process. In fact, in order to obtain high quality paint finishes, i.e. higher flake content, a lower efficiency process is required. Flake content is increased by increasing the overspray. Because the overspray has low flake content this increases the flake content deposited on the paint target. This is most often accomplished by adjusting the atomizing orifice size and the air velocity to form a finer spray literally blowing the fine low flake content drops away in the overspray. Since all the overspray is not examined, a total mass balance is not possible. Note, however, that the numbers for mass percent of aluminum in the overspray are less than the 100% figure indicating that these numbers could be representative of an overall mass balance.

4.4 Contrasts: Electrostatic and Mechanical Spraying

In the two devices there are many obvious differences

such as the spray pattern, paint flow rate, and efficiency. However, there are more subtle differences exposed in the data above. These fall into three major categories. First, the actual deposited flake content is quite different. The mechanical sprayer deposits, for a high quality paint job, an aluminum mass percent greater than 3.0% while the electrostatic process deposits approximately 1.85%. The electrostatic process has a larger spray pattern and the flake content varies from 1.40% flake in the middle to more than 3.30% at the edge. Only a sample which passes through the centre of the entire cloud ends up with 1.85%. This spatial variation presents a major industrial problem. Second, the flake distribution deposited by the two processes are quite different. The mechanical sprayer deposits flakes that on the average have twice the area as those deposited by the electrostatic sprayer. The average flake area deposited by the electrostatic sprayer also varies as a function of radius. Third, the drop distributions are different. Using flake paint, the mechanical sprayer deposits a much flatter spectrum of drops having almost three times the average drop diameter as the electrostatic sprayer. Note, the drop size obtained from the electrostatic sprayer is sensitive to the presence of the flake.

The effects of the aluminum content on the color are

analyzed by changing the aluminum content in the paint used by the mechanical sprayer. A series of various paint mixtures are used to create a table of color versus aluminum content, commonly called a color vector. This is done both in terms of the mass percent of aluminum in the paint before spraying and finally deposited. These results as well as the color of an electrostatic sample are illustrated in Table 4.24. Interpolating the mechanical sprayer data on the color coordinate L^* to match the electrostatic sample results in an aluminum content of 1.21%. This result is also illustrated in Table 4.24. Note, the b^* color coordinate matches almost exactly yet the a^* coordinate is quite different. Although changing the aluminum content does decrease the color variation, the lower flake content than actually observed in the electrostatic sample and the mismatch in color space indicate another mechanism plays an important role. This mechanism is most likely the deposited flake distribution. Unfortunately, changing the distribution of flake in the paint is more difficult and detailed color matching requires a more extensive paint facility.

	Color			%Al	
ΔE	L^*	a^*	b^*	before spraying	after cure
ref	52.3	-3.4	-19.4	0.70	3.27
2.4	50.9	-3.4	-21.5	0.59	2.78
5.3	48.0	-3.0	-22.6	0.49	2.24
9.0	45.3	-2.5	-25.0	0.37	1.73
16.0	40.3	-0.3	-29.6	0.21	1.03
21.1	29.3	4.9	-35.6	0.00	0.00
Electrostatic Sample					
15.8	41.6	-3.8	-28.8	0.70	1.85
Linear Interpolation on L^* to match electrostatic sample					
12.9	41.6	-0.9	-28.4	0.25	1.21

Note:
L^* - brightness
a^* - green → red
b^* - blue → yellow

Table 4.24
Color vs. Mass Percent Aluminum: Mechanical Sprayer

References

[1] Bell, G.C. and Hochberg, J., Private communication, 1985

[2] Bell, G.C. and Hochberg, J., "Mechanisms of electrostatic atomization, transport, and deposition of coatings", Seventh International Conference in Organic Science and Technology, Proc. of, Athens, Greece, 1981

[3] Anestos, T.C., "Electric Field Distributions in Electrostatic Sprays", Research Report: General Motors Research Laboratories (Electrical Engineering Department), Warren, Michigan, 1984

Chapter 5

Corona Induced Color Control

A method of producing localized flake orientation could provide a means of pattern construction in a paint surface. Present techniques for constructing patterns use masks and then another paint application to obtain trim stripes, labeling, or two tone effects. These techniques are labor intensive and costly. A substantial color variation in metallic paints can be obtained electrically with the original paint application and a non-contacting corona source.

As indicated in Chapter 3, a corona current can be used to obtain metallic flake orientation and a substantial color shift. The resolution can be controlled by shaping the electric field around the corona source. However, flake size and diffusion impose restrictions on the "best" resolution possible. The mechanism for flake orientation is a competition between an electric polarization force and viscous and (as will be shown) viscoelastic torques depending upon the rheology of the paint layer. The corona current has effects on the paint layer other than alignment of the flakes. The specifics of these mechanisms are discussed in the following sections.

5.1 Spatial Resolution of Corona Current

The low inertia and high mobility of the ions, constituting the corona current, cause the ion trajectories to essentially follow the electric field lines. Therefore, if the divergent nature of the electric field is reduced, the spread of the corona current is narrowed. Fig. 5.1 shows an electrode structure that narrows the corona current. This structure is moderately successful, narrowing the corona current by approximately a factor of three. Fig. 5.2 shows a more complex multiple electrode structure that is more successful. The resolution is approximately equal to that of the hole in the middle electrode. With the field between the corona point and the focusing plate equal to or less than that between the plate and the workpiece, the electric field in the hole tends to make the ion beam even finer than the hole. However, the effects of the ion self field and diffusion tend to disperse the beam. A disadvantage of this structure is the low currents to the paint layer in comparison to the current generated by the corona source. Using a spacing between the paint layer and the plate of 1cm and a hole diameter in the plate of approximately 1mm, lines of essentially 1mm width have been obtained. No attempt has been made to obtain finer resolution.

The resolution appears limited only by the electrode

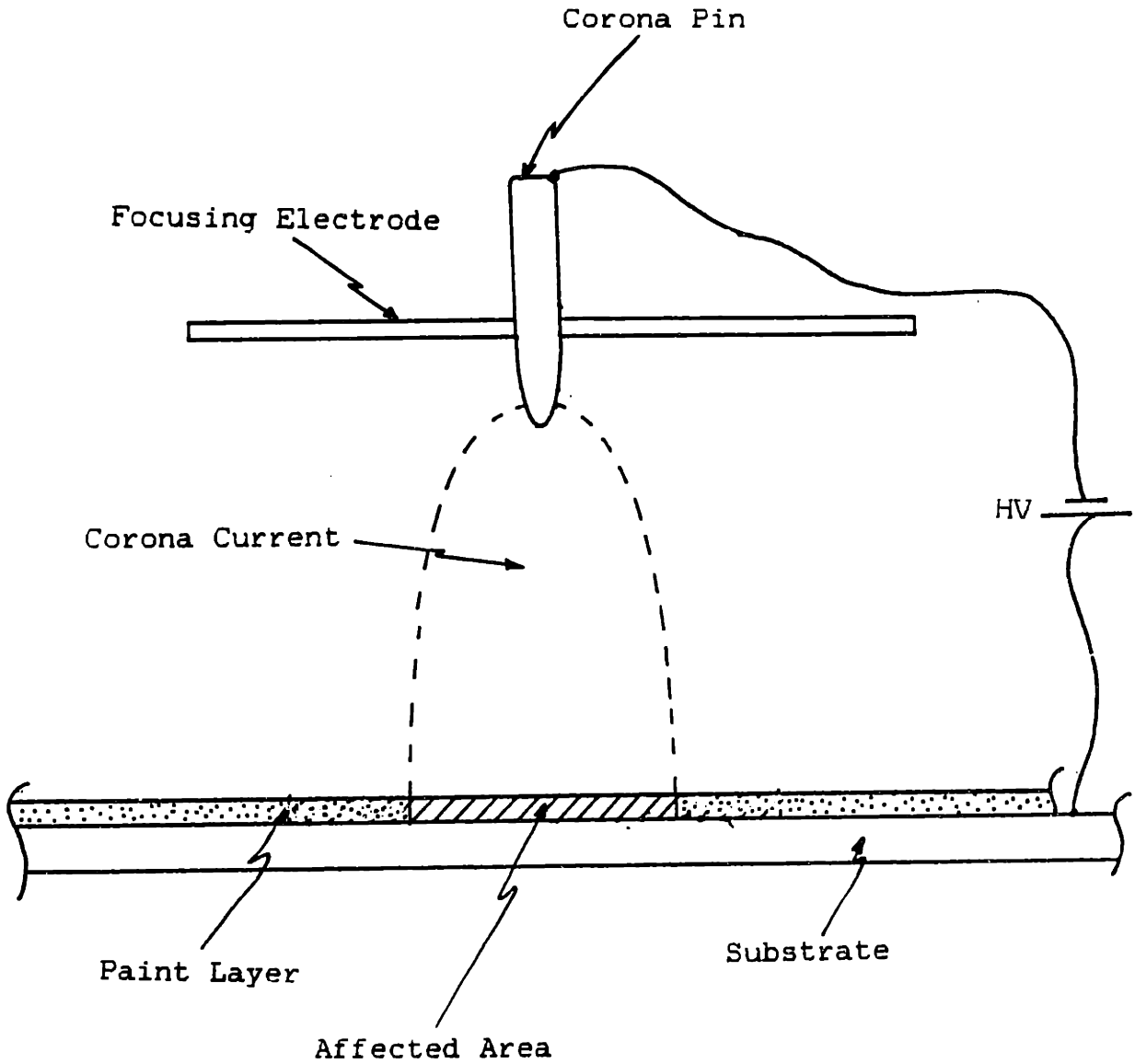

Fig. 5.1
Beam Focusing: Simple Electrode Structure

Fig. 5.2
Beam Focusing: Multiple Electrode Structure

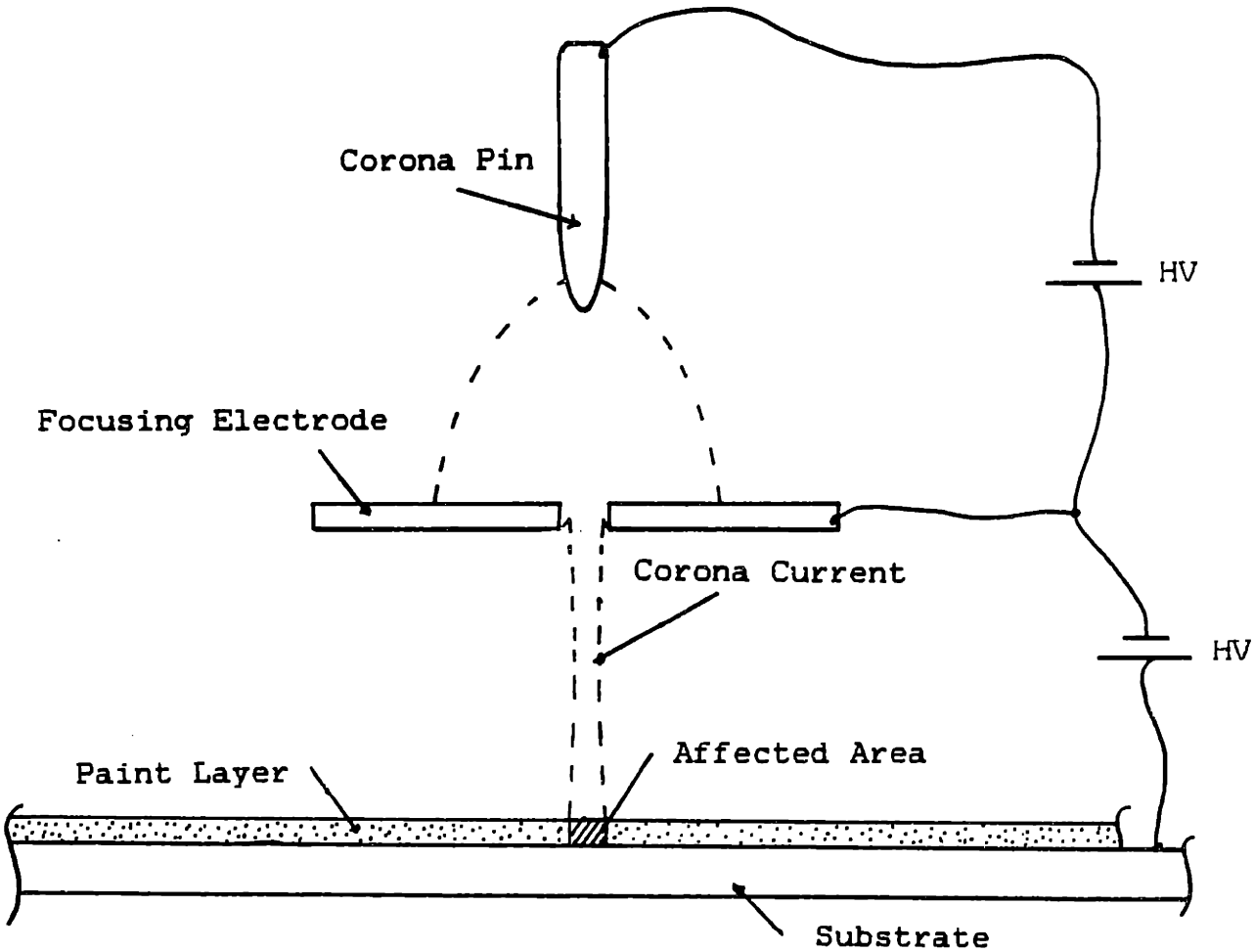

structure and diffusion. An estimate of the diffusion limit on resolution is possible for a given ion mobility, b, electric field, E, ion diffusion coefficient, D, (all in air) and the spacing, ℓ, between the electrode and the paint layer. The diffusion time is

$$\tau_d \simeq \frac{\Delta^2}{D}$$

The transit time for an ion is

$$\tau_t \simeq \frac{\ell}{bE}$$

Setting the the transit time equal to the diffusion time gives an estimate of the beam diameter, Δ, at which diffusion broadening would have an effect

$$\Delta \simeq \left(\frac{D\ell}{bE} \right)^{1/2} \qquad (5.1)$$

Using typical numbers of $D=2.5\times10^{-6}m^2/s$, $\ell=1.0\times10^{-2}m$, $b=1.0\times10^{-4}m^2/V\text{-}s$, and $E=1.0\times10^{6}V/m$ result in a diffusion length of $\Delta=16\mu m$. Note that, negative corona with its higher mobility can be used to obtain finer resolution than positive corona.

The effect of the ion self field can also be estimated. The current in the ion beam, I, is a constant.

$$I=\rho AbE \qquad (5.2)$$

where ρ is the charge density and A is the area of the beam.

The charge density is approximated by the expression for unipolar self precipitation [1]

$$\rho = \frac{\rho_o}{1 + \frac{t}{\tau_a}} \tag{5.3}$$

where

$$\tau_a = \frac{\varepsilon_o}{\rho_o b} \tag{5.4}$$

and ρ_o is the charge density at time t=0, taken as the time the charge passes through the hole in the focusing electrode. The time further along in the ion trajectory is approximately the distance from the hole, z, divided by the ion velocity, bE.

$$t = \frac{z}{bE} \tag{5.5}$$

Eqns. 5.2, 5.3, and 5.5 can be used to calculate the area of the ion beam.

$$A = \left(\frac{I}{\rho_o bE} \right) \left(1 + \frac{z\rho_o}{\varepsilon_o E} \right) \tag{5.6}$$

The first term in Eqn. 5.6 is approximately the area of the hole, A_o. The distance between the focusing electrode and the paint layer is substituted in Eqn. 5.6 to predict the beam area at the paint layer, A_ℓ.

$$A_\ell = A_o \left(1 + \frac{\ell\rho_o}{\varepsilon_o E} \right) \tag{5.7}$$

Evaluating Eqn. 5.6 at z=0 with a current of 1μA and a hole radius of 1mm, the initial charge density is $\rho_o=3.2\times10^{-3}$coul/m^3. Using Eqn. 5.7, the area of the beam at the paint layer is approximately $4.6A_o$ or the radius of the beam is 1.9 times the radius of the hole. As the size of the beam was found experimentally to be equal to the size of the hole the spreading is likely counteracted by the focusing of the electric field. Note, unlike diffusion the self field spreading does not represent the resolution of the technique. This effect is controlled by the electrode structure as shown by the relationship between the hole size and the beam size at the paint layer (Eqn. 5.7). However, the diffusion spreading is independent of the electrode structure.

The obtainable resolution is estimated by diffusion, Eqn. 5.1, and is on the order of the flake size. Because the flakes orient to produce the color shift, it is the size of the flakes that define the practical resolution. As a significant number of flakes should be oriented for a smooth color variation, the resolution is estimated as an order of magnitude larger than the flake size, approximately 0.2mm.

5.2 Observed Flake Orientation

An experiment has been developed to obtain curves of

discoloration versus duration of applied field, T, with electric field in the paint, E, as a parameter. Parameters effectively held fixed during these experiments were the mechanical and electrical properties, as well as the thickness of the paint layer.

Preliminary experiments showed that the corona current is extremely sensitive to the distance between the pin and the painted plate. Therefore, a corona current source using feedback control was constructed to maintain the current at any required level independent of the spacing. The electric field in the paint layer is a function of the current density. Therefore, the electric field depends on the square of radius and requires that the radius be measured accurately. There can be large uncertainty in these measurements because of the "fuzzy" boundaries of the discolored area obtained using a single pin corona source and no focusing structure. This is due to the spatial variation of current density from the pin, the current being highest in the centre of the beam and low, eventually zero, at the edge of the beam. Insulating molds have been constructed to exactly control the diameter of the discolored area. The details are indicated in Fig. 5.3. The molds have the advantage of using only the centre portion of the corona current, likely sampling a more uniform current. The sample is painted and then the discs, nine per sample,

Fig. 5.3
Corona Color Variation Experiment

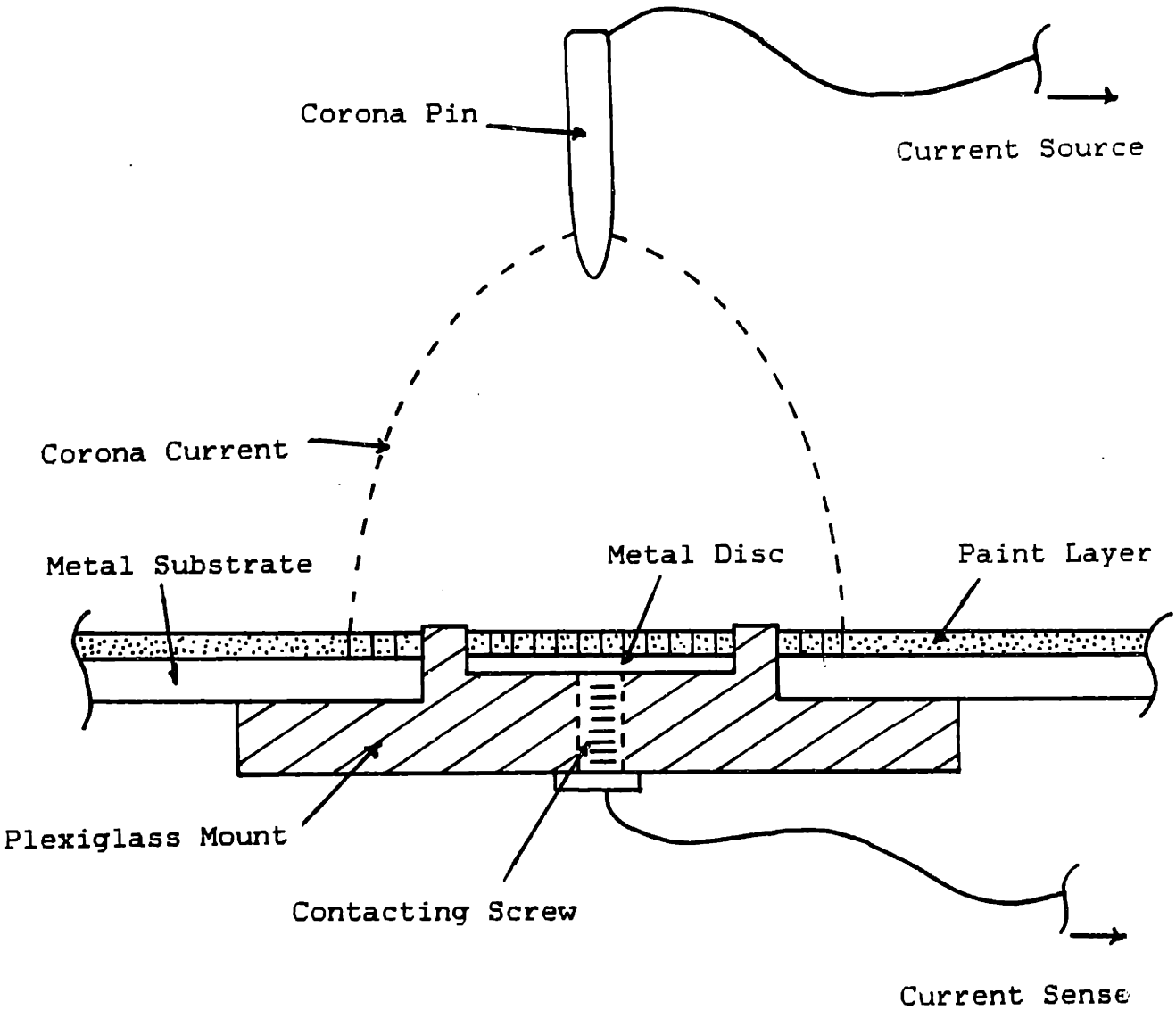

are exposed to a known current for a known period of time. The paint is cured and the paint thickness measured. Only samples having a final thickness between 60μm and 85μm were kept. The color of the samples was measured using a Minolta Chromameter II. The brightness difference, ΔL^*, between the sample and the paint not subjected to the current is recorded. The brightness has been shown by Wojtkowiak to correlate with flake orientation [2]. It should be noted that a numerical relation between flake orientation and L^* is not provided. Three current levels are used in the experiment, 1μA, 2μA, and 3μA. Fig. 5.4 shows the results plotted against the duration of field application. Long times for high current levels introduced effects thought to be associated with chemical affects of the ions on the surface and are not considered valid.

5.3 Scaling with Field Duration and Intensity for a Newtonian Fluid

As a first approximation, the paint layer is represented as Newtonian, having a constant viscosity, η. Therefore, the orientation of the flake, ignoring inertia, is approximated as a balance between an electric torque and a viscous torque. Assuming low Reynolds number flow such that viscous drag on a sphere, radius a, moving through the fluid at a velocity, U, is approximated as Stoke's drag, D_s.

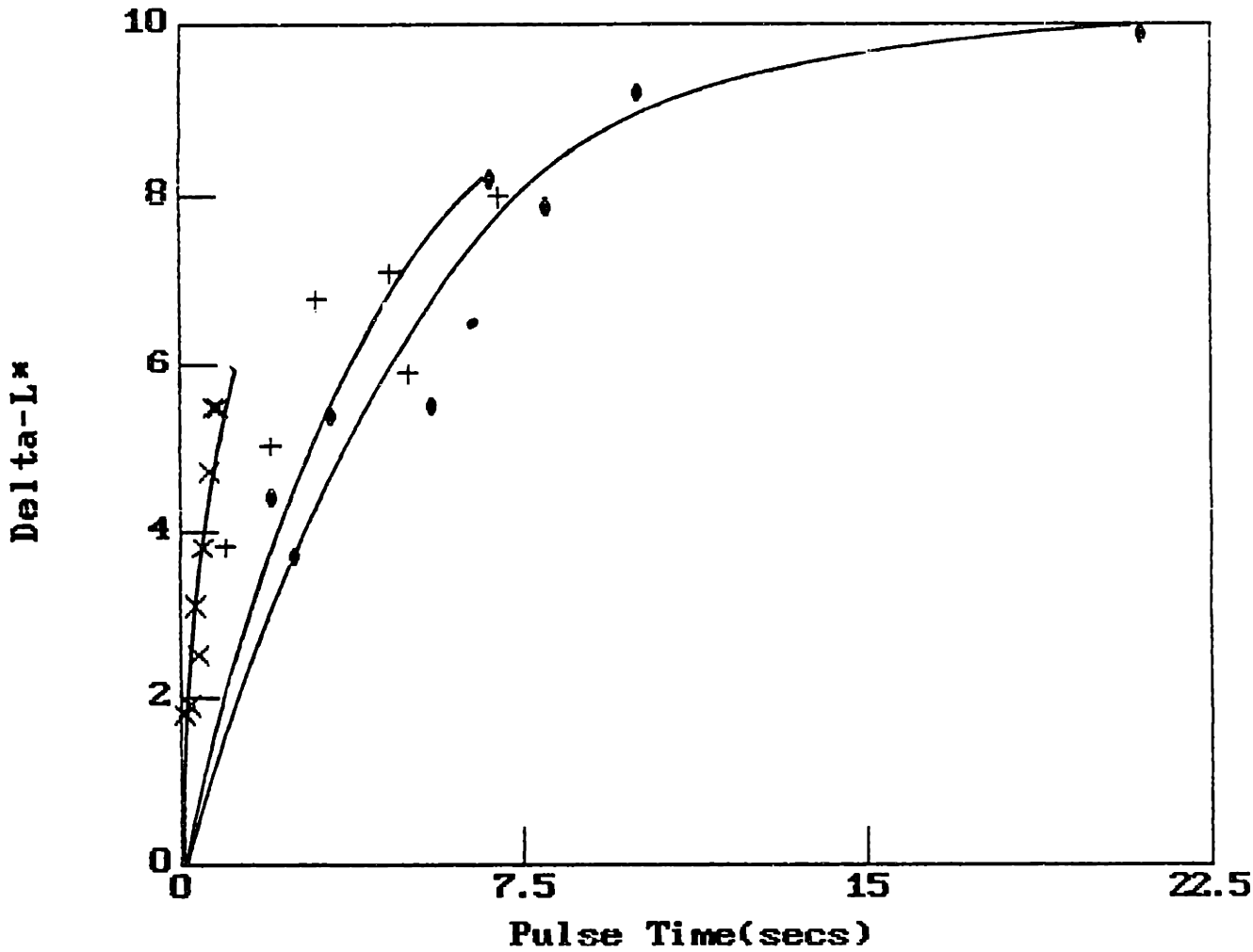

Fig. 5.4
Results of Corona Color Variation

Corona Current: dots - 1 microamp
plus - 2 microamps
cross - 5 microamps

$$D_s = 6\pi\eta a U \tag{5.8}$$

The viscous torque, T_v, is the drag times an effective lever arm, ℓ

$$T_v \simeq D_s \times \ell \tag{5.9}$$

The velocity is the lever arm times the angular velocity of the flake, Ω.

$$U = \ell\Omega = \ell\frac{d\theta}{dt} \tag{5.10}$$

All dimensions are assumed to be of the same order. The viscous torque is approximated as

$$T_v \simeq \eta\ell^3\frac{d\theta}{dt} \tag{5.11}$$

The electric torque, T_e, is approximated as the electric pressure, εE^2, multiplied by the area, ℓ^2, and the lever arm, ℓ.

$$T_e \simeq \ell^3\varepsilon E^2 f(\theta) \tag{5.12}$$

The function $f(\theta)$ represents the angular dependence of the electrical torque and is of the order of θ. Setting the electric torque equal to the viscous torque approximates (within a geometrical factor) the time for orientation, τ_{ev}

$$\frac{\eta\ell^3\theta}{\tau_{ev}} = \ell^3\varepsilon E^2\theta$$

$$\text{or } \tau_{ev} = \frac{\eta}{\varepsilon E^2} \tag{5.13}$$

The discoloration as a function of time, normalized to the electroviscous time, is expected to be a universal plot for all currents. This is true if the geometry is fixed and, therefore, the process is described by only one time. This argument has been used successfully in predicting the interaction between electric and viscous forces [3].

The experimental data has been normalized to the electroviscous time and is shown in Fig. 5.5. Extrapolating the data plotted against time, Fig. 5.4, does indicate a greater similarity between the curves for the normalized data, Fig. 5.5. However, the normalized data does not represent a universal curve as expected from the assumption of Newtonian viscosity. There appears to be other times of importance.

The first time investigated is the charge relaxation time. This time is on the order of 10^{-4}secs, much shorter than any of the pulse times used in the experiment and therefore, should not effect the results. A time associated with the viscoelastic nature of the paint may cause this trend in the data and is investigated in the following section.

5.4 A Technique for Determining the Viscoelastic Nature of Sprayed Paint

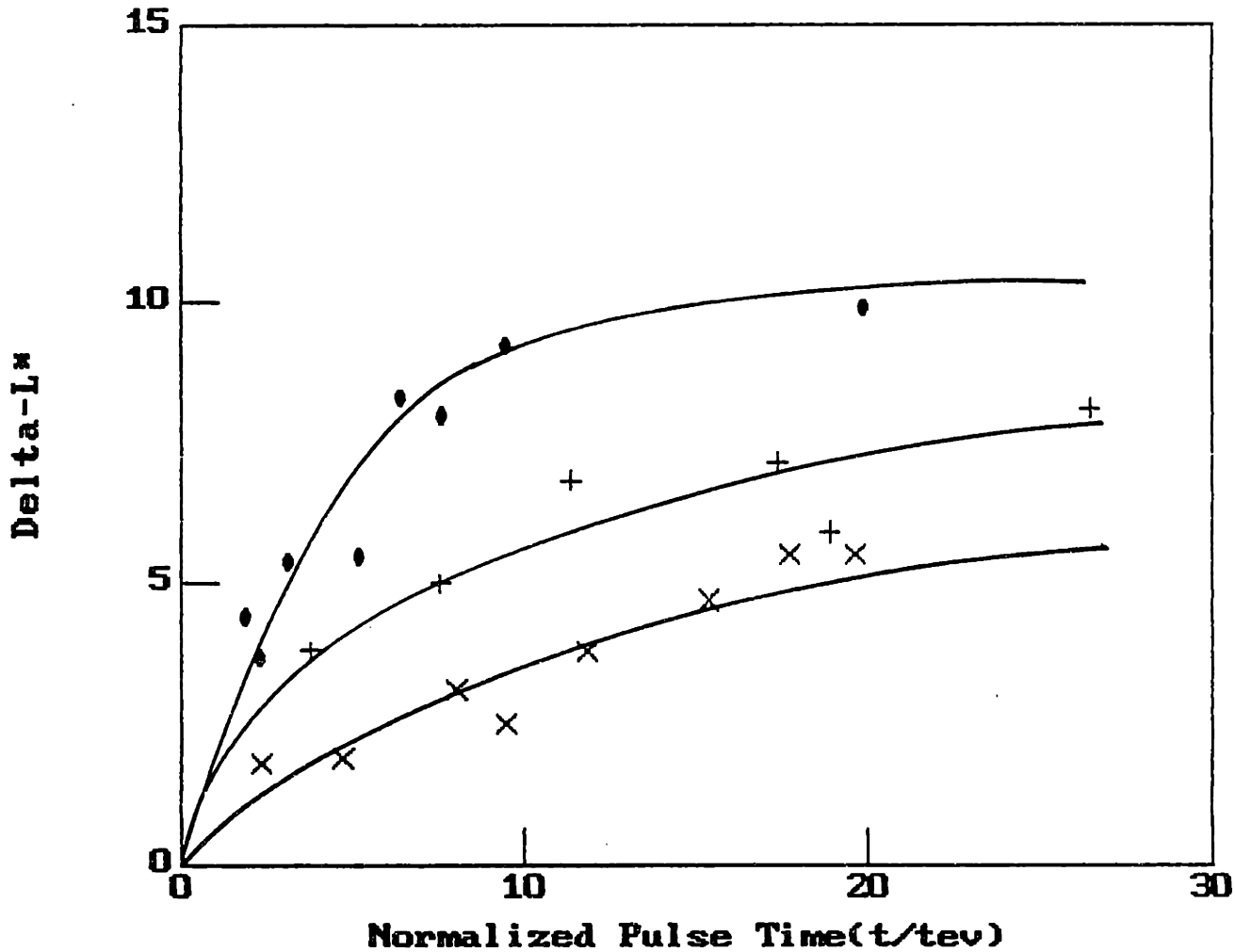

Fig. 5.5
Normalised Results of Corona Color Variation

Corona Current: dots - 1 microamp
plus - 2 microamps
cross - 5 microamps

Viscoelastic materials may have many characteristic times [4] [5]. An estimate of the dominant time will provide some insight as to the plausibility of viscoelasticity accounting for the experimental results. The simplest viscoelastic fluid model is Jeffrey's Model [4], a simplified Voight Model. In lumped parameter terms this model is represented by a dashpot in series with a dashpot and spring in parallel. This circuit and representative equations are shown in Fig. 5.6. The model corresponds to a point by point stress-strain relationship given by

$$\tau_{ij} + \lambda_1 \frac{\partial \tau_{ij}}{\partial t} = \eta_o \left(\frac{\partial \gamma_{ij}}{\partial t} + \lambda_2 \frac{\partial^2 \gamma_{ij}}{\partial t^2} \right) \qquad (5.14)$$

where τ_{ij} is the stress, γ_{ij} is the strain, λ_1 and λ_2 are characteristic times, and η_0 is the steady state viscosity.

The apparatus shown in Fig. 5.7 was used to estimate the parameters in this model. The normal electric field between the paint layer and the glass slide establishes a surface charge that is acted on by the tangential field imposed by the electrodes in the paint. This provides electrical control of the surface shear stress while not introducing unwanted inertia onto the layer. This stress is applied, then removed and the spring-back of the surface timed. Note, a viscoelastic fluid will exhibit both permanent deformation and spring-back of the surface. Using a microscope the surface of the layer is viewed through the

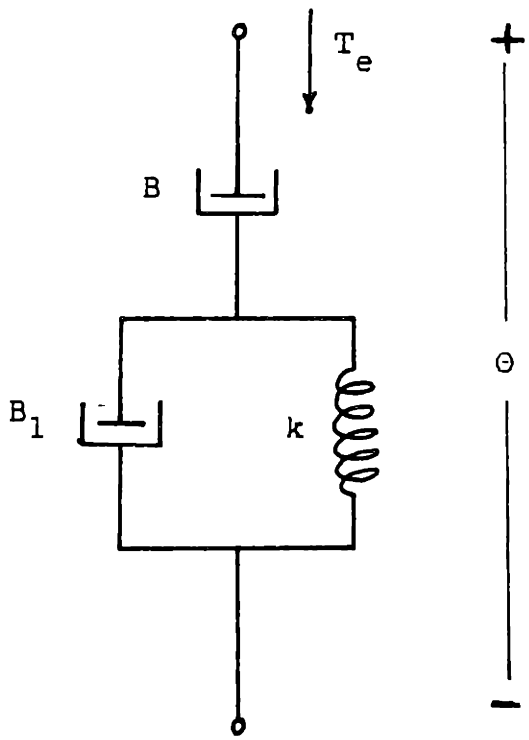

Lumped Parameter Representation of Jeffrey's Model

$$T_e + \lambda_1 \frac{\partial T_e}{\partial t} = B \left(\frac{\partial \Theta}{\partial t} + \lambda_2 \frac{\partial^2 \Theta}{\partial t^2} \right)$$

Fig. 5.6
Jeffrey's Circuit Model for a Viscoelastic Fluid

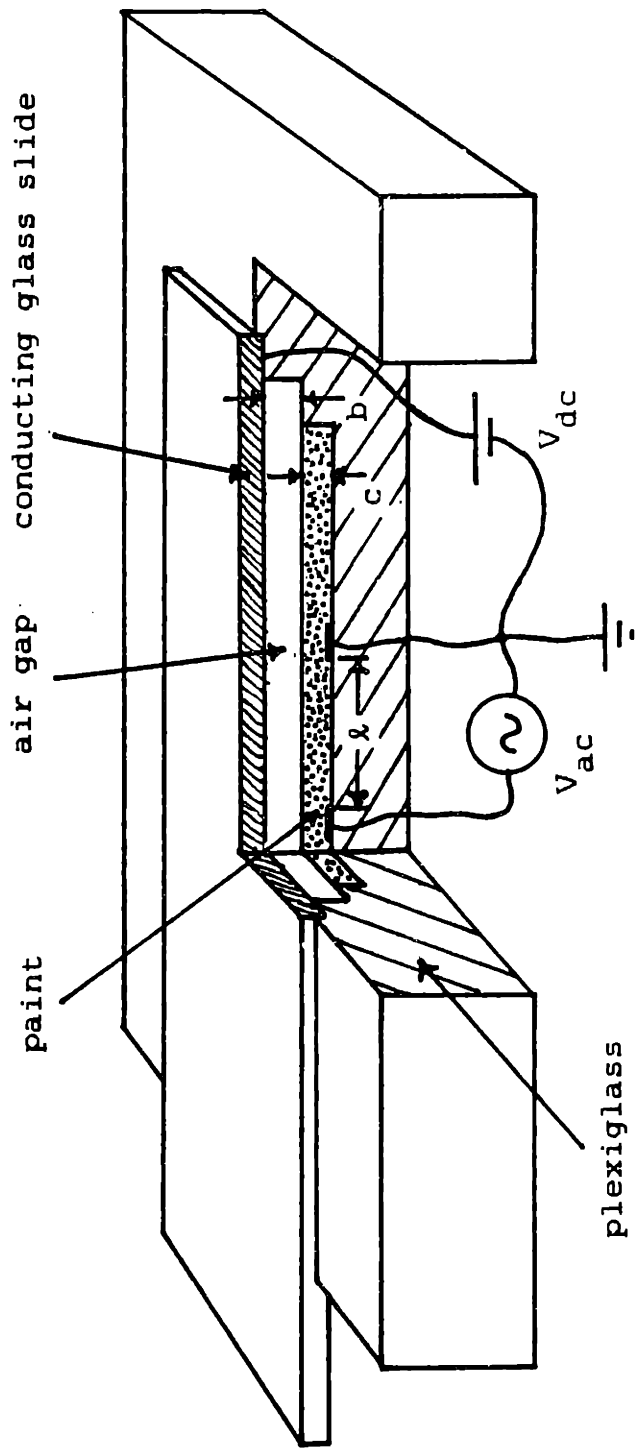

Fig. 5.7
Apparatus to Measure Viscoelastic Properties

conducting glass slide. Both permanent deformation and spring-back are observed. The decay time for the spring-back, representing the viscoelastic time, is approximately 5secs. Assuming an exponential model, Jeffrey's Model, this represents roughly three time constants. Therefore, the viscoelastic time is approximately 1.7secs.

A more thorough characterization of the fluid can be obtained using this apparatus. The frequency response of the fluid can be used to identify the parameters of the system. To ensure the inertia of the paint is not significant the viscous diffusion time, τ_{vd}, based on the thickness of the paint layer, ℓ, must be less than the inverse frequency.

$$\tau_{vd} = \frac{\rho \ell^2}{\eta} < 1/\omega \qquad (5.15)$$

or

$$\frac{\omega \rho \ell^2}{\eta} < 1 \qquad (5.16)$$

Typical values for these parameters are ω=1Hz (maximum), ρ=1000kg/m^3, ℓ=1mm, and η=1kg/s-m. Because the left hand side of the inequality, Eqn. 5.16, is approximately 0.006, inertia can be ignored.

The surface charge, σ_s, on the air/paint interface is held constant by applying a DC voltage, V_{dc}, to the glass

slide. The paint is a DC ground so this potential is applied across the spacing, b, between the glass slide and the paint.

$$\sigma_s = \varepsilon_o \frac{V_{dc}}{b} \tag{5.17}$$

The alternating field in the paint layer is established by applying a potential, V_{ac}, between the electrodes in the paint. The field between these electrodes is the potential divided by the spacing, c

$$E_{ac} = \frac{V_{ac}}{c} \tag{5.18}$$

Combining Eqns. 5.17 and 5.18, the surface force density, T_s, is

$$\begin{aligned} T_s &= \sigma_s \times E_{ac} \\ &= \varepsilon_o \frac{V_{dc} V_{ac}}{bc} \end{aligned} \tag{5.19}$$

Using Jeffrey's Model the response of the surface, d_s, in complex notation is given by

$$\tilde{d}_s = \frac{\tilde{T}_s(1+j\omega\lambda_1)}{j\omega B(1+j\omega\lambda_2)}$$

and the log of the amplitude is

$$\log(d_s) = \log(T_s/B) - \log(\omega) + \log(1+\omega^2\lambda_1^2)^{\frac{1}{2}} - \log(1+\omega^2\lambda_2^2)^{\frac{1}{2}} \tag{5.20}$$

The experimental results are shown in Fig. 5.8. Estimating the two break points gives λ_1 = 13.3 secs and λ_2 = 2.0 secs.

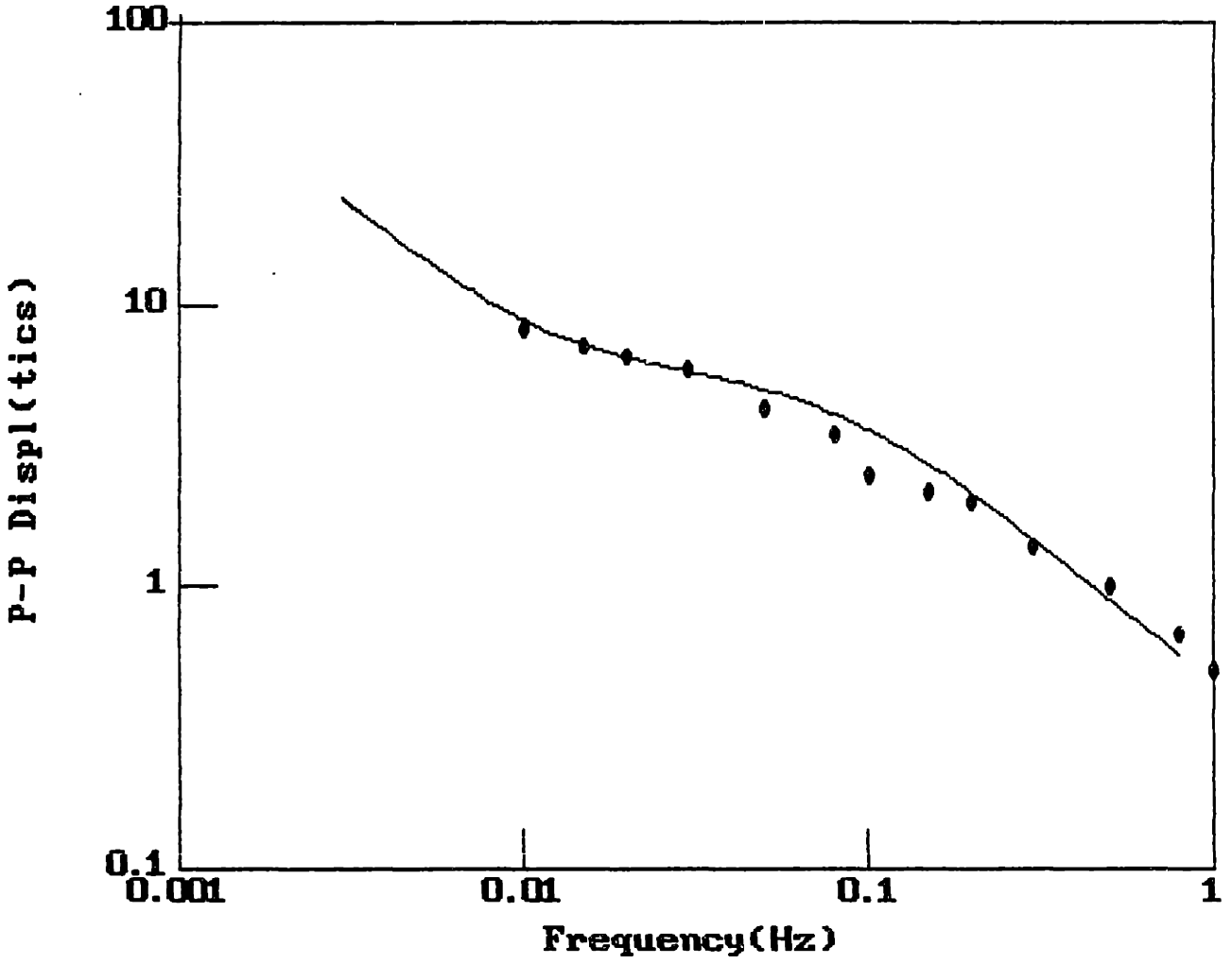

Fig. 5.8
Response of Sprayed Paint: Amplitude vs Frequency

solid curve - theoretical
3.1 tic = 1 mm

Using these results $B_1 = 0.177 \times B$. Numerical calculation of Eqn. 5.20 is possible using values for λ_1, λ_2, F_e and B. F_e is normalized to one and a value of 0.7 is chosen for B to represent the best fit to the experimental data. This is indicated as a solid line in Fig. 5.8. The close agreement between the curve and the data indicates Jeffrey's Model is an excellent model for the paint.

The value of the electrical force can be used to calculate absolute values of the parameters in Jeffrey's Model, λ_1, λ_2, and η_o. The times, λ_1 and λ_2, are known from the breakpoints in Fig. 5.8. Because viscous diffusion occurs rapidly through the paint layer the fluid velocity profile in the paint is assumed linear. Therefore, the strain is given by

$$\gamma = \frac{d_s}{c} \tag{5.21}$$

Solving Eqn. 5.14 in the sinusoidal steady state for the magnitude of the strain and using Eqn. 5.21 gives

$$\frac{d_s}{c} = \frac{T_s(1+\omega^2\lambda_1^2)^{\frac{1}{2}}}{\omega\eta_o(1+\omega^2\lambda_2^2)^{\frac{1}{2}}}$$

if $\omega >> 1/\lambda_1, 1/\lambda_2$ then

$$\frac{d_s}{c} = \frac{T_s\lambda_1}{\omega\eta_o\lambda_2}$$

or

$$\eta_o = \frac{T_s c \lambda_1}{d_s \omega \lambda_2}$$

Using the experimental parameters, $\eta_o = 5.51$.

5.5 Flake Orientation in a Viscoelastic Fluid

Interest is in the final value of flake angle after the application of a pulse of torque. This final value depends only on the value of the torque, length of the pulse, and the dashpot B. Therefore, the results would scale with the lumped parameter equivalent of the electroviscous time, τ_{evl}.

$$\theta_{final} = \frac{T_e}{B} \times \tau_{pulse} \qquad (5.22)$$

Taking the characteristic time as $\tau_{evl} = B/T_e$ the final angle is identical for all values of the electrical torque, T_e, when plotted against the pulse time normalized to this characteristic time, τ_{pulse}/τ_{evl}. This does not represent the physical situation accurately. The applied torque is a function of angle as is the competing fluid force because the flake radius is on the order of the paint layer thickness. These forces should have similar effects on the flake rotation. The electrical force decreases and the fluid force increases as the flake approaches perpendicular to the substrate, both resulting in a smaller alignment force.

To investigate the effect this nonlinearity would have

on the results, the electrical force is assumed to vary as the sin of twice the angle [6]. This force is used to simulate the angle of the flake as it is subjected to different torques and times.

Computer simulation of flake orientation requires that the torque, B, B_1, k, and the initial angle of the flake be specified. The initial angle of the flake is assumed to be 20 degrees, B is chosen to be 10 and the torque values are 1, 4, and 25, chosen to be similar to the scaling used experimentally and to achieve large flake angles. Large flake angles are necessary to observe the effects of the non-linearity and, as shown in Fig. 3.12, occur frequently. The values found for λ_1 and λ_2 are used to calculate B_1= 1.8 and k = 0.9. The pulse times are varied for each torque value such that the time multiplied by the torque gives normalized times between one and twenty-five. Fig. 5.9 shows the transient of flake orientation for a long pulse and low electric torque and Fig. 5.10 shows the transient for a short pulse and high electric torque. The final flake angle as a function of torque and normalized time are shown in Fig. 5.11. These curves exhibit the same trends as the normalized experimental data, Fig. 5.5. Although the fluid mechanics and the effects of flake angle on color are not quantified the similarity between these curves and the curves obtained experimentally indicates the viscoelastic

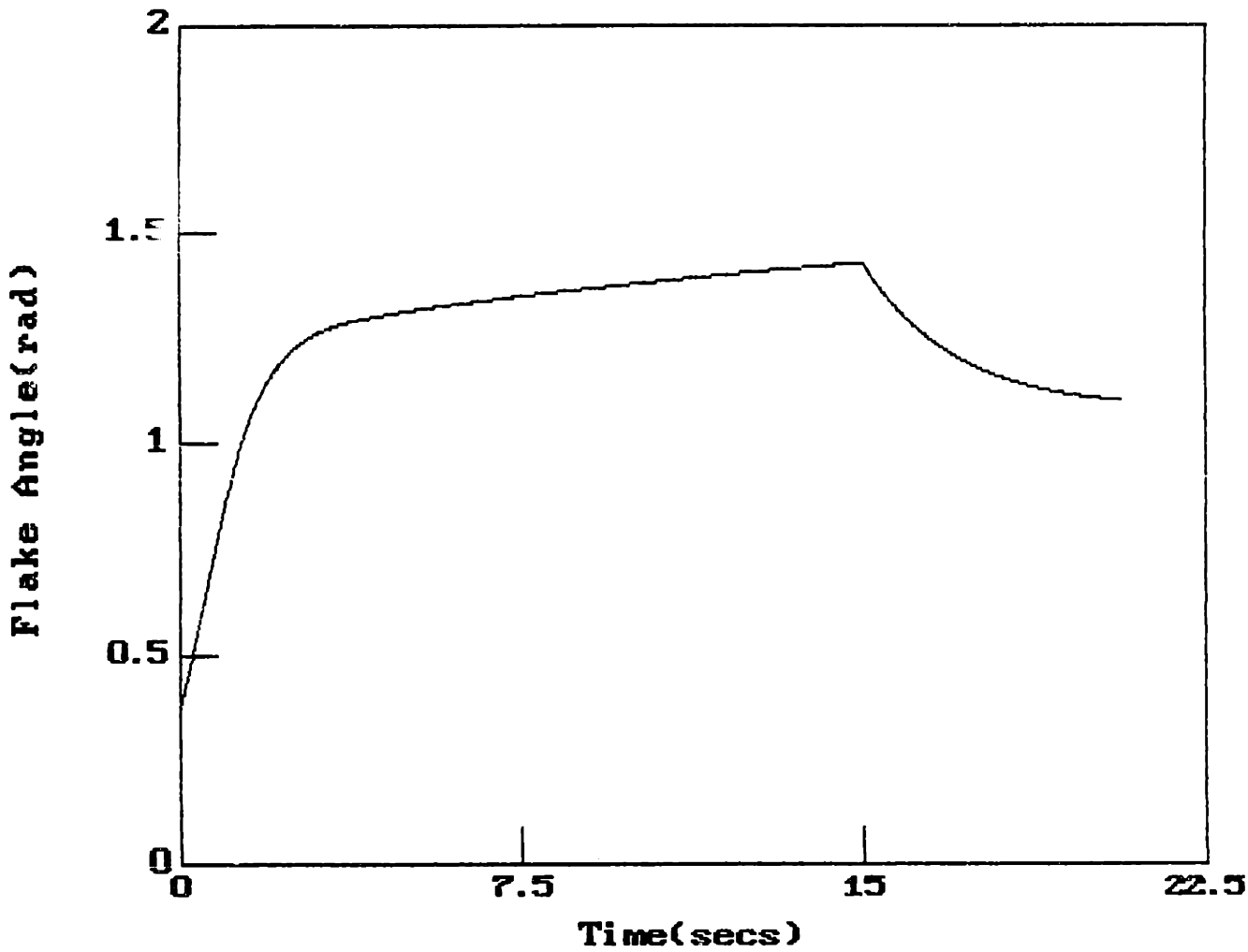

Fig. 5.9
Simulated Flake Transient

B=10, B1=1.8, k=0.9
torque - 1
pulse duration - 15 sec

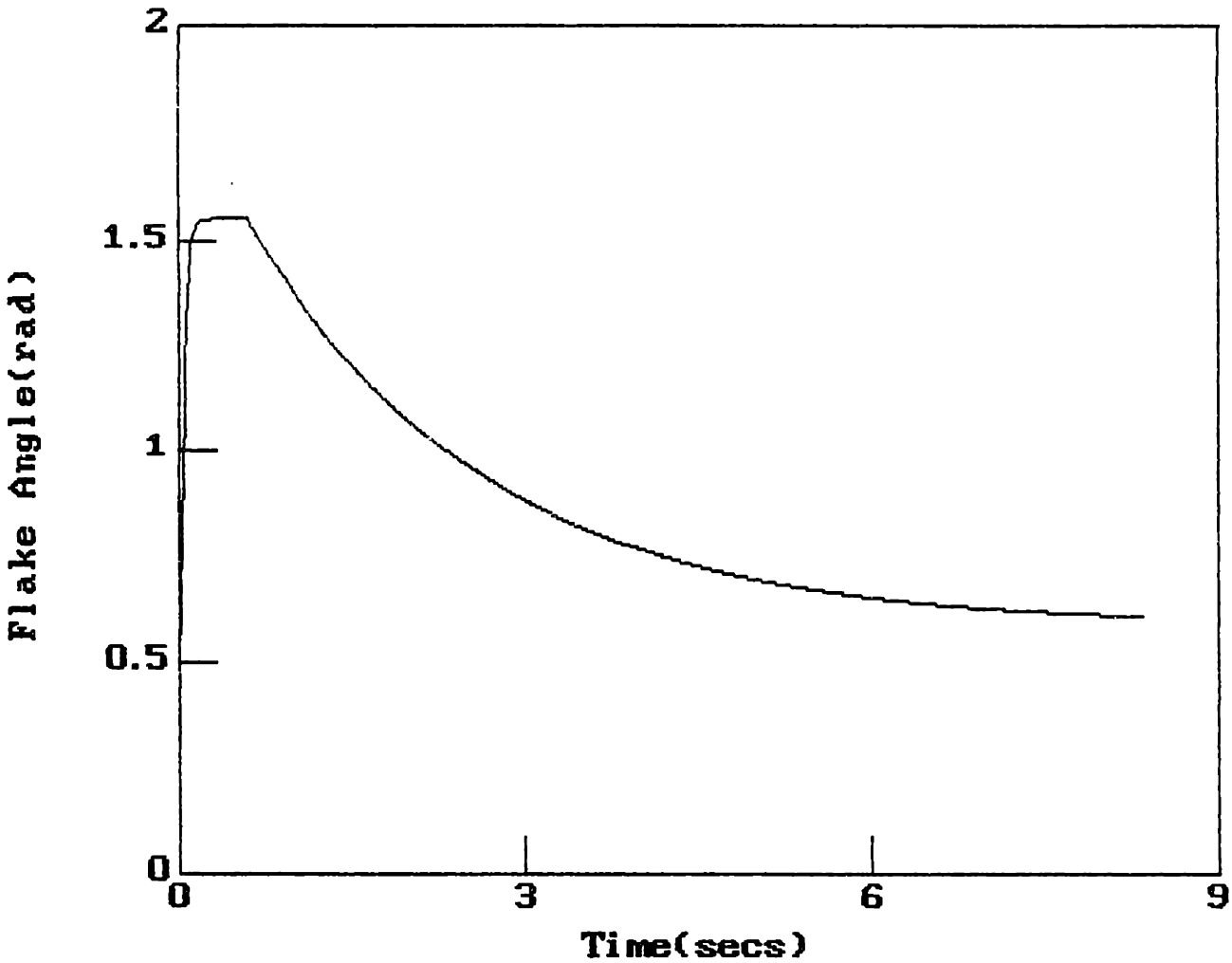

Fig. 5.10
Simulated Flake Transient

B=10, B1=1.8, k=0.9
torque - 25
pulse duration - 0.6 sec

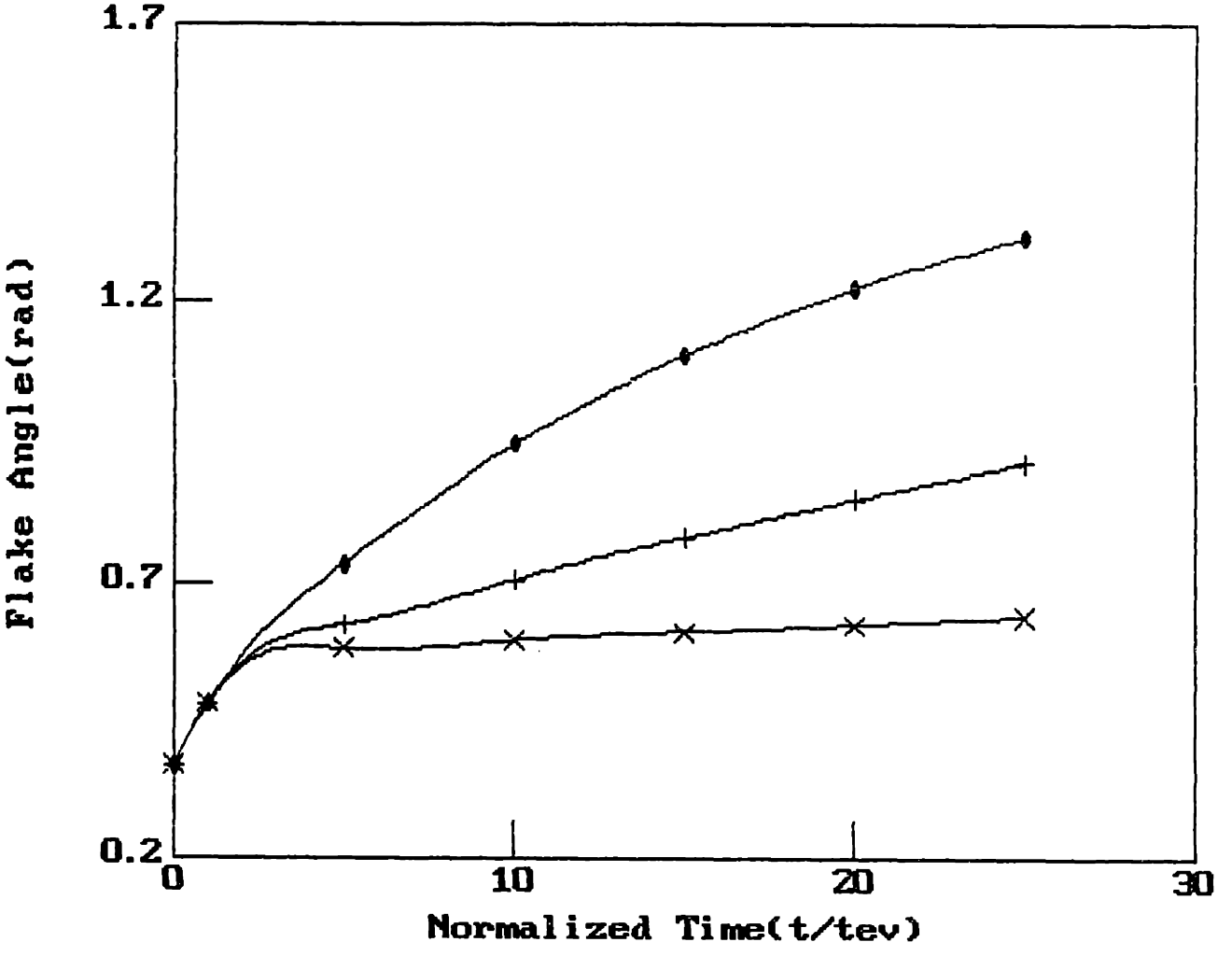

Fig. 5.11
Simulated Results of Flake Orientation

B=10, B1=1.8, k=0.9
Torque: dot - 1
plus - 4
cross - 25

nature of the paint may account for the discrepancy from the universal curve expected. The base material of the paint is high molecular weight hydrocarbons known for exhibiting viscoelastic behavior [5].

5.6 Effects of the Corona Current Other Than Flake Orientation

Exposing the paint layer to the corona current for extended periods of time results in a film on the surface of the paint layer. This film can be scraped off the surface as its properties are dramatically different from the base paint. Possibly this film is formed by a chemical reaction between the corona ions and the paint. The time for this film to form is, however, substantially longer than typical times required for corona color variation.

Electrophoresis of the flake and other pigments in the paint has been shown to occur at the field strengths used to orient the flakes. The time for noticeable electrophoresis is approximately five minutes, again much longer than times used to obtain flake alignment.

The spatial variation of the corona current and the surface charge on the paint layer can cause the paint surface to be electrically pumped in the radial direction causing the surface to be indented. An estimate of this

stress is possible by assuming the spatial distribution of the corona current. In cylindrical coordinates

$$J_z(r) = J_o \exp^{-\left(\frac{r}{a}\right)^2} \tag{5.23}$$

The constant J_o can be solved in terms of the total current, I, by integrating the current density over area.

$$J_o = \frac{I}{\pi a^2} \tag{5.24}$$

The paint layer is assumed ohmic with conductivity, σ, and therefore

$$E_z = \frac{J_z}{\sigma} \tag{5.25}$$

The electric field in the layer is irrotational

$$\nabla \times \bar{E} = 0$$

Assuming a quasi-one-dimensional model such that E_z is only a function of r

$$\frac{\partial E_z}{\partial r} = \frac{\partial E_r}{\partial z} = \frac{1}{\sigma} \frac{\partial J_z}{\partial r}$$

Integrating

$$E_r = \frac{1}{\sigma} \frac{\partial J_z}{\partial r} z + \text{constant} \tag{5.26}$$

Taking the conducting substrate to be at z=0, then E_r at z=0 must be zero and the constant in Eqn. 5.26 must also be zero. Using Eqn. 5.24 for J_z, Eqn. 5.26 becomes

$$E_r = \frac{I}{\sigma\pi a^2} \frac{2r}{a} \frac{z}{a} \exp^{-\left(\frac{r}{a}\right)^2} \tag{5.27}$$

The surface charge, σ_s, is

$$\sigma_s = \varepsilon_p E_p - \varepsilon_o E_a \tag{5.28}$$

where E_p is the normal electric field in the paint, E_a is the normal electric field above the paint, ε_o is the permittivity of free space, and ε_p is the permittivity of paint. Approximating the electric field above the paint layer as

$$E_a = \frac{V}{\ell} e^{-\left(\frac{r}{a}\right)^2} \tag{5.29}$$

where V is the potential applied to the corona source, and ℓ is the spacing between the corona source and the paint layer. Substituting Eqns. 5.29, 5.23, and 5.25 into Eqn. 5.28 gives

$$\sigma_s = \left(\varepsilon_p \frac{I}{\pi a^2 \sigma} - \frac{\varepsilon_o V}{\ell} \right) \exp^{-\left(\frac{r}{a}\right)^2} \tag{5.30}$$

The radial surface stress, T_s, is the surface charge times the radial electric field

$$T_s = E_r \sigma_s \tag{5.31}$$

Using Eqns. 5.27 and 5.30 evaluated at the paint/air interface, $z=\Delta$

$$T_s = \left(\varepsilon_p \frac{I}{\pi a^2 \sigma} - \frac{\varepsilon_o V}{\ell} \right) \frac{I}{\pi a^2 \sigma} \frac{2r\Delta}{a^2} \exp^{-2\left(\frac{r}{a}\right)^2} \tag{5.32}$$

This expression has a maximum at r=a/2 where the stress is

$$T_s = \left(\varepsilon_p \frac{I}{\pi a^2 \sigma} - \frac{\varepsilon_o V}{\ell} \right) \frac{I}{\pi a^2 \sigma} \frac{\Delta}{a} \exp^{-0.5} \qquad (5.33)$$

Typical values for the parameters in this expression are V=5000V, $\ell=10^{-2}$m, I=1μA, $a=0.5\times10^{-2}$m, $\sigma=10^{-7}\Omega^{-1}m^{-1}$, and Δ=70μm.

Substituted in Eqn. 5.33, the surface stress is

$$T_s = 1.97 \times 10^{-2} Nt/m^2$$

Balancing the surface stress against the viscous stress gives

$$\eta \frac{v}{\Delta} = T_s \qquad (5.34)$$

Using the thickness of the paint layer as the distance the surface would move before the surface was indented, the time for this distortion is

$$\tau = \frac{\eta}{T_s} \qquad (5.35)$$

This is an effective electroviscous time. Taking the viscosity of the layer to be 0.7poise (0.07kg/s-m), the time is

$$\tau = 35.6 secs \qquad (5.36)$$

The longest pulse time for one microamp of current was 25secs. Surface indentation was not observed using this

pulse time, however, indentation was observed if the current was applied for 40secs. Although surface indentation was not a problem, the higher pulse times were almost sufficient to cause this distortion. The threshold appears to be estimated closely by Eqns. 5.35 and 5.33.

References

[1] Melcher, J.R., Continuum Electromechanics , MIT Press, Cambridge, 1981

[2] J.J. Wojtkowiak, "Instrumental Method for Determining Degree of Aluminum Flake Orientation in Acrylic Coatings", Journal of Paint Tech., 47, No. 609, 79(1975)

[3] J.F. Hoburg and J.R. Melcher, "Electrohydrodynamic mixing and instability induced by colinear fields and conductivity gradients", Phys. Fluids 20, 6 (1977)

[4] Ferry, J.D., "Viscoelastic Properties of Polymers", John Wiley and Sons, New York, 1970

[5] Bird, R.B., Armstrong, R.C., Hassager, O., "Dynamics of Polymeric Liquids", John Wiley and Sons, New York, 1977

[6] Shine, A, "The Rotation of Suspended Ferromagnetic Fibers in a Magnetic Field", MIT PhD Thesis, 1982

Chapter 6

Conclusions

The breadth of the research makes it helpful to split the conclusions into six sections. Although related, these summarize distinguishable areas. The ordering of the following sections reflect the emphasis of the research. The first two sections deal with the color variation between mechanical and electrostatic spraying. This was the base objective of the project. The third section results from the data sampling techniques that were used to obtain information on the drops. These techniques are useful as general tools for understanding a spray process. Sections four and five deal with innovative ideas for use in the painting industry; corona color control and an electrostatic airless sprayer (Appendix A). The final section involves computer simulation of the spray equipment (Appendix B).

6.1 Dominant Mechanism for Color Variation

There are many obvious differences between electrostatic spraying and mechanical spraying such as the spray pattern, paint flow rate, and efficiency. However, there are other substantial differences and fundamental processes exposed in the data presented in Chapter 4. First, the actual deposited flake content is quite different. For a

high quality paint job, the mechanical sprayer deposits an aluminum mass percent greater than 3.0% while the electrostatic process deposits approximately 1.85%. The electrostatic process has a larger spray pattern and the flake content varies from 1.40% flake in the middle to more than 3.30% at the edge. Only a sample which passes through the entire cloud ends up with essentially a flake content consistent with depositing all of the paint on the work piece (1.85%). This spatial variation is most likely to be of practical importance in painting non-uniform areas, where the same time average exposure to the sprayer cannot be ensured at each point on the workpiece.

Second, the flake size distribution deposited by the two processes are quite different. The mechanical sprayer deposits flakes that, on the average, have twice the area per flake as the flakes deposited by the electrostatic sprayer. Again there is the complication that the distribution of flake area (size distribution) deposited by the electrostatic sprayer also varies as a function of radius. The investigation of the two types of sprayers is illustrated in Fig. 6.1 for the electrostatic sprayer and in Fig. 6.2 for the mechanical sprayer.

The data processing technique had an inherent error; drops smaller than 1μm were ignored. Also, the electrical

Fig. 6.1
Analysis of the Electrostatic Sprayer

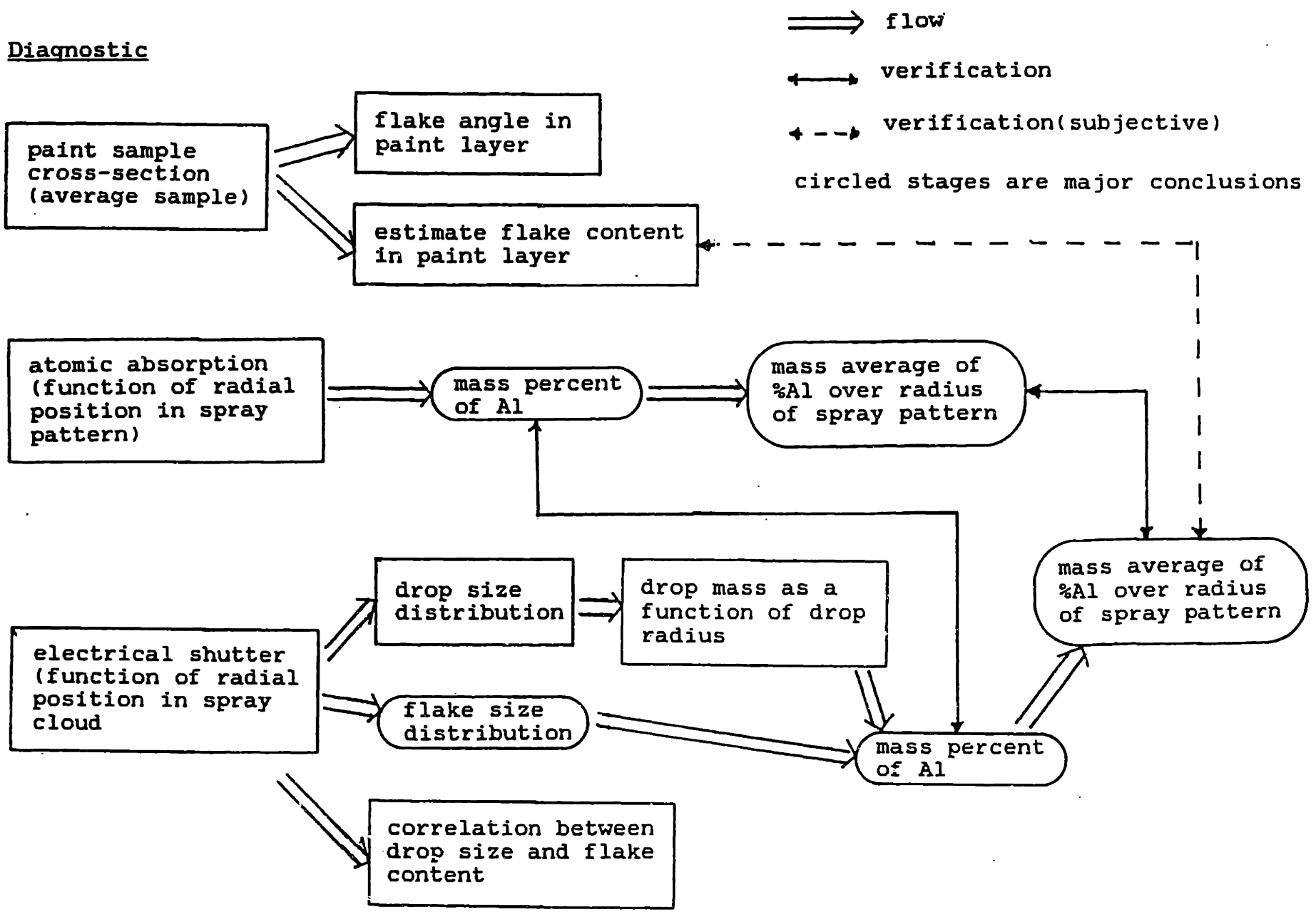

Fig. 6.2
Analysis of the Mechanical Sprayer

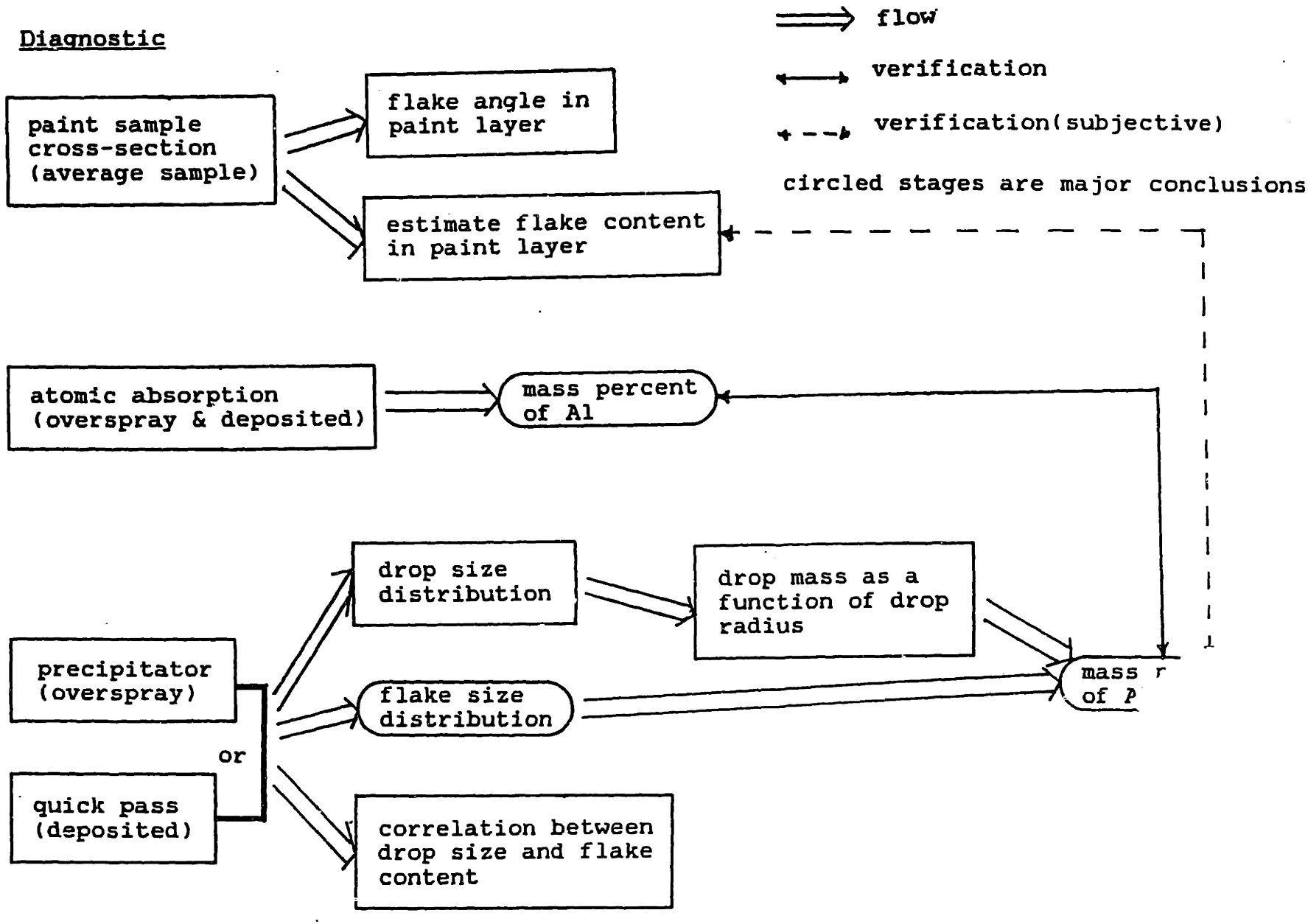

shutter was assumed not to affect the fluid flow. This is only true if the motion of the drops does not substantially affect the fluid. Atomic absorption measurements indicate that these errors did not significantly affect the results. No such check was done for the overspray precipitated from the mechanical sprayer. This data is only used to indicate the drop size and flake content of the general overspray. Also, caution should be exercised in using this data to spatially resolve the overspray distribution as the samples were taken only at three positions using a nozzle entrance that is large compared to the dense portion of the spray cloud.

The parameters of the mechanical sprayer can be adjusted to vary the transport efficiency. Therefore, the device can be tuned to provide different flake content and flake size distribution. Of course, the price paid is a loss of paint and an attendant air pollution problem. However, if the efficiency of the electrostatic sprayer is to be exploited there is no flexibility for tuning color by varying the flake content or flake size distribution. As this is a direct result of the high efficiency, all other highly efficient deposition process are similarly restricted. A more general approach to the painting system must be adopted where the paint, as well as the device, is tuned to obtain the required color. As the electrostatic

device is restricted in its ability to tune color, more emphasis should be placed on the tuning of the flake content and the flake size distribution in the paint.

The differences in the total flake and the distribution of flake size deposited by the electrostatic sprayer versus the mechanical sprayer has been accounted for by tracing in detail the mass transfer. The overspray from the mechanical sprayer was found to contain small drops with a low flake content. This same variation in flake with drop size also acts as a flake size selection filter. The mechanical sprayer deposits large drops containing large flakes and allows the small, low flake content drops to escape. On the average, the flake area deposited by the mechanical sprayer is twice as large as that deposited by the electrostatic sprayer. Flakes on the order of 1μm in diameter exhibit a different light scattering mechanism because their size is on the order of the wavelength of visible light whereas, the larger flakes will reflect in a manner predicted by geometrical optics. This scattering of light through the paint layer from the small flakes will affect the color because reflected light will actually travel through more of the paint and, therefore, have a stronger dependence on the other paint pigments. This may be one mechanism for color variation that is not accounted for by flake content differences.

Using an expansive flat workpiece (as opposed to an irregular shape object having corners and edges) the electrostatic sprayer deposits all constituents of the mixed paint, though there is spatial variation. In contrast, the mechanical sprayer selectively deposits constituents, and is literally a filter of aluminum flake content and size. The byproduct of the filter, the overspray, represents the inefficiency of the process. At present, the paint constituents are selected to function in conjunction with this filter. Once the filter is removed, the final finish must change. Using the mechanical sprayer results as representing the required flake content and distribution, the changes in the paint required to closely match the electrostatic process to the mechanical process are evident. This is also a result of the high efficiency of the electrostatic sprayer.

The high efficiency of bell-type electrostatic sprayers provides a strong incentive for their use. Our results imply a basic change in philosophy for tuning color using these and other highly efficient devices. Instead of attempting to tune the spray device, the paint should be tuned, thereby allowing the device to operate at as high an efficiency as possible. Also, it is important to obtain the same time-average exposure to positions in the spray cloud. In fact, this may be an area for further development of the

spray system as, unlike the high efficiency, it is difficult to imagine how this spatial variation could be useful.

The specific results presented here provide a framework for understanding other spray devices. For example, a common electrostatic spray gun uses an air atomization process almost identical to the Binks gun but also charges the drops and applies an electric field to increase the efficiency. The drop distribution will undoubtably be close to that of the Binks sprayer. The improved efficiency will deposit more of what was previously considered the overspray. A prediction of this portion of the overspray and a knowledge of the drop and flake distribution, will allow an estimation of the difference in the final paint finish. The characterization of the spray device, i.e. characterization of the spray filter's properties, can be accomplished by accounting for the mass transfer of both the base paint and associated pigments. These elements can be delivered to the surface in different manners and should be accounted for separately. For the devices considered, the content of the aluminum flake pigment is found to correlate strongly with the drop size. This allows the entire process to be closely characterized by analyzing the deposition efficiency for each drop size interval.

6.2 Second Order Effects

Flake orientation has not been ruled out as a second order effect. Some reports indicate [1] that very small orientation can account for noticeable color variation. However, flake orientation does not appear to be the dominate mechanism.

Electrophoresis of the flake or other pigments may also contribute some color variation. Experiments have shown that electrophoresis would represent small or negligible color variation. Solvent evaporation has also been briefly mentioned and not eliminated as a mechanism for color variation. Research on these aspects of electrostatic painting was not pursued when the dominant mechanism was identified, but this does not mean that they are not active mechanisms, simply that they are less important.

6.3 Characterization of a Paint Spraying Process

The experimental techniques developed to sample the drops can be used as a means of characterizing a spray process. In flaked paints, the mass transfer for the flake differs from the transfer of the paint resin. The aluminum flake is on the order of the drop size making this selective mechanism dominant. The same process could occur for other pigments, although they are usually much smaller than the drops and are fairly uniformly distributed. Regardless of

the content of the drops, the sampling technique provides details on the drop atomization and drop distribution as a function of position, either at the paint surface or in the overspray. The increased use of electrostatic spray equipment makes the use of the electrical shutter and modern pattern recognition equipment not only an ideal tool for investigating a process but for making a science of its application as well. Further development may also provide detailed information on the solvent evaporation in a particular drop range.

An example of the type of information obtained experimentally yet not used may be the specifics of the drop profiles. The difference in these profiles for different sized drops contains information on solvent evaporation. This can be seen by assuming the simplest case as an example. The drop impinges on the surface and the profile is specified by surface tension alone. The constant pressure inside the drop ensures that the profile is spherical since the radius of curvature must be a constant for surface tension to balance the pressure. At the surface

$$\frac{2\gamma}{R} = \text{pressure} \tag{6.1}$$

where γ is the surface tension and R is the radius of curvature. Assuming the surface tension is a constant, R must also be constant. The wetting angle on initial contact

between the paint and the base material (in the shutter experiments a glass slide) is measured. If, as the solvents evaporate, the interface between the paint, glass, and the air sticks in its initial position the amount of solvent evaporation is equal to the volume of the dried drop subtracted from the volume of a section of a sphere having a known contact angle (the original wetting angle) and perimeter. Automating the measurement of the drop profiles could provide the evaporation information for each drop size interval. In practice, this would require a more rigorous estimation for the surface tension and the wetting angle, particularly their dependence on the solvent concentration. This does make the interpretation of the drop profiles more difficult but possibly still practical. There may be other types of information obtainable from these samples.

The sampling technique is simple, fast, and easily instrumented yet it modifies the actual mechanics of the process minimally. This technique has been transferred to GM where automated pattern recognition equipment is being used to process the data.

6.4 Corona Induced Color Control

It has been shown that a corona current can be used to produce patterns in metallic paints. The resolution is

limited by the electrode shape, the flake size, and diffusion. However, lines of a millimeter thickness are easily obtainable in standard automotive metallic paints. The technique is fast and requires no masking or further application of a different color paint. The mechanism for alignment appears to be a competition between an electric polarization force and a viscoelastic force in the paint layer. The scaling of the technique to higher corona currents and shorter times can be roughly estimated using the electroviscous time. A more accurate scaling requires accounting for the viscoelastic nature of the paint. Long exposure times or high current levels bring into play other effects such as film formation on the paint surface, electrophoresis of the paint pigments, and electrically induced surface indentation.

The color variations may not present a large enough contrast for many applications. This may be improved by using an undercoat having a different color such that alignment of the flakes exposes more of the undercoat pigments thereby influencing the color of the area exposed to the corona current. The effects of the paint composition, particularly the flake size (size distribution), has not been thoroughly investigated. Tuning of the paint composition may result in better control of the color variation obtained by flake orientation. The long term

affects of the corona current on the paint layer have also not been investigated. For example, the possibility that paint exposed to a corona current may degrade faster shold be investigated.

Industrially the technique is simple, ideally suited to automation, and quite inexpensive. Further refinements on the electrode structure and corona source as well as the power supply will undoubtably improve the flexibility and ease of use of this technique.

6.5 Airless Paint Sprayer

A completely electrostatic paint sprayer has been developed and does show promise as a practical device. The mechanisms involved in the device's operation have been discussed and certain mechanisms, for example the current driven jets, are well understood. However, the effects of the viscoelastic properties of the paint and the effects of the film thickness are not completely understood. Therefore, the sensitivity of the device to varying parameters is difficult to predict. Further research should be directed to understand more rigorously the physical mechanisms of the device. This should result in an estimate of the sensitivity of the device to parameters such as the viscosity (possibly the viscoelasticity) and conductivity of the paint and the

operating parameters such as the applied field and the paint flow rate.

This work will provide a better estimate of the practicality of the device. A question of direct concern to the future of the device is its ability to be scaled up to compete with the delivery rates of presently available equipment. The device has the advantage of no moving parts, high efficiency, and the ability to spray highly viscous fluids with an associated lower solvent concentration. The development of inexpensive high voltage switching supplies complements this device that already has many attractive features.

6.6 Computer Simulation

The computer simulation of the paint sprayer using a state space formulation is a useful tool in evaluating the relative importance of various painting parameters and mechanisms. In its present state the program uses empirical input for the drop charge, average drop size, and the shaping air. The program is written in a block structure for easy modification of the routines as theoretical models or experimental inputs are improved. The electric field model has been modified at GM to reflect the actual bell geometry and irregular shaped targets. The formulation is not self

consistent and, although open to improvements, the nature of the formulation prevents it from being self consistent. Because the electrostatic sprayer deposits paint (and, in flake paints, the mass percent of flake) nonuniformly in space, there is a large incentive for predicting the trajectories of drops.

The continuum formulation of the paint sprayer has been proposed as a means of obtaining a self-consistent representation of the sprayer. The statistical approach would predict the evolution of a distribution function compatible with the electrical shutter results. This formulation is can in principle be used together with a model for turbulence. A reasonable starting point for work on this type of model has been outlined.

References

[1] Wojtkowiak, J.J., "Aluminum Flake Orientation of a Metallic Topcoat Exhibiting Telegraphing", Research Memorandum: General Motors Research Laboratories (Polymers Department), Warren, Michigan, 1983

Appendix A

Electrostatic Airless Paint Sprayer

Commercial paint sprayers almost exclusively use some form of mechanical atomization. The atomization may be aided by the application of an electric field but predominantly the atomization is mechanical. Typically this is accomplished by forcing paint through a nozzle using high pressure or by the use of high speed discs or bells. Both of these techniques involve mechanical parts and usually highly turbulent air flow. The edge devices investigated in the early stages of the development of electrostatic sprayers did not use a pressurized paint source, high velocity air flow, or a rotating disc. The atomization was totally electrostatic and the paint was delivered to the atomization surface by gravity. These devices proved unreliable mainly due to poor delivery of the paint to the edge.

The basic objectives for the design of a new spray device are:

(1) Atomization of the paint should be completely electrostatic to avoid the use of mechanical parts;

(2) Transport of the paint to the paint surface should be accomplished without shaping air and hence minimize the pollution problem; and

(3) The paint delivery rate and the surface finish must

be competitive with presently available devices. Two devices were designed to meet these objectives. Design considerations and the final geometry of these devices are described. Experimental results obtained from the sprayers are presented and are used to provide insight into the physical processes of the sprayer. The results are also used to make a preliminary comparison between the new devices and a standard sprayer extensively used in industry. It should be stressed that this development is in a preliminary stage and will hopefully continue in the future.

A.1 Configuration

A high electric stress is required to atomize the paint. Therefore, the geometry of the device must provide localized field concentration at the atomization surface. The required radius was chosen experimentally. Different diameter copper wires were coated with a layer of wet paint and then taken to a potential of 90kV. The spacing between the wire and a ground plane was 0.3m. Successful atomization occurred using a wire diameter of approximately 1mm or less. It was also observed that the atomization was effected by the paint film thickness on the wire. A paint film thickness on the order of 50 - 100μm was found to be the most successful in atomizing the paint. Therefore, the approximate geometry of the device was chosen based on these

dimensions.

The first device constructed resembles a ball point pen in two dimensions. A flat section of brass is hollowed out to form a narrow, 1mm, cavity. Paint is fed into the back of the cavity through small holes under low pressure (just enough to deliver the paint to the atomization edge). The atomization edge of the device is partially sealed by a cylindrical rod that is slightly smaller, approximately 50μm smaller, than the cavity. This allows paint to ooze around the rod. Initially the rod was rotated to aid in the transport of fluid around the rod, however, this was found to be unnecessary. The configuration of the device is shown in Fig. A.1 and the spray system is illustrated in Fig. A.2.

Investigation of the role played by the film thickness in the atomization process led to the design of a slightly different device. The geometry is similar to that described above except the cavity is narrower, 200μm, and there is no rod. Because there is no longer a thin film at the atomization surface this device eliminates the effects of this film on the process. Therefore, the role played by the film can be evaluated. The details of this device are shown in Fig. A.3. Note the radius of the device's edge is similar to the first device.

Fig. A.1
Airless Electrostatic Paint Sprayer I

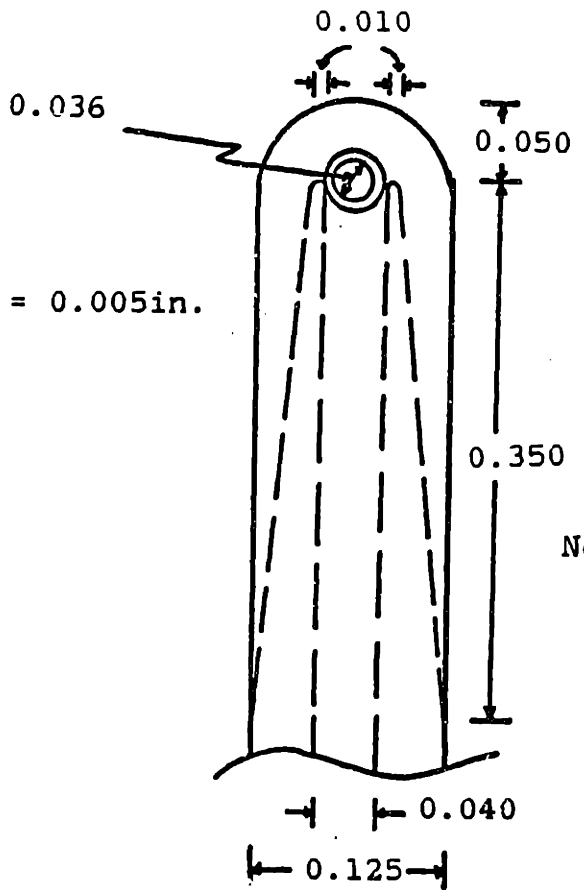

End View

Scale 1mm = 0.005in.

Note: All dimensions in inches

Side View

Scale 1mm = 0.020in.

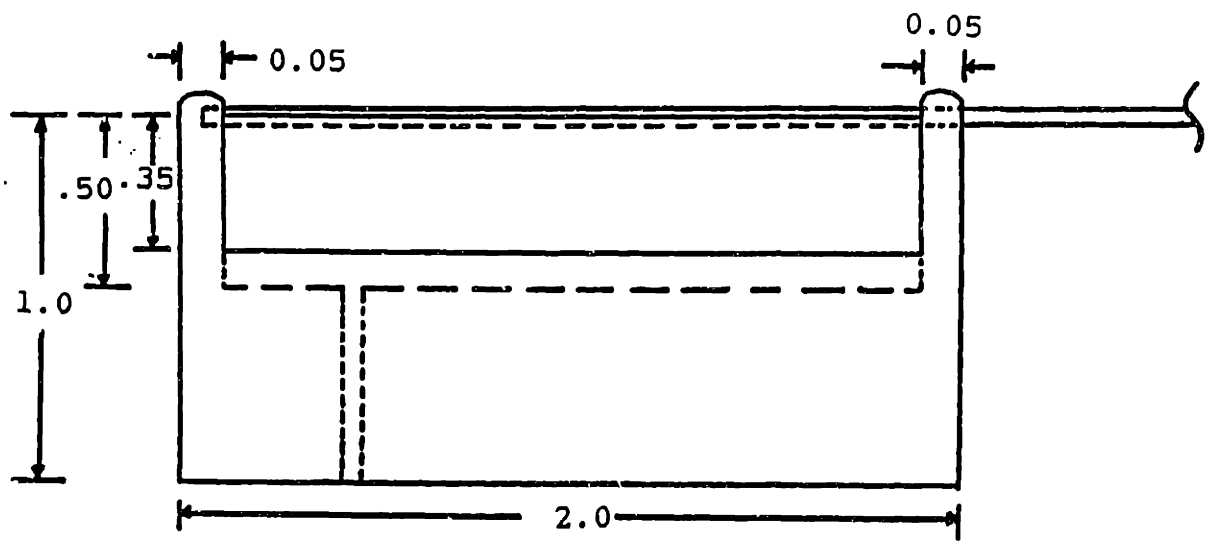

Fig. A.2
Configuration of New Spray System

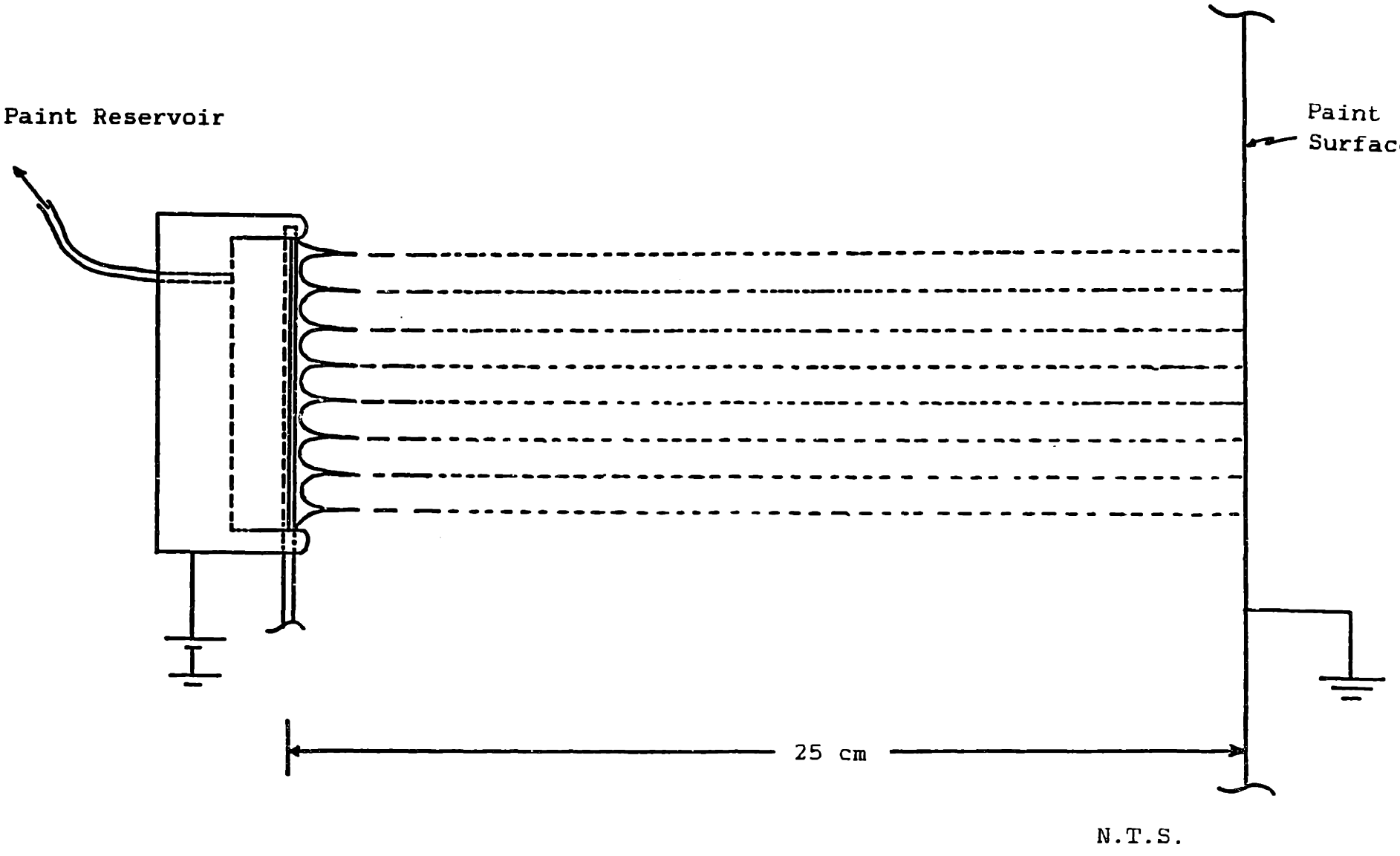

N.T.S.

Fig. A.3
Airless Electrostatic Paint Sprayer II

Edge View
Scale = 8:1

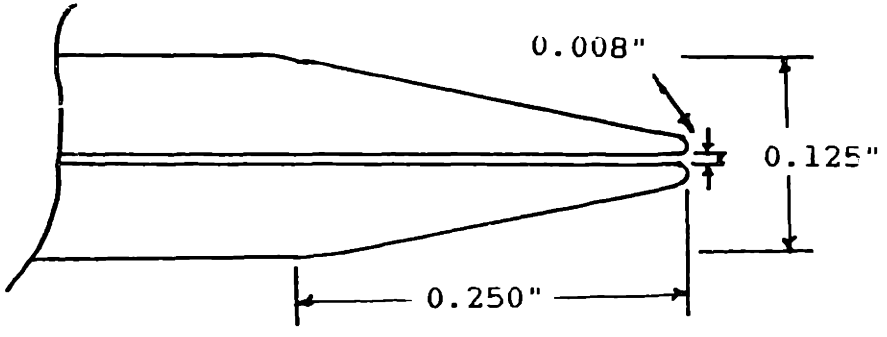

Side View
Scale = 1:1

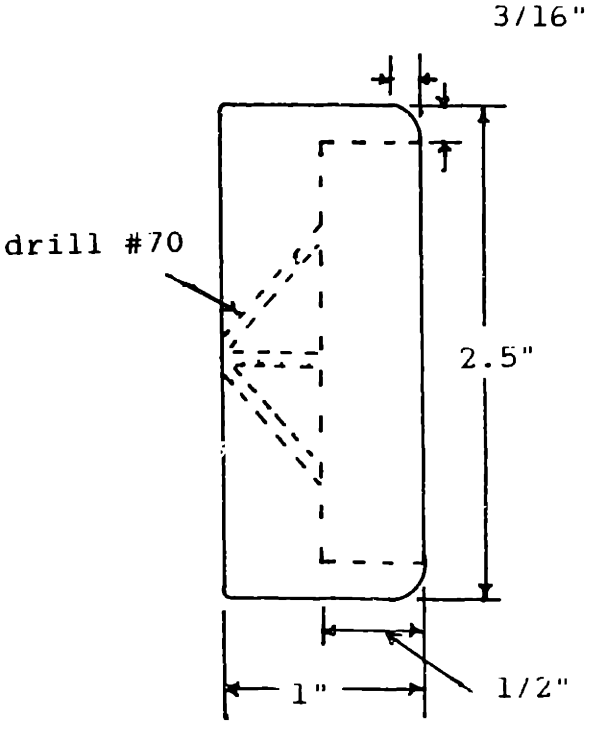

A.2 Experimental Results

The device without the cylindrical rod was only used in tentative experiments. A stable spraying regime could only be obtained by diluting the paint almost by a factor of 10 and using a high applied potential, approximately 100kV. The pressures required for delivery of the paint were in the range of 5-10psi, substantially higher than required in the other sprayer. This is a result of the the pressure drop in the long, narrow cavity and may account for the difficulty encountered in spraying highly viscous fluids. Also, it is felt that the cylindrical rod of the other device has the effect of stabilizing the jets, possibly making the device less sensitive to the properties of the fluid.

The sprayer using a cylindrical rod at the atomization surface was the most successful device and was therefore subjected to the more extensive testing. The input parameters for the device are the paint flow rate, Q, the applied potential, V, and the viscosity of the paint, η. The device is instrumented using the power supply voltmeter, a current sensor at the paint target, and high speed photography. Pictures at the device edge and in the space between the device and the grounded target are obtained using a Questar telescope and a high speed strobe. Shadow pictures are taken to provide the best contrast and to

overcome the low sensitivity to light (high f-stop) of the telescope. The current, I, was displayed on an oscilloscope so the presence of corona could be detected. Corona current has a unique waveform [1] that is easily recognized on the oscilloscope. The paint reservoir was kept below the sprayer, the hydraulic head was maintained constant at 30cm, and was pressurized using nitrogen. This provides controlled delivery of the paint to the sprayer.

No xylene was added to the paint so the bulk viscosity for both flake and no-flake paint is approximately 3poise(0.3nt/s-m). The pressure on the paint reservoir was maintained constant at 1.2psi. The results using flake paint are

V = 50kV Q = 1.2ml/min I = 12-15μA

V = 70kV Q = 1.6ml/min I = 11-16μA

The current from the sprayer at the lower voltage, 50kV, was not stable, occasionally jumping to one tenth of the more common value given above. Fig. A.4 shows the shape of the jets at the sprayer edge at an applied potential of 50kV while Fig. A.5 is the same picture obtained using a potential of 70kV. Note the regular spacing of the jets and the oblong shape of the paint drops immediately after they are formed from the jet.

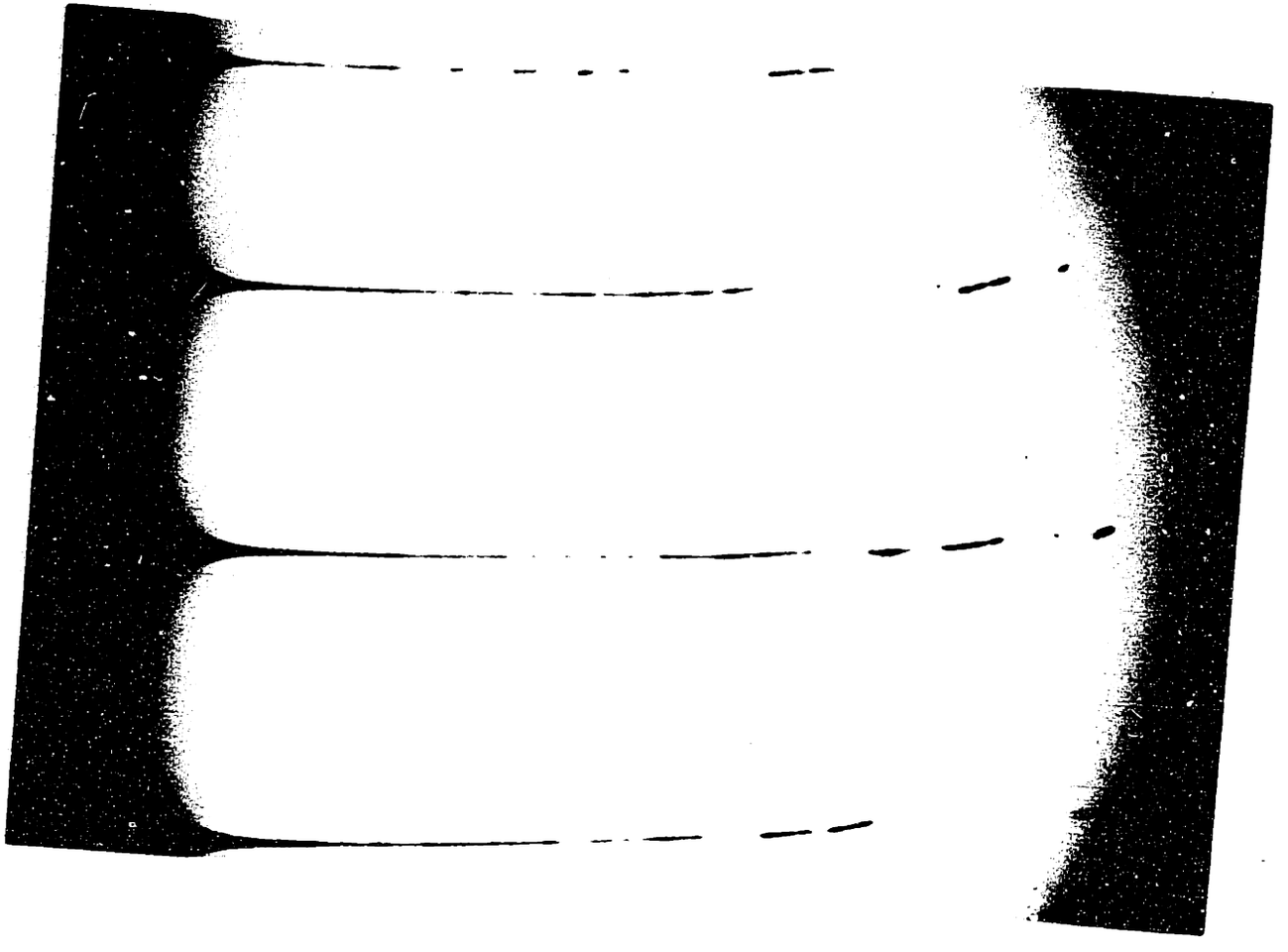

approx. mag. x10

Fig. A.4
Airless Sprayer: Flake Paint - 50kV

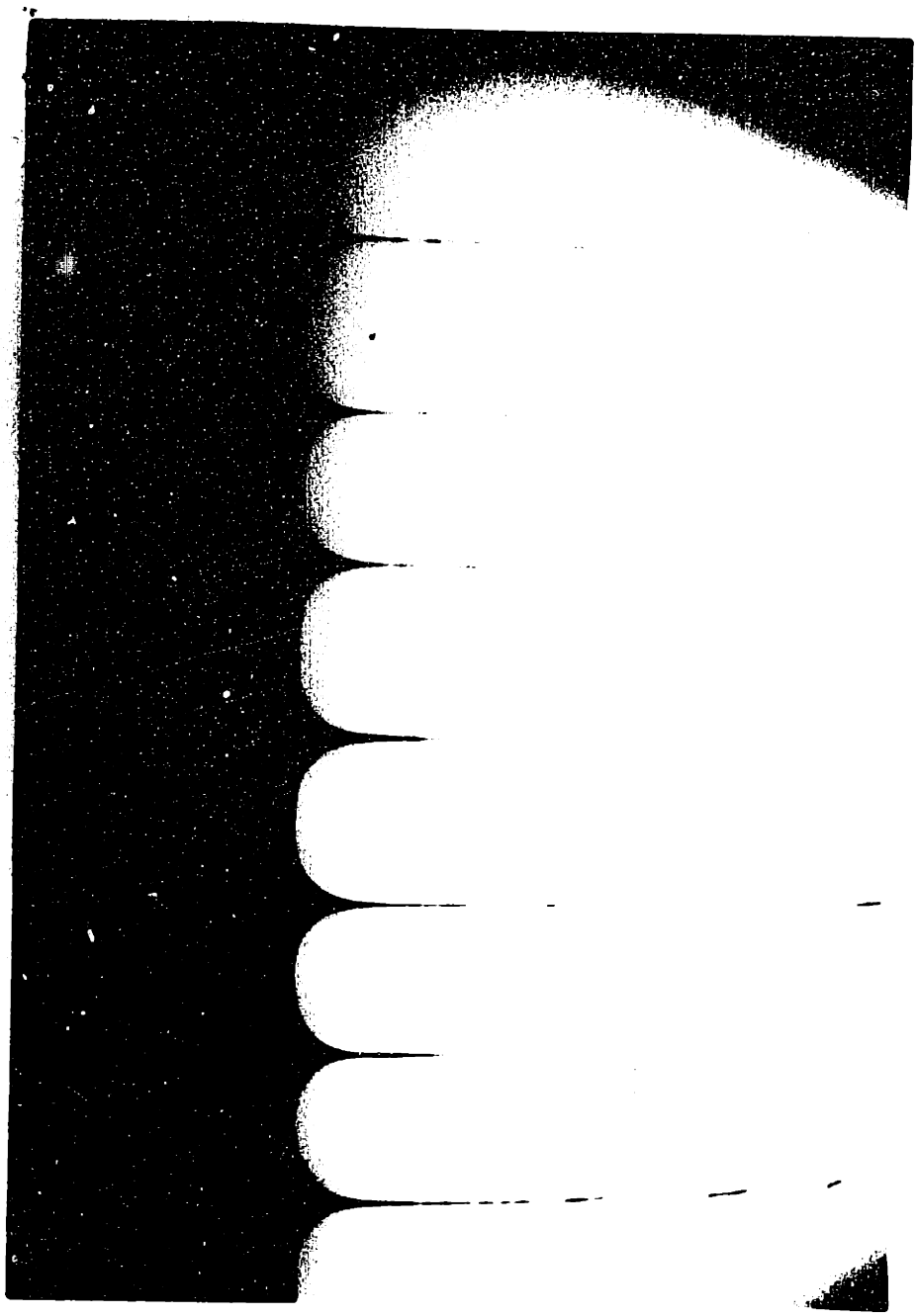

approx. mag. x10

Fig. A.5
Airless Sprayer: Flake Paint - 70kV

Using the same parameters and no-flake paint the results were surprisingly different

V = 50kV Q = 4.0ml/min I = 0.27μA

V = 70kV Q = 4.6ml/min I = 0.51μA

The jets and current readings were extremely stable during the testing of the no-flake paint. Fig. A.6 shows the edge of the sprayer using 50kV while Fig. A.7 indicates the effects of the higher potential, 70kV. Note the different spacing between the jets obtained using no-flake paint, Fig. A.6 , and flake paint, Fig. A.4. and also the random nature of the jet formation at the higher potential with no-flake paint, Fig. A.7, which is completely different than the results obtained with flake paint, Fig. A.5. No corona current was observed during the experiments, although a noticeable corona current was observed when the paint was exhausted. The edge of the device emits corona current in the absence of the paint. The paint reduces the field at the edge of the device preventing corona while painting. Although not measured on the current meter, a small corona emission could occasionally be detected visually at the ends of the device.

The instability of the sprayer while using flake paint may be explained by the presence of several long filaments of paint. These filaments were continuous between the

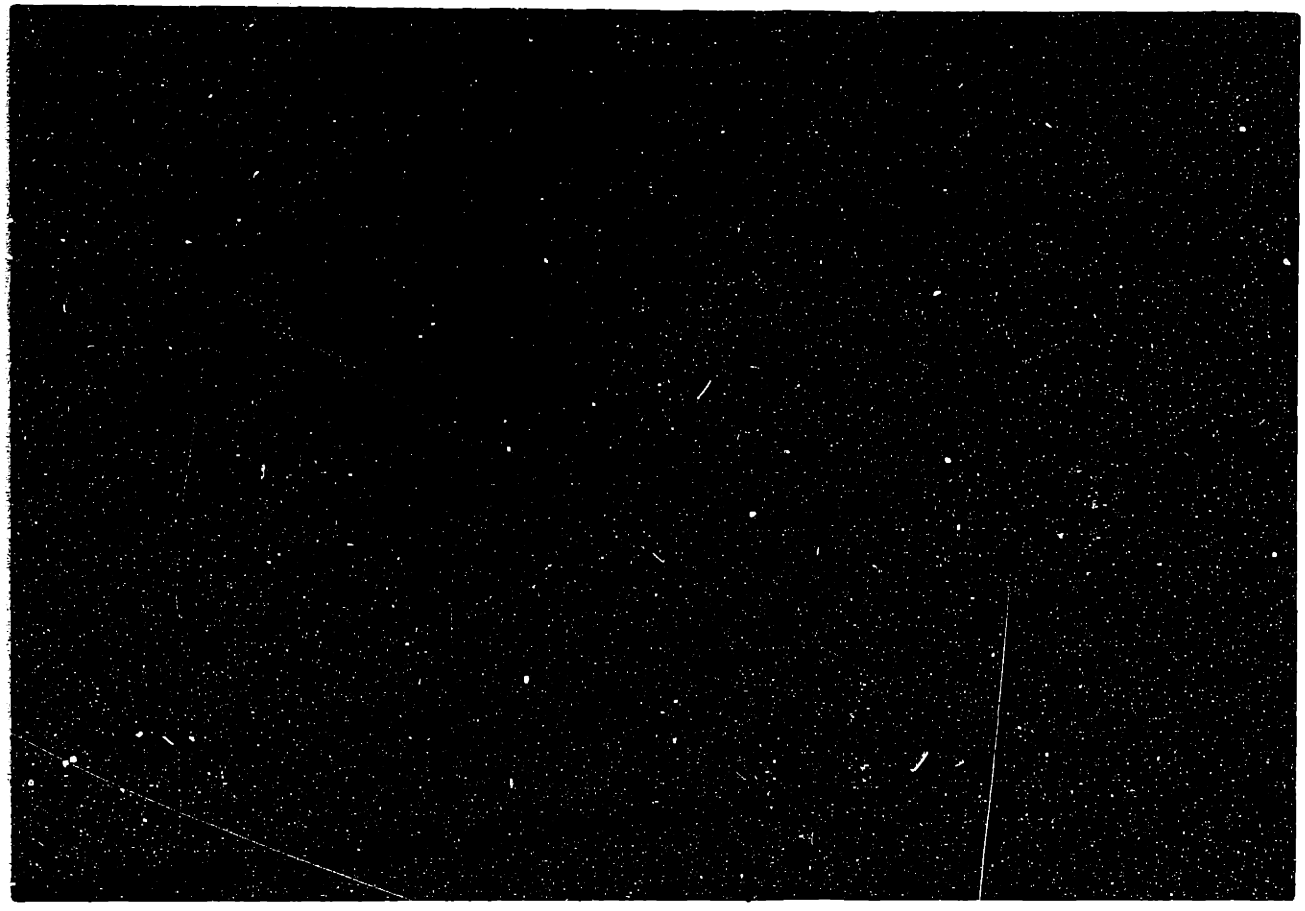

approx. mag. x10

Fig. A.6
Airless Sprayer: No-flake Paint - 50kV

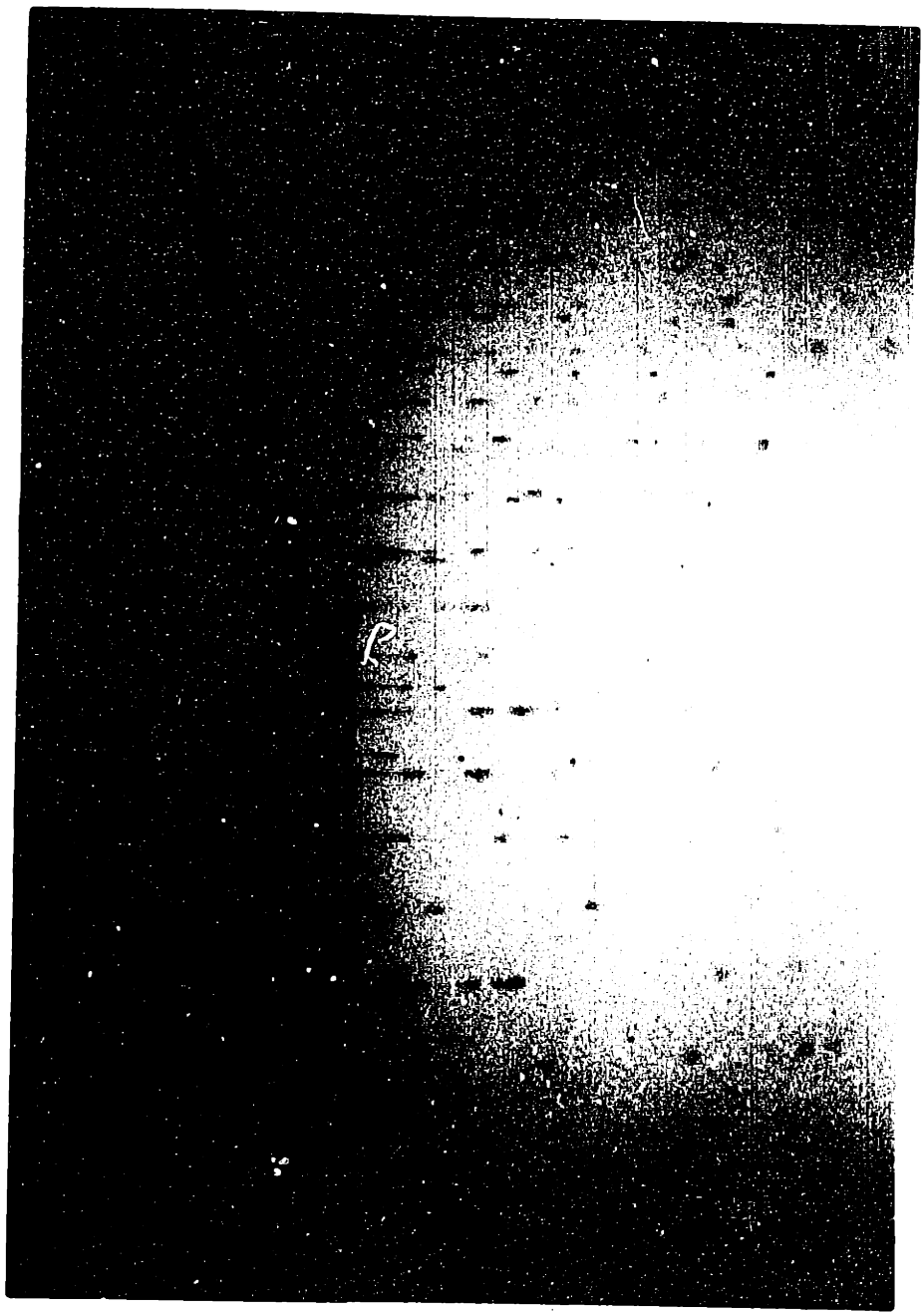

approx. mag. x10

Fig. A.7
Airless Sprayer: No-flake Paint - 70kV

sprayer and the target and appeared to have a large effect on the field around the sprayer and the current to the target. They seemed to occur as the paint built up on the lower edge of the device. This paint is then affected by heat from the lights and becomes more elastic so that the electric forces can stretch it between the sprayer and the target. To test this hypothesis the experiment was repeated ensuring the buildup did not occur. This is accomplished by carefully cleaning the edge and considering the jet before these filaments developed. The results are

$V = 50kV \quad I = 0.12\mu A$

$V = 70kV \quad I = 0.22\mu A \qquad \lambda \simeq 1mm$

$V = 70kV \quad I = 12\text{-}16\mu A \qquad \lambda \simeq 4mm$

where λ is the spacing between the jets. The existence of two regimes at 70kV was evident. The higher current regime was only found to occur after the sprayer had been running for several minutes. Close inspection did indicate the existence of very fine filaments although it was difficult to correlate their presence with a change in the regime of operation. The reason for the existence of two regimes only while using flake paint is not clear.

The data presented above can be used to calculate some of the more important parameters that describe the process. There are three positions in the paint that are considered.

Position one is taken shortly after the paint is emitted from the slit between the rod and the sprayer base, before the individual jets are formed. Position two is in the jet base far enough away from the rod so the jet is axially symmetric. The third position is at the point of jet breakup. These positions are shown in Fig. A.8.

At position one the processes of interest are the viscous drag on the fluid and the electrical surface stress. If the viscous diffusion time, τ_{vd}, is substantially less than the transit time, τ_t, of the fluid over the rod the fluid flow is approximated as fully developed with a linear profile. The viscous diffusion time is

$$\tau_{vd} = \frac{\rho\delta^2}{\eta} \qquad (A.1)$$

The mass density, ρ, and the viscosity, η, for flake and no-flake are similar and approximately $950kg/m^3$ and $0.3nt/m\text{-}s$ respectively. From the pictures of the device in operation the thickness of the film, δ, is estimated to be

$$\delta \simeq 1.7 \times 10^{-4}m \qquad \delta \simeq 2.5 \times 10^{-4}m$$

Therefore,

$$\tau_{vd} \simeq 9.1 \times 10^{-5}secs \qquad \tau_{vd} \simeq 2.0 \times 10^{-4}secs$$

Throughout this section the data from the paint sprayer at the lower potential, 50kV, is used. At this potential the

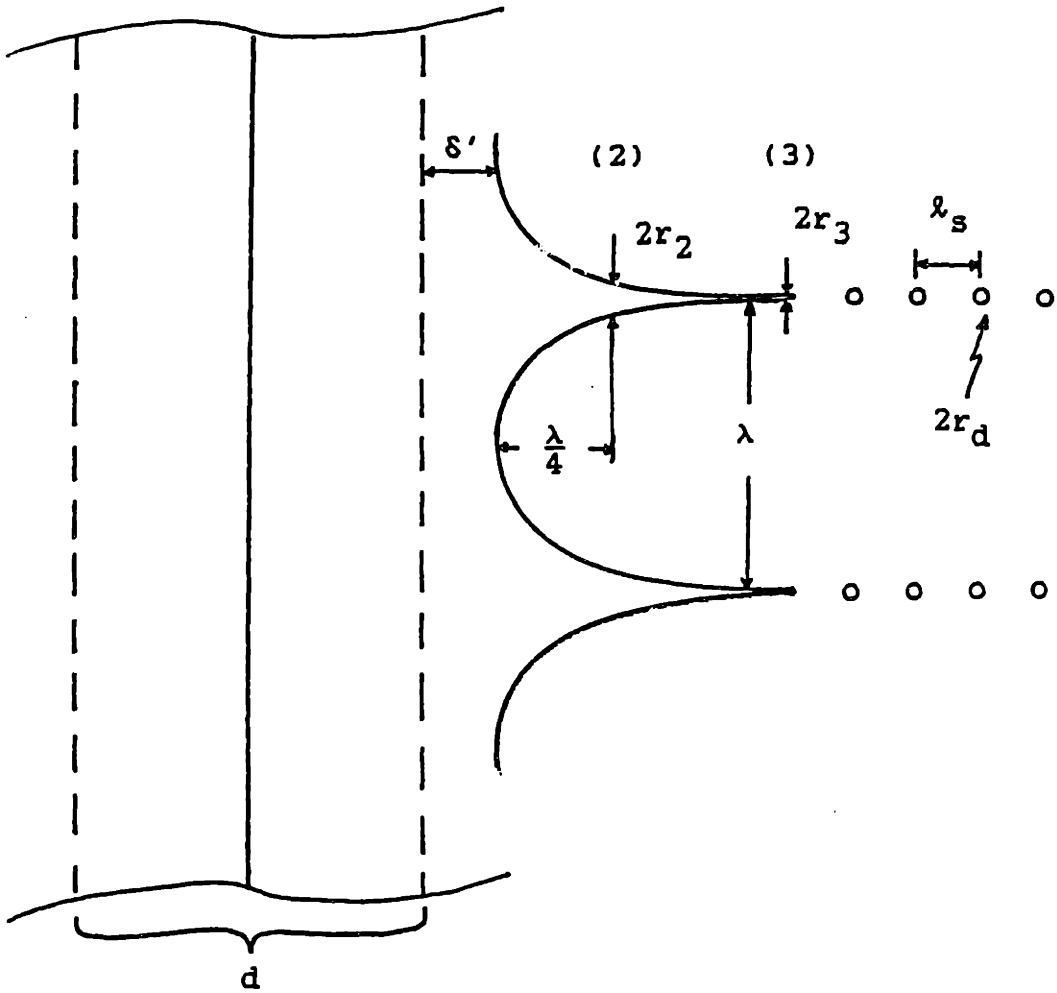

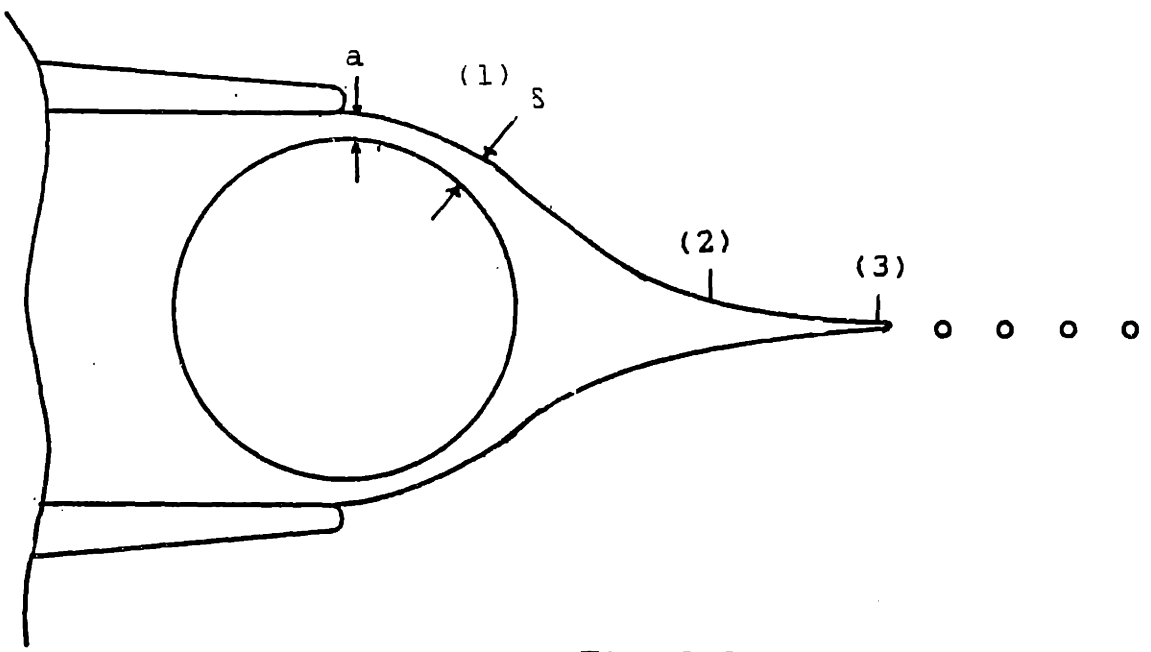

Fig. A.8
Sketch of Jet Formation

regimes of operation of the device using flake and no-flake paint are similar and it is reasonable to compare the results. The number on the left is for flake paint while the number on the right is for no-flake paint. This convention will be maintained. The average velocity of fluid flow can be calculated from the volume flow.

$$v_l = \frac{Q}{\delta L} \tag{A.2}$$

where

$$Q = 2.1 \times 10^{-8} m^3/sec \qquad Q = 6.6 \times 10^{-8} m^3/sec$$

and L is the edge length of the device, $2.5 \times 10^{-2} m$. Therefore,

$$v_l \simeq 4.9 \times 10^{-3} m \qquad v_l \simeq 1.1 \times 10^{-2} m$$

Basing the transit time on one quarter of the rod diameter, $\ell = 2.3 \times 10^{-4} m$, gives

$$\tau_t \simeq 4.7 \times 10^{-2} secs \qquad \tau_t \simeq 2.1 \times 10^{-2} secs$$

If the ratio of the viscous diffusion time to the transit time, the Reynolds number, R, is less than one, the flow is approximated as fully developed.

$$R \simeq 1.9 \times 10^{-3} \qquad R \simeq 9.5 \times 10^{-3}$$

These numbers are significantly less than one indicating

that viscous diffusion is complete. Therefore, the surface stress, assuming a Newtonian fluid and a linear velocity profile, is

$$T_s = \eta \frac{v_1}{\delta} \tag{A.3}$$

or using Eqn. A.2

$$T_s = \eta \frac{Q}{\delta^2 L} \tag{A.4}$$

Using the numerical values above

$T_s \simeq 8.7 nt/m^2$ $\qquad$ $T_s \simeq 12.7 nt/m^2$

The charge relaxation time is

$\tau_e \simeq 6.2 \times 10^{-5} secs$ $\qquad$ $\tau_e \simeq 6.3 \times 10^{-5} secs$

The ratio of the charge relaxation time to the transit time, the electric Reynolds number, R_e, provides a measure of the influence the fluid flow has on the electric field [2].

$R_e \simeq 1.3 \times 10^{-3} secs$ $\qquad$ $R_e \simeq 3.0 \times 10^{-3} secs$

Because these numbers are significantly less than one the rate of fluid motion (by contrast with the shape of the interface) has little effect on the electric charge. Charge conservation applied at the paint and air interface shows fields inside the paint are entirely tangential to the surface. Therefore, the electrical surface stress is

calculated knowing the fields external to the paint. The electrical surface stress is

$$T_s = \varepsilon_o E_n E_t \tag{A.5}$$

where E_n is the electric field normal to the paint interface and E_t is the electric field tangential to the paint interface. The total electric field, E, is

$$E^2 = E_n^{\,2} + E_t^{\,2} \tag{A.6}$$

Solving E_n using Eqns. A.5 and A.6 gives

$$E_n^2 = \frac{E^2 + \left(E^4 - 4 \left(\frac{T_s}{\varepsilon_o} \right)^2 \right)^{\frac{1}{2}}}{2} \tag{A.7}$$

Assuming a maximum field at the surface of $E = 3 \times 10^6$ V/m, the breakdown field strength in air, and using the surface stress calculated above (Eqn. A.4) the fields are

$E_n \simeq 3.0 \times 10^6$ V/m $\qquad$ $E_n \simeq 3.0 \times 10^6$ V/m

$E_t \simeq 3.3 \times 10^5$ V/m $\qquad$ $E_t \simeq 4.8 \times 10^5$ V/m

Therefore, reasonable field strengths can support the surface stress.

Position two is chosen to be one quarter of the jet spacing away from the paint film over the rod, see Fig. A.8. At position two the radius of the jet is

$r_2 \simeq 2.1 \times 10^{-4}$m $\qquad$ $r_2 \simeq 1.3 \times 10^{-4}$m

and the spacing between the jets is

$\lambda \simeq 2.0 \times 10^{-3}$m $\qquad$ $\lambda \simeq 1.4 \times 10^{-3}$m

From the flow rate and assuming the flow is uniform across the jet, the velocity of the fluid is

$$v_2 = \frac{Q\lambda}{\pi r_2^2 L} \tag{A.8}$$

Therefore,

$v_2 \simeq 1.2 \times 10^{-2}$m/s $\qquad$ $v_2 \simeq 7.0 \times 10^{-2}$m/s

The viscous diffusion time based on the radius of the jet is

$\tau_{vd} \simeq 1.4 \times 10^{-4}$secs $\qquad$ $\tau_{vd} \simeq 5.3 \times 10^{-5}$secs

Using the radius of the jet to calculate the transit time the Reynolds number is

$R \simeq 8.0 \times 10^{-3}$ $\qquad$ $R \simeq 1.9 \times 10^{-3}$

As these numbers are significantly less than one the original assumption of a uniform velocity profile across the jet is reasonable. The electric Reynolds number, based on the radius of the jet, is

$R_e \simeq 3.5 \times 10^{-3}$ $\qquad$ $R_e \simeq 3.4 \times 10^{-2}$

Therefore, the electric fields are accurately calculated

independent of the fluid motion. The current in the jet can be used to calculate the tangential electric field.

$$E_t = \frac{I\lambda}{\pi r_2^2 \sigma L} \tag{A.9}$$

where I is the total current and σ is the paint conductivity. The conductivity of the paint is

$$\sigma = 1.2 \times 10^{-6}(\Omega\text{-m})^{-1} \qquad \sigma = 1.0 \times 10^{-6}(\Omega\text{-m})^{-1}$$

The current obtained using flake paint is taken as the lower of the two values measured under the assumption that the higher current represents conduction in filaments and, as discussed previously, this is not the intended mode of operation. The tangential electric field is

$$E_t \simeq 6.0 \times 10^4 \text{V/m} \qquad E_t \simeq 2.8 \times 10^5 \text{V/m}$$

The critical radius, r_c, might be taken as that at which the conduction current is equal to the convection current. This is then the point where the stabilizing tangential electric field is reduced, allowing the jet to break into drops under capillary forces. This development is shown in Section 3.1.1 and the result is repeated here for clarity.

$$r_c^3 = \frac{2Q\varepsilon_o}{\pi\sigma} \tag{A.10}$$

Therefore, the radius of the jet at breakup, position three, is estimated to be

$r_c \simeq 2.1 \times 10^{-5}$m $\qquad$ $r_c \simeq 2.6 \times 10^{-5}$m

Position three is taken as the point immediately before the jet breaks into drops. From the pictures, Figs. A.4 and A.6, the jet radius at position three is

$r_3 \simeq 8.3 \times 10^{-6}$m $\qquad$ $r_3 \simeq 12 \times 10^{-6}$m

This is a factor of 2-3 less than predicted by Eqn. A.10. Using Eqn. A.8, evaluated at position 3, the fluid velocity is

$v_3 \simeq 8.2$m/s $\qquad$ $v_3 \simeq 8.8$m/s

Eqn. A.1 is used to calculate the viscous diffusion time based on the jet radius

$\tau_{vd} \simeq 2.2 \times 10^{-7}$secs $\qquad$ $\tau_{vd} \simeq 4.6 \times 10^{-7}$ secs

The transit time, again based on the jet radius, is used to calculate the Reynolds number

$R \simeq 0.22$ $\qquad$ $R \simeq 0.33$

Based as it is on the jet radius, this number indicates that the electrical shear stress at the jet surface is essentially in equilibrium with the volume. However, inertia plays a role for dimensions typical of the longitudinal direction. This length is taken as the wavelength of the instability that is approximated in Eqn. 3.7 to be 2.2 times

the jet radius. The photographes of the jet indicate this wavelength is actually much longer, maybe as much as an order of magnitude. Evaluation of the Reynolds number using this dimension results in a number significantly larger than one.

The electric Reynolds number is expected to be large as the assumption that the conduction and convection current are approximately equal (used to calculate r_c, Eqn. A.10) implies. The electric Reynolds number is

$$R_e \simeq 61 \qquad\qquad R_e \simeq 46$$

As expected these numbers are significantly larger than one. The increase in convection current is a result of the high velocity of the fluid not an increase in the surface charge. The surface charge is not expected to vary greatly because of the high conductivity of the paint and because the surface charge is limited by the breakdown electric field strength in air. This value has approximately been reached upstream. The surface charge, σ_s, on the jet now accounts for the majority of the current flow. Assuming all the current is due to convection

$$\sigma_s \simeq \frac{I\lambda}{2\pi r_3 v_3 L} \tag{A.11}$$

Therefore,

$$\sigma_s \simeq 2.4 \times 10^{-5} C/m^2 \qquad \sigma_s \simeq 2.4 \times 10^{-5} C/m$$

This surface charge is the source of the normal electric field.

$$\sigma_s \simeq \varepsilon_o E_n$$

Therefore, the normal electric field is

$$E_n \simeq 2.7 \times 10^{6} V/m$$

This field strength is approximately the breakdown electric field strength in air.

Once the stabilizing tangential electric field is small, capillary forces cause the jet to break into drops. Analysis of the jet instability has shown that the drop size after breakup is approximately twice the jet radius before breakup (see Section 3.1.1, Eqn. 3.7). Therefore, the drop size is

$$r_d \simeq 16.7 \times 10^{-6} m \qquad r_d \simeq 24 \times 10^{-6} m$$

The spacing between the drops, ℓ_s, is estimated from the pictures of drop breakup

$$\ell_s \simeq 1.0 \times 10^{-4} m \qquad \ell_s \simeq 1.4 \times 10^{-4} m$$

The charge on a drop is

$$q_d = \frac{I \ell_s \lambda}{v_d L} \tag{A.12}$$

The velocity of the drop, v_d, is estimated as the jet velocity before breakup. Therefore,

$$q_d \simeq 1.2 \times 10^{-13} C \qquad\qquad q_d \simeq 2.4 \times 10^{-13} C$$

These values are significantly below the Rayleigh limit for drops of this radius.

Assuming the drop motion is viscous limited and the drag is predicted by Stoke's drag, the velocity of a drop is

$$v_d = \frac{q_d}{6\pi\eta_{air} r_d} E$$

$$\text{or } E = \frac{v_d 6\pi\eta_{air} r_d}{q_d} \qquad \text{(A.13)}$$

Eqn. A.13 can be used to calculate the tangential electric field at jet breakup.

$$E \simeq 4 \times 10^5 V/m \qquad\qquad E \simeq 3 \times 10^5 V/m$$

This field can be used to evaluate the conduction current in the jet immediately before breakup.

$$I_c = \sigma E \pi r_3^2 \qquad \text{(A.14)}$$

Therefore,

$$I_c \simeq 1.0 \times 10^{-10} A \qquad\qquad I_c \simeq 1.4 \times 10^{-10} A$$

This current is insignificant compared to the total current as was assumed in the calculation of the surface charge on

the jet before breakup.

A.3 Implications of the Experimental Results

The jets formed by the sprayer have the shape of accelerated current driven jets [3]. The surface stress on the fluid as it flows around the rod can possibly be accounted for by an electric stress if electric field strengths on the order of the breakdown field strength in air are assumed. The high conductivity of the paint makes it unlikely that the tangential field required to apply this stress actually exists. This field (calculated in the previous section) would require a current in the paint layer (ignoring current through the conducting rod) of 0.8μA for flake paint and 0.9μA for no-flake paint. These currents are higher than the total current measured. The viscoelastic nature of the paint, demonstrated in Chapter 5, may account for a redistribution of forces exerted on the paint. Elastic forces can efficiently transmit a force exerted downstream to a portion of the fluid upstream, literally pulling the fluid out of the slit. A component of the force accounting for the paint flow around the rod may actually be transmitted from downstream by an elastic force.

The surface stress calculated from the paint flow in the previous section is less for flake paint than no-flake

paint. This is not consistent with the electric stress applied to the jets. The low electric Reynolds number of the flow (except near jet breakup, position 3) indicates that the rate of fluid flow does not effect the electric field. However, the geometry of the jets has a large influence on the electric field. The jet spacing is greater for flake paint than for no-flake paint. A greater jet spacing implies less electrical shielding between neighboring jets and, therefore, an increase in the electric field. The electric field near a given jet and the electric stress applied is greater for flake paint than no-flake paint. This would be consistent with an increase in the apparent viscosity of the flake paint, likely a result of the flake size being of the same order as the size of the slit. Therefore, a higher stress would have been calculated from the flow of the flake paint.

Another factor influencing the electric stress may be a change in the electrical properties of the flake paint as it is flows through the slit. This could occur as the flakes align themselves parallel to the flow to fit through the slit. Alignment of the flakes would result in a reduction of the electrical stress as the tangential electric field is reduced by the increased electrical conductivity. This tends to counter the effects of the higher electric field strength discussed above.

These may be the mechanisms accounting for the jet configurations obtained at higher potentials. The higher electrical stress exerted on the no-flake paint results in a shorter jet spacing that both decreases the electric field (and the electric stress) and increases the fluid forces (viscoelastic, inertial, and surface tension). As the applied potential is increased the electric stress can no longer be balanced by a stable jet regime resulting in the sporadic formation of jets as the fluid forces respond to balance the stress. A combination of increased electrical conductivity and increased viscosity may allow the stable spraying regime for flake paint to exist at higher applied potentials.

The preliminary data on this sprayer provides direction for further research. Many of the assumption made in discussing this sprayer can be tested by varying the paint parameters. For example, can the same characteristics as obtained with flake paint be obtained using a homogeneous fluid (no flakes) that is more viscous and more conducting than no-flake paint? An investigation of this type will also provide more details on the sensitivity of the device to paint parameters. This would have a direct impact on the industrial feasibility of the device.

A.4 Industrial Feasibility

The feasibility of the device using the cylindrical rod at the atomization surface is evaluated by comparing its operation to the Ransburg Turbobell. To date only basic parameters are compared. A more extensive testing is required to more thoroughly evaluate the device's usefulness. As mentioned in the preceding section, future emphasis should be placed on the device's sensitivity to paint parameters. Presently, the rate of mass transfer, the drop size, and the ability to paint a test sample are used to provide an estimate on the device's feasibility.

Operation of the Ransburg Turbobell is done at flow rates between 100ml/min and 300ml/min. The standard flow rate used throughout the project was 100ml/min. The paint density, after dilution with xylene for spraying, is 928kg/m^3. Therefore, the mass delivery rate is 92.8g/min. However, 60 percent of this mass is solvent and eventually evaporates. Therefore, the solids mass delivery rate is reduced to 37.1g/min. The total length of the bell edge is 23.3cm. Normalizing the mass delivery rate of solids to the edge length gives a mass flow rate, F, of 1.6g/min-cm.

The airless sprayer operating at 1.2psi delivers 0.94g of solids (after evaporation) in one minute. The device has an effective edge length of 2.5cm. The normalized mass delivery for the airless sprayer is 0.38g/min-cm. The mass

flow rate per unit edge length for the airless sprayer is less than the Ransburg Turbobell by a factor of 4.2. This is a reasonable range as the Turbobell has a very high solids flow rate (indicated in Chapter 2 by comparing its flow rate with the Bink's air sprayer). The lower solvent concentration of the paint used in the airless sprayer has the added advantage of reducing the solvent lost to the surrounding environment.

At standard operating parameters, the average drop radius from the Ransburg sprayer is approximately 9.5μm. Drops from the airless sprayer appear to be very monodisperse with a drop radius of approximately 8-12μm. The edges of the new sprayer do create practical problems. Corona emission at the edges cause a distortion of the spray pattern. The existence of fine continuous filaments also occasionally distort the spray pattern but more significantly they deposit globs of paint, often ruining the paint finish. Careful design of the device should eliminate these problems.

Several test samples were painted with the airless sprayer. Care was taken to avoid the formation of ligaments and corona emission from the edges. Still the occasional glob of paint did mar the final finish. The spray is confined to an area approximately having a width equal to

the diameter of the conducting rod and a height equal to the length of the sprayer. The sprayer was taken to high voltage using the Ransburg power supply and isolation structure. Therefore, the sprayer was immovable, necessitating moving the paint target relative to the sprayer. The paint booth, Fig. 2.1, was not equipped to move the target vertically as well as horizontally. The final paint finish does reflect this lack of geometrical freedom. However, this mainly reflects the restrictive nature of the apparatus and not necessarily the ability of the device. Regardless, the paint finish was of reasonable quality.

The techniques developed in Chapter 4 can be used to further characterize the device. The results may provide further insight into the feasibility and the physical processes of the device.

References

[1] Trichel, G.W., Phys. Rev. 54 1078-84, 1983

[2] Melcher, J.R., Continuum Electromechanics , MIT Press, Cambridge, 1981

[3] Melcher, J.R. and Warren, E.P., "Electrohydrodynamics of a current-carrying semi-insulating jet", J. Fluid Mech., 47, 1971

Appendix B

Computer Simulation of Drop Flight

There are two approaches for simulating the electrostatic paint sprayer considered. The objective in both is to obtain a detailed prediction of the paint drops as they travel from the atomization region to the paint surface. The first approach uses a state formulation to predict the trajectory of a single drop. This simulation uses empirical as well as theoretical models. This formulation has the advantage of simplicity and it has been developed into a usable tool. It is easily expanded as more empirical data is acquired or more theoretical models developed. The second approach is to formulate the problem using a totally theoretical model and then to examine the possible simplifications and problems of implementation. This formulation has not been completed, although enough work has been done to provide a starting point for further research.

B.1 State Space Model

The state space formulation is obtained from Newton's First Law applied to a single drop

$$\bar{F} = \frac{d(m\bar{v})}{dt} \qquad (B.1)$$

where $\bar{F}$ is the force, m is the drop mass, and $\bar{v}_d$ is the drop velocity. Taking each component of this equation in cylindrical coordinates results in

$$\frac{\partial v_r}{\partial t} = r\omega^2 - f\frac{v_r}{m} + \frac{F_r}{m} \tag{B.2}$$

$$\frac{\partial \omega}{\partial t} = \frac{F_\theta}{mr} - \frac{\omega f}{m} - \frac{2\omega v_r}{r} \tag{B.3}$$

$$\frac{\partial v_z}{\partial t} = \frac{F_z}{m} - \frac{v_z f}{m} \tag{B.4}$$

The velocities are defined from the coordinates of the drop

$$\frac{\partial r}{\partial t} = v_r \tag{B.5}$$

$$\frac{\partial \theta}{\partial t} = \omega \tag{B.6}$$

$$\frac{\partial z}{\partial t} = v_z \tag{B.7}$$

The change in drop mass is accounted for by the function f.

$$\frac{\partial m}{\partial t} = f \tag{B.8}$$

Therefore, there are seven state variables

v_r - radial velocity

ω - angular velocity

v_z - longitudinal velocity

r - radial position

θ - angular position

z - longitudinal position

m - drop mass

Note, f is a function of time and the state variables that accounts for the change in drop mass (evaporation of solvents) during the drop flight. Stepping through the solution of these equations first requires the initial state to be specified. For the Ransburg Turbobell the initial radial position is the bell radius and the initial drop velocity is completely rotational, specified by the bell speed. The initial mass is calculated from the initial drop radius, R, and the paint density, ρ.

$$m = \rho\frac{4}{3}\pi R^3 \tag{B.9}$$

The initial drop radius is obtained using experimental data from Bell-Hochberg [1]. Using these results an equation is developed relating the drop radius to the applied potential, V(volts), the bell speed, S(rpm), and the flow rate, F(ml/min).

$$R = aV^{-0.2} + bS^{-0.7} + cF^{0.4} - d \tag{B.10}$$

where $a=1.33\times10^{-3}$, $b=3.33\times10^{-2}$, $c=1.01\times10^{-5}$, and $d=2.06\times10^{-4}$. Calculation of the solvent evaporation requires the initial solvent concentration, C. This can be calculated from the mass percent of solvent, m_s, the density of the paint, and the molar mass of the solvent, M.

$$C = m_s\rho M \tag{B.11}$$

Once the initial conditions are established the components of the force are required. Two forces are considered, an electric force and the viscous drag. The electric force depends on the electric field and the charge on the drop. The charge to mass ratio, Q_m, has been found to depend on the applied potential and the paint resistivity, Res, given in Ransburg units(Rans) [1]. This relationship is approximately

$$Q_m=\left(6.6\times10^{-3}Res^{-0.21}+7.63\times10^{-12}|V|^{1.7}-3.4\times10^{-3}\right)sgn(V) \quad (B.12)$$

The electric field is estimated by modeling the bell as a sphere above an infinite ground plane. Because of cylindrical symmetry the electric field has only radial, E_r, and longitudinal, E_z, components.

$$E_r = aV\left[\left(r^2+(z+a)^2\right)^{-1.5} - \left(r^2+(2b+a-z)^2\right)^{-1.5}\right] r \quad (B.13)$$

$$E_z=aV\left[\left(r^2+(z+a)^2\right)^{-1.5}(z+a)-\left(r^2+(2b+a-z)^2\right)^{-1.5}(2b+a-z)\right] \quad (B.14)$$

where a is the radius of the bell, b is the spacing between the bell and the grounded target, and z=0 is taken at the centre of the bell. Note the effects of the charged drops (space charge) on the field are ignored. The electric force is the charge on the drop multiplied by the electric field.

$$\bar{F}_e = mQ_m\bar{E} \quad (B.15)$$

where the mass of the drop is calculated from the initial

drop radius. The drop charge does not change during flight.

The viscous force is calculated from the relative velocity between the air and drop, V_∞. The drag, F_d, is approximated as [2]

$$\bar{F}_d = \frac{\pi}{2} R^2 \rho \bar{V}_\infty C_d \qquad (B.16)$$

where $C_d = \frac{24}{R_e}$; $R_e < 1$

$= 18.5 R_e^{-0.6}$; $1 < R_e < 1000$

$= 0.44$; $R_e > 1000$

and $R_e = \frac{2RV_\infty \eta}{\rho}$

The drop velocity is given by the appropriate state variables and the air velocity is interpolated from a table of measured values. Note, these air velocity are made in the absence of the paint drops, ignoring the effects of the drops on the air flow.

The evaporation of the solvents, described by the function f, is assumed to be represented by the diffusion equation for a dilute substance. This is a large assumption because the solvent evaporation during flight is approximately 30 percent of the initial drop mass. The details of this solution are shown in Appendix C. This solution is repeated for each step in time and represents

the largest computational difficulty.

The solution for the state variables is calculated by making a step in time, Δt, calculating the change in the state variables using Eqns. B.2 - B.8 (Euler's Method), adding these changes to the present value of the state variables, and then repeating the procedure until the drop reaches the paint surface. The solution is stable only for small step sizes. However, this instability occurs at the bell tip where the drop velocity is the largest. The step size is varied with the inverse square of the drop velocity allowing the small step size required initially and a larger step size as the velocity decreases. This maintains the stability of the program and gains substantial savings in execution time. Two other methods for solution of the differential equations were tried, fourth order Runga-Kutta and the Bulirsh-Stuer implementation of a Richardson technique. Neither technique seemed to be as efficient as Euler's method with a varying step size. All techniques did converge to the same result. A predictor-corrector technique will allow an accurate evaluation of the error at each step providing a basis for changes in the step size. Although it has not been tested, this is a more rigorous approach than the adhoc square law presently used and possibly may be computationally more efficient.

The program is written in a block form making it simple to change the various routines. The structure of the program is illustrated by the flow chart of the main program, Fig. B.1, and the flow chart of the subroutine force Fig. B.2. The function of each subroutine is listed in Table B.3. For example, to add a more sophisticated model for the electric field the routine ifield is replaced. Improvements to the electric field model have already been implemented at General Motors [3]. All of the routines used in the program, whether they represent empirical estimates or theoretical models, are easily updated in a similar manner without interfering with the rest of the program.

The program is used as a diagnostic tool to evaluate the effects various parameters exert on the entire process. Absolute results, for example the prediction of a specific drop trajectory, are not stressed as the model ignores or simplifies some important mechanisms. However, the trends obtained from varying parameters are useful. Improvement of the models for the space charge, electric field, air flow and solvent evaporation may extend the use of the simulation. However, no amount of improvement in the individual routines will make the simulation consistently account for the coupling of the different physical mechanisms. Calculation of the space charge is one example of this problem. To calculate the space charge contribution

Fig. B.1
Flow Chart of the Main Program

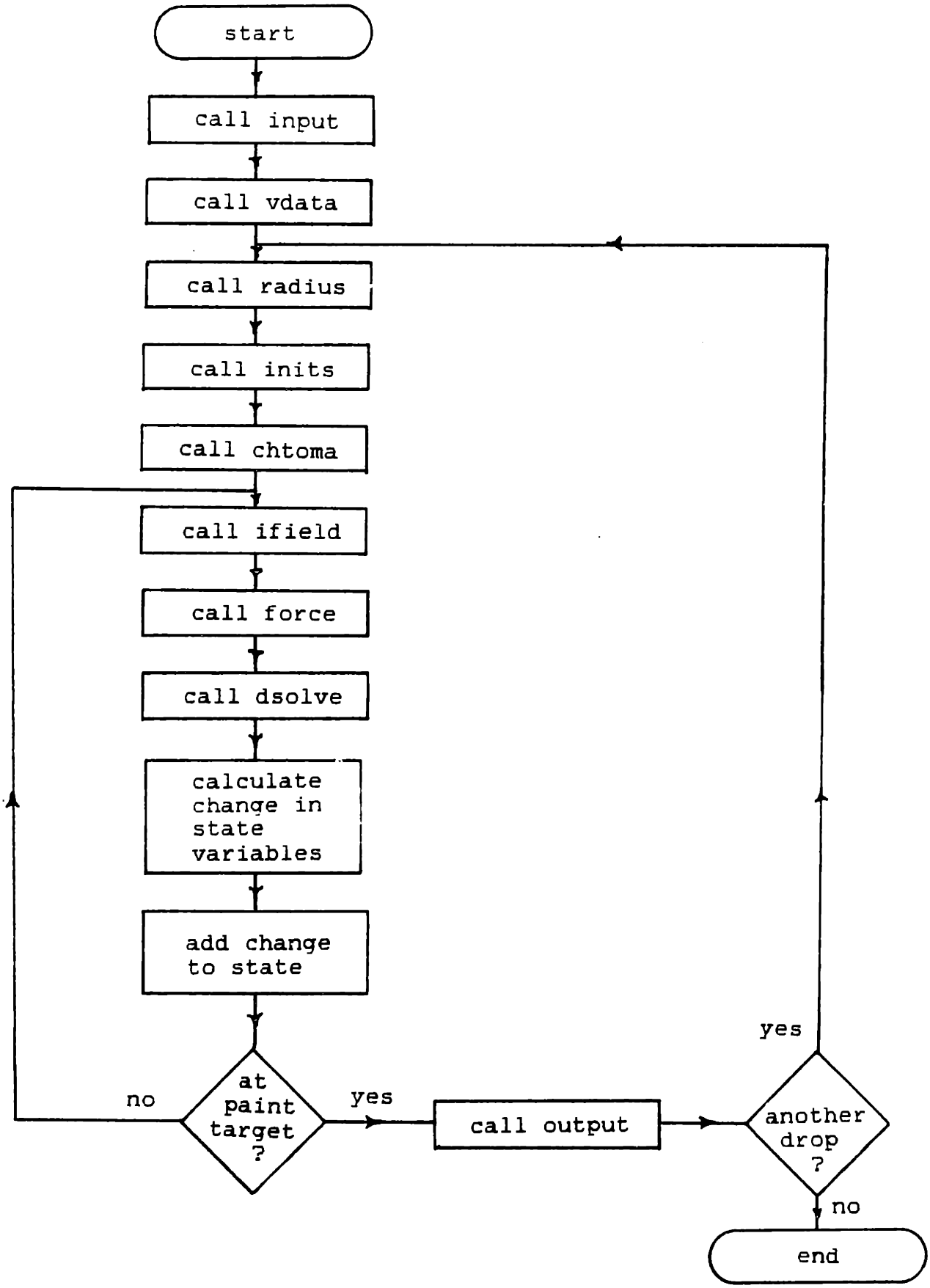

Fig. B.2
Flow Chart of the Subroutine FORCE

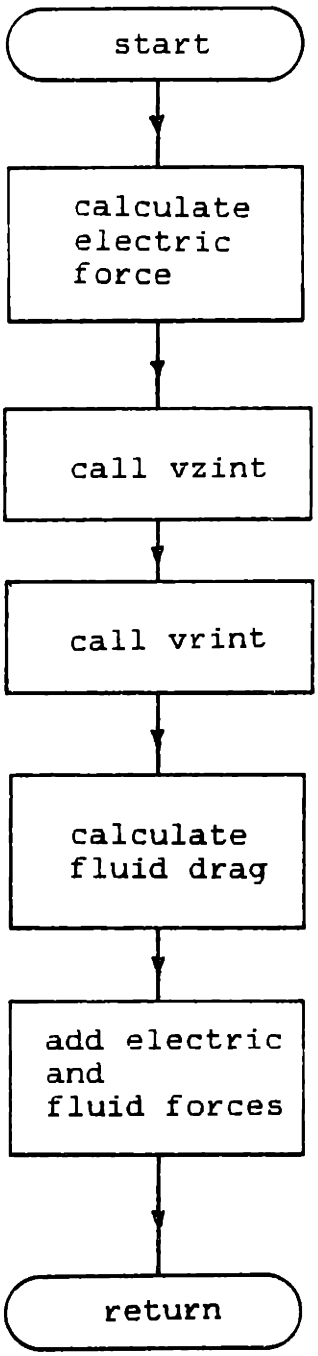

Fig. B.3
List of Subroutines

Subroutine	Function
input	handles input of all parameters
vdata	loads shaping air data
radius	calculates average drop radius
inits	calculates the initial values of the state variables
chtoma	calculates the charge to mass ratio and the charge on a drop
ifield	calculates the imposed electrical field
force	calculates the force on a drop
dsolve	calculates the solvent evaporation
vzint	interpolates the shaping air data for the longitudinal component of the air velocity
vrint	interpolates the shaping air data for the radial component of the air velocity

to the electric field requires knowledge of the drop trajectories, yet it is these trajectories that are the final solution of the simulation. This of course could be tackled iteratively but this is computationally quite difficult on a drop by drop basis because there are approximately 10^7 drops in the spray cloud. The problem is similar to predicting plasma properties based on a solution of each particle's motion [4]. As in plasma physics, a statistical viewpoint would appear to represent a more theoretically rigorous approach.

A sample run of the simulation program is shown in Fig. B.4 . The simulated drop trajectories do not accurately represent the spray cloud as observed experimentally. Fig. B.5 shows the trajectory of an average sized drop and an estimate, based on experiment, of the outer boundary of the spray cloud. The discrepancy between the two curves may be a result of the poor shaping air model and the absence of space charge effects in calculating the electric field. Throughout the development of this simulation the effect of turbulence has been ignored though the electrical shutter data in Chapter 4 shows that there is substantial mixing and indicates that a statistical distribution may be a more appropriate means of describing the process.

B.2 Continuum Model

```
*****************************************
*                                       *
*       Turbo-Bell Paint Simulator      *
*                                       *
*****************************************

This program simulates the flight of a
single paint drop to the paint surface


PRESENT OPERATING PARAMETERS ARE:

    Bell Voltage(volts) = -90000.      Distance to Target(m) =0.300

    Turbine Speed(rpm) =  28000.       Percentage Shaping Air = 20.

    Flow Rate(ml/min) = 100.0

Do you wish to change these values(n for no) ? (no)

PRESENT PROPERTIES OF PAINT

    Paint Density(kg/m3) = 870.0     Paint Resistance(Rans) =  1.00

    Initial Solvent Concentration(moles/m3) =   43.40

    Solvent Diffusion Coefficient(m2/sec) =  0.70E-07

    Diffusion Boundary Condition(m/sec) =    1.00

Do you wish to change these values ? (no)
Average drop radius =   9.61473870E-06
Do you wish to use a different drop size ? (no)
RUNNING
Do you wish to display the Operating Parameters ? (no)
Do you wish to display the Paint Properties ? (no)

    Flight Time =  0.229E+00          Charge on Drop = -0.169E-13

State Variables on Impact
    Radial Velocity =  0.841E-02
    Angular Velocity =  0.000E+00
    Longitudinal Velocity =  0.681E+00
    Drop Mass =  0.324E-11
    Radial Distance =  0.330E+00
    Angular Distance =  0.124E+01
    Longitudinal Distance =  0.300E+00

    Drop Radius =  0.778E-05
Do you wish to fly a different drop size ? (no)
```

Fig. B.4
Simulation Run

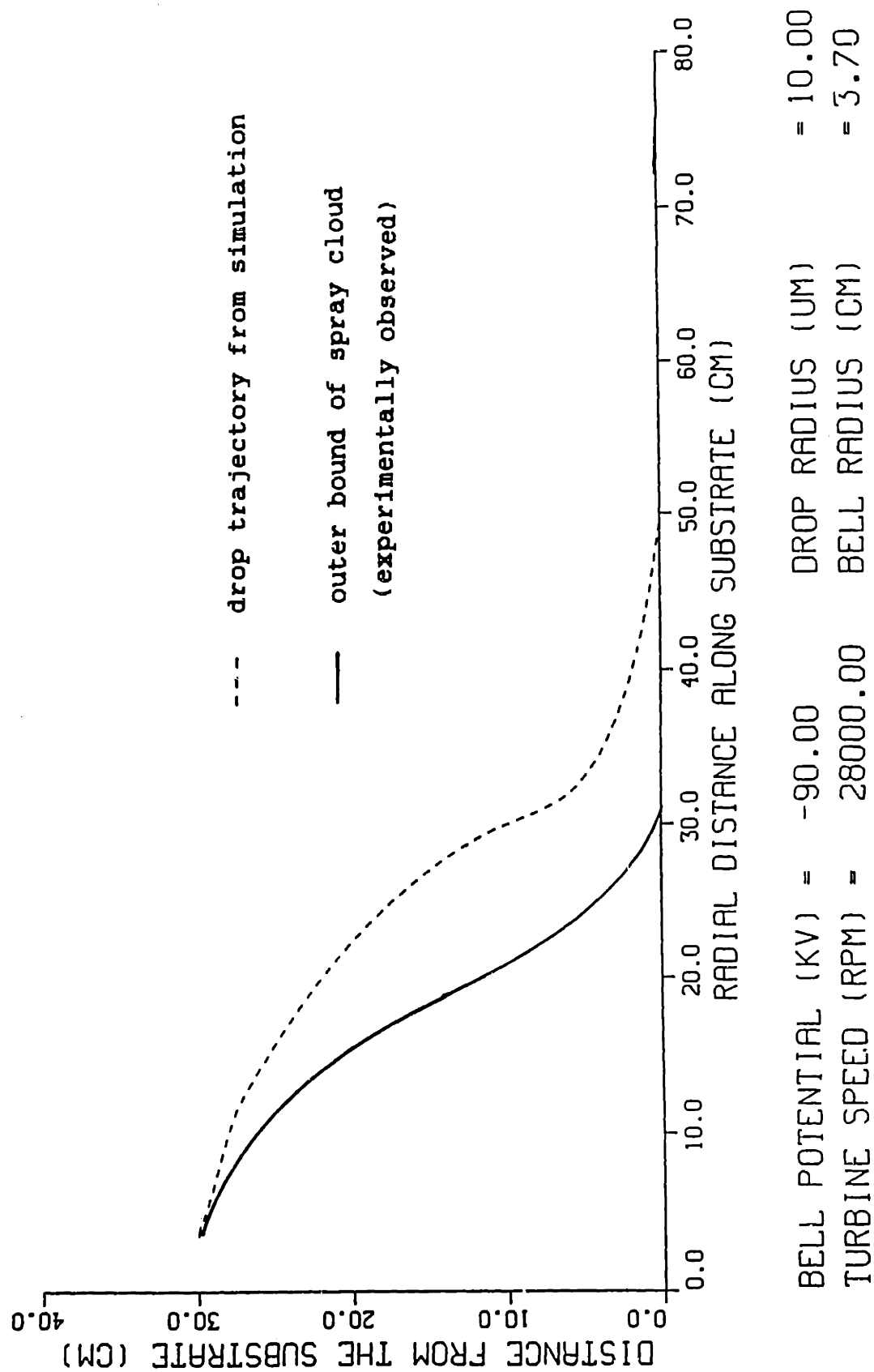

Fig. B.5
Drop Trajectory

The paint spraying process may be represented by a number distribution, n, that is a function of the spatial coordinates, $\bar{r}$, the velocity, $\bar{v}$, the drop radius, R, the charge, Q, and the drop content, specified by the density, ρ. Therefore the number of drops in a position between $\bar{r}$ and $\bar{r}+\Delta\bar{r}$, at a velocity between $\bar{v}$ and $\bar{v}+\Delta\bar{v}$, with drop radii between R and $R+\Delta R$, charge between Q and $Q+\Delta Q$, and drop content between ρ and $\rho+\Delta\rho$ is given by

$$\text{Number} = n(\bar{r},\bar{v},R,Q,\rho,t)\Delta\bar{r}\Delta\bar{v}\Delta R\Delta Q\Delta\rho \qquad (B.17)$$

The dimensions of this distribution function may be reduced if, from experimental data, the density and charge are found to relate to the drop radius. For example, the electrical shutter data indicates that the flake content is strongly related to the drop size. Assuming these relations are reasonable, Eqn. B.17 can be written as

$$\text{Number} = n(\bar{r},\bar{v},R,t)\Delta\bar{r}\Delta\bar{v}\Delta R \qquad (B.18)$$

A formulation involves the development of a set of equations defining the distribution function, n. The starting point for these types of models is often the Lagrangian description of a single drop.

$$m_d \frac{d\bar{v}_d}{dt} = \bar{F}_v + \bar{F}_e \qquad (B.19)$$

where $\bar{F}_v$ is the force due to the surrounding fluid, $\bar{F}_e$ is

the electric force, and $\bar{v}_d$ is the velocity of the drop. The electrical force is the charge on a drop, q_d, multiplied by the electric field.

$$\bar{F}_e = q_d \bar{E} \tag{B.20}$$

The force from the surrounding air is a function of the velocity of the drop and the velocity of the air, $\bar{v}_a$.

$$\bar{F}_v = g(\bar{v}_a, \bar{v}_d) \tag{B.21}$$

The equations representing the air flow and the electric field shape are required to close the model. The air flow is represented by the Navier Stoke's Equation.

$$\rho_a \left(\frac{\partial \bar{v}_a}{\partial t} + (\bar{v}_a \cdot \nabla)\bar{v}_a \right) + \nabla P = \eta \nabla^2 \bar{v}_a + \bar{F}_d \tag{B.22}$$

The external force imposed by the drops, $\bar{F}_d$, is

$$\bar{F}_d = \sum_d -\bar{F}_v \delta(\bar{r} - \bar{r}_d) \tag{B.23}$$

where δ is the Kronecker delta function and $\bar{r}_d$ is the position vector of a given drop. The electric field is defined by Gauss's Law and charge conservation.

$$\nabla \cdot \varepsilon \bar{E} = \rho_i \tag{B.24}$$

$$\frac{\partial \rho_i}{\partial t} + \nabla \cdot (\rho_i \bar{v}_d) = 0 \tag{B.25}$$

where ρ_i is the charge density (due to the drops) given by

$$\rho_i = \sum_d q_d \delta(\bar{r}-\bar{r}_d) \qquad (B.26)$$

Eqns. B.19 - B.26 may be used in a transformation described by Jazwinski [5] to obtain a set of equations describing the evolution of the distribution function n. The effects of turbulence may be incorporated into this formulation as shown by Radun [6] . Missing from this description of the process is an equation representing diffusion of the solvents.

The formulation of this model has not been developed beyond this preliminary stage. It is included only to provide a starting point for further work. One problem that has been identified is associated with the transformation commonly used. It appears to require that the process be linear. This process is not linear though a more general transformation or simplifications of the equations, approximating them as linear, may be possible. The advantage of this type of formulation is to provide a rigorous theoretical formulation for the evolution of the drop distribution, n. Results from the solution of this model would be in a statistical form similar to the electrical shutter data presented in Chapter 4.

References

[1] Bell, G.C. and Hochberg, J., "Mechanics of electrostatic atomization, transport, and deposition of coatings", Seventh International Conference in Organic Science and Technology, Proc. of, Athens, Greece, 1981

[2] Bachelor, G.K., An Introduction to Fluid Dynamics , Cambridge University Press, Cambridge, 1967

[3] Alaa, E.,Gerneral Motors Research Laboratories (Electrical Engineering), Private Communication, 1986

[4] Molvig, K., MIT Course Notes(6.651J), 1982

[5] Jazwinski, A.H., Stochastic Processes and Filtering Theory , Academic Press, 1970.

[6] Radun, A.V., PhD. Thesis, MIT, 1981.

Appendix C

Solvent Diffusion in a Paint Drop

A rigorous approach to the diffusion of solvents in the paint involves the consideration of a multitude of constituents. In order to introduce the basic physics it is assumed two constituents are dominant. These materials need not be actual materials but may represent an accumulation or average of many. Regardless of the specifics, one constituent may leave the drop, the solvent, while the other, the paint resin, defines the drop as a coherent mass through which the solvent can diffuse. Cellular convection due to the drops relative velocity to the surrounding air is ignored as is the diffusion velocity of the solvent. The solvent diffusion outside the drop is assumed perfect. This is partially justified because of the large diffusion coefficient in air, likely several orders of magnitude greater than that in paint, and the role of turbulent diffusion in the air flow around the drop. The world external to the drop is represented as a boundary condition.

All of these assumptions are vulnerable to criticism. The mass lost during a drop flight can be 30 percent of the drop's initial mass. This immediately places doubt on the assumption of zero diffusion velocity in the drop and the ability of the air surrounding the drop to transport the

solvents away from the drop such that internal diffusion is dominant. As the solvents evaporate from the drop the diffusion coefficient is assumed constant even though it is felt that the properties of the mixture are changing dramatically. However, this model does fit the general approach of the simulation in that it provides an estimate of evaporation based on a theoretical model which is easily modified when more detail is developed.

Under the above assumptions the diffusion equation is

$$\frac{\partial C}{\partial t} = D \nabla^2 C \qquad (C.1)$$

where C is the solvent concentration and D is the diffusion coefficient. Assuming spherical symmetry, only spatial derivatives with respect to radius are significant. In spherical coordinates the equation is

$$\frac{\partial C}{\partial t} = \frac{D}{r^2} \frac{\partial}{\partial r} \left(r^2 \frac{\partial C}{\partial r} \right) \qquad (C.2)$$

The initial concentration is constant and specified as C_o. The boundary condition at the drop radius, r=R, is

$$D \frac{\partial C}{\partial r} = -FC \qquad (C.3)$$

where F represents the surface constraint. Let U=Cr, then Eqn. C.2 becomes

$$\frac{\partial U}{\partial t} = D \frac{\partial^2 U}{\partial r^2} \qquad (C.4)$$

and the boundary condition is

$$\frac{\partial U}{\partial r}\Big|_R = \frac{-F}{D} U \Big|_R + \frac{U}{r}\Big|_R \qquad (C.5)$$

while the initial condition is

$$U\Big|_{t=0} = C_o r \qquad (C.6)$$

Assuming

$$U = T(t)Y(r) \qquad (C.7)$$

Eqn. C.4 is

$$\frac{1}{TD}\frac{dT}{dt} = \frac{1}{Y}\frac{d^2Y}{dr^2} \qquad (C.8)$$

Since the left hand side of Eqn C.8 is a function of time only and the right hand side is a function of radial position only, it must equal a constant.

$$\frac{1}{TD}\frac{dT}{dt} = \frac{1}{Y}\frac{d^2Y}{dr^2} = -\lambda^2 \qquad (C.9)$$

Therefore

$$\frac{dT}{dt} + \lambda^2 DT = 0 \qquad (C.10)$$

$$\frac{d^2Y}{dr^2} + \lambda^2 Y = 0 \qquad (C.11)$$

Solving Eqns. C.10 and C.11

$$T = e^{-\lambda^2 Dt} \qquad (C.12)$$

$$Y = A\cos(\lambda r) + B\sin(\lambda r) \qquad (C.13)$$

Using Eqn. C.7

$$U = \left(A \cos(\lambda r) + B \sin(\lambda r) \right) e^{-\lambda^2 Dt} \qquad (C.14)$$

The initial condition, Eqn. C.6, gives

$$C_o r = A \cos(\lambda r) + B \sin(\lambda r) \qquad (C.15)$$

The left hand side is zero at r=0, therefore, A=0. The boundary condition, Eqn. C.5, gives

$$B\lambda \cos(\lambda R) = \frac{BF}{D} \sin(\lambda R) + \frac{B}{R} \sin(\lambda R)$$

Simplifying

$$\lambda \operatorname{cotan}(\lambda R) = \left(\frac{1}{R} - \frac{F}{D} \right) \qquad (C.16)$$

Eqn. C.16 has an infinite number of solutions for λ indicating that many modes can exist to satisfy the initial condition. The solutions to Eqn. C.16 are the eigen frequencies, λ_n. Therefore, Eqn C.15 becomes

$$C_o = \sum_{n=1}^{\infty} B_n \sin(\lambda_n r) \qquad (C.17)$$

The orthogonality of modes

$$\int_0^R U_m U_n \, dr = 0 \text{ provided } m \neq n \qquad (C.18)$$

shows Eqn. C.17 can be manipulated to give

$$\int_0^R B_n \sin^2(\lambda_n r) \, dr = \int_0^R C_o r \sin(\lambda_n r) \, dr \qquad (C.19)$$

Solving for B_n

$$B_n = C_o \left[\frac{\frac{1}{\lambda_n^2} \sin(\lambda_n R) - \frac{R}{\lambda_n} \cos(\lambda_n R)}{\frac{R}{2} - \frac{\sin(2\lambda_n R)}{4\lambda_n}} \right] \qquad (C.20)$$

Therefore, using Eqns C.14 and C.20

$$C = \frac{1}{r} \sum_{n=1}^{\infty} \left(B_n \sin(\lambda_n r) \right) e^{-\lambda_n^2 Dt} \qquad (C.21)$$

Primary interest is in the change in the radius

$$\frac{dR}{dt} = \frac{MD}{\rho} \frac{\partial C}{\partial r} \Big|_R \qquad (C.22)$$

where M is the molar mass of solvent(kg/mole), ρ is the density of solvent(kg/m^3), and C is the concentration($mole/m^3$). Eqn. C.22 can now be used to predict the change in radius for a small change in time, Δt. The solution thus far has assumed the radius is fixed and the concentration is a constant. However, the solution developed above can be used for the more general problem of the drop radius decreasing as the solvents evaporate. Using Eqn C.21 the concentration at the end of an interval in time, Δt, can be evaluated. Eqn. C.22 is used to calculate a change in radius, ΔR. The new radius and concentration are then used to solve the problem using the same method. This procedure is then interated. The solution for B_n, Eqn. C.20, is only valid for the initial constant concentration but is easily

modified for the more general case.

$$B_n = \frac{\int_0^R \left\{ \sum_{n=1}^{\infty} B_n' \sin(\lambda_n' r)\, e^{-\lambda_n'^2 D t'} \right\} \sin(\lambda_n r)\, dr}{\frac{R}{2} - \frac{\sin(2\lambda_n R)}{4\lambda_n}} \qquad (C.23)$$

where B_n', λ_n', t' correspond to previous step and B_n, λ_n, R correspond to present step. At each step the volume of solvent, ΔV, lost can be calculated

$$\Delta V = \frac{4}{3}\pi \left(R'^3 - R^3 \right) \qquad (C.24)$$

or the change in mass, Δm, is

$$\Delta m = \rho\, \Delta V$$

The routine "dsolve" does these calculations in the simulation model for each step in time until the drop impacts the surface or the change in drop radius in a step of time, Δt, becomes insignificant. The simulation requires the input of the diffusion coefficient, D, the boundary condition, F, and the initial concentration, C_o. The molar mass and the density of the solvent are internally set to represent Xylene.

Appendix D

Drop Height versus Drop Diameter

The mass percent of aluminum can only be obtained from the discrete drop data if the mass of paint solids in each splattered drop is known. The density of paint solids is known, therefore, it is the volume of drop solids that is required. The profile of the drop is dependent on the radius. A relationship between the drop diameter and the average drop height is generated.

A Dektac surface analyzer, normally used for measuring the surfaces of semiconductors, is used to measure the drop height profiles for the range of drop diameters acquired from the electrical shutter experiment. The device scans across the surface and has as its output the height of the surface versus the distance along the surface. Care is taken that each drop is scanned directly through the centre of the drop avoiding error from scanning an off-centre chord where both the drop profile and the drop diameter would be in error. The average drop height is calculated for each drop and the data is curve fitted using a fourth order polynomial. Drop volume is taken as average height multiplied by the area. This data was used in processing the electrical shutter data and resulted in aluminum mass percent of approximately 6 percent. This is well out of the

range measured using atomic absorption measurements. To reconcile this apparent difference the drop height data was more closely analyzed.

The diamond tip of the scanning arm is 25μm in radius and introduces significant error in measuring the drop profiles. As shown in Fig. D.1 the profiles measured reflect the shape of the diamond tip at the drop edge, not the drop profile. This adds error in two ways. First the drop diameter is measured to be larger and second, the average height is measured smaller. A correction for this problem is to extrapolate the drop profile using a region where the diamond tip does not effect the reading as greatly. Each drop profile was plotted in detail and the drop profile extrapolated to obtain the final diameter and average height. An example profile and extrapolation is shown in Fig. D.2 . The data is again curve fitted and then used to process the electrical shutter data. The aluminum content obtained, 1.83% closely matches the atomic absorption results of 1.86%. This comparison is discussed in Section 4.3.2.

Fig. D.1
Measurement of Splattered Drop Height

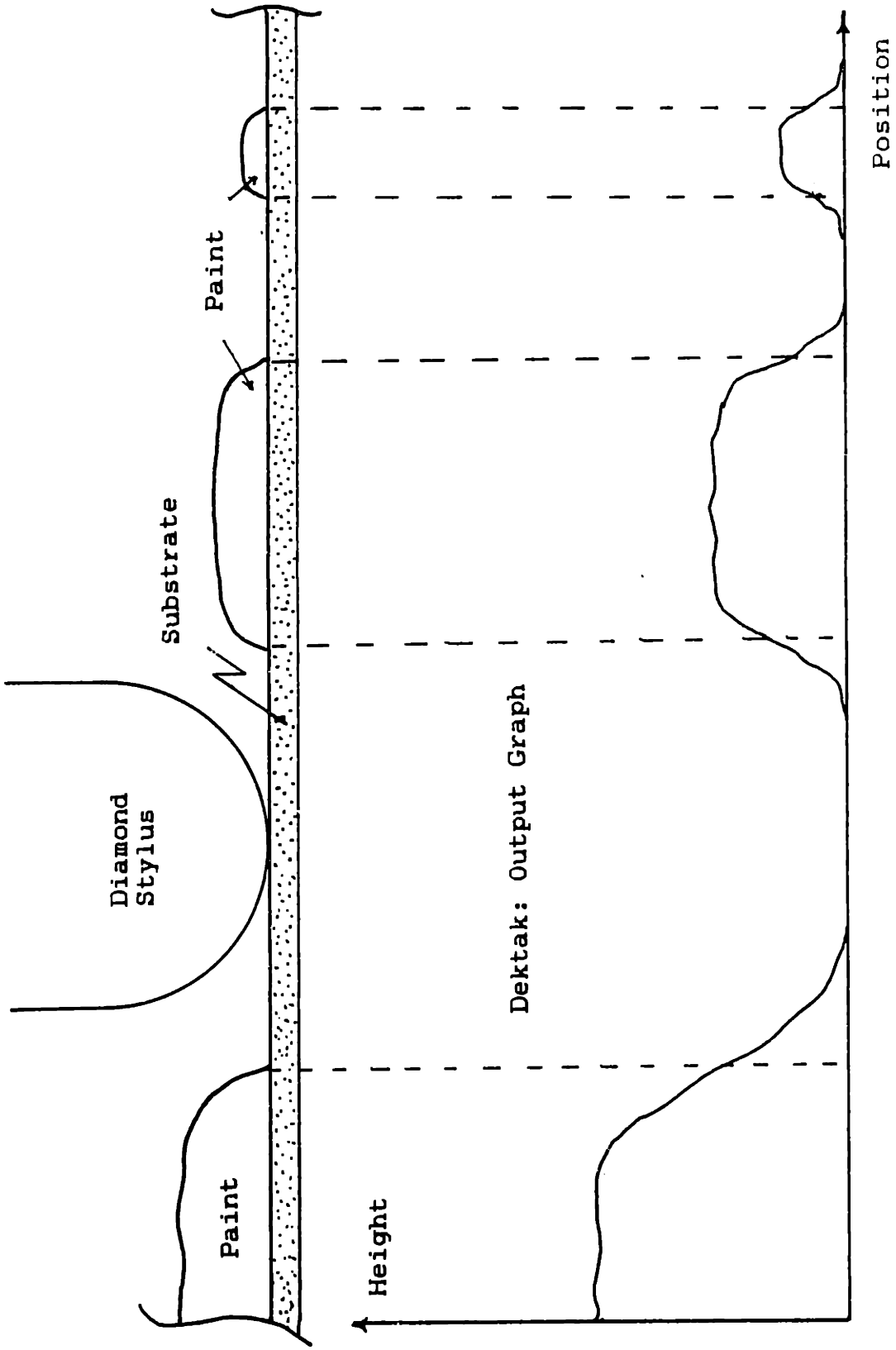

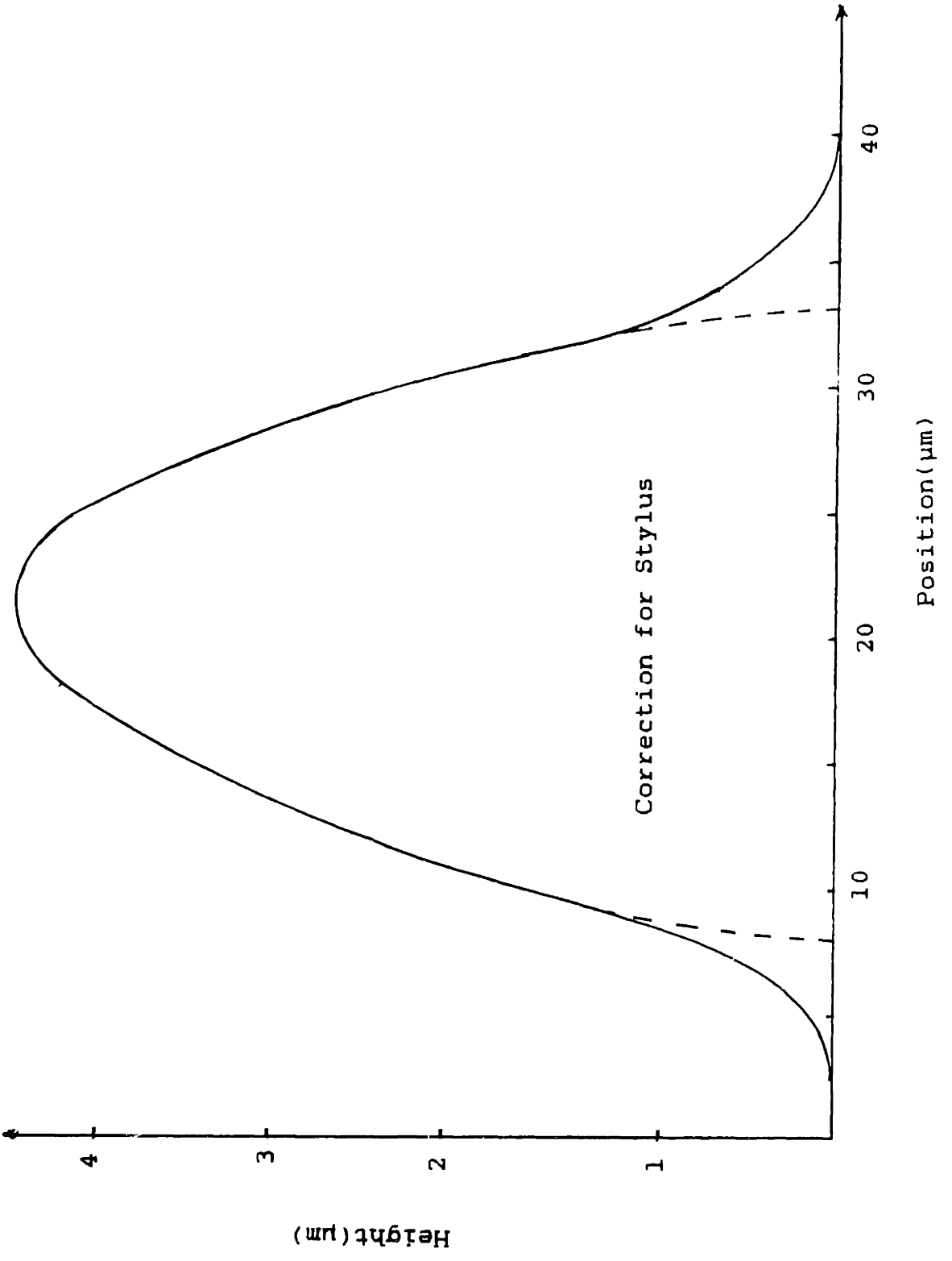

Fig. D.2
Drop Profile

Appendix E

Electrical Shutter Data

A series of tables was chosen to represent the electrical shutter data. There is one table for each position sampled on the paint target. Each table has basic statistics on the entire sample followed by a listing of the data in terms of drop diameter. Drop diameter is divided into 10 intervals starting at 0μm and ending at 50μm in steps of 5μm. The eleventh row contains drops whose diameter is larger than 50μm. Data marked by an asterisk indicates that there is less than 10 in the sample. A table is followed by a plot of the drop distribution for that position.

The five samples are taken at spacings of 10cm. They are numbered starting at the edge of the spray pattern working into the centre. Therefore, the sample at the edge of the spray cloud is number one and the sample at the centre of the spray cloud is number 5. Details of the sample positions are shown in Fig 4.5. The experiment is done using both flake and no-flake paint. The following is a listing of the tables and figures in this appendix.

Table E.1 Flake Paint #1

Fig. E.2 Flake Paint #1

Table E.3 Flake Paint #2

Drops

Average drop diameter(μm) = 7.1 Std. dev.(μm) = 9.6

With a probability of 95%
Error in the mean = 0.83
Standard deviation is between 9.16 and 10.00

Total number of drops = 505

Flakes

Average flake area(μm^2) = 34.2 Std. dev.(μm^2) = 83.0

With a probability of 95%
Error in the mean = 14.55
Standard deviation is between 76.92 and 90.94

Total number of flakes = 125

Mass Data

Total mass(μg): drops = 0.262 flake = 8.65×10^{-3}

Percentage of flake by mass = 3.30

Data for Drop Intervals

1	2	3	4	5	6	7
57.23	0.00*	0.54	0.00	0.00	-	5.0
30.69	0.00*	1.94	0.00	0.00	-	10.0
4.36*	1.60*	1.50	0.22	0.48	4.6	15.0
1.78*	0.80*	1.57	0.19	0.40	8.1	20.0
0.99*	1.60*	1.97	1.76	2.95	37.6	25.0
1.58*	11.20*	5.97	9.92	5.48	30.3	30.0
0.59*	4.80*	3.98	3.48	2.89	24.8	35.0
0.40*	4.80*	3.42	4.95	4.78	35.2	40.0
0.79*	10.40	9.91	10.17	3.38	33.4	45.0
0.59*	16.00	10.72	10.20	3.14	21.8	50.0
0.99*	48.80	58.49	59.11	3.33	41.4	∞

Key
1 - Number of drops as a percent of the total
2 - Number of flakes as a percent of the total
3 - Mass as a percent of the total
4 - Flake mass as a percent of the total flake mass
5 - Mass percent of flake
6 - Average flake area
7 - Maximum drop diameter for this interval

Table E.1
Electrostatic Sprayer: Flake Paint #1

Fig. E.2
Drop Distribution: Flake Paint #1

Drops

Average drop diameter(μm) = 9.8 Std. dev.(μm) = 15.1

With a probability of 95%
Error in the mean = 1.27
Standard deviation is between 14.44 and 15.72

Total number of drops = 536

Flakes

Average flake area(μm^2) = 56.6 Std. dev.(μm^2) = 104.3

With a probability of 95%
Error in the mean = 14.68
Standard deviation is between 97.49 and 112.24

Total number of flakes = 194

Mass Data

Total mass(μg): drops = 0.780 flake = 2.22×10^{-2}

Percentage of flake by mass = 2.85

Data for Drop Intervals

1	2	3	4	5	6	7
53.92	0.00*	0.17	0.00	0.00	-	5.0
27.80	0.52*	0.67	0.04	0.18	4.5	10.0
4.85	1.03*	0.60	0.05	0.23	2.7	15.0
2.80*	1.03*	0.93	0.35	1.08	19.3	20.0
1.68*	3.09*	1.14	1.30	3.25	23.8	25.0
0.93*	1.03*	1.26	0.14	0.31	7.6	30.0
0.93*	3.09*	1.90	1.53	2.30	28.0	35.0
0.75*	8.25	2.49	2.19	2.51	15.0	40.0
0.93*	6.70*	4.17	6.36	4.35	53.7	45.0
0.37*	3.09*	2.33	2.14	2.63	39.3	50.0
5.06	72.16	84.34	85.90	2.91	67.4	∞

Key
1 - Number of drops as a percent of the total
2 - Number of flakes as a percent of the total
3 - Mass as a percent of the total
4 - Flake mass as a percent of the total flake mass
5 - Mass percent of flake
6 - Average flake area
7 - Maximum drop diameter for this interval

Table E.3
Electrostatic Sprayer: Flake Paint #2

Fig. E.4 Flake Paint #2

Table E.5 Flake Paint #3

Fig. E.6 Flake Paint #3

Table E.7 Flake Paint #4

Fig. E.8 Flake Paint #4

Table E.9 Flake Paint #5

Fig. E.10 Flake Paint #5

Table E.11 No-flake Paint #1

Fig. E.12 No-flake Paint #1

Table E.13 No-flake Paint #2

Fig. E.14 No-flake Paint #2

Table E.15 No-flake Paint #3

Fig. E.16 No-flake Paint #3

Table E.17 No-flake Paint #4

Fig. E.18 No-flake Paint #4

Table E.19 No-flake Paint #5

Fig. E.20 No-flake Paint #5

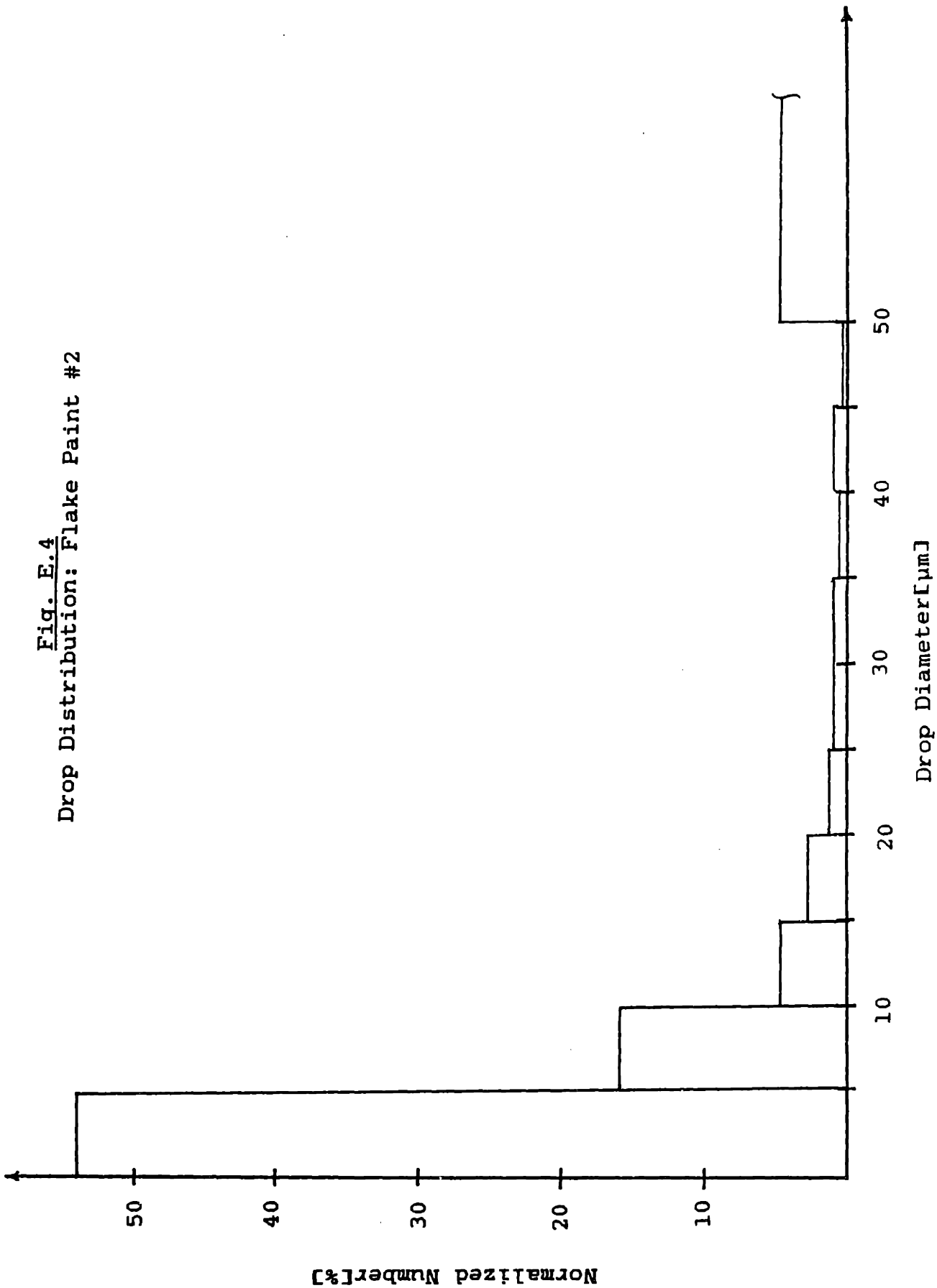

Fig. E.4
Drop Distribution: Flake Paint #2

Drops

Average drop diameter(μm) = 13.1 Std. dev.(μm) = 13.5

With a probability of 95%
Error in the mean = 0.84
Standard deviation is between 13.13 and 13.97

Total number of drops = 1002

Flakes

Average flake area(μm^2) = 31.6 Std. dev.(μm^2) = 62.8

With a probability of 95%
Error in the mean = 6.67
Standard deviation is between 59.64 and 66.33

Total number of flakes = 341

Mass Data

Total mass(μg): drops = 1.21 flake = 2.18×10^{-2}

Percentage of flake by mass = 1.81

Data for Drop Intervals

1	2	3	4	5	6	7
34.53	0.00*	0.18	0.00	0.00	-	5.0
28.24	0.00*	0.87	0.00	0.00	-	10.0
7.68	0.00*	1.22	0.00	0.00	-	15.0
8.38	2.93	3.77	0.68	0.32	7.3	20.0
5.79	4.40	5.26	0.88	0.30	6.3	25.0
3.49	7.33	5.66	2.96	0.95	12.6	30.0
3.59	11.14	9.19	6.22	1.22	17.6	35.0
1.90	7.33	7.25	4.84	1.21	20.9	40.0
1.90	12.90	10.72	12.46	2.10	30.5	45.0
1.50	12.90	11.22	12.79	2.06	31.3	50.0
2.99	41.06	44.65	59.17	2.39	45.5	∞

Key
1 - Number of drops as a percent of the total
2 - Number of flakes as a percent of the total
3 - Mass as a percent of the total
4 - Flake mass as a percent of the total flake mass
5 - Mass percent of flake
6 - Average flake area
7 - Maximum drop diameter for this interval

Table E.5
Electrostatic Sprayer: Flake Paint #3

Fig. E.6
Drop Distribution: Flake Paint #3

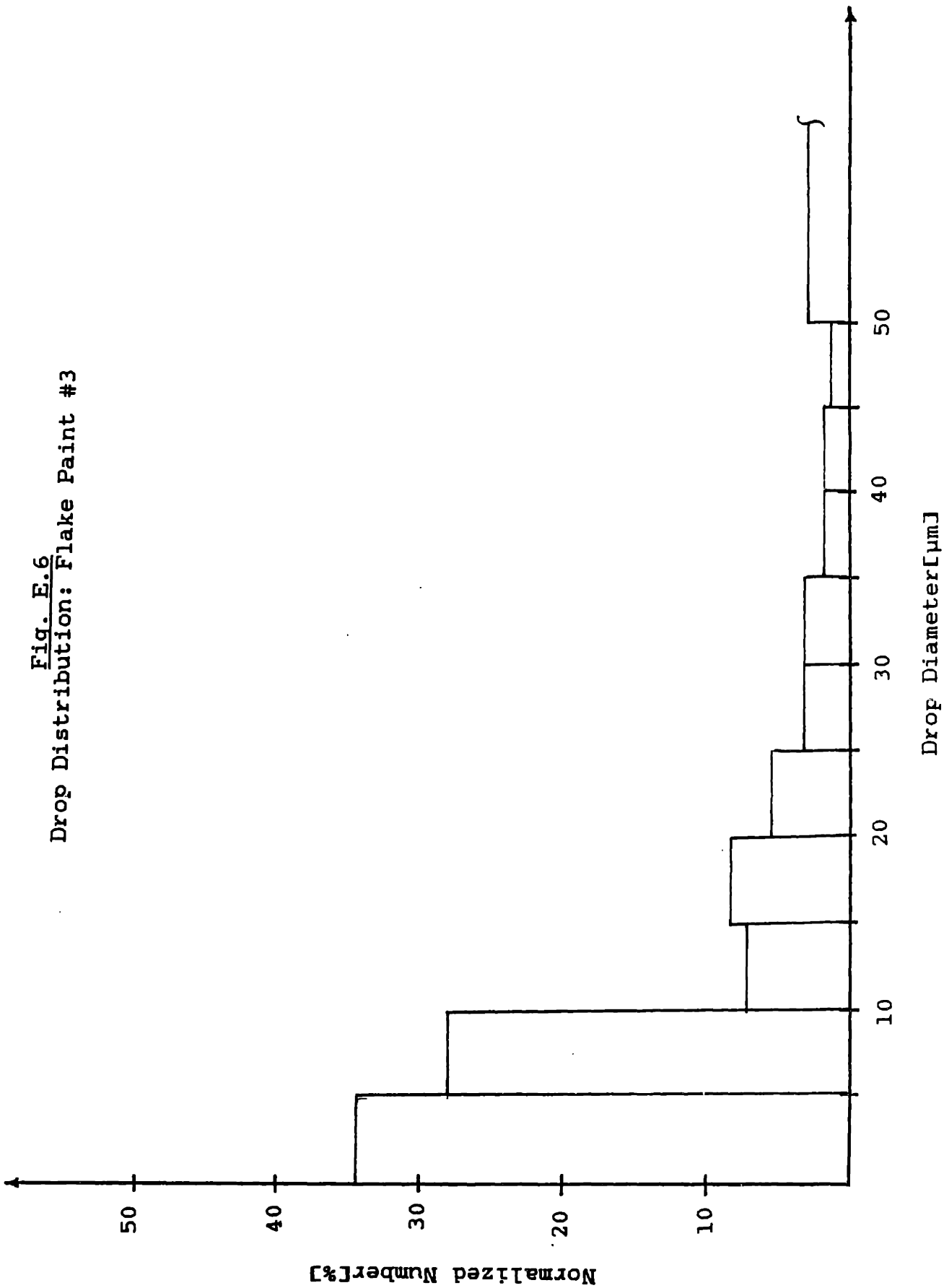

Drops

Average drop diameter(μm) = 17.1 Std. dev.(μm) = 14.9

With a probability of 95%
Error in the mean = 0.96
Standard deviation is between 14.44 and 15.40

Total number of drops = 926

Flakes

Average flake area(μm^2) = 28.2 Std. dev.(μm^2) = 66.1

With a probability of 95%
Error in the mean = 6.66
Standard deviation is between 62.94 and 69.62

Total number of flakes = 379

Mass Data

Total mass(μg): drops = 1.62 flake = 2.16×10^{-2}

Percentage of flake by mass = 1.33

Data for Drop Intervals

1	2	3	4	5	6	7
27.97	0.00*	0.08	0.00	0.00	-	5.0
15.87	0.00*	0.34	0.00	0.00	-	10.0
11.23	0.53*	1.34	0.35	0.35	18.9	15.0
10.48	1.32*	3.18	0.28	0.12	0.6	20.0
8.32	3.42	5.07	1.34	0.35	11.0	25.0
6.91	9.76	7.37	4.23	0.76	12.2	30.0
6.48	13.19	11.55	7.75	0.89	16.5	35.0
4.23	16.62	11.60	13.25	1.52	22.5	40.0
2.92	15.30	10.66	10.79	1.35	19.9	45.0
2.38	10.03	11.92	9.69	1.08	27.2	50.0
3.13	29.82	36.88	52.32	1.89	49.4	∞

Key
1 - Number of drops as a percent of the total
2 - Number of flakes as a percent of the total
3 - Mass as a percent of the total
4 - Flake mass as a percent of the total flake mass
5 - Mass percent of flake
6 - Average flake area
7 - Maximum drop diameter for this interval

Table E.7
Electrostatic Sprayer: Flake Paint #4

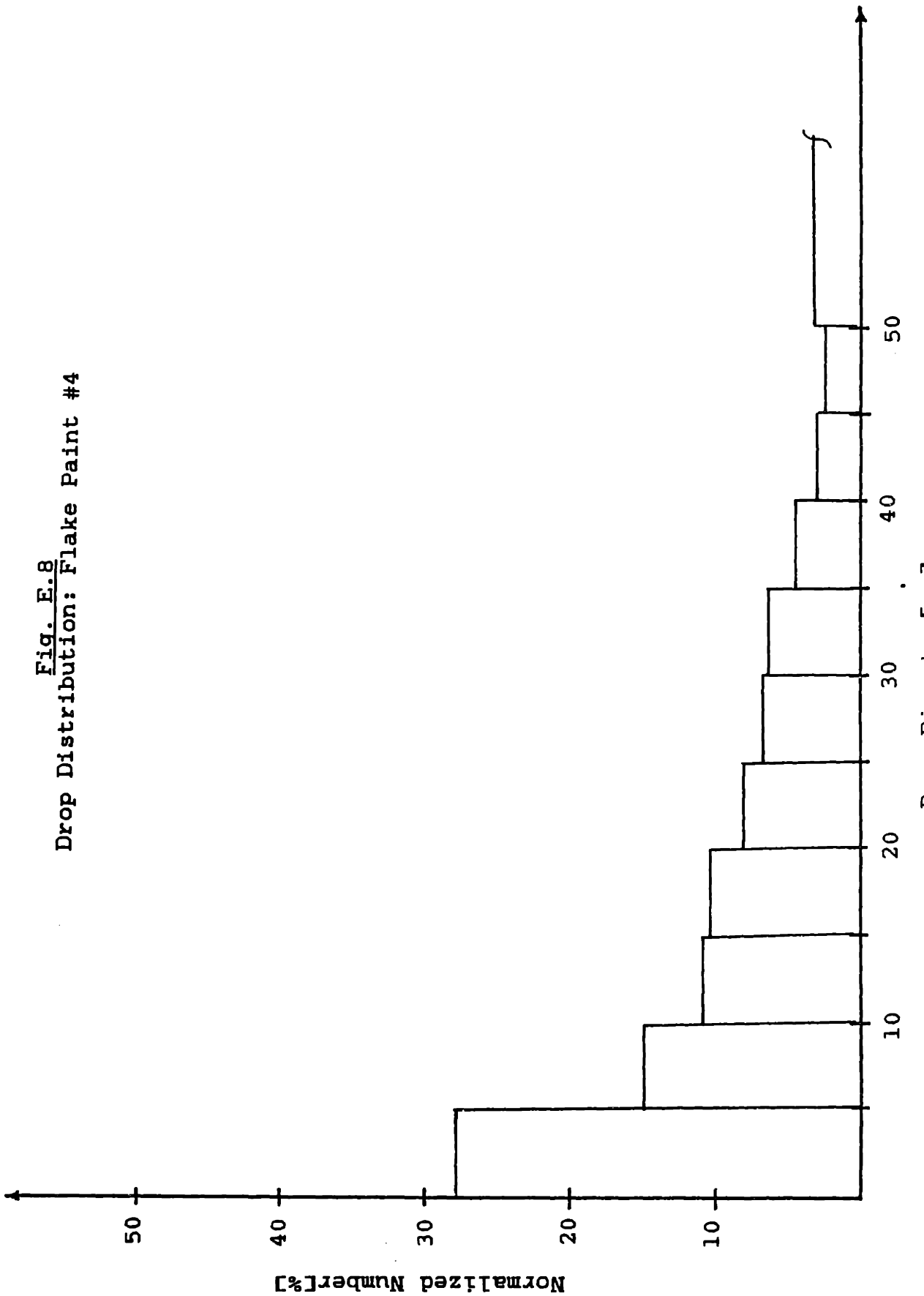

Fig. E.8
Drop Distribution: Flake Paint #4

Drops

Average drop diameter(μm) = 13.8 Std. dev.(μm) = 10.3

With a probability of 95%
Error in the mean = 0.68
Standard deviation is between 9.94 and 10.61

Total number of drops = 879

Flakes

Average flake area(μm^2) = 22.6 Std. dev.(μm^2) = 36.3

With a probability of 95%
Error in the mean = 5.02
Standard deviation is between 33.93 and 38.97

Total number of flakes = 201

Mass Data

Total mass(μg): drops = 0.658 flake = 9.19×10^{-3}

Percentage of flake by mass = 1.40

Data for Drop Intervals

1	2	3	4	5	6	7
22.98	0.00*	0.17	0.00	0.00	-	5.0
22.64	0.00*	1.19	0.00	0.00	-	10.0
16.61	2.99*	4.52	0.62	0.19	4.7	15.0
13.54	7.96*	9.66	3.44	0.50	9.7	20.0
8.53	9.95	12.36	4.35	0.49	9.9	25.0
6.94	20.40	17.05	12.73	1.04	14.1	30.0
4.55	18.91	18.45	14.73	1.21	17.6	35.0
2.28	17.91	13.89	13.49	1.36	17.0	40.0
1.14*	11.94	10.39	26.28	3.53	49.7	45.0
0.46*	3.48	5.71	8.38	2.05	54.4	50.0
0.34*	6.47	6.60	15.97	3.38	55.8	∞

Key
1 - Number of drops as a percent of the total
2 - Number of flakes as a percent of the total
3 - Mass as a percent of the total
4 - Flake mass as a percent of the total flake mass
5 - Mass percent of flake
6 - Average flake area
7 - Maximum drop diameter for this interval

Table E.9
Electrostatic Sprayer: Flake Paint #5

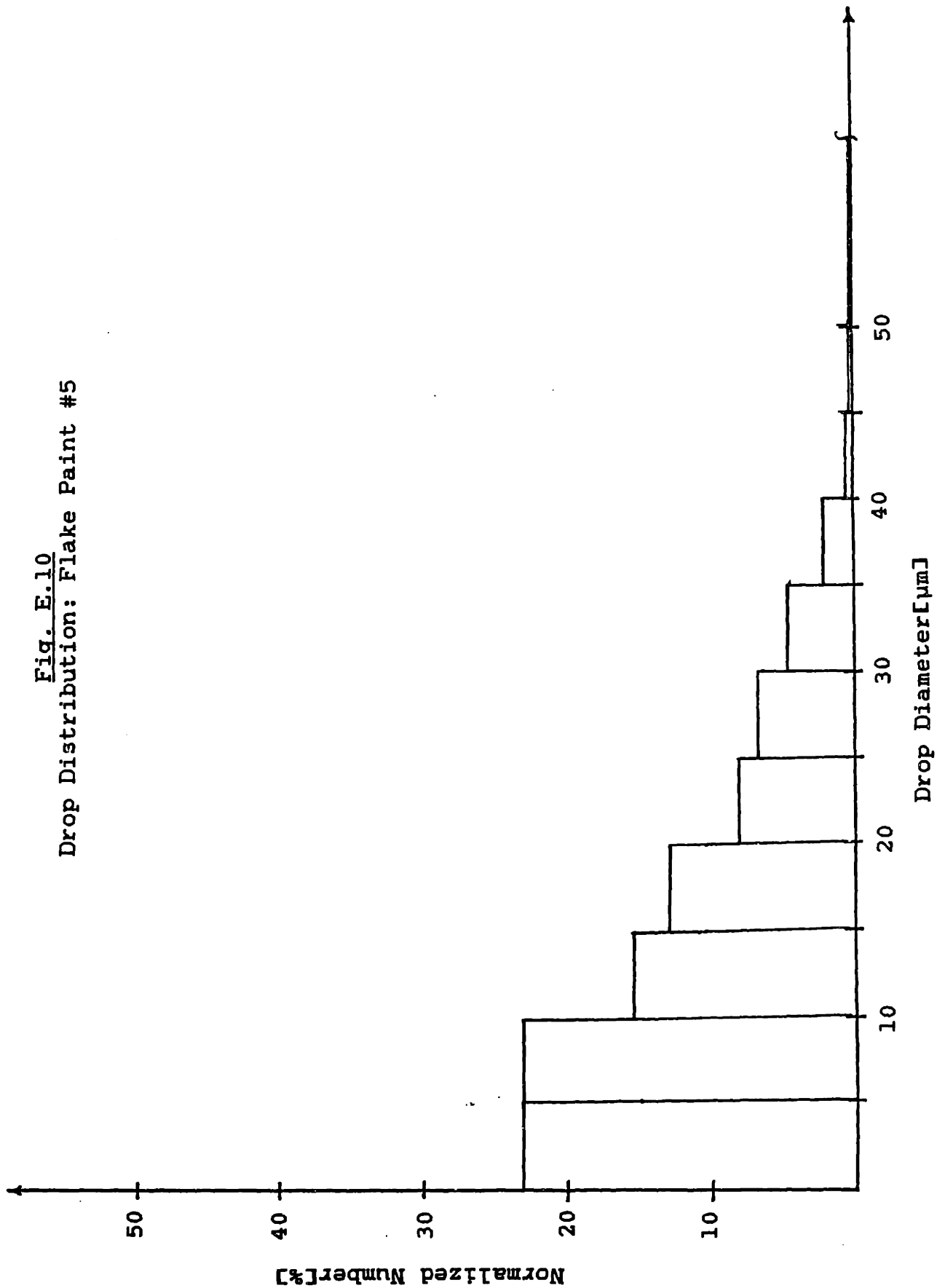

Fig. E.10
Drop Distribution: Flake Paint #5

Drops

Average drop diameter(μm) = 14.6 Std. dev.(μm) = 12.9

With a probability of 95%
Error in the mean = 4.04
Standard deviation is between 11.13 and 15.28

Total number of drops = 39

Total number of flakes = 0

Mass Data

Total mass(μg): drops = 4.34×10^{-2}

Data for Drop Intervals

Number of Drops % of Total	Mass % of Total	Maximum Drop Diameter
23.08*	0.08	5.0
30.77*	1.02	10.0
7.69*	1.36	15.0
10.26*	5.84	20.0
7.69*	6.11	25.0
7.69*	12.32	30.0
2.56*	8.14	35.0
5.13*	22.17	40.0
0.00*	0.00	45.0
2.56*	18.54	50.0
2.56*	14.44	∞

Table E.11
Electrostatic Sprayer: No-flake Paint #1

Fig. E.12
Drop Distribution: No-flake Paint #1

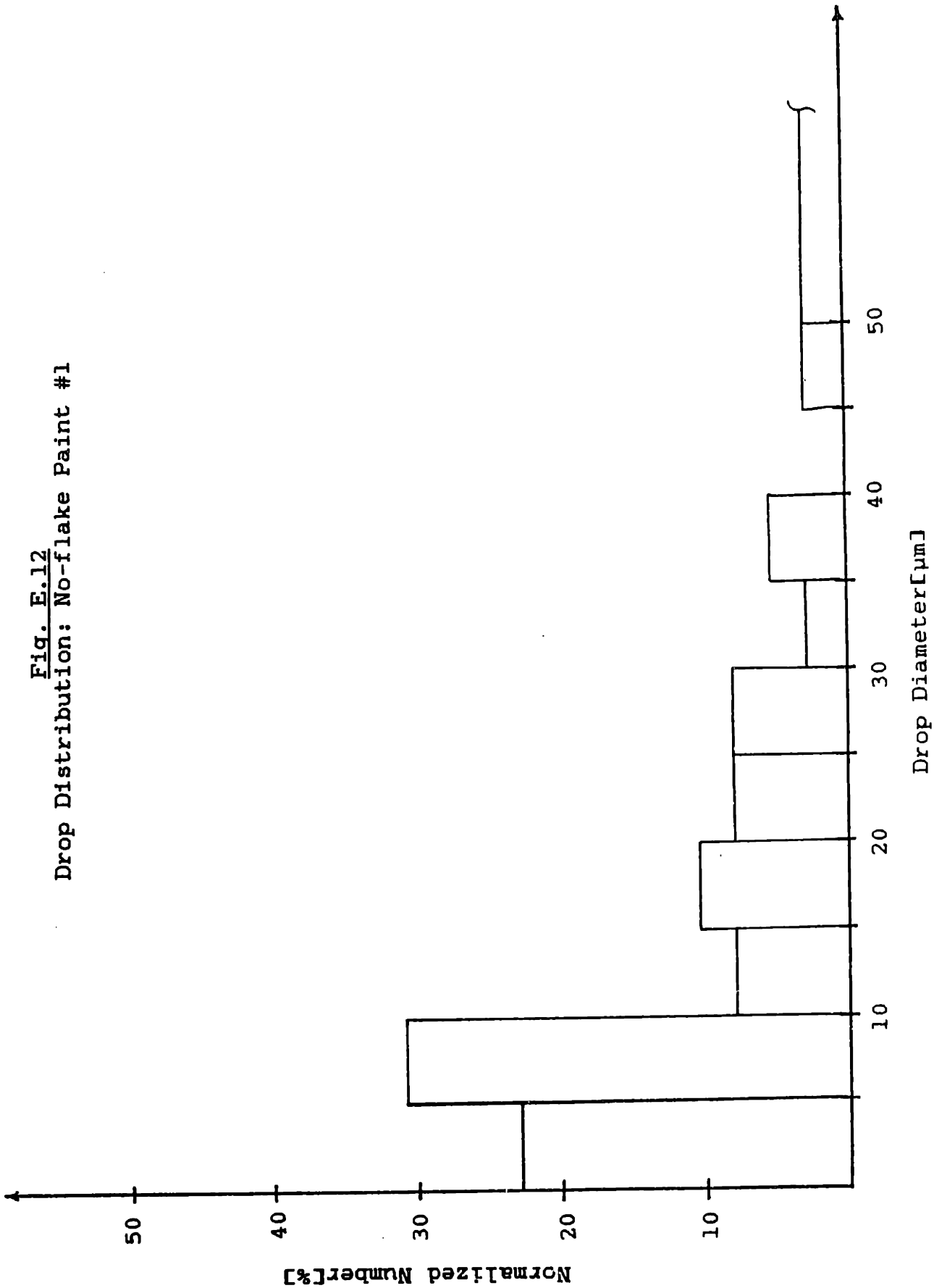

Drops

Average drop diameter(μm) = 35.1 Std. dev.(μm) = 26.7

With a probability of 95%
Error in the mean = 5.84
Standard deviation is between 24.04 and 29.95

Total number of drops = 80

Total number of flakes = 0

Mass Data

Total mass(μg): drops = 0.789

Data for Drop Intervals

Number of Drops % of Total	Mass % of Total	Maximum Drop Diameter
2.50*	0.00	5.0
7.50*	0.03	10.0
13.75	0.30	15.0
12.50	0.68	20.0
12.50*	1.51	25.0
8.75*	1.73	30.0
10.00*	2.99	35.0
3.75*	1.70	40.0
5.00*	3.31	45.0
1.25*	1.05	50.0
22.50	86.72	∞

Table E.13
Electrostatic Sprayer: No-flake Paint #2

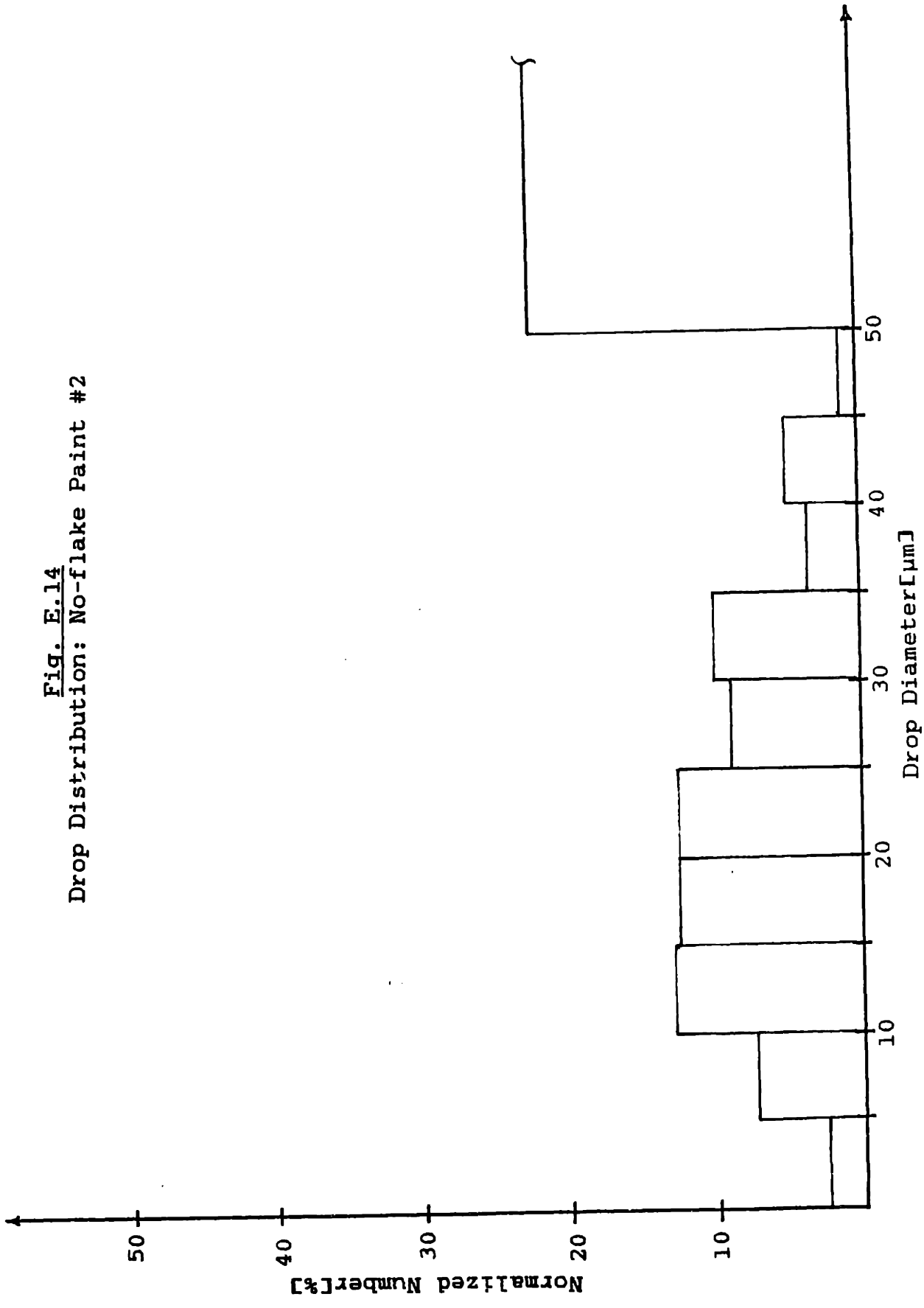

Fig. E.14
Drop Distribution: No-flake Paint #2

Drops

Average drop diameter(μm) = 36.3 Std. dev.(μm) = 18.7

With a probability of 95%
Error in the mean = 1.74
Standard deviation is between 17.92 and 19.66

Total number of drops = 448

Total number of flakes = 0

Mass Data

Total mass(μg): drops = 3.19

Data for Drop Intervals

Number of Drops % of Total	Mass % of Total	Maximum Drop Diameter
0.89*	0.00	5.0
5.36	0.04	10.0
5.80	0.16	15.0
9.37	0.74	20.0
8.71	1.37	25.0
10.94	3.05	30.0
12.28	5.34	35.0
10.49	6.95	40.0
8.04	7.39	45.0
4.69	5.99	50.0
23.44	68.96	∞

Table E.15
Electrostatic Sprayer: No-flake Paint #3

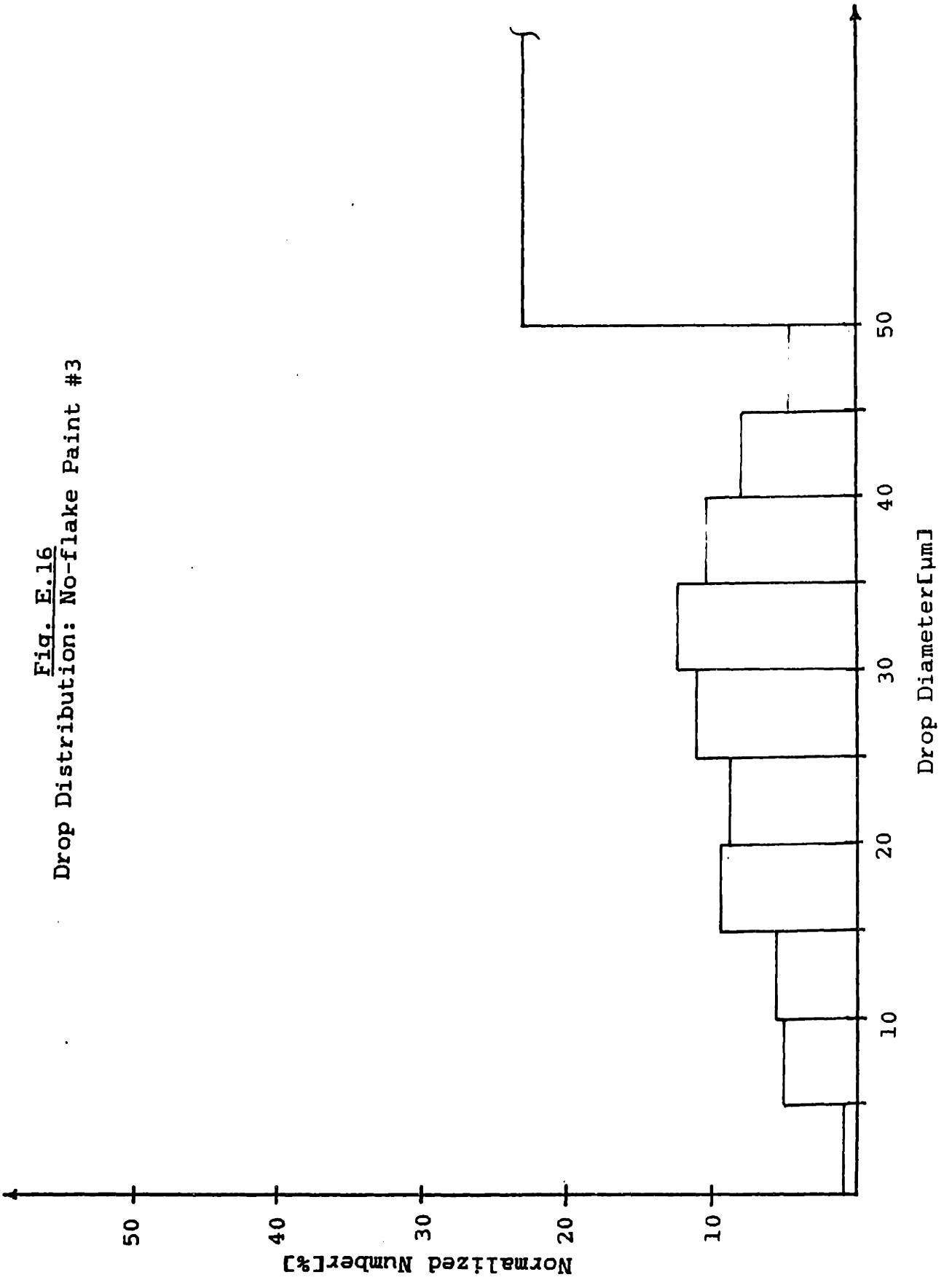

Fig. E.16
Drop Distribution: No-flake Paint #3

Drops

Average drop diameter(μm) = 33.6 Std. dev.(μm) = 18.2

With a probability of 95%
Error in the mean = 1.89
Standard deviation is between 17.34 and 19.23

Total number of drops = 358

Total number of flakes = 0

Mass Data

Total mass(μg): drops = 2.14

Data for Drop Intervals

Number of Drops % of Total	Mass % of Total	Maximum Drop Diameter
1.96*	0.00	5.0
7.82	0.06	10.0
7.82	0.27	15.0
8.94	0.80	20.0
12.29	2.31	25.0
7.26	2.42	30.0
9.78	5.23	35.0
8.94	7.03	40.0
8.38	9.16	45.0
4.75	7.04	50.0
22.07	65.67	∞

Table E.17
Electrostatic Sprayer: No-flake Paint #4

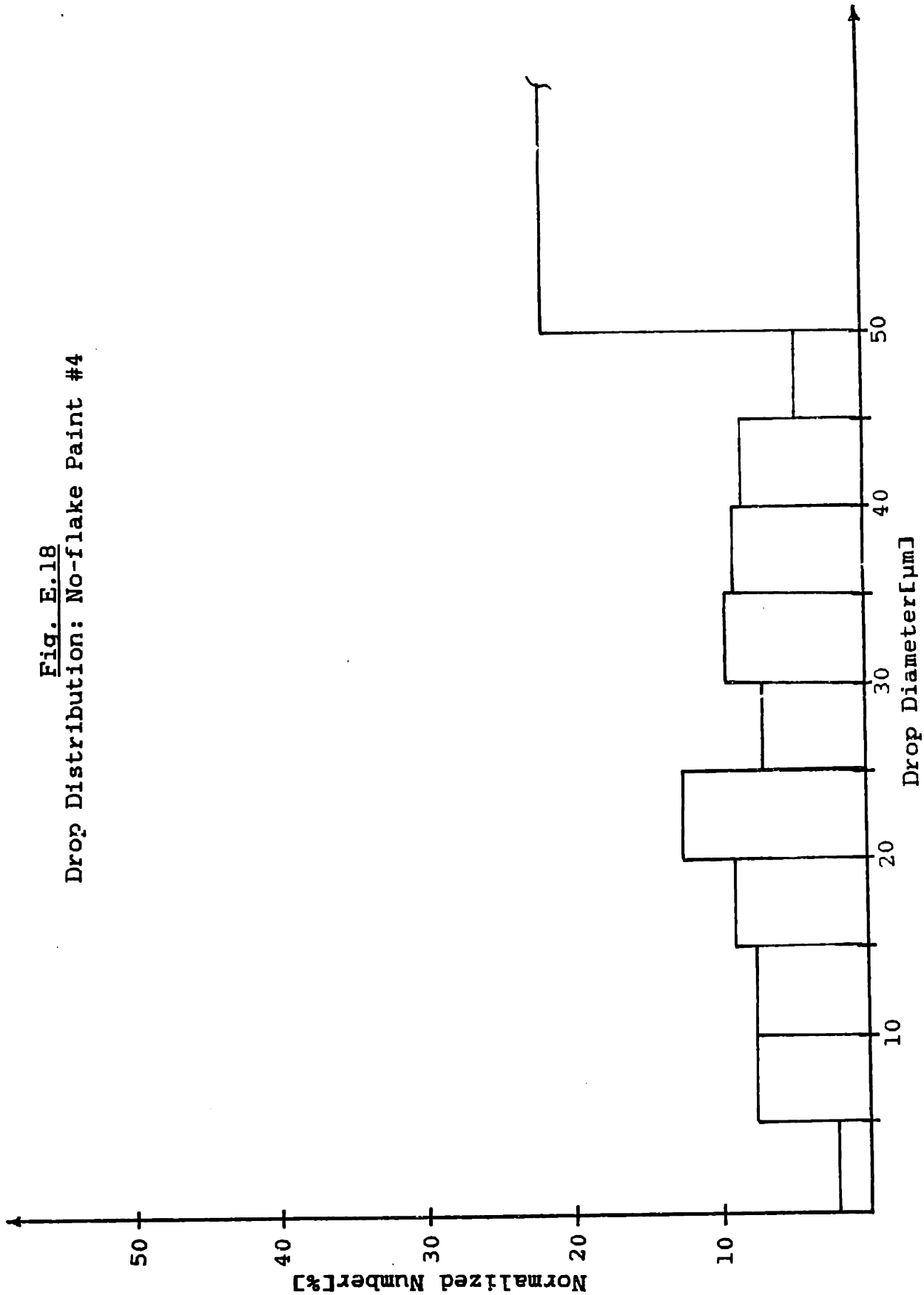

Fig. E.18
Drop Distribution: No-flake Paint #4

Drops

Average drop diameter(μm) = 31.4 Std. dev.(μm) = 15.7

With a probability of 95%
Error in the mean = 1.63
Standard deviation is between 14.91 and 16.54

Total number of drops = 357

Total number of flakes = 0

Mass Data

Total mass(μg): drops = 1.65

Data for Drop Intervals

Number of Drops % of Total	Mass % of Total	Maximum Drop Diameter
3.08	0.01	5.0
4.48	0.04	10.0
7.56	0.35	15.0
11.20	1.32	20.0
11.76	2.73	25.0
11.76	4.74	30.0
10.08	6.92	35.0
12.04	12.23	40.0
7.56	10.74	45.0
7.56	14.70	50.0
12.89	46.23	∞

Table E.19
Electrostatic Sprayer: No-flake Paint #5

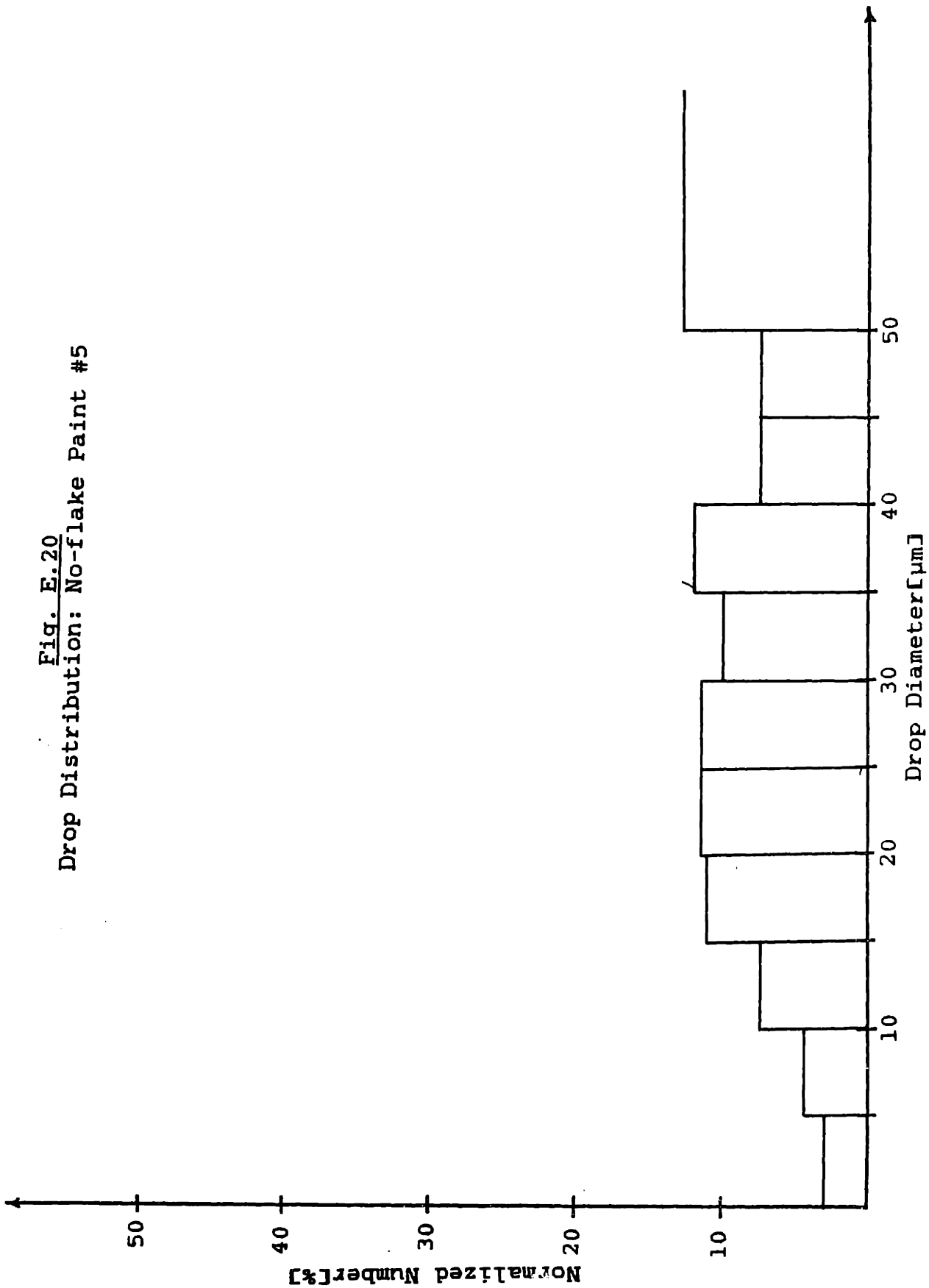

Fig. E.20
Drop Distribution: No-flake Paint #5

Appendix F

Mechanical Sprayer Results

The sampling techniques are discussed in detail in Chapter 4. Four samples are taken, samples one to three are taken in the overspray and sample four is on the paint surface. Sample four represents the material deposited in a normal paint finish while the other samples are from the overspray (material that is normally wasted). The format of the data is identical to that in Appendix B. A table and a drop distribution is given for each sample. The following is a list of the tables and figures in this appendix.

Table F.1 Flake Paint #1

Fig. F.2 Flake Paint #1

Table F.3 Flake Paint #2

Fig. F.4 Flake Paint #2

Table F.5 Flake Paint #3

Fig. F.6 Flake Paint #3

Table F.7 Flake Paint #4

Fig. F.8 Flake Paint #4

Table F.9 No-flake Paint #1

Fig. F.10 No-flake Paint #1

Table F.11 No-flake Paint #2

Fig. F.12 No-flake Paint #2

Table F.13 No-flake Paint #3

Drops

Average drop diameter(μm) = 6.5 Std. dev.(μm) = 3.7

With a probability of 95%
Error in the mean = 0.19
Standard deviation is between 3.58 and 3.77

Total number of drops = 1472

Flakes

Average flake area(μm^2) = 16.3 Std. dev.(μm^2) = 13.6

With a probability of 95%
Error in the mean = 4.88
Standard deviation is between 11.57 and 16.61

Total number of flakes = 30

Mass Data

Total mass(μg): drops = 0.100 flake = 9.88×10^{-4}

Percentage of flake by mass = 0.99

Data for Drop Intervals

1	2	3	4	5	6	7
42.87	0.00*	5.79	0.00	0.00	-	5.0
46.26	3.33*	20.88	0.36	0.02	1.7	10.0
6.59	10.00*	17.57	4.38	0.25	7.1	15.0
2.58	23.33*	17.00	26.57	1.54	18.5	20.0
1.02*	30.00*	16.25	19.78	1.16	10.7	25.0
0.48*	23.33*	12.09	30.16	2.46	21.0	30.0
0.14*	10.00*	5.55	18.75	3.33	30.5	35.0
0.07*	0.00*	4.38	0.00	0.00	-	40.0
0.00*	0.00*	0.00	0.00	-	-	45.0
0.00*	0.00*	0.00	0.00	-	-	50.0
0.00*	0.00*	0.00	0.00	-	-	∞

Key
1 - Number of drops as a percent of the total
2 - Number of flakes as a percent of the total
3 - Mass as a percent of the total
4 - Flake mass as a percent of the total flake mass
5 - Mass percent of flake
6 - Average flake area
7 - Maximum drop diameter for this interval

Table F.1
Mechanical Sprayer: Flake Paint #1

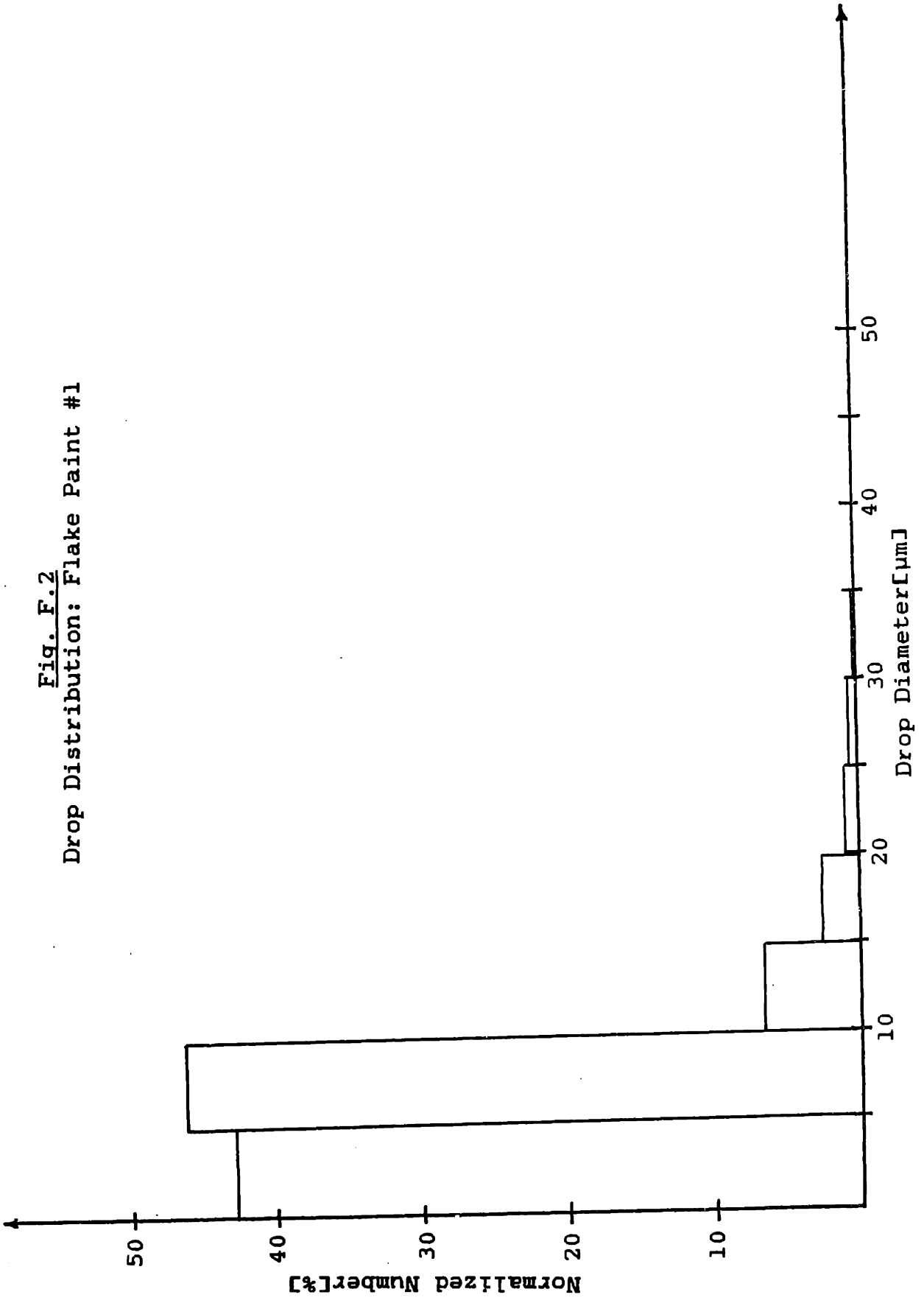

Fig. F.2
Drop Distribution: Flake Paint #1

Drops

Average drop diameter(μm) = 6.8 Std. [illegible] (μm) = 2.7

With a probability of 95%
Error in the mean = 0.11
Standard deviation is between 2.69 ar[illegible]

Total number of drops = 2339

Flakes

Average flake area(μm^2) = 11.0 Std. dev.(μm^2) = 4.7

With a probability of 95%
Error in the mean = 2.19
Standard deviation is between 3.85 and 6.16

Total number of flakes = 18

Mass Data

Total mass(μg): drops = 0.125 flake = 4.02×10^{-4}

Percentage of flake by mass = 0.32

Data for Drop Intervals

1	2	3	4	5	6	7
17.96	0.00*	3.18	0.00	0.00	-	5.0
73.92	0.00*	45.45	0.00	0.00	-	10.0
5.94	11.11*	18.95	13.88	0.24	13.8	15.0
1.50*	50.00*	14.41	47.77	1.07	10.5	20.0
0.38*	16.67*	7.62	15.83	0.67	10.5	25.0
0.30*	22.22*	10.39	22.52	0.70	11.2	30.0
0.00*	0.00*	0.00	0.00	-	-	35.0
0.00*	0.00*	0.00	0.00	-	-	40.0
0.00*	0.00*	0.00	0.00	-	-	45.0
0.00*	0.00*	0.00	0.00	-	-	50.0
0.00*	0.00*	0.00	0.00	-	-	∞

Key
1 - Number of drops as a percent of the total
2 - Number of flakes as a percent of the total
3 - Mass as a percent of the total
4 - Flake mass as a percent of the total flake mass
5 - Mass percent of flake
6 - Average flake area
7 - Maximum drop diameter for this interval

Table F.3
Mechanical Sprayer: Flake Paint #2

Fig. F.4
Drop Distribution: Flake Paint #2

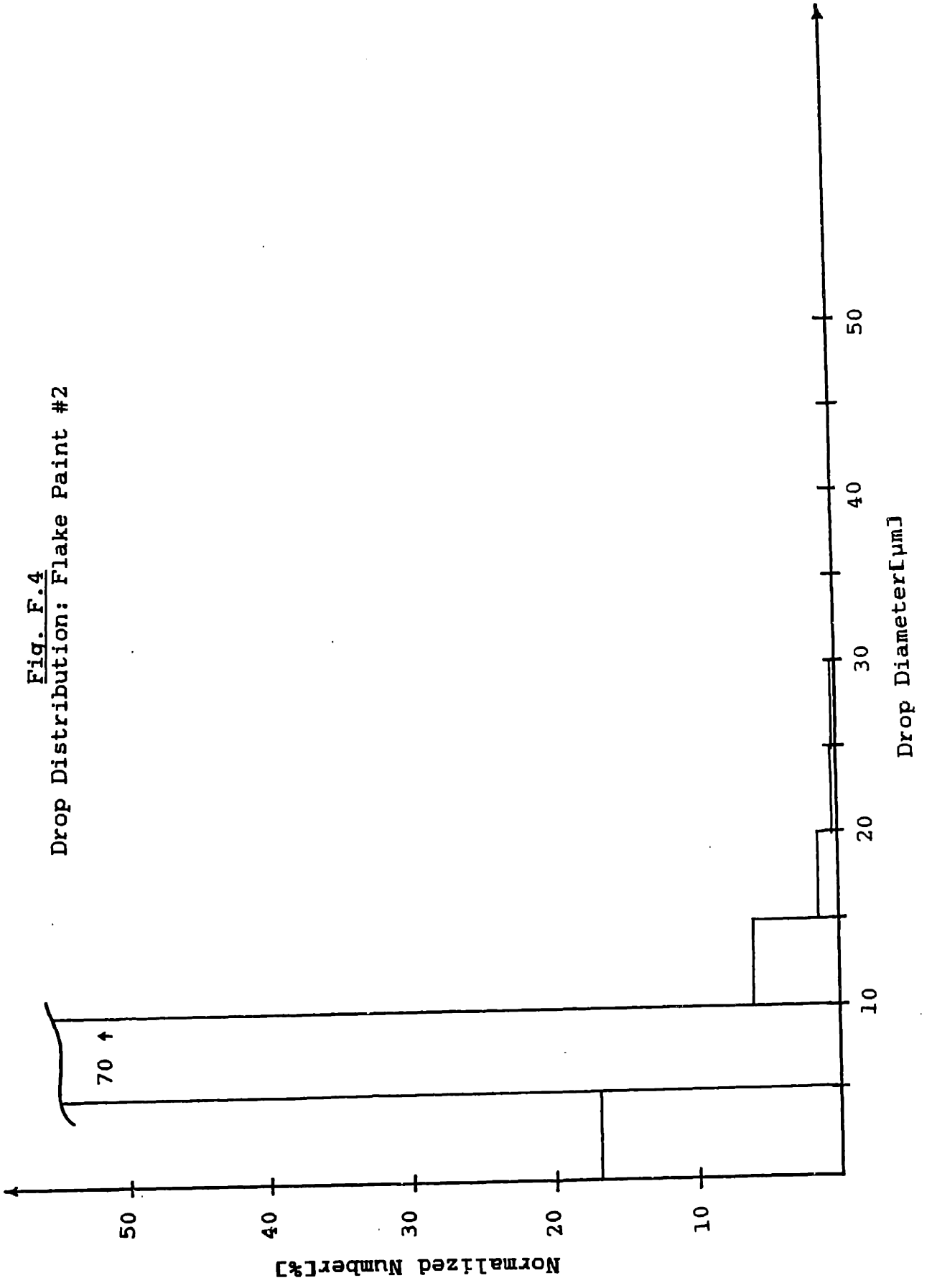

Drops

Average drop diameter(μm) = 5.7 Std. dev.(μm) = 3.6

With a probability of 95%
Error in the mean = 0.16
Standard deviation is between 3.53 and 3.70

Total number of drops = 1850

Flakes

Average flake area(μm^2) = 14.2 Std. dev.(μm^2) = 18.0

With a probability of 95%
Error in the mean = 6.80
Standard deviation is between 15.17 and 22.22

Total number of flakes = 27

Mass Data

Total mass(μg): drops = 9.63×10^{-2} flake = 7.75×10^{-4}

Percentage of flake by mass = 0.80

Data for Drop Intervals

1	2	3	4	5	6	7
54.97	0.00*	6.08	0.00	0.00	-	5.0
36.00	0.00*	23.48	0.00	0.00	-	10.0
5.95	22.22*	20.91	10.56	0.41	6.7	15.0
1.84	25.93*	17.62	20.86	0.95	11.4	20.0
0.81	40.74*	17.46	47.91	2.21	16.7	25.0
0.43	11.11*	14.44	20.67	1.15	26.3	30.0
0.00	0.00	0.00	0.00	-	-	35.0
0.00	0.00	0.00	0.00	-	-	40.0
0.00	0.00	0.00	0.00	-	-	45.0
0.00	0.00	0.00	0.00	-	-	50.0
0.00	0.00	0.00	0.00	-	-	∞

Key
1 - Number of drops as a percent of the total
2 - Number of flakes as a percent of the total
3 - Mass as a percent of the total
4 - Flake mass as a percent of the total flake mass
5 - Mass percent of flake
6 - Average flake area
7 - Maximum drop diameter for this interval

Table F.5
Mechanical Sprayer: Flake Paint #3

Fig. F.6
Drop Distribution: Flake Paint #3

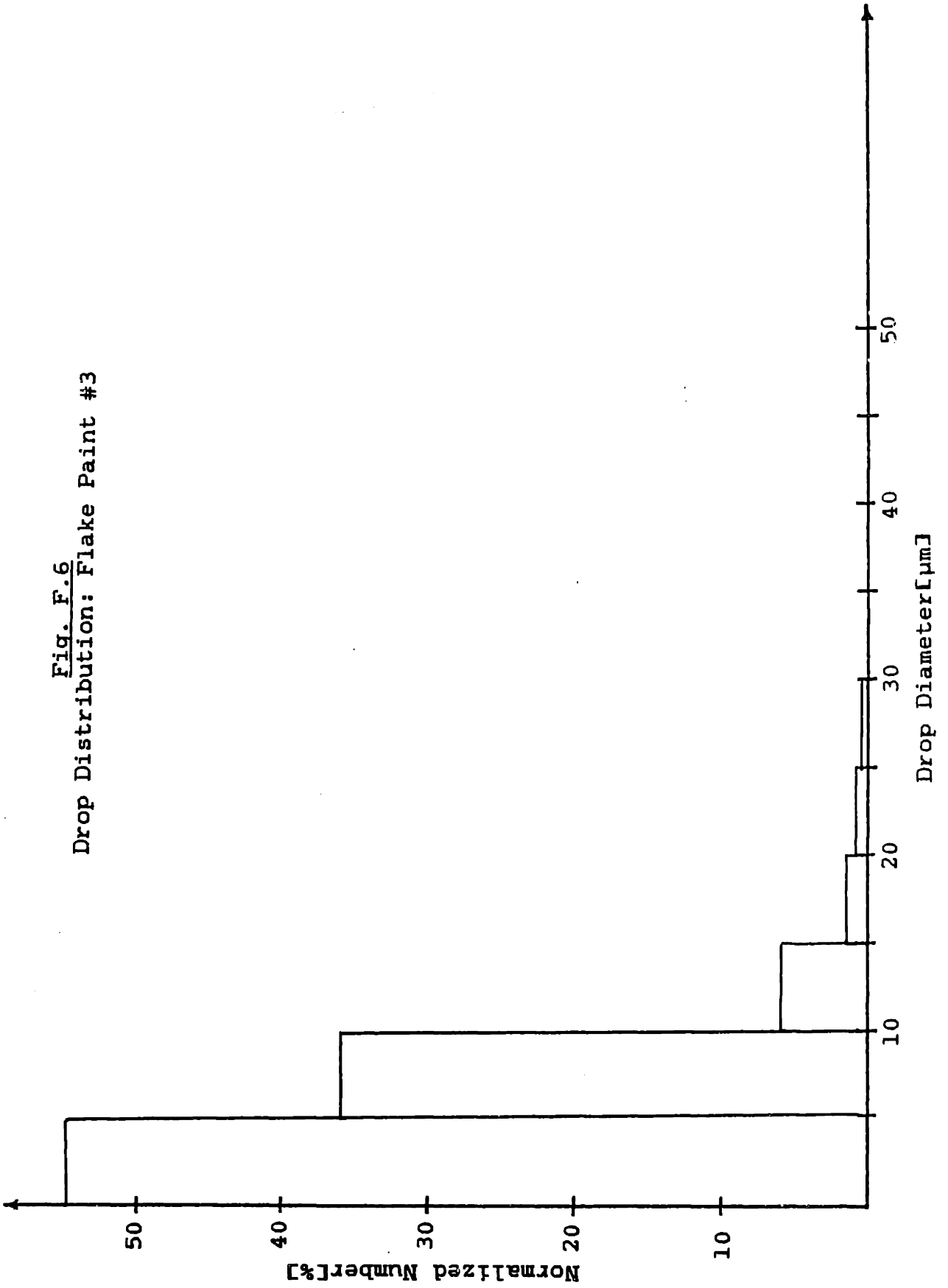

Drops

Average drop diameter(μm) = 36.0 Std. dev.(μm) = 29.0

With a probability of 95%
Error in the mean = 3.76
Standard deviation is between 27.28 and 31.06

Total number of drops = 229

Flakes

Average flake area(μm^2) = 74.2 Std. dev.(μm^2) = 149.6

With a probability of 95%
Error in the mean = 15.77
Standard deviation is between 142.16 and 157.97

Total number of flakes = 346

Mass Data

Total mass(μg): drops = 2.68 flake = 5.20×10^{-2}

Percentage of flake by mass = 1.94

Data for Drop Intervals

1	2	3	4	5	6	7
1.75*	0.00*	0.00	0.00	0.00	-	5.0
8.30	0.00*	0.04	0.00	0.00	-	10.0
13.10	0.00*	0.21	0.00	0.00	-	15.0
13.97	1.73*	0.66	0.86	2.55	37.0	20.0
12.66	2.60*	1.24	0.52	0.82	14.9	25.0
8.73	2.89	1.50	1.28	1.66	33.0	30.0
7.86	2.89	2.03	2.00	1.91	51.4	35.0
2.18*	1.16*	0.93	0.64	1.34	41.3	40.0
3.49	3.18	2.03	0.90	0.85	20.9	45.0
4.80	7.23	3.60	1.35	0.73	13.8	50.0
23.14	78.32	87.77	92.44	2.04	87.5	∞

Key
1 - Number of drops as a percent of the total
2 - Number of flakes as a percent of the total
3 - Mass as a percent of the total
4 - Flake mass as a percent of the total flake mass
5 - Mass percent of flake
6 - Average flake area
7 - Maximum drop diameter for this interval

Table F.7
Mechanical Sprayer: Flake Paint #4

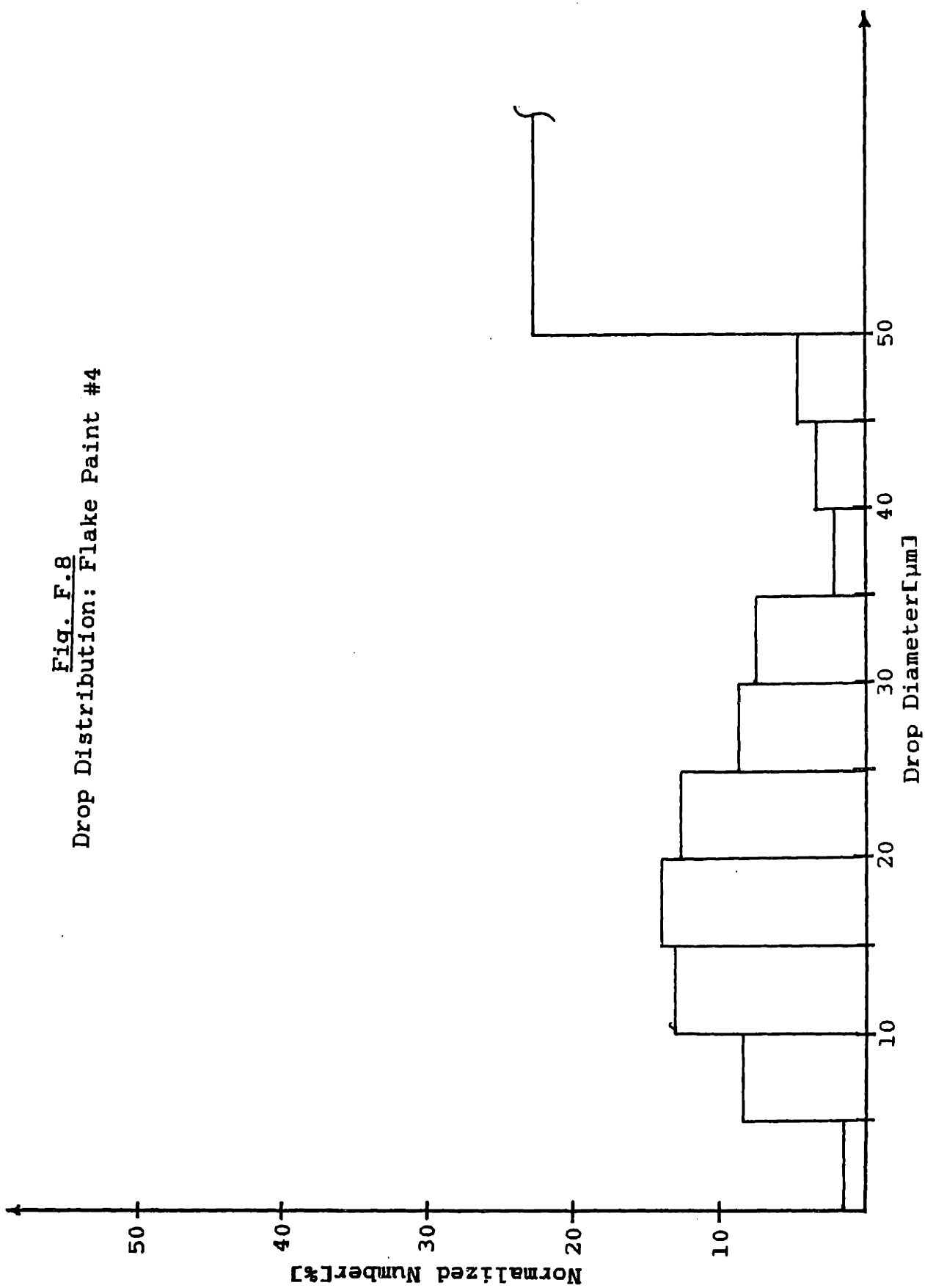

Fig. F.8
Drop Distribution: Flake Paint #4

Drops

Average drop diameter(μm) = 6.9 Std. dev.(μm) = 4.0

With a probability of 95%
Error in the mean = 0.22
Standard deviation is between 3.88 and 4.10

Total number of drops = 1237

Total number of flakes = 0

Mass Data

Total mass(μg): drops =

Data for Drop Intervals

Number of Drops % of Total	Mass % of Total	Maximum Drop Diameter
40.50	3.56	5.0
44.46	23.00	10.0
10.75	23.77	15.0
3.07	19.69	20.0
0.81	10.04	25.0
0.24*	5.28	30.0
0.00*	0.00	35.0
0.00*	0.00	40.0
0.16*	14.66	45.0
0.00*	0.00	50.0
0.00*	0.00	∞

Table F.9
Mechanical Sprayer: No-flake Paint #1

Fig. F.10
Drop Distribution: No-flake Paint #1

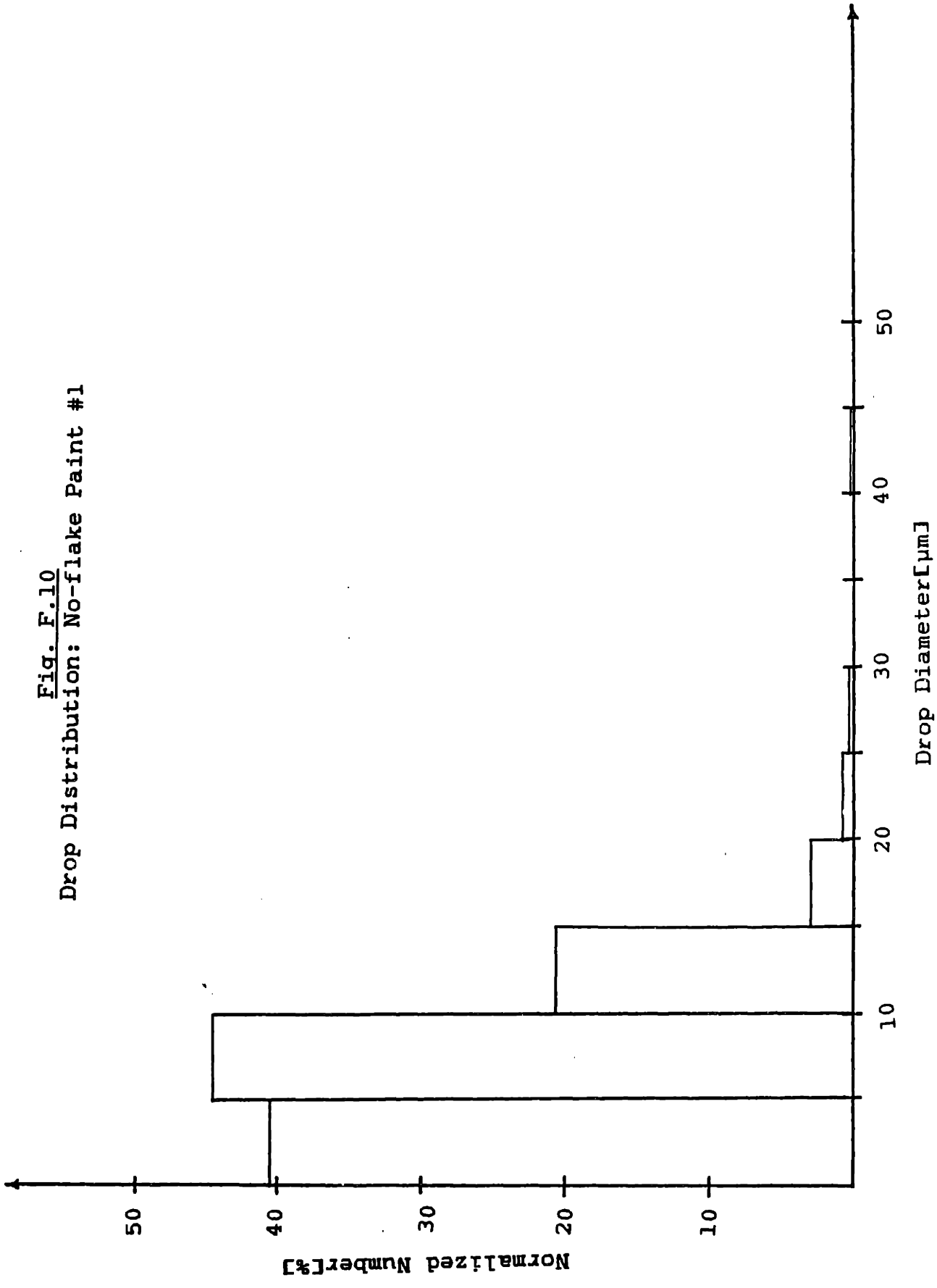

Drops

Average drop diameter(μm) = 6.6 Std. dev.(μm) = 3.6

With a probability of 95%
Error in the mean = 0.20
Standard deviation is between 3.55 and 3.75

Total number of drops = 1220

Total number of flakes = 0

Mass Data

Total mass(μg): drops = 7.66×10^{-2}

Data for Drop Intervals

Number of Drops % of Total	Mass % of Total	Maximum Drop Diameter
42.62	4.42	5.0
44.26	27.96	10.0
9.43	27.96	15.0
2.95	24.76	20.0
0.49*	8.19	25.0
0.25*	7.40	30.0
0.00*	0.00	35.0
0.00*	0.00	40.0
0.00*	0.00	45.0
0.00*	0.00	50.0
0.00*	0.00	∞

Table F.11
Mechanical Sprayer: No-flake Paint #2

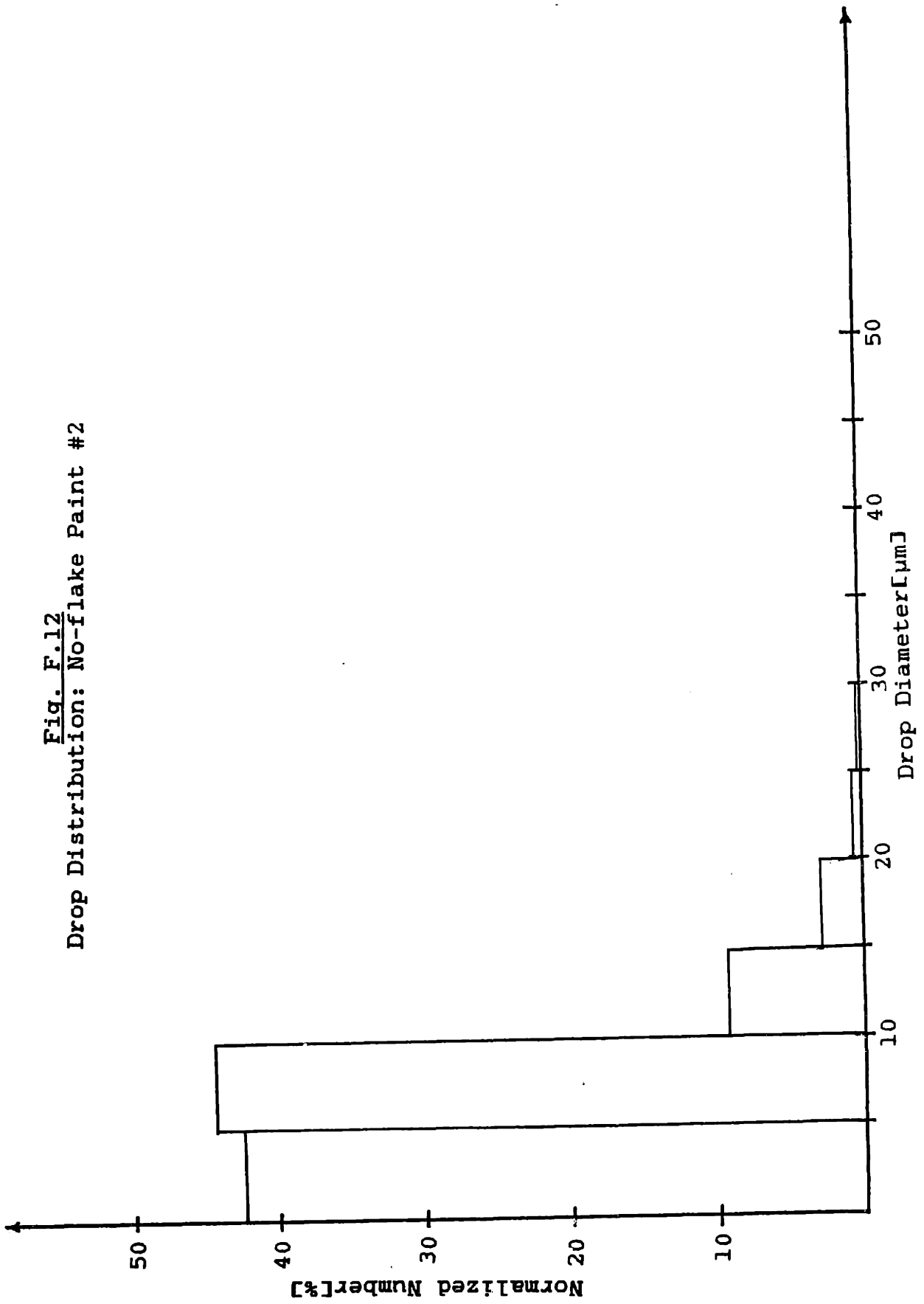

Fig. F.12
Drop Distribution: No-flake Paint #2

Drops

Average drop diameter(μm) = 6.3 Std. dev.(μm) = 3.3

With a probability of 95%
Error in the mean = 0.24
Standard deviation is between 3.16 and 3.40

Total number of drops = 743

Total number of flakes = 0

Mass Data

Total mass(μg): drops = 3.81×10^{-2}

Data for Drop Intervals

Number of Drops % of Total	Mass % of Total	Maximum Drop Diameter
45.36	5.83	5.0
44.41	35.83	10.0
7.67	27.84	15.0
2.29	22.09	20.0
0.13*	2.50	25.0
0.13*	5.91	30.0
0.00*	0.00	35.0
0.00*	0.00	40.0
0.00*	0.00	45.0
0.00*	0.00	50.0
0.00*	0.00	∞

Table F.13
Mechanical Sprayer: No-flake Paint #3

Fig. F.14 No-flake Paint #3

Table F.15 No-flake Paint #4

Fig. F.16 No-flake Paint #4

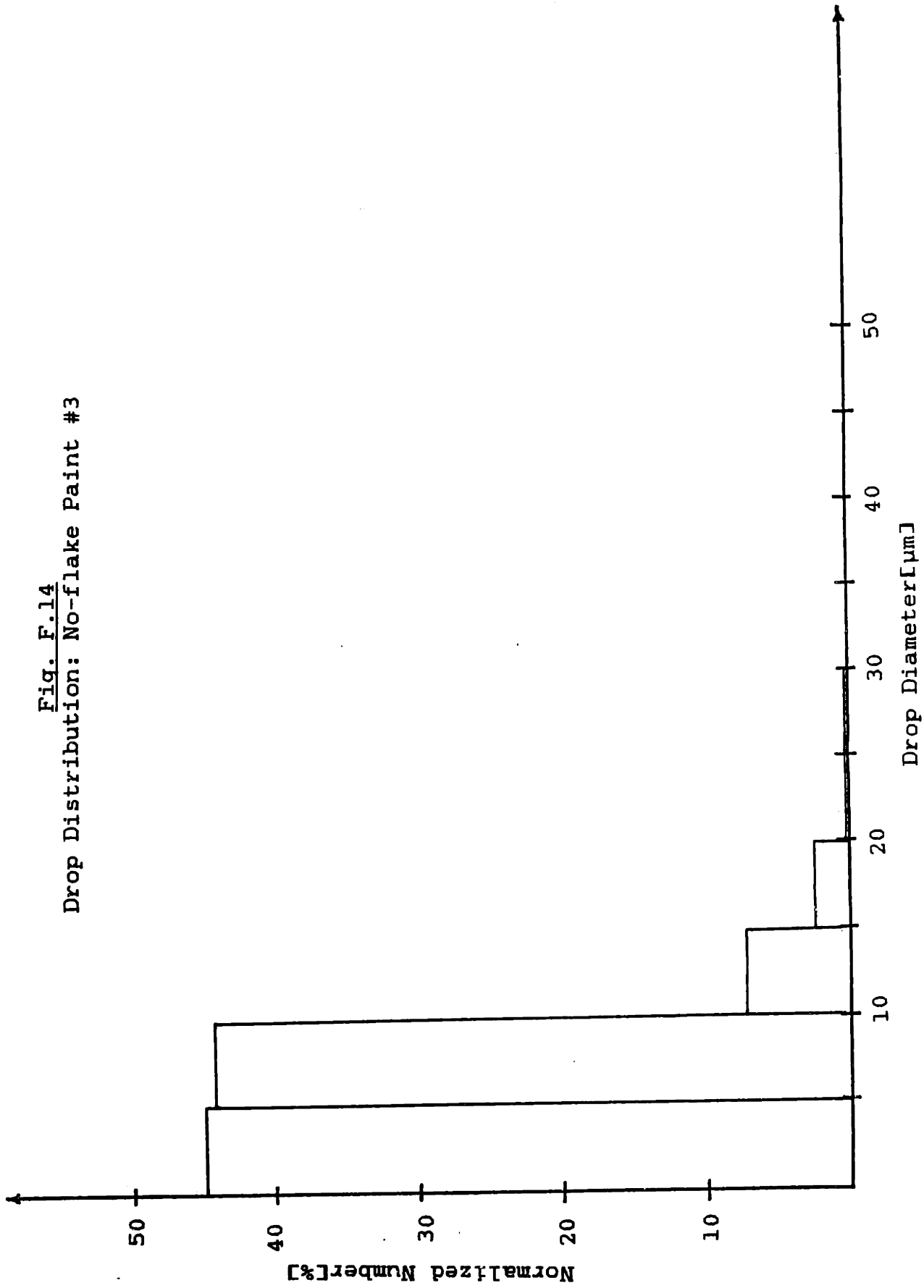

Fig. F.14
Drop Distribution: No-flake Paint #3

Drops

Average drop diameter(μm) = 38.0 Std. dev.(μm) = 37.1

With a probability of 95%
Error in the mean = 5.32
Standard deviation is between 34.60 and 39.95

Total number of drops = 187

Total number of flakes = 0

Mass Data

Total mass(μg): drops = 3.25

Data for Drop Intervals

Number of Drops % of Total	Mass % of Total	Maximum Drop Diameter
1.60*	0.00	5.0
11.76	0.04	10.0
13.90	0.19	15.0
15.51	0.42	20.0
11.23	0.69	25.0
4.81*	0.53	30.0
4.81*	0.90	35.0
3.21*	0.85	40.0
3.74*	1.45	45.0
3.74*	1.90	50.0
25.67	93.40	∞

Table F.15
Mechanical Sprayer: No-flake Paint #4

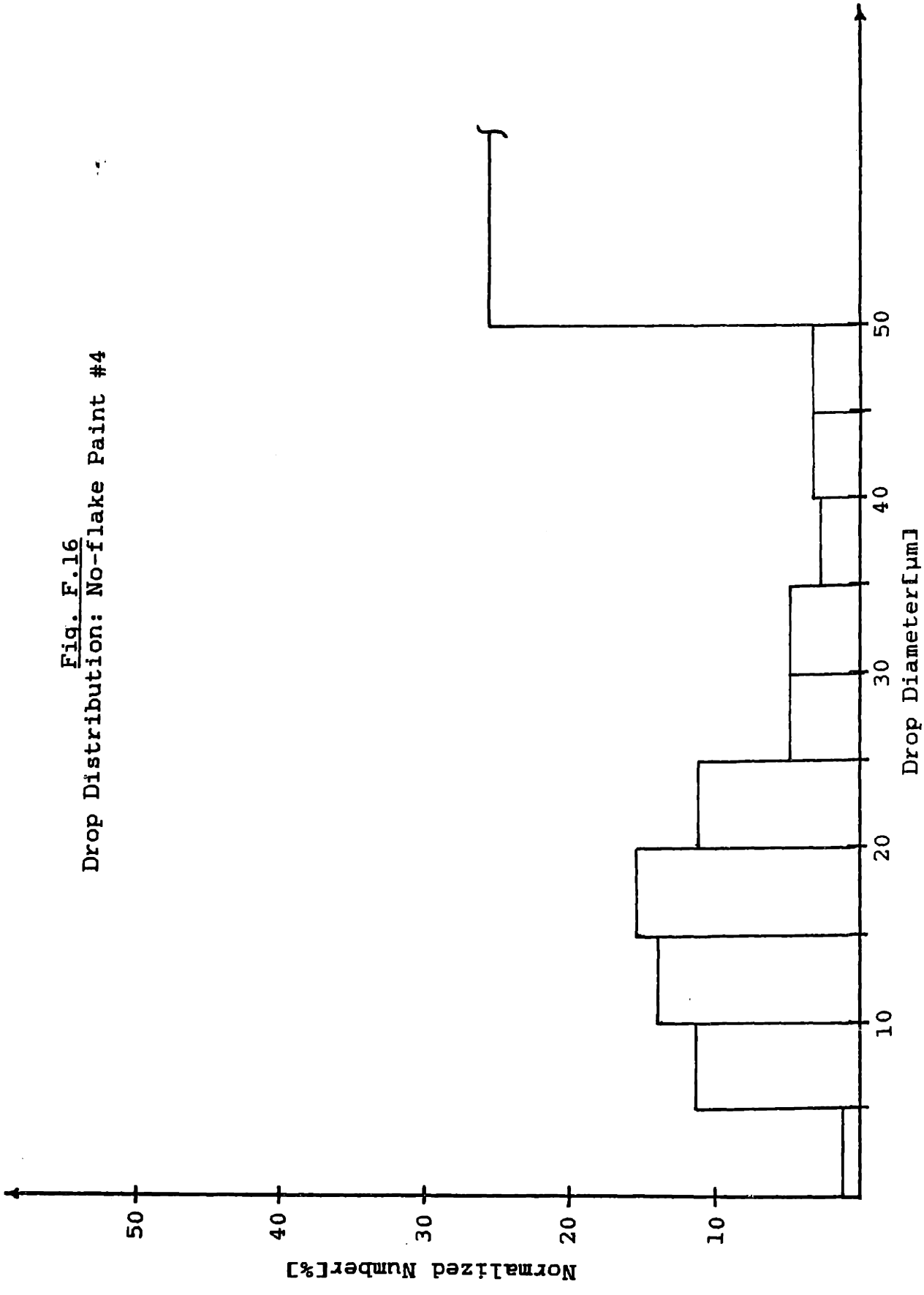

Fig. F.16
Drop Distribution: No-flake Paint #4